Mathematical modelling for tendon tissue engineering in a humanoid robotic bioreactor

Amy Kent

St Anne's College

University of Oxford

A thesis submitted for the degree of

Doctor of Philosophy

Michaelmas 2022

Abstract

Tendon tissue engineering aims to grow functional tissue *in vitro*. Tissue is grown in bioreactors which regulate the biochemical and mechanical environment of the growing cells. This thesis develops mathematical models motivated by the Humanoid Robotic Bioreactor under development at the Nuffield Department of Orthopaedics, Rheumatology and Musculoskeletal Sciences. Cells grow on a scaffold consisting of many aligned, flexible strings, surrounded by cell media. The focus of this work is modelling fluid-induced shear stresses and metabolite transport within this fluid-fibre composite.

We begin in chapter 1 by providing background on tissue engineering and introducing the humanoid robotic bioreactor. In chapter 2, we develop methods required in later chapters, identifying the correct way to treat integral constraints in multiple scales problems with a slowly varying domain. We consider a simple example from electrostatics, using a particular limit of the problem treated with standard multiple scales to identify the correct method to treat integral constraints directly. We apply this method in chapter 3, where we use homogenisation theory to obtain an effective model for the fluid-string interaction in the bioreactor scaffold. We solve the model in simple cases to explore how the cell shear stress depends on the imposed forcing. In chapter 4, we homogenise the metabolite transport problem, outlining the different effective models that arise for various regimes. We consider simple solutions to each case and identify the most relevant regime to the humanoid robotic bioreactor. We draw conclusions and outline directions for future work in chapter 5.

Acknowledgements

Firstly I would like to thank my supervisors, Jon Chapman, James Oliver and Sarah Waters, for sharing their knowledge. I feel fortunate to have learnt how to conduct research with the guidance and help of such phenomenal mathematicians. Your drive, vast number of ideas and endless passion for asymptotics are an inspiration.

Pierre Mouthuy, thank you for welcoming me into the bioreactor project and sharing an application rich in modelling problems. Nicole Dvorak, I appreciate your patience in helping me to understanding the humanoid robotic bioreactor and for the images used in figures 1.3 and 5.1.

I'm grateful to the researchers in OCIAM and the Mathematical Institute who make it a great place to work. In particular, I'd like to thank Mohit Dalwadi and Ian Hewitt for being open to discussing ideas and offering some sage advice. Michael McPhail and Jessica Williams for help when learning FEniCS. Edwina Yeo, Helen Saville, Michael Negus and Matt Shirley, your friendship throughout the DPhil has been invaluable.

Outside of the MI, I'm thankful to the friends I have met in Oxford who have made time away from the desk so enjoyable.

Lastly, I'd like to thank my family for their love and support. Stuart, for always being there. My sisters, Issy and Beccy, for chats involving some words of wisdom but mostly lots of laughter. Mick, for being a kind and calm influence amidst the chaos of Green Moor. My parents, for all your encouragement. I feel incredibly lucky that you have supported me in pursuing the things I enjoy.

Statement of Originality

The modelling and analysis presented in this thesis is my own work, performed under the supervision of Professor Sarah Waters, Professor James Oliver, Professor Jon Chapman and Professor Pierre Mouthuy. At the time of writing an article based on portions of chapter 3, authored by A. Kent, S. L. Waters, J. M. Oliver and S. J. Chapman is awaiting review, following submission to the SIAM Journal on Applied Mathematics.

A number of figures used to support review material are adapted from previous literature: figure 1.1 from [122], figure 1.2 from [85], figure 1.3 from [85], figure 1.5 from [85], figure 3.1.c from [6] and figure 3.1.d from [117]. Permission for reuse has been granted in each case and is detailed with the first appearance of the figure.

Contents

Chapter 1

Introduction

1.1 Tendon tissue engineering

Tendon is a connective tissue which joins muscle to bone [114]. The predominant solid component of tendon is collagen, a protein which is arranged into different structures at different length scales [121], giving tendon a hierarchical structure as shown in figure 1.1. In tendons, the collagen structures are highly aligned, producing a tissue capable of transmitting force from muscle to bone [114]. Due to the large mechanical forces tendons experience *in vivo*, and a relatively poor intrinsic ability to repair, injury is common, resulting from both acute damage and degeneration from repeated loading. While treatments such as physiotherapy and extracorporeal shockwave therapy have given reasonable outcomes for some conditions [32], more invasive measures such as surgery may be required when serious tissue damage has occurred. Current surgical techniques typically use anchors to fix tendon to bone, combined with sutures to hold the tendon in place [79, 102]. Patient outcomes are not consistently good, with 40% of repairs for supraspinatus tendons failing within two years [22]. Often associated with poor tissue regeneration, re-tears are a particular problem in elderly patients [22].

An alternative approach to tendon repair surgery uses tissue grafts. The best surgical outcomes for large tears are observed using autografts, where tissue to

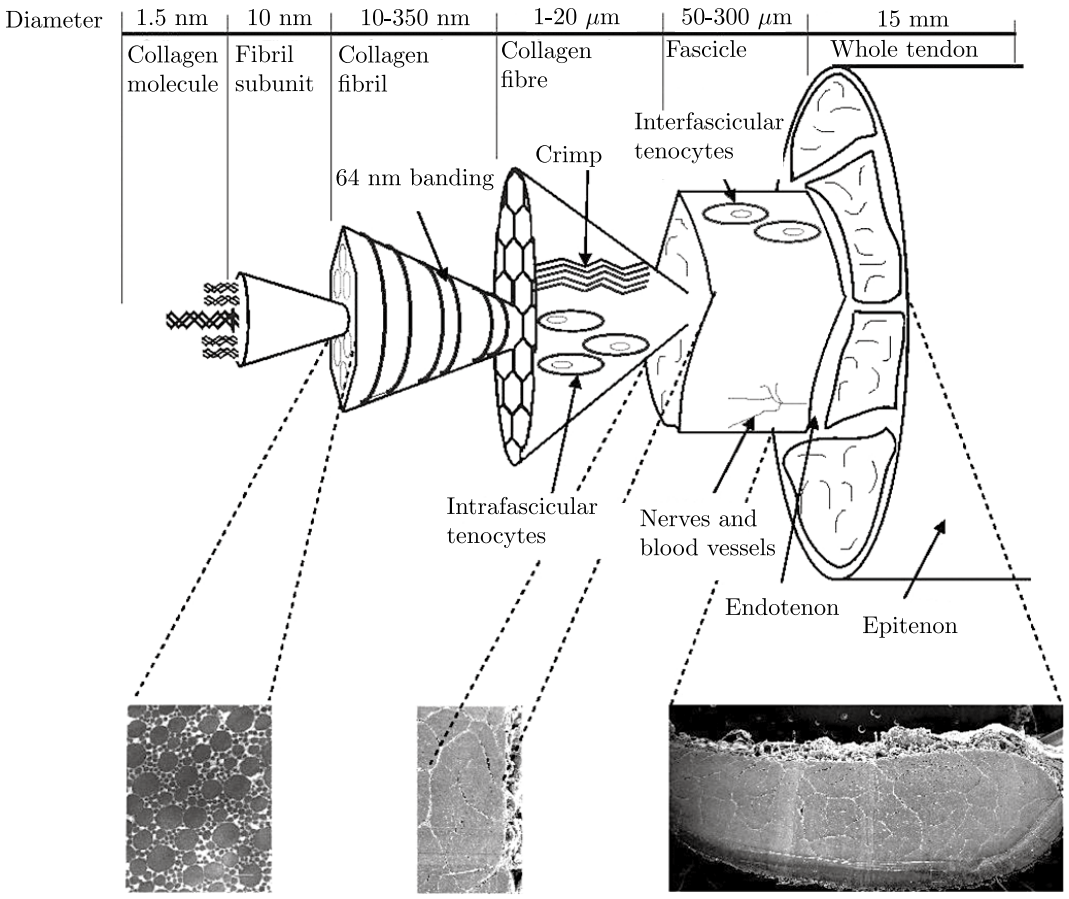

Figure 1.1: *Tendon schematic and microscopic images showing structure of tendon at different scales. Figure is adapted by permission from Wiley ©EJV Ltd [122].*

make the repair is taken from another part of the patient's body, although questions of compromised functionality of the site where the graft was taken mean that donor tissues (allografts) are increasingly used [74]. Using tissue from another individual increases the likelihood of an immune response and failure, which may be attributed to differences in age, body weight and activity between donor and patient [74]. Tissue grafts grown outside the body using cells from the patient offer potential solutions to these problems.

Tissue engineering aims to grow functional biological structures *in vitro* for transplant into the body [110]. Cells are grown on a scaffold material which aims

to mimic the role of the extracellular matrix (ECM) *in vivo*, providing structural support. The scaffold is placed inside a bioreactor which controls the environment of the growing cells, setting or monitoring the pH, temperature, flow profile and mechanical stimulation provided to the growing cells [28].

Early tendon bioreactors consisting of tissue explants held between two grips, see for example [41], showed that tendon tissue is mechanosensitive, meaning that its behaviour is modulated by the forces it experiences [46]. An alternative approach cultured cells isolated from tendons to explore their characteristics [14, 46], looking at the response to properties of the surface they were grown on and to mechanical loading [105, 134]. Whilst explant bioreactors and bioreactors culturing cell layers provide insights into tendon cell biology, developing tissue grafts requires a three dimensional construct. Three dimensional tissue grafts can be grown by seeding cells throughout a three dimensional scaffold. Many scaffold materials have been used, including decellularised tendon, human umbilical veins, and polymeric materials such as silk, polyurethane, collagen-coated polydimethylsiloxane and polycaprolactone, reviewed in [136]. In general scaffolds are chosen to be biocompatible, porous and mechanically able to withstand physiological forces, whilst being sufficiently flexible so as to transmit mechanical stimulation to the cells as they develop [28].

As referenced above, tendon tissue is mechanosensitive; mechanical stimulation within a suitable range is required for the tissue to remain healthy [29]. Mechanical loads which are too high can cause damage to the collagen microstructure, causing tears of the collagen fibres [108, 116]. Loading which generates high strain (in the region of 20%) also causes excessive apoptosis [108]. Conversely, the absence of sufficient stress causes resorption of the ECM, causing a decrease in tensile strength [56, 133]. Stress deprivation also alters the collagen structure and results in a decrease in the number of fibroblasts, which become more rounded in contrast to their usual elongated shape [56]. Within the range of physiological strains (less than 8%), applying cyclic mechanical loading increases cell density [2], collagen deposition [109] and the elastic modulus [56]. Mechanical stimulation induces changes in the gene expression profiles, generating an upregulation of tendon-related marker genes for mesenchymal stem cells as described in [29] and the

references therein. Both fluid-induced shear stress and strains due to deformation of the ECM play a role in tendon mechanotransduction [72]. To provide mechanical stimulation to cell, bioreactors typically impose an axial or biaxial loading to the tissue construct [126]. However, *in vivo* tendons experience multiaxial stresses [104], motivating the development of the humanoid robotic bioreactor we introduce in section 1.2 which aims to mimic physiological stresses.

In addition to a suitable mechanical environment, tendon cells require an adequate supply of nutrients. We defer a more detailed description of the role of nutrients relevant in tendon tissue engineering to chapter 4, where we develop models for nutrient transport. Here, we focus on features of bioreactor design which affect transport processes. In bioreactors where the culture media is static, nutrients can only be delivered to cells by diffusive processes. Whilst this may be suitable for quasi-two dimensional structures, diffusive mass transport becomes insufficient for larger three dimensional structures. Imposing a flow by mixing media or rotating the bioreactor chamber is one method to increase the rate of nutrient delivery [82]. Perfusion bioreactors further increase nutrient delivery to the interior of the construct by flowing media through a porous scaffold [26]. In addition to increasing the rate of nutrient transport, introducing flow to the bioreactor system provides mechanical stimulation in the form of fluid shear stress.

Having outlined general features of tendon bioreactors, we turn to describing the humanoid robotic bioreactor which motivates this thesis.

1.2 The humanoid robotic bioreactor

Musculoskeletal humanoid robots aim to mimic the human musculoskeletal system (bones, muscles and tendon) using string actuators to replicate the range of motion and forces observed in the body [11]. The humanoid robotic bioreactor consists of a robotic shoulder which is constructed to mimic shoulder physiology, as shown in figure 1.2. The humerus and the glenoid socket and coracoid process of the scapula are additively manufactured, and a surgical shoulder implant ensures smooth motion at their junction. Six string 'muscles' actuate the robotic joint,

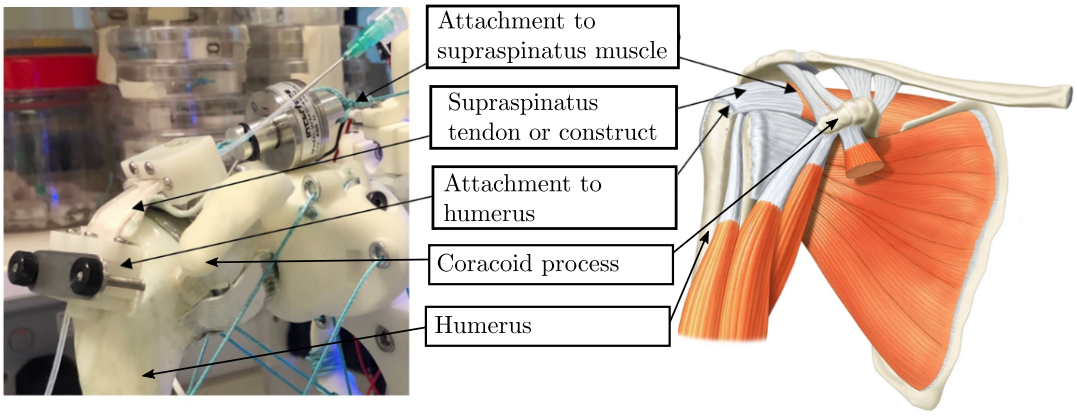

Figure 1.2: Structure of the humanoid robotic shoulder (left) compared with the human shoulder joint (right). *Figure adapted from [85] under the CC-BY licence [1].*

mimicking the profile, speed and forces of physiological motions [85]. Cells are cultured in a flexible bioreactor chamber, fixed in the position of the supraspinatus tendon, as shown in figure 1.2 [85]. The chamber, photographed in figure 1.3.b, consists of a deformable, polyurethane, outer membrane which encloses the cell media and maintains sterility. The membrane encases a scaffold made from 200 flexible fibres. These fibres are made from polycaprolactone, a polymer which degrades in the body at a similar rate to ECM growth. Manufactured using electrospinning and drawing, the fibres display an aligned microstructure similar to that of native tendon fascicles [84]. The flexible chamber is fixed at each end to additively-manufactured inserts which attach to the robotic shoulder and to the inlet and outlet tubing used to deliver culture media to the growing cells, as seen in figure 1.3.b.

We list typical scales of experimental parameters in table 1.1, which will inform the modelling we present in later chapters. In particular, we note that there is separation between the typical scale of the fibre spacing and the chamber width. In chapter 2 we will introduce homogenisation *via* multiscale asymptotics, a modelling method that exploits such scale separation. In addition, the flow velocity, media properties and the chamber length are such that the Reynolds number $Re = \rho_m UL/\mu = 0.3$. As such, we anticipate that the inertial terms in the fluid flow will

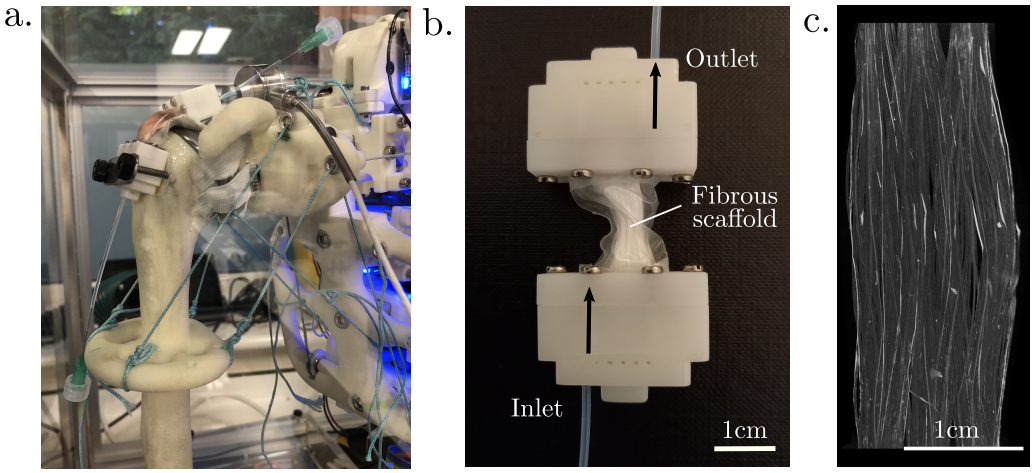

Figure 1.3: The humanoid robotic bioreactor. *a. The humanoid robotic shoulder with the bioreactor chamber attached in the position of the rotator cuff tendon. b. The bioreactor chamber consists of a flexible outer membrane and a fibrous scaffold material. Media is flowed through the chamber via the inlet and outlet photographed. c. Micro-CT of two bundles like those which comprise the bioreactor scaffold. Images are with thanks to Nicole Dvorak, NDORMS.*

be small. In chapter 3 we review modelling methods for interactions between slow, viscous flow and flexible fibres. In table 1.1 we have only included parameters relevant to modelling the fluid flow problem. Full details of the components of the bioreactor system and its construction are given in [85].

1.2.1 Operation

The initial step in the tissue engineering process is *cell seeding*, wherein cells suspended in culture media are injected into the chamber through the inlet tube shown in figure 1.3.b.

Physical quantity		Scale
Chamber length	L	3 cm
Fibre spacing	l	0.4 mm
Fibre radius	b	70 μm
Perfusion velocity	U	0.01 mm/s
Cell media dynamic viscosity	μ	0.9 mPa s
Cell media density	ρ_m	1 g/cm^3

Table 1.1: Experimental parameters

1.2.1.1 Mechanical stimulation

After a period of rest following cell seeding, the inlet and outlet ports to the chamber are blocked, and the chamber is attached to the robotic arm as shown in figure 1.3.a. A programmed motion of adduction (figure 1.4.a) and abduction (figure 1.4.b) is carried out daily for 30 minutes, applying forces to the growing cells. The abduction-adduction motion was chosen as *in vivo* this recruits the supraspinatus tendon, offering a simple in-plane motion for primary studies on the effects of mechanical stimulation. Future experimental work aims to incorporate further degrees of motion to facilitate rotation and more complex motions [85]. Adduction and abduction motion is programmed which has a total range of around 60^o, moving either side of the line parallel to the trunk as shown in figure 1.4. The cycle frequency imposed is around 0.07Hz, and a break of 5 seconds is imposed every two cycles (see figure 1.5). The tension in the string supraspinatus muscle can be adjusted to alter the maximum force exerted through the construct, informed by the estimated forces experienced by the supraspinatus *in vivo*. The forces exerted on the tissue construct throughout these forcing cycles are measured by a force gauge placed between the upper end of the chamber and the top string

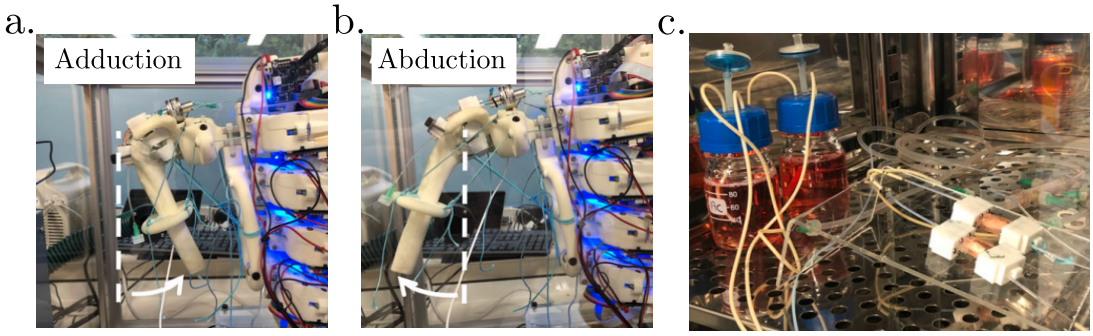

Figure 1.4: *Modes of operation for the tendon bioreactor. a.-b. The chamber is attached to the robotic shoulder. String 'muscles' cause the shoulder to abduct and adduct, exerting forces on the bioreactor scaffold. c. Cell media is pumped through the chamber to supply nutrients to the growing tissue. Figures are adapted from [85] under the CC-BY licence.*

muscle [85]. The variation in the motion of the robotic arm and forces imposed on the scaffold are shown in figure 1.5. Averaged maximum forces measured on the construct between 11-45N result in a scaffold strain of $2.6 - 8\%$ in the direction of the scaffold fibres, representative of strains estimated for tendon *in vivo*. The cyclic forcing imposed is within the bounds estimated for forces experienced by the supraspinatus tendon undergoing small amplitude abduction-adduction motion.

In an experiment exploring the effects of different forcing regimes on cell expression, higher proliferation rates were observed for the control scaffold compared with those subject to cyclic forcing. Few cells remained on the scaffold subject to the high forcing regime (imposed force up to 45N), suggesting apoptosis or detachment of the cells from the scaffold [85]. Thus, whilst the forces imposed on the whole scaffold match those experienced by the tendon *in vivo*, the differences in microstructure may give rise to different microscale shear stresses, which may have a detrimental effect on cell development. Mathematical modelling of the bioreactor scaffold may be able to offer some insight into the reason for apoptosis. Developing a model that links the shear stresses experienced by cells on the microscale to forces imposed by the robotic shoulder will enable an estimation of the shear stresses experienced in the different operating regimes. Further, modelling

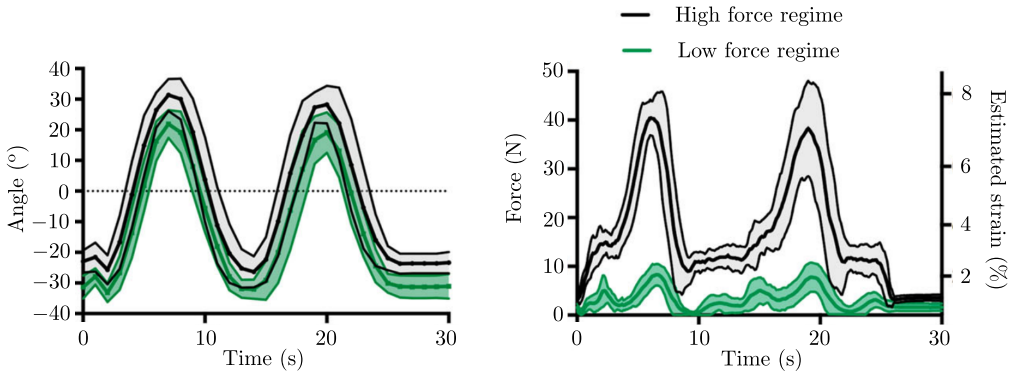

Figure 1.5: Forces that are exerted on the bioreactor scaffold through two cycles of abduction and adduction. *Left: angle between the robot arm and vertical. Right: The corresponding force exerted on the chamber as the robotic arm is in the position shown on the left. Figure adapted from [85] under the CC-BY licence [1].*

may be able to offer suggestions for alterations of the microstructure or operating parameters which could result in microscale shear stresses in the bioreactor better resembling those *in vivo*. We will aim to develop a multiscale model of the interaction between fluid flow and the scaffold in chapter 3 where we illustrate how the microscale shear stress can be estimated.

1.2.1.2 Perfusion

When not attached to the robotic shoulder, the chamber is connected to a perfusion system, which pumps media into the chamber to supply nutrients to the growing cells and facilitates the removal of the waste products, as shown in figure 1.4.c. The concentrations of glucose, oxygen and lactate are monitored in the efflux, each playing a key role in tendon tissue development as we will discuss in chapter 4. Oxygen concentration in the media flowing through the chamber outlet is measured by a chemical optical sensor which determines the concentration by the degree of fluorescence quenching which is induced by the presence of oxygen. The sensor is attached to the outlet tubing meaning that changes in the efflux in time can be monitored. To measure the concentration of lactate and glucose, a biological

sensor is used. The chamber must be disconnected from the perfusion system to measure the lactate and glucose concentrations and so it cannot be measured continuously.

The metabolite measurement techniques all provide an indication of the total concentration in the chamber at the time of measurement. Here, mathematical modelling can provide some insight into the spatial distribution of metabolites across the bioreactor chamber rather than an averaged measure derived from experimental measurements of the efflux. Modelling could identify of areas within the scaffold which do not receive sufficient nutrient which may be difficult to attain experimentally without imaging various endpoint studies. Spatial models of the nutrient distribution may offer some insight into the number of cells observed to undergo apoptosis or detachment. Developing a multiscale model can also facilitate analysis of the influence of varying rates of cell uptake, both in time and spatially if, for example, the cells were not distributed evenly across the bioreactor scaffold. We will outline the development of a multiscale model of nutrient transport in the bioreactor in chapter 4. In addition to ensuring sufficient delivery of essential nutrients, the perfusion process will exert fluid-induced shear stresses on the growing cells. Combining the results of modelling nutrient transport with shear stress can aid in selecting parameter regimes that support healthy tissue growth without requiring repeated experiments.

1.3 Thesis overview

In this thesis, we present the development of multiscale models of flow and solute transport in fluid-fibre composite, consisting of Stokes flow interacting with assemblies of deformable fibres. Homogenisation *via* multiscale asymptotics is used to derive the effective models in each case. The primary application motivating this work is the humanoid robotic bioreactor under development at the Nuffield Department of Rheumatology and Musculoskeletal Sciences for tendon tissue engineering applications as described in section 1.2.

In chapter 2, we introduce homogenisation *via* multiscale asymptotics which is

a method used to derive the effective properties of composite materials, typically with a periodic microstructure. A discussion of the standard method is given before outlining extensions to the technique which can be used to treat problems where the microstructure is locally periodic, or when the problem involves an integral constraint. The aim of this chapter is to develop the method to treat integral constraints in multiple scales problems which are posed on a slowly varying domain. We consider a simple problem from electrostatics, where the effective model derived using standard multiple scales techniques can be compared with the method devised to treat integral constraints on a slowly varying domain directly.

The result obtained in chapter 2 is applied in chapter 3, where we develop an effective model of fluid-string interaction. We begin by reviewing various methods which have been used to model fluid-structure interaction in fibre ensembles. We present the model derivation using homogenisation *via* multiscale asymptotics, which results in an effective model for the fluid-string composite as a deformable porous medium. The material permeability is given by the averaged solution to a microscale problem which also gives the local variation in shear stress at the string surface. We solve the model in some simple geometries and identify parameters which influence the shear stress for various boundary conditions.

In chapter 4, we couple the fluid-structure model developed in chapter 3 with the nutrient transport. We discuss nutrient transport in tendon tissue engineering and outline modelling techniques applied in tissue engineering before considering multiscale modelling of transport processes in general. We again use homogenisation *via* multiscale asymptotics to identify effective models for nutrient transport in the fluid-string composite. We consider the effective models which result in various regimes determined by the relative size of advective and diffusive transport processes and cell uptake.

We conclude in chapter 5 by summarising the thesis and implications of the work we present. We outline possible directions of future work, highlighting areas to develop in view of the bioreactor system, extensions to other applications and some problems of mathematical interest.

Chapter 2

Homogenisation of problems with integral constraints in a slowly varying domain

Homogenisation *via* multiscale asymptotics is a technique for deriving the effective properties of composite materials. The method was initially applied to materials with an exactly periodic microstructure, although the theory has been extended to treat problems with a microstructure that slowly varies. An additional extension to the standard theory of homogenisation was developed to treat problems with integral conditions. In this chapter, we set out to combine these two methods, establishing the correct way to write integral constraints on a slowly varying domain in multiple scales form. This knowledge will be required in chapter 3 where we derive a homogenised model of fluid-structure interaction in the bioreactor scaffold. We consider a simple problem from electrostatics which can be written both in terms of integral constraints and in a form amenable to homogenisation using standard multiple scales. A comparison of homogenised model obtained *via* the two approaches provides validation for the proposed method.

We begin in section 2.1 with an introduction to homogenisation *via* multiscale asymptotics. We provide examples of literature using homogenisation in slowly varying domains or integral constraints. In section 2.2, we introduce the electro-

statics problem in one-dimension. The insights here prove useful in section 2.3 where we consider the two-dimensional problem. We illustrate the problems that arise and seek inspiration from a transport theorem to identify how to write the integral condition in multiple scales form. We discuss the work in section 2.4.

2.1 Introduction

Homogenisation *via* multiscale asymptotics is an upscaling technique that can be used to derive the effective properties of composite materials, see for example [62, 64]. The disparity between the length scale describing microstructural variation, the *fast scale*, and variation on the scale of the whole material, the *slow scale*, can be used to simplify the problem. The method considers a series of problems parameterised by the magnitude of this disparity, obtaining the effective material properties in the limit where this disparity becomes very large. Instead of solving the governing equations on a complicated domain, or with rapidly varying coefficients, applying the homogenisation method results in two simpler problems: the microscale problem and the macroscale problem. Typically, there is a one-way coupling between these two problems as the averaged solutions to the microscale problem provide the coefficients in the macroscale problem. Thus, homogenisation provides a way to derive the effective material properties systematically from the microstructure. The technique has been applied in various systems with a hierarchy of scales, for example: modelling fluid flow in porous media, wave propagation in poroelastic materials, filtration systems and flow in biological tissues [36, 64, 68, 112].

The method proceeds by treating the fast and slow scales independently, transforming the governing equations into multiple scales form. Posing multiple-scales expansions for all dependent variables, we then derive the form of the microscale and macroscale problems by comparing coefficients at each order in the expansion. Typically, we find that the leading-order term in the expansion is independent of the fast variable. At higher orders, we obtain a microscale problem, or cell problem, which describes the microscale variation of higher order terms. The assumption of a periodic microstructure provides a necessary constraint to close the

microscale problem. Upon averaging the microscale solution, we obtain the coefficients for the macroscale problem which itself is given by the average of a higher order equation.

2.1.1 Multiple scales problems on a slowly varying domain

In some applications, material heterogeneity means that the assumption of exact periodicity at the microscale breaks down [34]. Homogenisation *via* multiscale asymptotics can still be useful for such applications providing the problem is locally periodic. The simplest example of slow variation is where the unit cell remains fixed but the dimensions of subdomains vary, such as a porous material consisting of cylinders with a slowly varying radius [20]. When the dimensions of the unit cell vary across the domain, a mapping must be used to transform the equations to a periodic reference configuration where homogenisation can be performed.

Perhaps the simplest example of such a mapping is given in [13, 24], where there is one-dimensional variation in the microstructure. A mapping transforms the system to an exactly periodic reference configuration where homogenisation can be carried out. As the mapping depends only on the slow scale, the multiple scales analysis can be performed in the exactly periodic configuration before inverting the mapping. A more general map accounting for shear, stretch and rotation is considered in [100] and mappings can also account for growth [30]. After multiple scales analysis and map inversion, the deformation gradient of the mapping appears in the coefficients of the macroscale model [100]. In many instances, the mapping to the reference configuration is a prescribed function of slow position or time [31, 100]. It is possible for the mapping to be a function of the dependent variables. For example Peter and Böhm considered a problem where the temporal evolution of the mapping was coupled to the dependent variables [97]. The result was another equation in the homogenised model for map evolution which must be solved in conjunction with the homogenised model.

A mapping of the fast-coordinate has been used in modelling transport in spatially varying porous media [20]. Here, the transformed microscale problem retains some global variation despite being locally periodic. When the microscale

domain slowly varies, extra care must be taken in transforming Neumann and Robin boundary conditions into multiple scales form [20]. Naively, we may write the normal in multiple scales form by considering the geometry in a single unit cell. This approach fails in problems with a slowly varying domain, as illustrated in [20], because the normal will vary as we move across the domain. Describing the boundary location using a level set function, it can be shown that this variation enters at first-order - the correction being in the tangent direction with a magnitude related to the rate of change of the domain with the slow scale. Many examples of multiple scales problems that use a level set function to treat Neumann conditions exist in the literature, among them [13, 17, 20, 36, 35, 34, 48, 71, 77, 99, 100, 107, 124].

2.1.2 Integral constraints in multiple scales problems

A different class of problems that require an extension to standard homogenisation methods are those involving integral constraints. The result of a conservation condition, integral constraints appear in applications such as modelling wave propagation in bubbly liquids, radiation in porous media and the electric potential within nematic crystals [17, 25, 101]. For point-wise boundary conditions, we can treat the macroscale coordinate within a given unit cell as fixed. For integral conditions, the macroscale coordinate will vary across the inclusion boundary giving rise to first-order contributions to the integral expansion which can appear in the macroscale problem [25].

In the multiscale modelling of thermal radiation in porous media, an integral appears in the boundary condition for radiative transfer [101]. The heat flux due to radiation on surface is equal to the difference between emitted and absorbed radiation. The emitted radiation can be calculated point-wise using the Stefan-Boltzmann law but the incident radiation is written as the convolution of the Stefan-Boltzmann law with the view factor. In effect, the integral sums over the radiation emitted by all surfaces in view of a point to calculate the incident radiation [101]. It is shown that the naive approach of neglecting the variation of the slow-coordinate over the unit cell results in different parameters in the

macroscale model as terms are missed from the boundary condition [101].

Integral constraints on a slowly varying domain have appeared in the literature, see [10, 17, 38]. In the model developed to identify the resonant frequencies of a nuclear reactor, the fuel rods were modelled as rigid cylinders, surrounded by a viscous fluid, that were tethered to their original position by Hookean springs [10]. The force balance between rod inertia, the spring restoring force and hydrodynamic stress contained an integral posed over a slowly varying domain as the rod displacement varied over the domain [10]. In a multiscale model of a nematic crystal, the influence of metal dopant particles on the material properties of a defect-free crystal was considered [17]. The rotation of dopant particles about a fixed location on a square, periodic lattice was set by the surrounding flow of viscous fluid and externally applied electric field [17]. An integral appears in this problem in the equations for the electric potential in the crystal phase, forming a boundary condition which ensures charge conservation on each dopant particle [17]. In a model of soil as a mixture of air, solid and a poroelastic mixed phase consisting of elastic colloids saturated with pore water, the solid phase translated as a rigid body. The slowly varying displacement was coupled to the mixed and air phases by balancing the total stress on the solid-air and solid-mixed phase boundaries with gravitational forces; the calculation of the total stress involves an integral constraint. We have been unable to recover the same homogenised model as presented in [10, 17, 38]. In section 2.3.2.1, we illustrate the additional terms that arise if we follow the method of [17, 38] where the normal is expanded within the integral constraint applied to a simple problem in electrostatics. We then identify the multiple scales form of integral constraints on a slowly varying domain that leads to the correct homogenised problem.

The correct way to write integral constraints in multiple scales form was identified by considering a simple problem from electrostatics which can be written as a particular limit of a standard multiple scales problem [25]. The problem was homogenised with standard methods and the correct form of the macroscale problem was identified by taking the limit of one parameter being infinite. The problem with integral constraints was then treated directly by expanding the dependence of the slow scale on the fast scale within the integrand [25]. The multiple scales

form of the integral constraint was validated by comparison of the homogenised models obtained *via* each approach. In this chapter, we adopt a similar approach to that used to derive the multiple scales form for integral constraints [25]. We again work with a simple problem from electrostatics with modified scaling to highlight all terms that appear in the multiple scales form. We begin considering a one-dimensional problem before moving to the multidimensional problem where the expansion of the normal adds complication.

2.2 One-dimensional problem

We consider the electric potential $\phi = \phi(x)$ in an composite consisting of a dielectric Ω_e of permittivity ε_e interspersed with dielectric inclusions Ω_i of permittivity ε_i. The layers Ω_i are periodically spaced at a distance l up to its width L, as shown in figure 2.1. The coordinate x measures the distance from the left edge of the composite as shown in figure 2.1. The half-width of the perfectly dielectric inclusion $a = a(x)$ is a piece-wise constant function defined by

$$a(x) = a(x_0^k) \quad \text{for} \quad (k-1)l < x < kl, \tag{2.1}$$

where $x_0^k = (k - 1/2)l$ is the midline of the kth inclusion for $k \in \mathbb{Z}^+$, with a given inclusion referenced by the superscript index. The kth inclusion is then defined by $\Omega_i^k = \{x : x_0^k - a(x_0^k) < x < x_0^k + a(x_0^k)\}$, with Ω_i being the union of all layers with permittivity ε_i. The remaining space is the dielectric with permittivity ε_e, that is $\Omega_e = \{x : (k-1)l < x < x_0^k - a(x_0^k) \text{ or } x_0^k + a(x_0^k) < x < kl, \text{ for } k \in \mathbb{Z}^+\}$.

The electric potential satisfies Gauss's law in the dielectric

$$\frac{d}{dx}\left(\varepsilon_e \frac{d\phi}{dx}\right) = -\rho \qquad \text{in} \quad \Omega_e, \tag{2.2}$$

$$\frac{d}{dx}\left(\varepsilon_i \frac{d\phi}{dx}\right) = -\rho \qquad \text{in} \quad \Omega_i. \tag{2.3}$$

where $\rho = \rho(x)$ is the charge density, which we assume is known *a priori*. We assume that the electrical permittivity within each region is constant. At the

boundary between the two dielectrics, we have continuity in the electric displacement,

$$\left[\varepsilon\frac{d\phi}{dx}\right]_i^e = 0, \tag{2.4}$$

where $[.]_i^e$ denotes the jump in a quantity at the interface between the two dielectrics, located at $x_0^k \pm a(x_0^k)$ for $k \in \mathbb{Z}^+$. For the electric field to be defined everywhere, we require the electric potential to be continuous at each interface, that is

$$[\phi]_i^e = 0. \tag{2.5}$$

We nondimensionalise the problem using the following scales,

$$x = L\hat{x}, \quad \rho = \rho_c\hat{\rho}, \quad \phi = \frac{L^2\rho_c}{\varepsilon_e}\hat{\phi}, \quad a = L\hat{a}, \tag{2.6}$$

where ρ_c is a characteristic charge density, chosen so that dimensionless charge density is $O(1)$ at all points in the domain. We do not specify the distribution of the charge density; the analysis which follows will hold for all distributions which slowly vary. To simplify calculations, we introduce the dimensionless permittivity $\hat{\varepsilon}$ which takes the values $\hat{\varepsilon} = \hat{\varepsilon}_e = 1$ in Ω_e and $\hat{\varepsilon} = \hat{\varepsilon}_i = \varepsilon_i/\varepsilon_e$ in the inclusions Ω_i.

Using the scales in (2.6) we nondimensionalise (2.2)-(2.3), which gives

$$\frac{d}{dx}\left(\varepsilon_e\frac{d\phi}{dx}\right) = -\rho \quad \text{in} \quad \Omega_e, \tag{2.7}$$

$$\frac{d}{dx}\left(\varepsilon_i\frac{d\phi}{dx}\right) = -\rho \quad \text{in} \quad \Omega_i, \tag{2.8}$$

where we have dropped hats on dimensionless quantities. The dimensionless condition on displacement (2.4) becomes

$$\left[\varepsilon\frac{d\phi}{dx}\right]_i^e = 0, \tag{2.9}$$

and the continuity condition on the electric potential (2.5) is

$$[\phi]_i^e = 0. \tag{2.10}$$

Our aim is to establish an effective model for the composite in the limit where the inclusion layers are perfectly dielectric, that is when ε_i is infinite. There are

two approaches that may be taken to obtain the form of the homogenised in the limit $\varepsilon \to \infty$: we can homogenise (2.7)-(2.10) then take the limit, or take the limit $\varepsilon \to \infty$ before deriving the homogenised model.

If the limit $\varepsilon_i \to \infty$ is taken before homogenisation, (2.7) and (2.5) are unchanged. In the inclusion, taking $\varepsilon_i \to \infty$ in (2.8)-(2.9) gives

$$\frac{d^2\phi_0}{dx^2} = 0 \quad \text{in} \quad \Omega_i, \tag{2.11}$$

with

$$\left.\frac{d\phi}{dx}\right|_i = 0. \tag{2.12}$$

Thus, we have a constant potential in each inclusion

$$\phi = \phi_0^k \quad \text{in} \quad \Omega_i^k, \tag{2.13}$$

where the constant may be different in each Ω_i^k. In taking this limit, we have lost one condition coupling the two dielectric regions in (2.9). We can obtain a condition to close the problem by considering the integral of (2.8) over Ω_i, which gives

$$\left[\varepsilon_i \frac{d\phi}{dx}\right]_{x_0^k - a(x_0^k)}^{x_0^k + a(x_0^k)} = -\int_{\Omega_i^k} \rho dx, \tag{2.14}$$

where we have evaluated the integral limits on the left-hand side. Applying (2.9), we have

$$\left[\varepsilon_e \frac{d\phi}{dx}\right]_{x_0^k - a(x_0^k)}^{x_0^k + a(x_0^k)} = -\int_{\Omega_i^k} \rho dx, \tag{2.15}$$

where we again can take the limit $\varepsilon_i \to \infty$. The integral constraint (2.15) is a statement of charge conservation on the perfect dielectric.

In section 2.2.1, we will homogenise (2.7)-(2.10) using standard homogenisation techniques. Taking the limit $\varepsilon_i \to \infty$ in the homogenised model will give the effective model for a composite consisting of a dielectric with perfectly dielectric inclusions. We will compare this result with the model obtained from the homogenisation of (2.7), (2.10), (2.13) and (2.15). In the second formulation, we extend methodology developed in [25] treat the integral condition directly, identifying the multiple scales form of (2.15). Here, we need to establish the correct way to extend this work to deal with the slow variation in the inclusion width. We will present this approach in section 2.2.2.

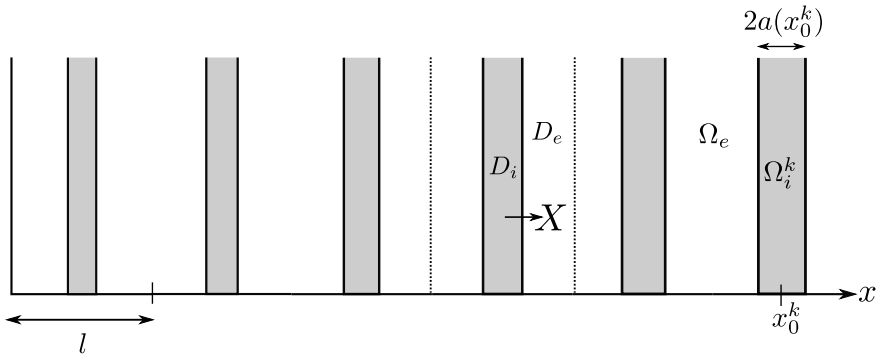

Figure 2.1: *Schematic of the one-dimensional composite. Perfectly dielectric layers which have a width $2a(x)$ that varies slowly across the domain are shown in grey. The unit cell is marked by dashed lines; within a given unit cell, the exterior region is D_e and the region occupied by the perfectly dielectric inclusion is D_i.*

2.2.1 Standard multiple scales

We consider a material constructed from layered dielectrics, as shown in figure 2.1. The electric potential will satisfy Gauss's law,

$$\frac{d}{dx}\left(\varepsilon\frac{d\phi}{dx}\right) = -\rho, \tag{2.16}$$

where the permittivity ε is a piece-wise constant function, taking on the value $\varepsilon = \hat{\varepsilon}_e = 1$ in the exterior region and $\varepsilon = \hat{\varepsilon}_i = \varepsilon_i/\varepsilon_e$ in the inclusions. Henceforth, we drop hats denoting the dimensionless form of the permittivity. We have continuity of the electric field and electric potential at each interface, that is

$$\left[\varepsilon\frac{d\phi}{dx}\right]_i^e = 0, \tag{2.17}$$

$$[\phi]_i^e = 0. \tag{2.18}$$

Assuming that the material is constructed from many of the layers shown in figure 2.1, we can define a small parameter $\delta = l/L \ll 1$ that gives the ratio of the separation of the perfectly dielectric regions to the length of the material. We introduce a slow scale x, which describes the variations across the whole material and a fast scale $X = x/\delta - 1/2 - \lfloor x/\delta \rfloor$, which describes variations across a single repeating unit of the composite, the 'unit cell'. The unit cell for this problem D is

highlighted by dashed lines in figure 2.1, where $-1/2 \leq X \leq 1/2$. The perfectly dielectric region of the unit cell is given by $D_i = \{X : -A < X < A\}$ where $A = a(x)/\delta$ is the inclusion width measured in fast coordinates. The dielectric region with permittivity ε_e is $D_e = \{X : -1/2 < X < -A \text{ and } A < X < 1/2\}$. As the inclusion width slowly varies across the domain, both D_e and D_i are functions of the slow position.

We apply the chain rule to write derivatives in multiple scales form, treating the fast and slow scales independently, which gives

$$\frac{d}{dx} \to \frac{\partial}{\partial x} + \frac{1}{\delta}\frac{\partial}{\partial X}. \tag{2.19}$$

We pose an multiple scales expansion for the electric potential:

$$\phi = \phi_0(x, X) + \delta\phi_1(x, X) + O(\delta^2) \tag{2.20}$$

as $\delta \to 0$, each term in the expansion is assumed to be 1-periodic in X, motivated by the composite microstructure, meaning that $\phi_i(x, X + 1) = \phi_i(x, X)$. We also assume that the derivatives of each term are 1-periodic in X. We write the governing equations (2.16)-(2.18) in multiple scales form, substitute the expansion (2.20) and compare coefficients at each order of δ.

At leading-order, we find

$$\frac{\partial}{\partial X}\left(\varepsilon\frac{\partial \phi_0}{\partial X}\right) = 0 \quad \text{in} \quad D, \tag{2.21}$$

$$\left[\frac{\partial \phi_0}{\partial X}\right]_i^e = 0, \tag{2.22}$$

$$[\phi_0]_i^e = 0. \tag{2.23}$$

There is nothing to force any fast scale variation in (2.21)-(2.23) and thus we have a potential that is independent of the fast scale at leading-order, *i.e.* $\phi_0 = \phi_0(x)$.

At first-order, we find

$$\frac{\partial}{\partial X}\left(\varepsilon\left(\frac{\partial \phi_1}{\partial X} + \frac{d\phi_0}{dx}\right)\right) = 0 \quad \text{in} \quad D, \tag{2.24}$$

$$\left[\varepsilon\left(\frac{\partial \phi_1}{\partial X} + \frac{d\phi_0}{dx}\right)\right]_i^e = 0, \tag{2.25}$$

$$[\phi_1]_i^e = 0. \tag{2.26}$$

We can integrate (2.24) once with respect to the fast scale to obtain

$$\varepsilon\left(\frac{\partial\phi_1}{\partial X}+\frac{d\phi_0}{dx}\right)=b_0(x), \tag{2.27}$$

where b_0 is a function of integration which must satisfy a closure condition that comes from the $O(\delta^2)$ equations. Integrating (2.27) over the unit cell, we find

$$\frac{d\phi_0}{dx}=b_0\int_{-1/2}^{1/2}\frac{1}{\varepsilon}dX=b_0\left(\frac{2A}{\varepsilon_i}+\frac{1-2A}{\varepsilon_e}\right), \tag{2.28}$$

where integrals involving ϕ_1 vanish due to periodicity in the fast scale, as ϕ_1 will take the same value at each edge of the unit cell ($X=\pm 1/2$).

We can determine the form of homogenised problem by considering the $O(\delta^2)$ equations,

$$\frac{\partial}{\partial X}\left(\varepsilon\left(\frac{\partial\phi_2}{\partial X}+\frac{\partial\phi_1}{\partial x}\right)\right)+\frac{\partial}{\partial x}\left(\varepsilon\left(\frac{\partial\phi_1}{\partial X}+\frac{\partial\phi_0}{\partial x}\right)\right)=-\rho \quad \text{in} \quad D, \tag{2.29}$$

$$\left[\varepsilon\left(\frac{\partial\phi_2}{\partial X}+\frac{d\phi_1}{dx}\right)\right]_i^e=0, \tag{2.30}$$

$$[\phi_1]_i^e=0. \tag{2.31}$$

Substituting the first integral from the first-order equation (2.27) into (2.29), we find

$$\frac{\partial}{\partial X}\left(\varepsilon\left(\frac{\partial\phi_2}{\partial X}+\frac{\partial\phi_1}{\partial x}\right)\right)+\frac{db_0}{dx}=-\rho \quad \text{in} \quad D. \tag{2.32}$$

Integrating (2.32) across a unit cell gives

$$\begin{aligned}\int_{D_i}\frac{\partial}{\partial X}\left(\varepsilon_i\left(\frac{\partial\phi_2}{\partial X}+\frac{\partial\phi_1}{\partial x}\right)\right)dX+\int_{D_e}\frac{\partial}{\partial X}\left(\varepsilon_e\left(\frac{\partial\phi_2}{\partial X}+\frac{\partial\phi_1}{\partial x}\right)\right)dX\\ +\frac{db_0}{dx}=-\rho_{\text{eff}},\end{aligned} \tag{2.33}$$

where

$$\rho_{\text{eff}}=\int_{-1/2}^{1/2}\rho dX \tag{2.34}$$

is the effective charge density. Evaluating the first two integrals using the continuity condition (2.30) and periodicity in the derivatives, we find that their contributions vanish. Substituting the expression for b_0, equation (2.28), we obtain the

form of the homogenised problem

$$\frac{d}{dx}\left(\epsilon\frac{d\phi_0}{dx}\right) = -\rho_{\text{eff}}, \tag{2.35}$$

where we have defined the effective permittivity ϵ as

$$\epsilon = \left(\int_{-1/2}^{1/2}\frac{1}{\varepsilon}dX\right)^{-1} = \left(\frac{2A}{\varepsilon_i} + \frac{1-2A}{\varepsilon_e}\right)^{-1}. \tag{2.36}$$

2.2.1.1 Taking the limit $\varepsilon_i \to \infty$

To obtain the form of the homogenised problem when the interior layers are perfectly dielectric, we would like to find the form of the homogenised problem (2.35)-(2.36) in the limit $\varepsilon_i \to \infty$. Taking this limit, the effective permeability becomes

$$\frac{d}{dx}\left(\epsilon_p\frac{d\phi_0}{dx}\right) = -\rho_{\text{eff}}, \tag{2.37}$$

where

$$\epsilon_p = \frac{\varepsilon_e}{1-2A}. \tag{2.38}$$

We have now established the form of the homogenised problem derived from (2.7)-(2.10). In the next section, we aim to recover this result using direct multiple scales, thereby developing an understanding of how to treat non-local constraints in multiple scales problems that have a slowly varying domain.

2.2.2 Multiple scales with a non-local constraint

In this section, we approach homogenisation of the composite with perfectly dielectric layers (2.7)-(2.10) directly, identifying the multiple scales form of the non-local constraint, equation (2.15). We use the same multiple scales setup as in section 2.2.1, introducing a fast and slow scale which we treat independently and pose a multiple scales expansion for the potential (2.20). We look to write (2.7), (2.10), (2.13) and (2.15) in multiple scales form, beginning with the non-local constraint (2.15).

2.2.2.1 The non-local constraint

As highlighted in [25], when dealing with a non-local constraint, we must be careful when writing the condition in multiple scales form. For standard multiple scales problems like that discussed in section 2.2.1, we can treat the slow scale coordinate as constant in a given cell. With non-local constraints, such as (2.15), we must account for the small variation in the slow coordinate as we move from one side of the unit cell to the other [25]. This drift in coordinate will create a change in flux as we move across the unit cell. This variation becomes explicit if write a point in slow coordinates as its position in fast coordinates relative to an arbitrary fixed point in the same unit cell $\hat{x}$: following [25], we write

$$x = \hat{x} + \delta(X - b), \tag{2.39}$$

where $b = \hat{x}/\delta - \lfloor \hat{x}/\delta \rfloor$ gives the displacement of fixed point relative to the left hand side of the unit cell. We can choose $\hat{x}$ to simplify calculations and henceforth, we choose the reference point $\hat{x}$ to be at the left edge of the unit cell, fixing $b = 0$. The role of slow variation with the fast scale is clearer if we work with a flux, defined as

$$Q = \frac{1}{\delta}\frac{\partial \phi}{\partial X} + \frac{\partial \phi}{\partial x} = \delta^{-1}Q_{-1} + Q_0 + \delta Q_1 + O(\delta^2). \tag{2.40}$$

The jump condition (2.15) written in terms of the flux takes the form

$$Q(x_R, A) - Q(x_L, -A) = -\frac{\delta}{\varepsilon_e}\int_{D_i} \rho dX, \tag{2.41}$$

where x_R and x_L respectively denote the slow position of the right- and left-hand edge of the inclusion, and the δ on the right-hand side is from transforming slow to fast integration variables. Expanding the slow argument of the flux as in [25] about $\hat{x}$, we obtain

$$\left[Q(\hat{x}, X) + \delta X \frac{\partial Q(\hat{x}, X)}{\partial x} + O(\delta^2)\right]_{-A}^{A} = -\frac{\delta}{\varepsilon_e}\int_{D_i} \rho dX. \tag{2.42}$$

As the width of the inclusion depends on slow position, we must also expand the argument of boundary location about a fixed slow position by writing $A(x) = A(\hat{x} + \delta X)$. Performing this expansion in (2.42), we find

$$\left[Q(\hat{x}, X) + \delta X \frac{\partial Q(\hat{x}, X)}{\partial x} + \delta X \frac{\partial A(\hat{x})}{\partial x}\frac{\partial Q(\hat{x}, X)}{\partial X} + O(\delta^2)\right]_{-A(\hat{x})}^{A(\hat{x})} = -\frac{\delta}{\varepsilon_e}\int_{D_i} \rho dX. \tag{2.43}$$

We will establish that this is the correct form of the non-local condition by comparing the homogenised model we obtain with this approach with that obtained in section 2.2.1.

We now return to the multiple scales expansions of the governing equations (2.7), (2.10), (2.13) and (2.15). We cannot easily write (2.13) in multiple scales form and so follow the method of [25] in writing the condition as

$$\frac{d\phi}{dx} = 0 \quad \text{in} \quad \Omega_i. \tag{2.44}$$

We substitute the multiple scales expansion of the potential (2.20) into (2.7), (2.10), (2.43) and (2.44), then compare coefficients. At $O(1)$, we obtain

$$\frac{\partial}{\partial X}\left(\varepsilon_e \frac{\partial \phi_0}{\partial X}\right) = 0 \quad \text{in} \quad D_e, \tag{2.45}$$

$$\frac{\partial \phi_0}{\partial X} = 0 \quad \text{in} \quad D_i, \tag{2.46}$$

$$\left[\frac{\partial \phi_0}{\partial X}\right]_{-A}^{A} = 0, \tag{2.47}$$

$$[\phi_0]_i^e = 0, \tag{2.48}$$

with ϕ_0 1-periodic in X. We conclude that the leading-order potential is independent of the fast scale, *i.e.* $\phi_0 = \phi_0(x)$.

At $O(\delta)$, we find

$$\frac{\partial}{\partial X}\left(\varepsilon_e \left(\frac{\partial \phi_1}{\partial X} + \frac{\partial \phi_0}{\partial x}\right)\right) = 0 \quad \text{in} \quad D_e, \tag{2.49}$$

$$\frac{\partial \phi_1}{\partial X} + \frac{\partial \phi_0}{\partial x} = 0 \quad \text{in} \quad D_i, \tag{2.50}$$

$$\left[\frac{\partial \phi_1}{\partial X} + \frac{\partial \phi_0}{\partial x}\right]_{-A}^{A} = 0, \tag{2.51}$$

$$[\phi_1]_i^e = 0, \tag{2.52}$$

with ϕ_1 1-periodic in X. As the leading-order potential is independent of the fast scale, we can view its derivative as a forcing term in equations (2.50)-(2.51). Writing

$$\phi_1 = \Psi \frac{\partial \phi_0}{\partial x} + \overline{\phi}_1, \tag{2.53}$$

we can obtain a decoupled microscale problem governing the fast variation of ϕ_1. Here, $\overline{\phi_1}$ is a function only of the slow scale which can be determined by a solvability condition at next order. The microscale problem for Ψ takes the form

$$\frac{\partial^2 \Psi}{\partial X^2} = 0 \quad \text{in} \quad D_e, \tag{2.54}$$

$$\frac{\partial \Psi}{\partial X} + 1 = 0 \quad \text{in} \quad D_i, \tag{2.55}$$

$$\left[\frac{\partial \Psi}{\partial X}\right]_{-A}^{A} = 0, \tag{2.56}$$

$$[\Psi]_i^e = 0, \tag{2.57}$$

with the condition

$$\int_D \Psi dX = 0 \tag{2.58}$$

to fix the constant of integration, and Ψ being 1-periodic in X. We can solve (2.54)-(2.58) to obtain

$$\Psi = \begin{cases} \dfrac{-A(2X+1)}{2A-1} & \text{if } -1/2 \leq X \leq -A, \\ -X & \text{if } -A \leq X \leq A, \\ \dfrac{-A(2X-1)}{2A-1} & \text{if } A \leq X \leq 1/2. \end{cases} \tag{2.59}$$

We now return to the multiple scales expansion of the governing equations to determine the form of the homogenised problem. At $O(\delta^2)$, we obtain

$$\frac{\partial}{\partial X}\left(\varepsilon_e\left(\frac{\partial \phi_2}{\partial X} + \frac{\partial \phi_1}{\partial x}\right)\right) + \frac{\partial}{\partial x}\left(\varepsilon_e\left(\frac{\partial \phi_1}{\partial X} + \frac{\partial \phi_0}{\partial x}\right)\right) = -\rho \quad \text{in} \quad D_e, \tag{2.60}$$

$$\frac{\partial \phi_2}{\partial X} + \frac{\partial \phi_1}{\partial x} = 0 \quad \text{in} \quad D_i, \tag{2.61}$$

$$\left[\frac{\partial \phi_2}{\partial X} + \frac{\partial \phi_1}{\partial x} + X\frac{\partial}{\partial x}\left(\frac{\partial \phi_1}{\partial X} + \frac{\partial \phi_0}{\partial x}\right)\right]_{-A}^{A} = -\frac{1}{\varepsilon_e}\int_{D_i} \rho dX, \tag{2.62}$$

$$[\phi_2]_i^e = 0. \tag{2.63}$$

In (2.62), we see that terms involving the slow derivative of the boundary position in (2.43) have vanished as Q_0 was independent of the fast scale. In the two-dimensional case we will consider the limit of large charge density which ensures

that the equivalent term is not exactly zero. We integrate (2.60) over the exterior region D_e,

$$\left[\varepsilon_e\left(\frac{\partial\phi_2}{\partial X}+\frac{\partial\phi_1}{\partial x}\right)\right]_{-1/2}^{-A}+\left[\varepsilon_e\left(\frac{\partial\phi_2}{\partial X}+\frac{\partial\phi_1}{\partial x}\right)\right]_{A}^{1/2}+\int_{-1/2}^{-A}\frac{\partial}{\partial x}\left(\varepsilon_e\left(\frac{\partial\phi_1}{\partial X}+\frac{\partial\phi_0}{\partial x}\right)\right)dX + \int_{A}^{1/2}\frac{\partial}{\partial x}\left(\varepsilon_e\left(\frac{\partial\phi_1}{\partial X}+\frac{\partial\phi_0}{\partial x}\right)\right)dX=-\int_{D_e}\rho dX. \tag{2.64}$$

Using the periodicity in the derivatives of the expansion coefficients and substituting the non-local condition (2.62), we obtain

$$\left[\varepsilon_e X\frac{\partial}{\partial x}\left(\frac{\partial\phi_1}{\partial X}+\frac{\partial\phi_0}{\partial x}\right)\right]_{-A}^{A}+\int_{-1/2}^{-A}\frac{\partial}{\partial x}\left(\varepsilon_e\left(\frac{\partial\phi_1}{\partial X}+\frac{\partial\phi_0}{\partial x}\right)\right)dX + \int_{A}^{1/2}\frac{\partial}{\partial x}\left(\varepsilon_e\left(\frac{\partial\phi_1}{\partial X}+\frac{\partial\phi_0}{\partial x}\right)\right)dX=-\rho_{\text{eff}}, \tag{2.65}$$

where

$$\rho_{\text{eff}}=\int_{-1/2}^{1/2}\rho dX \tag{2.66}$$

is the effective charge. From the first-order equation in the exterior region (2.49), we learn that the integrand over the exterior region is independent of the fast scale, and so we can evaluate the remaining integrals to obtain

$$\left[\varepsilon_e X\frac{\partial}{\partial x}\left(\frac{\partial\phi_1}{\partial X}+\frac{\partial\phi_0}{\partial x}\right)\right]_{-A}^{A}+(1-2A)\frac{\partial}{\partial x}\left(\varepsilon_e\left(\frac{\partial\phi_1}{\partial X}+\frac{\partial\phi_0}{\partial x}\right)\right)=-\rho_{\text{eff}}. \tag{2.67}$$

Simplifying (2.67) gives

$$\frac{\partial}{\partial x}\left(\varepsilon_e\left(\frac{\partial\phi_1}{\partial X}+\frac{\partial\phi_0}{\partial x}\right)\right)=-\rho_{\text{eff}}. \tag{2.68}$$

After substituting for ϕ_1 using (2.53), we find the form of the homogenised problem

$$\frac{\partial}{\partial x}\left(\epsilon\frac{\partial\phi_0}{\partial x}\right)=-\rho_{\text{eff}}, \tag{2.69}$$

where the effective permittivity is

$$\epsilon=\varepsilon_e\left(1+\left.\frac{\partial\Psi}{\partial X}\right|_e\right), \tag{2.70}$$

where the derivative of the microscale solution is evaluated in the exterior region. For the solution to the microscale problem (2.59), the effective permittivity takes the form

$$\epsilon = \frac{\varepsilon_e}{1 - 2A}, \tag{2.71}$$

and we recover the same homogenised model (2.37)-(2.38) as that obtained by taking the limit of the problem with finite permittivity. It is useful to reflect on terms which appear in the homogenisation of the one-dimensional problem. We note that in using the jump condition, for example in (2.67), the additional terms arising from the expansion of the boundary position as $A(x) = A(\hat{x}) + \delta X A(\hat{x})_x$ were identically zero. In the two dimensional case, we will nondimensionalise on different scales, considering the limit of large charge density to establish whether the proposed approach is correct. In the limit we consider in section 2.3 the terms in the proposed expansion (2.43) are non-zero.

2.3 Two-dimensional problem

In this section we extend the analysis of section 2.2 to multiple dimensions. To approach the problem directly in the one-dimensional case, we needed to establish how to write the non-local constraint with slowly varying limits in multiple scales form. For multidimensional problems, the non-local constraint typically involves the conservation of the normal component of a function, for example flux through the surface. The normal vector to a slowly varying domain is usually written as the gradient of a function with level sets defining the boundary position [20]. In treating the problem with integral constraints on a slowly varying domain, we need to establish how to combine the multiple scales expansion of the normal with the expansion of integral constraints. We take the same approach as in section 2.2; first, we establish the form of the homogenised problem by taking a limit of a standard multiple scales problem in section 2.3.1 before dealing with the integral constraint directly in section 2.3.2.

2.3.1 Standard multiple scales

As in section 2.2.1, we formulate the problem for a composite of two dielectrics and homogenise the problem with standard multiple scales before taking the limit of perfectly dielectric inclusions where $\varepsilon_i \to \infty$.

We consider the electric potential $\phi = \phi(\boldsymbol{x})$ in a two-dimensional composite of width and height L, shown in figure 2.2. The composite consists of a dielectric with permittivity ε_e which occupies the region Ω_e, periodically interspersed with perfectly dielectric inclusions Ω_i that are separated by a distance l. We take the origin of Cartesian coordinates (x, y) to be the bottom, left-hand corner of the composite as illustrated in figure 2.2. The kth inclusion centred at $\boldsymbol{x}_0^k = (x_0^k, y_0^k)$ has a radius $a(\boldsymbol{x})$. Thus, the kth perfectly dielectric inclusion is given by the region $\Omega_i^k = \{\boldsymbol{x} : |\boldsymbol{x} - \boldsymbol{x}_0^k| \leq a(\boldsymbol{x}_0^k)\}$. The small parameter $\delta = l/L$ gives the ratio between the microscale and macroscale.

We assume that the electric potential satisfies Gauss's law,

$$\nabla \cdot (\varepsilon \nabla \phi) = -\rho, \tag{2.72}$$

where the permittivity is piecewise constant, taking the values $\varepsilon = \varepsilon_j$ in Ω_j for $j = i, e$. We consider a material which is locally charge neutral (see equation (2.79)). We have continuity of electric field and potential at each interface

$$[\hat{\boldsymbol{n}} \cdot (\varepsilon \nabla \phi)]_i^e = 0, \tag{2.73}$$

$$[\phi]_i^e = 0, \tag{2.74}$$

where $\hat{\boldsymbol{n}}$ is the outward-facing normal to the inclusion boundary.

We nondimensionalise (2.72)-(2.74) using the following scales

$$\boldsymbol{x} = L\hat{\boldsymbol{x}}, \quad \rho = \rho_c \hat{\rho}, \quad \phi = \frac{\delta L^2 \rho_c}{\varepsilon_e} \hat{\phi}, \quad a = L\hat{a}, \tag{2.75}$$

where hats denote dimensionless variables. We assume that all dimensionless variables are order one and thus we consider the limit of large charge. In this regime, terms in the proposed multiple scales form for the integral are non-zero, as opposed to the limit considered in [25] and in section 2.2 where some terms vanish automatically.

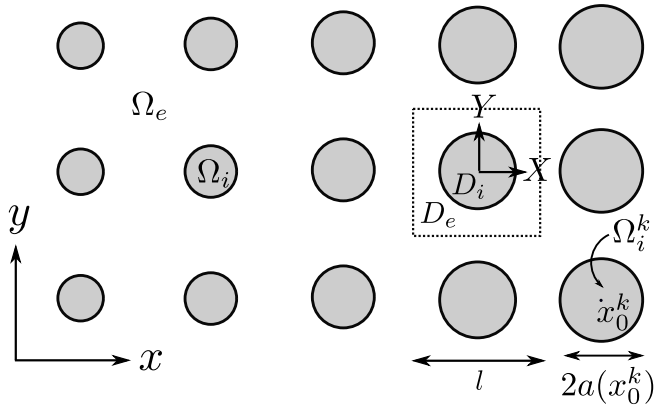

Figure 2.2: *Schematic of the two-dimensional composite. Perfectly dielectric inclusions shown in grey lie on a periodic array within a dielectric with permittivity ε_e. The inclusions have a radius $a(x)$ which slowly varies across the domain.*

In nondimensional form Gauss's law (2.72) becomes

$$\nabla \cdot (\varepsilon \nabla \phi) = -\frac{\rho}{\delta}. \tag{2.76}$$

Henceforth, we drop hats on dimensionless variables. The dimensionless permittivity ε takes the values 1 in the region Ω_e and $\varepsilon_i/\varepsilon_e$ in the dielectric inclusion Ω_i. After nondimensionalisation, the boundary conditions (2.73)-(2.74) become

$$[\hat{\boldsymbol{n}} \cdot (\varepsilon \nabla \phi)]_i^e = 0, \tag{2.77}$$

$$[\phi]_i^e = 0, \tag{2.78}$$

We assume that the composite can be constructed from unit cells D that are shown in figure 2.2. We introduce the slow scale $\boldsymbol{x}$, which describes the variation over the whole composite and the fast scale $\boldsymbol{X} = \boldsymbol{x}/\delta - \mathbf{1}/2 - \lfloor \boldsymbol{x}/\delta \rfloor$, which describes variations in the potential on the scale of a single inclusion. The origin of fast scale coordinates is at the centre of the inclusion as shown in figure 2.2. The region of the unit cell occupied by the perfect dielectric is then $D_i = \{\boldsymbol{X} : |\boldsymbol{X}| \leq A(\boldsymbol{x})\}$, where $A = a(\boldsymbol{x})/\delta$ is the inclusion radius in fast coordinates. As for the one-dimensional problem, D_i and $D_e = D \backslash D_i$ will depend on the slow scale. The condition that the material is locally charge neutral is then

$$\int_D \rho dS_X = 0, \tag{2.79}$$

where $dS_X = dXdY$ is the area element in fast coordinates.

We pose a multiple scales expansion for the potential

$$\phi = \phi_0(\boldsymbol{x}, \boldsymbol{X}) + \delta\phi_1(\boldsymbol{x}, \boldsymbol{X}) + O(\delta^2) \tag{2.80}$$

as $\delta \to 0$, where the expansion coefficients are **1**-periodic in $\boldsymbol{X}$ so that $\phi_i(\boldsymbol{x}, \boldsymbol{X} + (1,1)) = \phi_i(\boldsymbol{x}, \boldsymbol{X})$. As for the one-dimensional problem, we assume periodicity in the first derivatives of the expansion coefficients. Before transforming (2.76)-(2.78) into multiple scales form, we establish the multiple scales form of the normal to the inclusion boundary. To identify the normal expansion, we introduce a level set function

$$h = |\boldsymbol{X}| - A(\boldsymbol{x}) \tag{2.81}$$

which defines the inclusion boundaries at $h = 0$. The normal to the inclusion boundary can be obtained as the gradient of this level set function,

$$\hat{\boldsymbol{n}} = \frac{\nabla h}{|\nabla h|}, \tag{2.82}$$

which transforms into multiple scales form as follows

$$\hat{\boldsymbol{n}} = \frac{\nabla_{\boldsymbol{X}} h + \delta\nabla_{\boldsymbol{x}} h}{|\nabla_{\boldsymbol{X}} h + \delta\nabla_{\boldsymbol{x}} h|} = \hat{\boldsymbol{n}}_0 + \delta\hat{\boldsymbol{n}}_1 + O(\delta^2). \tag{2.83}$$

Calculating the form of the first two terms in the normal expansion in terms of the level set function, we have

$$\hat{\boldsymbol{n}}_0 = \frac{\nabla_{\boldsymbol{X}} h}{|\nabla_{\boldsymbol{X}} h|}, \qquad \hat{\boldsymbol{n}}_1 = \frac{\nabla_{\boldsymbol{x}} h}{|\nabla_{\boldsymbol{X}} h|} - \frac{(\nabla_{\boldsymbol{x}} h \cdot \nabla_{\boldsymbol{X}} h)\nabla_{\boldsymbol{X}} h}{|\nabla_{\boldsymbol{X}} h|^3}. \tag{2.84}$$

We transform (2.76)-(2.78) into multiple scales form using $\nabla \to \nabla_x + \delta^{-1}\nabla_X$ and (2.83), which gives

$$(\nabla_{\boldsymbol{X}} + \delta\nabla_{\boldsymbol{x}}) \cdot \big(\varepsilon(\nabla_{\boldsymbol{X}} + \delta\nabla_{\boldsymbol{x}})\phi\big) = -\delta\rho, \tag{2.85}$$

$$\big[(\hat{\boldsymbol{n}}_0 + \delta\hat{\boldsymbol{n}}_1 + \cdots) \cdot \big(\varepsilon(\nabla_{\boldsymbol{X}}\phi + \delta\nabla_{\boldsymbol{x}}\phi)\big)\big]_i^e = 0, \tag{2.86}$$

$$[\phi]_i^e = 0. \tag{2.87}$$

Substituting the multiple scales form of the potential into (2.85)-(2.87), we obtain the leading-order equations

$$\nabla_{\boldsymbol{X}}\cdot(\varepsilon\nabla_{\boldsymbol{X}}\phi_0)=0 \quad \text{in} \quad D, \tag{2.88}$$

$$[\hat{\boldsymbol{n}}_0\cdot(\varepsilon\nabla_{\boldsymbol{X}}\phi_0)]_i^e=0, \tag{2.89}$$

$$[\phi_0]_i^e=0, \tag{2.90}$$

with ϕ_0 $\mathbf{1}$-periodic in $\boldsymbol{X}$. There is no forcing or boundary condition forcing fast scale dependence of the solution to (2.88)-(2.90). Thus, at leading-order we have a potential which is independent of the fast scale $\phi_0=\phi_0(x)$.

At next order, we find

$$\nabla_{\boldsymbol{X}}\cdot(\varepsilon\nabla_{\boldsymbol{X}}\phi_1)=-\rho \quad \text{in} \quad D, \tag{2.91}$$

$$[\hat{\boldsymbol{n}}_0\cdot(\varepsilon(\nabla_{\boldsymbol{X}}\phi_1+\nabla_{\boldsymbol{x}}\phi_0))]_i^e=0, \tag{2.92}$$

$$[\phi_1]_i^e=0, \tag{2.93}$$

with ϕ_1 periodic in $\boldsymbol{X}$, where we have used the fast scale independence of the leading-order potential. Writing

$$\phi_1=\boldsymbol{\Psi}\cdot\nabla_{\boldsymbol{x}}\phi_0+\xi+\overline{\phi}_1, \tag{2.94}$$

for $\overline{\phi}_1=\overline{\phi_1}(\boldsymbol{x})$, we obtain cell problems for $\boldsymbol{\Psi}=\boldsymbol{\Psi}(\boldsymbol{x},\boldsymbol{X})$ and $\xi=\xi(\boldsymbol{x},\boldsymbol{X})$ which determine the fast scale variation of the first-order potential. The first cell problem satisfies the inhomogeneous boundary condition

$$\nabla_{\boldsymbol{X}}\cdot(\varepsilon\nabla_{\boldsymbol{X}}\boldsymbol{\Psi})=0 \quad \text{in} \quad D, \tag{2.95}$$

$$[\hat{\boldsymbol{n}}_0\cdot(\varepsilon(\nabla_{\boldsymbol{X}}\boldsymbol{\Psi}+I))]_i^e=0, \tag{2.96}$$

$$[\boldsymbol{\Psi}]_i^e=0, \tag{2.97}$$

with $\boldsymbol{\Psi}$ $\mathbf{1}$-periodic in $\boldsymbol{X}$. We impose

$$\int_D \boldsymbol{\Psi}\,dS_X=\mathbf{0}, \tag{2.98}$$

to fix the arbitrary constant in $\boldsymbol{\Psi}$. The second cell problem for ξ satisfies the inhomogeneous forcing due to the fast variations in the potential induced by charge

density in the bulk,

$$\nabla_{\boldsymbol{X}} \cdot (\varepsilon \nabla_{\boldsymbol{X}} \xi) = -\rho \quad \text{in} \quad D, \tag{2.99}$$

$$[\hat{\boldsymbol{n}}_0 \cdot (\varepsilon \nabla_{\boldsymbol{X}} \xi)]_i^e = 0, \tag{2.100}$$

$$[\xi]_i^e = 0, \tag{2.101}$$

with ξ $\mathbf{1}-$periodic in $\boldsymbol{X}$ and again

$$\int_D \xi dS_X = 0. \tag{2.102}$$

We now identify the compatibility condition for (2.99)-(2.101). Integrating (2.99) over the exterior region and applying the divergence theorem, we obtain

$$-\int_{\partial D_e} \nabla_{\boldsymbol{X}} \xi \cdot \hat{\boldsymbol{n}}_0 dl_X = -\int_{D_e} \rho dS_X. \tag{2.103}$$

Applying (2.100) we have

$$-\int_{\partial D_i} \nabla_{\boldsymbol{X}} \xi \cdot \hat{\boldsymbol{n}}_0 dl_X = -\int_{D_e} \rho dS_X. \tag{2.104}$$

Applying the divergence theorem to take the first integral into the interior and using (2.99), we obtain the following compatibility condition

$$\int_{D_i} \rho dS_X + \int_{D_e} \rho dS_X = 0. \tag{2.105}$$

Hence, the assumption of local charge neutrality (2.79) ensures that the cell problem is well-posed. A homogenised problem may also be obtained in the limit where the material is approximately charge neutral, having zero average in the fast coordinates at leading-order and local variations in ρ at $O(\delta)$, but we do not consider this limit further.

Our next aim is to derive the form of the homogenised problem. Comparing coefficients at $O(\delta^2)$, we find

$$\nabla_{\boldsymbol{X}} \cdot (\varepsilon(\nabla_{\boldsymbol{X}} \phi_2 + \nabla_{\boldsymbol{x}} \phi_1)) + \nabla_{\boldsymbol{x}} \cdot (\varepsilon(\nabla_{\boldsymbol{X}} \phi_1 + \nabla_{\boldsymbol{x}} \phi_0)) = 0 \quad \text{in} \quad D, \tag{2.106}$$

$$[\hat{\boldsymbol{n}}_0 \cdot (\varepsilon(\nabla_{\boldsymbol{X}} \phi_2 + \nabla_{\boldsymbol{x}} \phi_1))]_i^e + [\hat{\boldsymbol{n}}_1 \cdot (\varepsilon(\nabla_{\boldsymbol{X}} \phi_1 + \nabla_{\boldsymbol{x}} \phi_0))]_i^e = 0, \tag{2.107}$$

$$[\phi_2]_i^e = 0. \tag{2.108}$$

We integrate (2.106) over the unit cell to obtain

$$\begin{aligned}\int_{D_e} \nabla_{\boldsymbol{X}}\cdot\left(\varepsilon_e(\nabla_{\boldsymbol{X}}\phi_2+\nabla_{\boldsymbol{x}}\phi_1)\right)dS_X+\int_{D_i} \nabla_{\boldsymbol{X}}\cdot\left(\varepsilon_i(\nabla_{\boldsymbol{X}}\phi_2+\nabla_{\boldsymbol{x}}\phi_1)\right)dS_X+\\ \int_{D_e} \nabla_{\boldsymbol{x}}\cdot\left(\varepsilon_e(\nabla_{\boldsymbol{X}}\phi_1+\nabla_{\boldsymbol{x}}\phi_0)\right)dS_X+\int_{D_i} \nabla_{\boldsymbol{x}}\cdot\left(\varepsilon_i(\nabla_{\boldsymbol{X}}\phi_1+\nabla_{\boldsymbol{x}}\phi_0)\right)dS_X=0.\end{aligned} \tag{2.109}$$

Applying the divergence theorem to the first two terms and using the continuity condition on the electric field (2.107), we find

$$\begin{aligned}\int_{\partial D_e} \varepsilon_e\left(\nabla_{\boldsymbol{X}}\phi_1+\nabla_{\boldsymbol{x}}\phi_0\right)\cdot\hat{\boldsymbol{n}}_1 dl_X-\int_{\partial D_i} \varepsilon_i\left(\nabla_{\boldsymbol{X}}\phi_1+\nabla_{\boldsymbol{x}}\phi_0\right)\cdot\hat{\boldsymbol{n}}_1 dl_X+\\ \int_{D_e} \nabla_{\boldsymbol{x}}\cdot\left(\varepsilon_e(\nabla_{\boldsymbol{X}}\phi_1+\nabla_{\boldsymbol{x}}\phi_0)\right)dS_X+\int_{D_i} \nabla_{\boldsymbol{x}}\cdot\left(\varepsilon_i(\nabla_{\boldsymbol{X}}\phi_1+\nabla_{\boldsymbol{x}}\phi_0)\right)dS_X=0,\end{aligned} \tag{2.110}$$

where ∂D_i and ∂D_e denote the interior and exterior of the inclusion boundary respectively. We can use the Reynolds transport theorem to remove the slow derivatives from the integral:

$$\frac{\partial}{\partial t}\int_\Omega \mathbf{F}\,dV=\int_\Omega \frac{\partial \mathbf{F}}{\partial t}dV+\int_{\partial\Omega}\mathbf{F}\,\mathbf{v}\cdot\hat{\boldsymbol{n}}\,dS, \tag{2.111}$$

for a boundary $\partial\Omega$ bounding the volume Ω, where $\mathbf{v}$ is the boundary velocity and $\hat{\boldsymbol{n}}$ is the outward-facing normal. Applying (2.111), taking account of the normal direction into the exterior region, we find

$$\begin{aligned}\int_{\partial D_e} \varepsilon_e\left(\nabla_{\boldsymbol{X}}\phi_1+\nabla_{\boldsymbol{x}}\phi_0\right)\cdot\hat{\boldsymbol{n}}_1 dl_X-\int_{\partial D_i} \varepsilon_i\left(\nabla_{\boldsymbol{X}}\phi_1+\nabla_{\boldsymbol{x}}\phi_0\right)\cdot\hat{\boldsymbol{n}}_1 dl_X\\ +\int_{\partial D_e} \varepsilon_e\left(\nabla_{\boldsymbol{X}}\phi_1+\nabla_{\boldsymbol{x}}\phi_0\right)\cdot\boldsymbol{V}\cdot\hat{\boldsymbol{n}}_0 dl_X-\int_{\partial D_i} \varepsilon_i\left(\nabla_{\boldsymbol{X}}\phi_1+\nabla_{\boldsymbol{x}}\phi_0\right)\cdot\boldsymbol{V}\cdot\hat{\boldsymbol{n}}_0 dl_X\\ +\nabla_{\boldsymbol{x}}\cdot\int_{D_e}\left(\varepsilon_e(\nabla_{\boldsymbol{X}}\phi_1+\nabla_{\boldsymbol{x}}\phi_0)\right)dS_X+\nabla_{\boldsymbol{x}}\cdot\int_{D_i}\left(\varepsilon_i(\nabla_{\boldsymbol{X}}\phi_1+\nabla_{\boldsymbol{x}}\phi_0)\right)dS_X=0.\end{aligned} \tag{2.112}$$

Applying the transport theorem to remove the divergence gives a tensor 'velocity' $\boldsymbol{V}=\nabla_{\boldsymbol{x}}\boldsymbol{R}^b$ for boundary positions $\boldsymbol{R}^b=A\hat{\boldsymbol{E}}_R$ where $\hat{\boldsymbol{E}}_R$ is the radial unit vector in microscale coordinates. This velocity gives the variation in inclusion boundary position as we alter the slow position. We look to simplify (2.112) by obtaining an expression for $\hat{\boldsymbol{n}}_1+\boldsymbol{V}\cdot\hat{\boldsymbol{n}}_0$ using the level set function and normal expansion (2.84). Taking the total slow derivative of $h=0$ gives

$$\nabla_{\boldsymbol{x}}h+\boldsymbol{V}\cdot\nabla_{\boldsymbol{X}}h=\mathbf{0}. \tag{2.113}$$

Dividing (2.113) by $|\nabla_{\boldsymbol{X}} h|$, this gives an expression for $\boldsymbol{V} \cdot \hat{\boldsymbol{n}}_0$. Combining this with the form for $\hat{\boldsymbol{n}}_1$ given in (2.84), we have

$$\hat{\boldsymbol{n}}_1 + \boldsymbol{V} \cdot \hat{\boldsymbol{n}}_0 = \frac{\nabla_{\boldsymbol{x}} h}{|\nabla_{\boldsymbol{X}} h|} - \frac{(\nabla_{\boldsymbol{X}} h \cdot \nabla_{\boldsymbol{x}} h)\nabla_{\boldsymbol{X}} h}{|\nabla_{\boldsymbol{X}} h|^3} - \frac{\nabla_{\boldsymbol{x}} h}{|\nabla_{\boldsymbol{X}} h|} = -\frac{\hat{\boldsymbol{n}}_0 \cdot \nabla_{\boldsymbol{x}} h}{|\nabla_{\boldsymbol{X}} h|}\hat{\boldsymbol{n}}_0 \quad (2.114)$$

Substituting (2.114) in (2.112), we find

$$\begin{aligned} &- \int_{\partial D_e} \varepsilon_e (\nabla_{\boldsymbol{X}} \phi_1 + \nabla_{\boldsymbol{x}} \phi_0) \cdot \hat{\boldsymbol{n}}_0 \frac{(\hat{\boldsymbol{n}}_0 \cdot \nabla_{\boldsymbol{x}} h)}{|\nabla_{\boldsymbol{X}} h|} dl_X \\ &\qquad + \int_{\partial D_i} \varepsilon_i \left(\nabla_{\boldsymbol{X}} \phi_1 + \nabla_{\boldsymbol{x}} \phi_0\right) \cdot \hat{\boldsymbol{n}}_0 \frac{(\hat{\boldsymbol{n}}_0 \cdot \nabla_{\boldsymbol{x}} h)}{|\nabla_{\boldsymbol{X}} h|} dl_X \\ &+ \nabla_{\boldsymbol{x}} \cdot \int_{D_e} (\varepsilon_e (\nabla_{\boldsymbol{X}} \phi_1 + \nabla_{\boldsymbol{x}} \phi_0)) dS_X + \nabla_{\boldsymbol{x}} \cdot \int_{D_i} \left(\varepsilon_i (\nabla_{\boldsymbol{X}} \phi_1 + \nabla_{\boldsymbol{x}} \phi_0)\right) dS_X = 0. \end{aligned} \quad (2.115)$$

Using the point-wise boundary condition (2.25), the boundary terms cancel to leave

$$\nabla_{\boldsymbol{x}} \cdot \int_{D_e} \left(\varepsilon_e (\nabla_{\boldsymbol{X}} \phi_1 + \nabla_{\boldsymbol{x}} \phi_0)\right) dS_X + \nabla_{\boldsymbol{x}} \cdot \int_{D_i} \left(\varepsilon_i (\nabla_{\boldsymbol{X}} \phi_1 + \nabla_{\boldsymbol{x}} \phi_0)\right) dS_X = 0. \quad (2.116)$$

Substituting (2.94), we find the form of the homogenised problem

$$\nabla_{\boldsymbol{x}} \cdot (\epsilon \nabla_{\boldsymbol{x}} \phi_0) = -\rho_{\text{eff}}, \quad (2.117)$$

where the effective permittivity ϵ is given by

$$\epsilon = \int_D \varepsilon \left(I + \nabla_{\boldsymbol{X}} \boldsymbol{\Psi}\right) dS_X, \quad (2.118)$$

and the effective charge density is

$$\rho_{\text{eff}} = \nabla_{\boldsymbol{x}} \cdot \int_D \varepsilon \nabla_{\boldsymbol{X}} \xi \, dS_X, \quad (2.119)$$

where $\boldsymbol{\Psi}$ is the solution to (2.95)-(2.97) and ξ satisfies (2.99)-(2.99). Thus, the slow variation in microscale charge distribution induces an effective charge on the macroscale.

2.3.1.1 Taking the limit $\varepsilon_i \to \infty$

We now obtain the form of the homogenised problem for perfectly dielectric inclusions by taking the limit $\varepsilon_i \to \infty$.

First, we take the limit $\varepsilon_i \to \infty$ in the cell problem (2.95)-(2.97) which becomes

$$\nabla_{\boldsymbol{X}} \cdot (\varepsilon_e \nabla_{\boldsymbol{X}} \boldsymbol{\Psi}) = 0 \quad \text{in} \quad D_e, \tag{2.120}$$

$$\nabla^2_{\boldsymbol{X}} \boldsymbol{\Psi} = \mathbf{0} \quad \text{in} \quad D_i, \tag{2.121}$$

$$\hat{\boldsymbol{n}}_0 \cdot (\nabla_{\boldsymbol{X}} \boldsymbol{\Psi} + I) = 0 \quad \text{on} \quad \partial D_i, \tag{2.122}$$

$$[\boldsymbol{\Psi}]^e_i = 0, \tag{2.123}$$

with

$$\int_D \boldsymbol{\Psi} dS_X = \mathbf{0}. \tag{2.124}$$

Next, we expand the form of the permittivity in the homogenised model (2.118) with a view to attaining a form where the limit can be taken; attempting to take the limit directly results in infinity multiplied by zero. Using (2.95), we can write

$$\epsilon_{lj} = \int_{D_i} \varepsilon_i \delta_{lj} dS_X + \int_{D_e} \varepsilon_e \delta_{lj} dS_X + \int_{D_i} \varepsilon_i \partial_{Xk}(X_j \partial_{X_k} \Psi_l) dS_X + \int_{D_e} \varepsilon_e \partial_{Xk}(X_j \partial_{X_k} \Psi_l) dS_X. \tag{2.125}$$

Applying the divergence theorem to the final two terms gives

$$\begin{aligned} \epsilon_{lj} = &\int_{D_i} \varepsilon_i \delta_{lj} dS_X + \int_{D_e} \varepsilon_e \delta_{lj} dS_X + \int_{\partial D_i} \varepsilon_i (X_j \partial_{X_k} \Psi_l) \hat{n}_k dl_X \\ &- \int_{\partial D_e} \varepsilon_e (X_j \partial_{X_k} \Psi_l) \hat{n}_k dl_X + \int_{\partial D} \varepsilon_e (X_j \partial_{X_k} \Psi_l) \hat{n}_k dl_X. \end{aligned} \tag{2.126}$$

Using the boundary condition (2.96), we obtain

$$\begin{aligned} \epsilon_{lj} = &\int_{D_i} \varepsilon_i \delta_{lj} dS_X + \int_{D_e} \varepsilon_e \delta_{lj} dS_X - \int_{\partial D_i} \varepsilon_i X_j \hat{n}_l dl_X \\ &+ \int_{\partial D_e} \varepsilon_e X_j \hat{n}_l dl_X + \int_{\partial D} \varepsilon_e (X_j \partial_{X_k} \Psi_l) \hat{n}_k dl_X. \end{aligned} \tag{2.127}$$

We can then use the divergence theorem to take the integrals over the inclusion boundary to an integral over its interior. Terms involving ε_i cancel, leaving

$$\epsilon_{p_{lj}} = \varepsilon_e \left(\delta_{lj} + \int_{\partial D} X_j \partial_{X_k} \Psi_l \hat{n}_k dl_X \right). \tag{2.128}$$

In (2.128), we have obtained an effective permittivity which is independent of ε_i so we can take the limit $\varepsilon_i \to \infty$.

We repeat this process for the second cell problem. In the limit $\varepsilon_i \to \infty$, the cell problem for ξ becomes

$$\nabla_{\boldsymbol{X}} \cdot (\varepsilon_e \nabla_{\boldsymbol{X}} \xi) = -\rho \quad \text{in} \quad D_e, \tag{2.129}$$

$$\nabla^2_{\boldsymbol{X}} \xi = 0 \quad \text{in} \quad D_i, \tag{2.130}$$

$$\hat{\boldsymbol{n}}_0 \cdot \nabla_{\boldsymbol{X}} \xi = 0 \quad \text{on} \quad \partial D_i, \tag{2.131}$$

$$[\xi]^e_i = 0, \tag{2.132}$$

$$\int_D \xi dS_X = 0. \tag{2.133}$$

We switch to index notation to establish the form of the effective charge ρ_{eff} in the limit $\varepsilon_i \to \infty$,

$$\rho_{\text{eff}} = \partial_{x_i} \int_D \varepsilon \partial_{X_i} \xi dS_X \tag{2.134}$$

We write (2.134) in a form where the divergence theorem may be applied

$$\rho_{\text{eff}} = \partial_{x_i} \int_D \varepsilon \partial_{X_j} \left(X_i \partial_{X_j} \xi \right) dS_X - \partial_{x_i} \int_D \varepsilon X_i \partial_{X_j} \partial_{X_j} \xi dS_X. \tag{2.135}$$

Applying the divergence theorem to the first term and using (2.100), we have

$$\rho_{\text{eff}} = \partial_{x_i} \int_{\partial D} \varepsilon_e X_i \partial_{X_j} \xi \, n_j dl_X - \partial_{x_i} \int_D \varepsilon X_i \partial_{X_j} \partial_{X_j} \xi dS_X. \tag{2.136}$$

Substituting (2.129)-(2.130) into the final term, we have

$$\rho_{\text{eff}} = \partial_{x_i} \int_{\partial D} \varepsilon_e X_i \partial_{X_j} \xi \, n_j dl_X + \partial_{x_i} \int_{D_e} X_i \rho dS_X. \tag{2.137}$$

Since we have eliminated all dependence on ε_i, we can now take the limit $\varepsilon_i \to \infty$.

In equation (2.117) and the coefficients (2.128) and (2.137), we have established the homogenised problem in the limit where the inclusions are perfectly dielectric. In the next section, we aim to recover this result by taking an alternative route in which we treat the integral directly.

2.3.2 Multiple scales with integral constraints

In this section we aim to develop the direct approach to derive the homogenised equations for the electric potential in a composite with periodically arranged, perfectly dielectric inclusions as shown in figure 2.2. The geometry and coordinates for this problem are as described in section 2.3.1.

In the exterior region, we assume that the electric potential satisfies Gauss's law

$$\nabla\cdot(\varepsilon_e\nabla\phi) = -\rho \quad \text{in} \quad \Omega_e. \tag{2.138}$$

There must be no electric field within each perfectly dielectric inclusion, meaning that the potential there is constant. As per the one-dimensional problem considered in section 2.2.2, we enforce this by setting

$$\nabla\phi = \mathbf{0} \quad \text{in} \quad \Omega_i. \tag{2.139}$$

We expect the electric potential to be continuous at the inclusion boundary,

$$[\phi]_i^e = 0, \tag{2.140}$$

and the electric field on the inclusion is determined by the distribution of charges in its interior, given by Gauss's law,

$$\int_{\partial\Omega_e} \nabla\phi\cdot\hat{\boldsymbol{n}}dl = -\frac{1}{\varepsilon_e}\int_{\Omega_i}\rho ds, \tag{2.141}$$

where $\partial\Omega_e$ denotes the exterior side of the inclusion boundary and $\hat{\boldsymbol{n}}$ is the outward facing normal to the inclusion boundary.

We nondimensionalise (2.138)-(2.141) using the scales in (2.75). In dimensionless form, Gauss's law (2.138) becomes

$$\nabla\cdot(\varepsilon_e\nabla\phi) = -\frac{\rho}{\delta} \quad \text{in} \quad \Omega_e, \tag{2.142}$$

where we have dropped hats on dimensionless variables. Again, we use the dimensionless permittivity which takes the value 1 in the exterior region, Ω_e. We keep ε_e in our calculations explicitly to facilitate easier comparison with analysis in the previous section. The equation for constant potential in the inclusion (2.139) is

$$\nabla\phi = \mathbf{0}, \tag{2.143}$$

and the condition for charge continuity (2.140) is

$$[\phi]_i^e = 0 \quad \text{in} \quad \Omega_i. \tag{2.144}$$

Finally, we have the dimensionless form of the integral constraint (2.141)

$$\int_{\partial\Omega_e} \nabla\phi \cdot \hat{\boldsymbol{n}} dl = -\frac{1}{\delta\varepsilon_e} \int_{\Omega_i} \rho ds \tag{2.145}$$

In the next sections we outline the derivation of the macroscale model obtained *via* homogenisation of (2.142)-(2.145).

2.3.2.1 Expansion of the normal and integrand

In this section, we illustrate the issues that arise if the instinctive approach is taken, where both the normal and the integrand are expanded. We follow a similar method to section 2.3.1, introducing a multiple scales expansion for the potential of the form (2.80) and writing the governing equations (2.142)-(2.145) in multiple scales form,

$$(\nabla_{\boldsymbol{X}} + \delta\nabla_{\boldsymbol{x}}) \cdot (\varepsilon_e(\nabla_{\boldsymbol{X}} + \delta\nabla_{\boldsymbol{x}})\phi) = -\delta\rho \quad \text{in} \quad D_e, \tag{2.146}$$

$$(\nabla_{\boldsymbol{X}} + \delta\nabla_{\boldsymbol{x}})\phi = \boldsymbol{0} \quad \text{in} \quad D_i, \tag{2.147}$$

$$[\phi]_i^e = 0. \tag{2.148}$$

To write (2.145) in multiple scales form, we combine the normal expansion with the multiple scales form of the integrand. In [25], the multiple scales form of the integral over the inclusion surface was proposed to be

$$\int_{\partial\Omega} \boldsymbol{Q} \cdot \hat{\boldsymbol{n}} dl \to \delta \int_{\partial D_e} (\boldsymbol{Q} + \delta \boldsymbol{X} \cdot \nabla_{\boldsymbol{x}} \boldsymbol{Q} + \cdots) \cdot \hat{\boldsymbol{n}} dl_X, \tag{2.149}$$

where we have taken the surface to be the one-dimensional curve relevant to the problem we consider here. Combining the normal expansion (2.84) with (2.149) to write (2.145) in multiple scales form, we obtain

$$\int_{\partial D_e} (\boldsymbol{Q} + \delta \boldsymbol{X} \cdot \nabla_{\boldsymbol{x}} \boldsymbol{Q} + \cdots) \cdot (\hat{\boldsymbol{n}}_0 + \delta\hat{\boldsymbol{n}}_1 + \cdots) dl_X = -\frac{1}{\varepsilon_e} \int_{D_i} \rho dS_X, \tag{2.150}$$

where $\boldsymbol{Q} = \delta^{-1}\nabla_{\boldsymbol{X}}\phi + \nabla_{\boldsymbol{x}}\phi$ is the flux. Comparing coefficients at $O(1)$, we have

$$\nabla^2_{\boldsymbol{X}}\phi_0 = 0 \quad \text{in} \quad D_e, \tag{2.151}$$

$$\nabla_{\boldsymbol{X}}\phi_0 = \boldsymbol{0} \quad \text{in} \quad D_i, \tag{2.152}$$

$$[\phi]^e_i = 0, \tag{2.153}$$

$$\int_{\partial D_e} \nabla_{\boldsymbol{X}}\phi_0 \cdot \hat{\boldsymbol{n}}_0 dl_X = 0. \tag{2.154}$$

Thus, we again have that the leading-order potential is a function only of the slow scale. At next order, we obtain

$$\nabla^2_{\boldsymbol{X}}\phi_1 = -\frac{\rho}{\varepsilon_e} \quad \text{in} \quad D_e, \tag{2.155}$$

$$\nabla_{\boldsymbol{X}}\phi_1 + \nabla_{\boldsymbol{x}}\phi_0 = \boldsymbol{0} \quad \text{in} \quad D_i, \tag{2.156}$$

$$[\phi_1]^e_i = 0, \tag{2.157}$$

$$\int_{\partial D_e} (\nabla_{\boldsymbol{X}}\phi_1 + \nabla_{\boldsymbol{x}}\phi_0) \cdot \hat{\boldsymbol{n}}_0 dl_X = -\frac{1}{\varepsilon_e}\int_{D_i} \rho dS_X. \tag{2.158}$$

To derive the cell problems, we use (2.94). The cell problem for $\boldsymbol{\Psi}$ satisfies the inhomogeneous forcing due to the slow variation of the leading-order potential,

$$\nabla^2_{\boldsymbol{X}}\boldsymbol{\Psi} = \boldsymbol{0} \quad \text{in} \quad D_e, \tag{2.159}$$

$$\nabla_{\boldsymbol{X}}\boldsymbol{\Psi} + I = 0 \quad \text{in} \quad D_i, \tag{2.160}$$

$$[\boldsymbol{\Psi}]^e_i = \boldsymbol{0}, \tag{2.161}$$

with

$$\int_D \boldsymbol{\Psi} dS_X = \boldsymbol{0} \tag{2.162}$$

and $\boldsymbol{\Psi}$ $\boldsymbol{1}$-periodic in $\boldsymbol{X}$. The cell problem for ξ satisfies the problem with inhomogeneous forcing and homogeneous boundary conditions, reflecting the contribution of the charge density to the first-order potential:

$$\nabla^2_{\boldsymbol{X}}\xi = -\frac{\rho}{\varepsilon_e} \quad \text{in} \quad D_e, \tag{2.163}$$

$$\nabla_{\boldsymbol{X}}\xi = \boldsymbol{0} \quad \text{in} \quad D_i, \tag{2.164}$$

$$[\xi]^e_i = 0, \tag{2.165}$$

$$\int_{\partial D_e} \nabla_{\boldsymbol{X}}\xi \cdot \hat{\boldsymbol{n}}_0 dl_X = -\frac{1}{\varepsilon_e}\int_{D_i} \rho dS_X, \tag{2.166}$$

with ξ periodic in $\boldsymbol{X}$. Considering the integral of (2.163) over the exterior region, we can apply the divergence theorem and use (2.166) to obtain the same compatibility condition as for the standard case, equation (2.105).

To this point, all of the analysis matches that of the limit problem found using standard multiple scales in section 2.3.1. The problems with the current approach of expanding both the normal and the integrand become apparent in the derivation of the homogenised model. Equating coefficients at $O(\delta^2)$, we have

$$\nabla_{\boldsymbol{X}} \cdot (\varepsilon_e(\nabla_{\boldsymbol{X}}\phi_2 + \nabla_{\boldsymbol{x}}\phi_1)) + \nabla_{\boldsymbol{x}} \cdot (\varepsilon_e(\nabla_{\boldsymbol{X}}\phi_1 + \nabla_{\boldsymbol{x}}\phi_0)) = 0 \quad \text{in} \quad D_e, \tag{2.167}$$

$$\nabla_{\boldsymbol{X}}\phi_2 + \nabla_{\boldsymbol{x}}\phi_1 = \boldsymbol{0} \quad \text{in} \quad D_i, \tag{2.168}$$

$$[\phi_2]_i^e = 0, \tag{2.169}$$

$$\int_{\partial D_e} \varepsilon_e(\nabla_{\boldsymbol{X}}\phi_2 + \nabla_{\boldsymbol{x}}\phi_1)\cdot \hat{\boldsymbol{n}}_0 dl_X + \int_{\partial D_e} \varepsilon_e \boldsymbol{X}\cdot \nabla_{\boldsymbol{x}}(\nabla_{\boldsymbol{X}}\phi_1+\nabla_{\boldsymbol{x}}\phi_0)\cdot \hat{\boldsymbol{n}}_0 dl_X + \int_{\partial D_e} \varepsilon_e(\nabla_{\boldsymbol{X}}\phi_1 + \nabla_{\boldsymbol{x}}\phi_0)\cdot \hat{\boldsymbol{n}}_1 dl_X = 0. \tag{2.170}$$

Integrating (2.167) over the exterior region and applying the divergence theorem, we find

$$-\int_{\partial D_e} (\nabla_{\boldsymbol{X}}\phi_2 + \nabla_{\boldsymbol{x}}\phi_1)\cdot \hat{\boldsymbol{n}}_0 dl_X + \int_{D_e} \nabla_{\boldsymbol{x}} \cdot (\nabla_{\boldsymbol{X}}\phi_1 + \nabla_{\boldsymbol{x}}\phi_0) dS_X = 0. \tag{2.171}$$

We substitute (2.170) to eliminate ϕ_2 and apply Reynolds transport theorem to the final term, which gives

$$\int_{\partial D_e} \boldsymbol{X}\cdot \nabla_{\boldsymbol{x}}(\nabla_{\boldsymbol{X}}\phi_1 + \nabla_{\boldsymbol{x}}\phi_0)\cdot \hat{\boldsymbol{n}}_0 dl_X + \int_{\partial D_e} (\nabla_{\boldsymbol{X}}\phi_1 + \nabla_{\boldsymbol{x}}\phi_0)\cdot \hat{\boldsymbol{n}}_1 dl_X + \nabla_{\boldsymbol{x}} \cdot \int_{D_e} (\nabla_{\boldsymbol{X}}\phi_1 + \nabla_{\boldsymbol{x}}\phi_0) dS_X + \int_{\partial D_e} (\nabla_{\boldsymbol{X}}\phi_1 + \nabla_{\boldsymbol{x}}\phi_0)\cdot \boldsymbol{V}\cdot \hat{\boldsymbol{n}}_0 dl_X = 0, \tag{2.172}$$

where the positive sign in the final term arises as the normal points into the exterior region. Writing the first term in index notation, we have

$$\int_{\partial D_e} X_i \partial_{x_i}(\partial_{X_j}\phi_1+\partial_{x_j}\phi_0) n_{0j} dl_X = \int_{\partial D_e} X_i \partial_{x_i}\partial_{X_j}\phi_1 n_{0j} dl_X + \partial_{x_i}\partial_{x_j}\phi_0 \int_{\partial D_e} X_i n_{0j} dl_X, \tag{2.173}$$

where we have used the fast scale independence of the leading-order potential to remove it from the integral. We apply the divergence theorem to the second term,

taking it into the inclusion interior, which gives

$$\int_{\partial D_e} X_i \partial_{x_i}(\partial_{X_j}\phi_1 + \partial_{x_j}\phi_0) n_{0j} dl_X = \int_{\partial D_e} X_i \partial_{x_i}\partial_{X_j}\phi_1 n_{0j} dl_X + |D_i|\partial_{x_i}\partial_{x_i}\phi_0, \quad (2.174)$$

where $|D_i|$ denotes the area of the inclusion. To manipulate the first term, we require the flux transport theorem for a closed surface $\partial\Omega$,

$$\frac{\partial}{\partial t}\int_{\partial\Omega} \mathbf{F}\cdot\hat{\boldsymbol{n}}\, dS = \int_{\partial\Omega}\left(\frac{\partial \mathbf{F}}{\partial t} + (\nabla\cdot\mathbf{F})\mathbf{v}\right)\cdot\hat{\boldsymbol{n}}\, dS, \quad (2.175)$$

where $\mathbf{F}$ is a tensor quantity and we have taken the divergence of a tensor to be defined such that the contraction occurs with its second index. Applying (2.175) to the first term in (2.174), we find

$$\begin{aligned}\int_{\partial D_e} X_i \partial_{x_i}(\partial_{X_j}\phi_1 + \partial_{x_j}\phi_0) n_{0j} dl_X = \partial_{x_i}\int_{\partial D_e} X_i \partial_{X_j}\phi_1 n_{0j} dl_X \\ - \int_{\partial D_e} \partial_{X_j}(X_i\partial_{X_j}\phi_1) V_{ik} n_{0k} dl_X + |D_i|\partial_{x_i}\partial_{x_i}\phi_0,\end{aligned} \quad (2.176)$$

where $V_{ik} = \partial R^b_k/\partial x_i$. Applying the divergence theorem in the first term, we obtain

$$\begin{aligned}\int_{\partial D_e} X_i \partial_{x_i}(\partial_{X_j}\phi_1 + \partial_{x_j}\phi_0) n_{0j} dl_X = -\partial_{x_i}\int_{D_e} \partial_{X_j}(X_i\partial_{X_j}\phi_1) dS_X \\ + \partial_{x_i}\int_{\partial D} X_i\partial_{X_j}\phi_1 n_{0j} dl_X - \int_{\partial D_e}\partial_{X_j}(X_i\partial_{X_j}\phi_1) V_{ik} n_{0k} dl_X \\ + |D_i|\partial_{x_i}\partial_{x_i}\phi_0.\end{aligned} \quad (2.177)$$

We substitute the form of ϕ_1 into the first and second terms which gives

$$\begin{aligned}\int_{\partial D_e} X_i \partial_{x_i}(\partial_{X_j}\phi_1 + \partial_{x_j}\phi_0) n_{0j} dl_X = \frac{1}{\varepsilon_e}\partial_{x_i}\int_{D_e} X_i \rho dS_X - \partial_{x_i}\int_{D_e}\partial_{X_i}\phi_1 dS_X \\ + \partial_{x_i}\int_{\partial D} X_i\partial_{X_j}\Psi_k\partial_{x_k}\phi_0 n_{0j} dl_X + \partial_{x_i}\int_{\partial D} X_i\partial_{X_j}\xi n_{0j} dl_X \\ - \int_{\partial D_e}\partial_{X_j}(X_i\partial_{X_j}\phi_1) V_{ik} n_{0k} dl_X + |D_i|\partial_{x_i}\partial_{x_i}\phi_0.\end{aligned} \quad (2.178)$$

Returning to (2.172), we compare the homogenised equations to that obtained using the standard method. Substituting (2.178) into (2.172), we find

$$\nabla_{\boldsymbol{x}} \cdot (\varepsilon_{\text{eff}} \nabla_{\boldsymbol{x}} \phi_0) - \int_{\partial D_e} \varepsilon_e \nabla_{\boldsymbol{X}} \cdot (\boldsymbol{X} \nabla_{\boldsymbol{X}} \phi_1) \cdot \boldsymbol{V} \cdot \hat{\boldsymbol{n}}_0 dl_X + \int_{\partial D_e} \varepsilon_e (\nabla_{\boldsymbol{X}} \phi_1 + \nabla_{\boldsymbol{x}} \phi_0) \cdot \hat{\boldsymbol{n}}_1 dl_X + \int_{\partial D_e} \varepsilon_e (\nabla_{\boldsymbol{X}} \phi_1 + \nabla_{\boldsymbol{x}} \phi_0) \cdot \boldsymbol{V} \cdot \hat{\boldsymbol{n}}_0 dl_X = -\rho_{\text{eff}}, \tag{2.179}$$

where ε_{eff} is given by (2.128) and ρ_{eff} by (2.137). Thus we have the same terms as in the homogenised problem derived in section 2.3.1, but with several boundary integrals that do not cancel. We note that while the second and third integrals were present in the standard multiple scales problem and integrated to zero in that example, it was due to a point-wise boundary condition on the inclusion surface. Here, it appears we are double counting some terms; the motion of the boundary appears twice suggesting that we do not need to expand both the integrand and the normal in (2.145).

2.3.2.2 Writing the integral constraint in multiple scales form

To identify the correct way to write the integral condition in multiple scales form, we extend the analysis presented by Chapman and McBurnie [25]. In [25], the proposed multiple scales form of the integral constraint (2.149) accounted for a change in value of the integrand as the slow coordinate varies at different points in the unit cell. To obtain (2.149), the dependence of the slow scale on the fast scale was written explicitly as $\boldsymbol{x} = \hat{\boldsymbol{x}} + \delta \boldsymbol{X}$ and the integrand was expanded about the fixed slow coordinate $\hat{\boldsymbol{x}}$. When the domain slowly varies, we must also expand the boundary position; we look to expand

$$\int_{\partial\Omega} \boldsymbol{Q} \cdot \hat{\boldsymbol{n}} ds = \delta^2 \int_{\partial\Omega(\hat{\boldsymbol{x}} + \delta \boldsymbol{X})} \boldsymbol{Q}(\hat{\boldsymbol{x}} + \delta \boldsymbol{X}, \boldsymbol{X}) \cdot \hat{\boldsymbol{n}} dS_X \tag{2.180}$$

onto the boundary at $\hat{\boldsymbol{x}}$. For generality, we consider a two-dimensional, open surface $\partial\Omega(\boldsymbol{x})$ which varies with slow position, as illustrated schematically in figure 2.3. The associated curve which bounds $\partial\Omega(\boldsymbol{x})$ is $\Gamma(\boldsymbol{x})$. As the slow position varies, so too does the surface; the volume swept through as the slow position

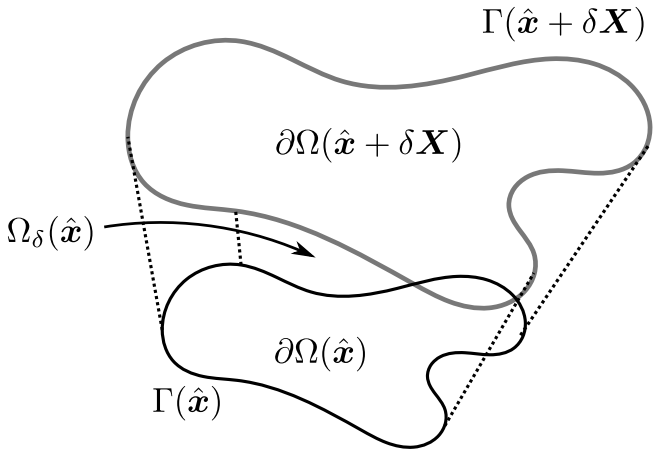

Figure 2.3: *Schematic of the open surface $\partial\Omega(\boldsymbol{x})$ changing as slow coordinate is varies within a unit cell from $\hat{\boldsymbol{x}}$ to $\hat{\boldsymbol{x}}+\delta\boldsymbol{X}$.*

changes from $\hat{\boldsymbol{x}}$ to $\hat{\boldsymbol{x}}+\delta\boldsymbol{X}$ is $\Omega_\delta(\hat{\boldsymbol{x}})$ as shown in figure 2.3. As in [25], we expand the integrand in (2.180) about $\hat{\boldsymbol{x}}$ which gives

$$\int_{\partial\Omega}\boldsymbol{Q}\cdot\hat{\boldsymbol{n}}ds=\delta^2\int_{\partial\Omega(\hat{\boldsymbol{x}}+\delta\boldsymbol{X})}\big(\boldsymbol{Q}(\hat{\boldsymbol{x}},\boldsymbol{X})+\delta\boldsymbol{X}\cdot\nabla_{\boldsymbol{x}}\boldsymbol{Q}(\hat{\boldsymbol{x}},\boldsymbol{X}))\big)\cdot\hat{\boldsymbol{n}}dS_X+\cdots. \quad (2.181)$$

Our aim now is to project the right-hand side of (2.181) onto the boundary at fixed slow position, $\partial\Omega(\hat{\boldsymbol{x}})$. To do this, we take a similar approach to one which may be used to derive the flux transport theorem heuristically, see for example [39]. Applying the divergence theorem to the first term in the right-hand side of (2.181) on the geometry shown in figure 2.3, we can write

$$\begin{aligned}\int_{\partial\Omega(\hat{\boldsymbol{x}}+\delta\boldsymbol{X})}\boldsymbol{Q}(\hat{\boldsymbol{x}},\boldsymbol{X})\cdot\hat{\boldsymbol{n}}\,dS_X=\int_{\Omega_\delta(\hat{\boldsymbol{x}})}\nabla_{\boldsymbol{X}}\cdot\boldsymbol{Q}(\hat{\boldsymbol{x}},\boldsymbol{X})dV_X+\int_{\partial\Omega(\hat{\boldsymbol{x}})}\boldsymbol{Q}(\hat{\boldsymbol{x}},\boldsymbol{X})\cdot\hat{\boldsymbol{n}}dS_X\\-\int_{\partial\Omega_\delta(\hat{\boldsymbol{x}})}\boldsymbol{Q}(\hat{\boldsymbol{x}},\boldsymbol{X})\cdot\hat{\boldsymbol{n}}dS_X,\end{aligned} \quad (2.182)$$

where $\partial\Omega_\delta$ is the boundary containing the dashed lines in figure 2.3. In the limit $\delta\to 0$, the volume element of Ω_δ in fast coordinates dV_X can be written as the product of the area element of $\partial\Omega(\hat{\boldsymbol{x}})$ with the height of the Ω_δ volume. Hence,

we have $dV_X = \delta \boldsymbol{X} \cdot \boldsymbol{V} \cdot \hat{\boldsymbol{n}}\, dS_X$, where $\boldsymbol{V} = \nabla_{\boldsymbol{x}} \boldsymbol{R}^b$ is the 'velocity' of the boundary for positions $\boldsymbol{R}^b$ on $\partial\Omega(\hat{\boldsymbol{x}})$. The area element of $\partial\Omega_\delta$ can be written as the cross product of the line element of $\Gamma(\hat{x})$, $d\boldsymbol{r}$, with the height of the Ω_δ, that is $\hat{\boldsymbol{n}} dS_X = -\delta \boldsymbol{X} \cdot \boldsymbol{V} \times d\boldsymbol{r}$, where the negative sign ensures the normal is outward-facing. Substituting the form for the volume element of Ω_δ and area element of $\partial\Omega_\delta$ into (2.182), we have

$$\begin{aligned}\int_{\partial\Omega(\hat{\boldsymbol{x}}+\delta\boldsymbol{X})} \boldsymbol{Q}(\hat{\boldsymbol{x}}, \boldsymbol{X}) \cdot \hat{\boldsymbol{n}}\, dS_X = \int_{\partial\Omega(\hat{\boldsymbol{x}})} \delta(\nabla_{\boldsymbol{X}} \cdot \boldsymbol{Q}) \boldsymbol{X} \cdot \boldsymbol{V} \cdot \hat{\boldsymbol{n}}\, dS_X \\ + \int_{\partial\Omega(\hat{\boldsymbol{x}})} \boldsymbol{Q} \cdot \hat{\boldsymbol{n}} dS_X + \int_{\Gamma(\hat{\boldsymbol{x}})} \delta \boldsymbol{Q} \cdot (\boldsymbol{X} \cdot \boldsymbol{V}) \times d\boldsymbol{r},\end{aligned} \tag{2.183}$$

Combining (2.183) with (2.181), the correct multiple scales form for integral constraints on a slowly varying domain appears to be

$$\begin{aligned}\int_{\partial\Omega} \mathbf{Q} \cdot \hat{\boldsymbol{n}}\, dS \to \delta^2 \int_{\partial\Omega} (\mathbf{Q} + \delta \mathbf{X} \cdot \nabla_{\boldsymbol{x}} \mathbf{Q} + \delta(\nabla_{\boldsymbol{X}} \cdot \mathbf{Q}) \mathbf{X} \cdot \boldsymbol{V}) \cdot \hat{\boldsymbol{n}}\, dS_X \\ + \delta^2 \int_{\Gamma} \delta \boldsymbol{Q} \cdot (\boldsymbol{X} \cdot \boldsymbol{V}) \times d\boldsymbol{r}.\end{aligned} \tag{2.184}$$

Thus, we find that it is not necessary to include the multiple scales expansion of the normal. The additional terms that appear in (2.184) account for the variation in the integrand with the slow scale as we move across the unit cell and the variation due to slow variation of the inclusion boundary. Hence, the normal in (2.184) is to the boundary evaluated at fixed $\hat{\boldsymbol{x}}$; we would have a normal expansion in the integral only if the level set defining the boundary (2.81) had a dependence on δ at fixed slow position.

For the two-dimensional problem we are considering, where the inclusion surfaces are closed, (2.184) reduces to

$$\int_{\partial\Omega_e} \mathbf{Q} \cdot \hat{\boldsymbol{n}}\, dl \to \delta \int_{\partial D_e} (\mathbf{Q} + \delta \mathbf{X} \cdot \nabla_{\boldsymbol{x}} \mathbf{Q} + \delta(\nabla_{\boldsymbol{X}} \cdot \mathbf{Q}) \mathbf{X} \cdot \boldsymbol{V}) \cdot \hat{\boldsymbol{n}}_0\, dl_X, \tag{2.185}$$

where we have gained δ in changing to fast integration variables on a line rather than δ^2 when changing to fast integration variables in an area element.

In this section, we validate this proposal by considering (2.142)-(2.145). The multiple scales form of (2.142)-(2.144) is given by (2.146)-(2.148) and the multiple

scales form of (2.145) is taken to be (2.185). The analysis exactly follows section 2.3.2.1 until $O(\delta^2)$, where differences in the multiple scales form of the integral constraints become apparent. Using (2.185), the $O(\delta^2)$ problem becomes,

$$\nabla_{\boldsymbol{X}} \cdot (\varepsilon_e(\nabla_{\boldsymbol{X}}\phi_2 + \nabla_{\boldsymbol{x}}\phi_1)) + \nabla_{\boldsymbol{x}} \cdot (\varepsilon_e(\nabla_{\boldsymbol{X}}\phi_1 + \nabla_{\boldsymbol{x}}\phi_0)) = 0 \quad \text{in} \quad D_e, \tag{2.186}$$

$$\nabla_{\boldsymbol{X}}\phi_2 + \nabla_{\boldsymbol{x}}\phi_1 = \mathbf{0} \quad \text{in} \quad D_i, \tag{2.187}$$

$$[\phi_2]_i^e = 0, \tag{2.188}$$

$$\int_{\partial D_e} \varepsilon_e(\nabla_{\boldsymbol{X}}\phi_2 + \nabla_{\boldsymbol{x}}\phi_1)\cdot \hat{\boldsymbol{n}}_0 dS + \int_{\partial D_e} \varepsilon_e \boldsymbol{X}\cdot \nabla_{\boldsymbol{x}}(\nabla_{\boldsymbol{X}}\phi_1 + \nabla_{\boldsymbol{x}}\phi_0)\cdot \hat{\boldsymbol{n}}_0 dS + \int_{\partial D_e} \varepsilon_e \nabla_{\boldsymbol{X}}\cdot (\nabla_{\boldsymbol{X}}\phi_1 + \nabla_{\boldsymbol{x}}\phi_0)\mathbf{X}\cdot \mathbf{V}\cdot \hat{\boldsymbol{n}}_0 dS = 0. \tag{2.189}$$

Integrating (2.186) over the exterior region and applying the divergence theorem to the first term, gives

$$-\int_{\partial D_e} \varepsilon_e(\nabla_{\boldsymbol{X}}\phi_2 + \nabla_{\boldsymbol{x}}\phi_1)\cdot \hat{\boldsymbol{n}}_0 \, dl_X + \int_{D_e} \nabla_{\boldsymbol{x}}\cdot(\varepsilon_e(\nabla_{\boldsymbol{X}}\phi_1 + \nabla_{\boldsymbol{x}}\phi_0)) \, dS_X = 0, \tag{2.190}$$

where the integral over the exterior boundary of the unit cell vanishes due to periodicity in the derivatives of the expansion coefficients. The derivatives take the same value on opposing edges of the unit cell and so the boundary integral is equivalent to integrating out and back along a line. Substituting (2.189) to eliminate ϕ_2, we have

$$\int_{\partial D_e} \varepsilon_e \boldsymbol{X}\cdot \nabla_{\boldsymbol{x}}(\nabla_{\boldsymbol{X}}\phi_1 + \nabla_{\boldsymbol{x}}\phi_0)\cdot \hat{\boldsymbol{n}}_0 dl_X + \int_{\partial D_e} \varepsilon_e \nabla_{\boldsymbol{X}}\cdot (\nabla_{\boldsymbol{X}}\phi_1 + \nabla_{\boldsymbol{x}}\phi_0)\mathbf{X}\cdot \mathbf{V}\cdot \hat{\boldsymbol{n}}_0 dl_X + \int_{D_e} \nabla_{\boldsymbol{x}} \cdot (\varepsilon_e(\nabla_{\boldsymbol{X}}\phi_1 + \nabla_{\boldsymbol{x}}\phi_0)) \, dS_X = 0.$$

Applying transport theorems (2.175) and (2.111) to the first and final integrals gives

$$\nabla_{\boldsymbol{x}}\cdot \int_{\partial D_e} \varepsilon_e \boldsymbol{X}(\nabla_{\boldsymbol{X}}\phi_1 + \nabla_{\boldsymbol{x}}\phi_0)\cdot \hat{\boldsymbol{n}}_0 dl_X - \int_{\partial D_e} \varepsilon_e \nabla_{\boldsymbol{X}}\cdot (\boldsymbol{X}(\nabla_{\boldsymbol{X}}\phi_1 + \nabla_{\boldsymbol{x}}\phi_0))\cdot \mathbf{V}\cdot \hat{\boldsymbol{n}}_0 dl_X + \int_{\partial D_e} \varepsilon_e \nabla_{\boldsymbol{X}}\cdot (\nabla_{\boldsymbol{X}}\phi_1 + \nabla_{\boldsymbol{x}}\phi_0)\mathbf{X}\cdot \mathbf{V}\cdot \hat{\boldsymbol{n}}_0 dl_X + \nabla_{\boldsymbol{x}} \cdot \int_{D_e} (\varepsilon_e(\nabla_{\boldsymbol{X}}\phi_1 + \nabla_{\boldsymbol{x}}\phi_0)) \, dS_X + \int_{\partial D_e} \varepsilon_e(\nabla_{\boldsymbol{X}}\phi_1 + \nabla_{\boldsymbol{x}}\phi_0)\cdot \mathbf{V}\cdot \hat{\boldsymbol{n}}_0 dl_X = 0. \tag{2.191}$$

Expanding the divergence in the second integral, we find that some of the boundary terms cancel, which leaves

$$\nabla_{\boldsymbol{x}}\cdot\int_{\partial D_e}\varepsilon_e\boldsymbol{X}(\nabla_{\boldsymbol{X}}\phi_1+\nabla_{\boldsymbol{x}}\phi_0)\cdot\hat{\boldsymbol{n}}_0 dl_X+\nabla_{\boldsymbol{x}}\cdot\int_{D_e}\left(\varepsilon_e(\nabla_{\boldsymbol{X}}\phi_1+\nabla_{\boldsymbol{x}}\phi_0)\right)\,dS_X=0. \tag{2.192}$$

As ϕ_0 is independent of the fast scale, we can apply the divergence theorem to the first integral, taking it into the inclusion to give

$$\nabla_{\boldsymbol{x}}\cdot(\varepsilon_e\nabla_{\boldsymbol{x}}\phi_0)+\nabla_{\boldsymbol{x}}\cdot\int_{\partial D_e}\varepsilon_e\boldsymbol{X}\nabla_{\boldsymbol{X}}\phi_1\cdot\hat{\boldsymbol{n}}_0 dl_X+\nabla_{\boldsymbol{x}}\cdot\int_{D_e}\varepsilon_e(\nabla_{\boldsymbol{X}}\phi_1)\,dS_X=0. \tag{2.193}$$

Applying the divergence theorem to the second integral, we have

$$\begin{aligned}&\nabla_{\boldsymbol{x}}\cdot(\varepsilon_e\nabla_{\boldsymbol{x}}\phi_0)-\nabla_{\boldsymbol{x}}\cdot\int_{D_e}\varepsilon_e\nabla_{\boldsymbol{X}}\cdot(\boldsymbol{X}\nabla_{\boldsymbol{X}}\phi_1)dS_X\\&\quad+\nabla_{\boldsymbol{x}}\cdot\int_{\partial D}\varepsilon_e\boldsymbol{X}\nabla_{\boldsymbol{X}}\phi_1\cdot\hat{\boldsymbol{n}}_0 dl_X+\nabla_{\boldsymbol{x}}\cdot\int_{D_e}\varepsilon_e(\nabla_{\boldsymbol{X}}\phi_1)\,dS_X=0.\end{aligned} \tag{2.194}$$

Cancelling terms and using the cell problem (2.163) we have

$$\nabla_{\boldsymbol{x}}\cdot(\varepsilon_e\nabla_{\boldsymbol{x}}\phi_0)+\nabla_{\boldsymbol{x}}\cdot\int_{D_e}\mathbf{X}\rho dS_X+\nabla_{\boldsymbol{x}}\cdot\int_{\partial D}\varepsilon_e\boldsymbol{X}\nabla_{\boldsymbol{X}}\phi_1\cdot\hat{\boldsymbol{n}}_0 dl_X=0. \tag{2.195}$$

Thus, we have the homogenised problem

$$\nabla_{\boldsymbol{x}}\cdot(\epsilon_p\nabla_{\boldsymbol{x}}\phi_0)=-\rho_{\text{eff}} \tag{2.196}$$

where

$$\epsilon_{p_{ij}}=\varepsilon_e\left(\delta_{ij}+\int_{\partial D}X_i\frac{\partial\Psi_j}{\partial X_k}\hat{\boldsymbol{n}}_{0k}dl_X\right). \tag{2.197}$$

The effective charge is given by

$$\rho_{\text{eff}}=\nabla_{\boldsymbol{x}}\cdot\left(\int_{D_e}\rho\mathbf{X}dS_X+\int_{\partial D}\varepsilon_e\mathbf{X}\nabla_{\boldsymbol{X}}\xi\cdot\hat{\boldsymbol{n}}_0 dl_X\right). \tag{2.198}$$

By writing the integral condition in multiple scales form using (2.185), we have obtained the same homogenised problem as derived as a limit of a standard multiple scales problem in section 2.3.1.

2.4 Discussion

In this chapter we have established how to treat integral constraints in multiple scales problems with a slowly varying microscale. We presented two approaches to homogenisation of a simple example problem in both one and two dimensions, considering the electric potential in a dielectric periodically interspersed with perfectly dielectric inclusions. The first approach involved taking a limit of the problem of a dielectric composite that can be tackled using standard multiple scales, establishing the correct form of the homogenised problem. We began by considering the one dimensional problem presented in the original paper which identified the multiple scales form of integral constraints [25]. The proposed multiple scales form of the integral constraint expands the integrand as in [25] but also the boundary position about a fixed slow position. In the one dimensional case some of the additional terms vanished for the regime considered.

In two dimensions we considered the limit of large charge, where the additional terms from the boundary expansion are no longer identically zero. We found that expanding the slow variation in the integrand and the boundary position in the integral constraint produces the same homogenised problem as the standard approach. To expand the boundary position, we used the flux transport theorem applied to spatial variables. It was not necessary to include the multiple scales expansion of the normal as required when using Neumann or Robin boundary conditions on a slowly varying domain. We showed in section 2.3.2.1 that including both the normal expansion and expansion of the integrand results in additional terms so that the standard homogenised model is not recovered.

In summary, this chapter provides justification for the multiple scales form of integral constraints in a slowly varying domain, equation (2.184). We will encounter such a constraint in chapter 3, although this method will be applicable to other multiple scales problems involving integral constraints.

Chapter 3

A homogenised model of fluid-string interaction

In this chapter, we develop an effective model for the bioreactor scaffold, modelling it as a fluid-string composite. To derive the model describing the interaction between string displacement, fluid velocity and pressure, we use homogenisation *via* multiscale asymptotics, employing the methods developed in chapter 2. Here, the microscale is given by the spacing between fibres that constitute the scaffold, with the scaffold dimensions characterising the macroscale. There is a one-way coupling between the microscale and macroscale problems; the microscale problem can be solved independently, providing the local flow field and, when averaged, the permeability. This coupling enables analysis of the relationship between microscale shear stress and boundary conditions imposed on the macroscale. The macroscale model consists of Darcy's law, a mass conservation condition and homogenised force balance. Darcy's law links the fluid velocity relative to the moving strings to the pressure gradients. The mass conservation condition relates the fluid flux to string density and the homogenised force balance couples the hydrodynamic stresses and string displacements. We solve the model in a simple geometry and identify scaling laws relating the frequency of imposed oscillation of the string ends to microscale shear stress. We also consider driving the flow with a fluid flux, where the solid fraction dictates the distribution of microscale shear stress.

The structure of this chapter is as follows. We introduce modelling approaches for fluid-fibre interaction in section 3.1, beginning by considering purely transverse displacement of the strings. The model setup is presented in section 3.2 and nondimensionalised in section 3.3. We homogenise the equations in section 3.4, identifying the form of the microscale and macroscale problems. We solve the resulting equations in section 3.5 in simplified geometries. We then extend the model in 3.6, where we illustrate how to incorporate axial fibre deformation. We discuss the results and summarise the work in 3.7.

3.1 Introduction

The interaction between deformable fibres and slow, viscous flow is found in numerous applications such as cell mechanics, textile production and biological sensing [65, 89, 120]. Various theoretical, numerical and experimental techniques have been developed to study the interaction of fibres with Stokes flow [45, 73]. Some methods that track the deformation of each fibre individually become untenable when there is a large number of fibres in the system. We do not consider these approaches here; instead we focus on methods applicable to modelling many fibre systems.

3.1.1 Interaction of rigid fibres with flow

The simplest examples of interactions between fibre ensembles and slow flow occur when fibre deformation is a subdominant effect. That is, the bending rigidity of the fibres is much greater than viscous forces,

$$\frac{\delta B}{\mu U L^3} \gg 1, \tag{3.1}$$

where B is the bending rigidity, δ the beam deflection nondimensionalised by its length L, μ is the dynamic viscosity of the fluid and U is its typical velocity. In the absence of tension, such as beams with a free end, the left-hand side of (3.1) is the relevant dimensionless number characterising the relative size of the stress required

to induce an $O(1)$ bending deformation to the magnitude of fluid stress. For the regime (3.1), where the stress required to induce deformation is much greater than the characteristic size of fluid stress, the coupling between the fibres and fluid is one-way; the presence of the fibres influences the flow field but the flow does not induce fibre deformation.

Experimental and theoretical studies of this regime have been motivated by modelling diving of semi-aquatic mammals, which have a pelt trapping air for insulation, and nectar feeding birds, which have a tongue coated in fibres to enhance nectar uptake [87, 88]. One study considered experiments where a plate covered with elastomer 'hairs' was plunged into or drawn from a bath of silicone oil (figure 3.1.a). When the flow saturates the fibres, in modelling motivated by crustacean sensing, it was found that the magnitude of the upstream velocity perpendicular to the fibre axes sets the flow configuration through the fibres shown in 3.1.b [63]. Estimates of the boundary layer thickness, derived from fitting numerical simulations of flow around a single fibre as the Reynolds number varied between 0.003 and 25, were used to predict the flow regime. Fluid flowed through the fibres with little deflection when the boundary layers surrounding a single fibre were small. At intermediate values, flow was deflected perpendicular to the upstream flow direction and when the boundary layers of adjacent fibres overlapped, flow was deflected around the fibre bed [63]. While this study allows the flow regime to be identified, it does not facilitate calculation of the velocity field across the domain, which would be required to estimate microscale shear stresses throughout the bioreactor scaffold, without direct simulation.

One approach used to model flow in fibre composites which does facilitate calculation of the microscale shear stress is homogenisation *via* multiscale asymptotics, introduced in detail in chapter 2. In filters with a fibrous microstructure that does not deform in response to the flow, an effective model can be obtained that incorporates the microscale geometry *via* the model parameters, see for example [36, 35, 98, 71]. This coupling between microscale and macroscale enables a calculation of the shear stress across the domain. We will return to homogenised models in section 3.1.3 where we consider problems with two-way fluid-structure interaction.

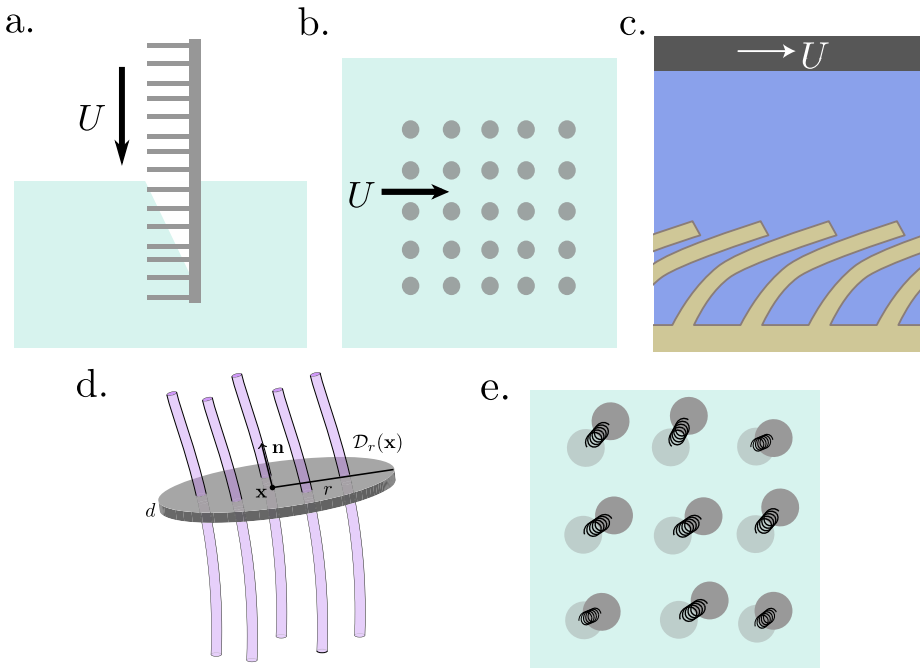

Figure 3.1: *Fluid-fibre systems considered in the literature. a. A fibre-covered plate is plunged into a bath of viscous fluid [88]. The direction of velocity is reversed in the draining problem considered in [87]. b. Flow streams through or is directed perpendicularly from the initial flow direction depending on the Reynolds number [63]. c. Taylor-Couette flow over a deformable fibre bed. Figure adapted by permission from Springer Nature Customer Service Centre GmbH: Nature, Nature Physics [6]. d. Representative volume element used in deriving a coarse-grained model of fluid-structure interaction in fibre beds. Figure reused from [117] with permission from APS and David Stein. e. Microstructure for the homogenised model of fluid-string interaction presented in [9, 10]. Rods are tethered to their initial positions by Hookean springs and interact with viscous flow.*

3.1.2 Models of fluid-fibre interaction

When fibre elasticity is on the same order as viscous effects, the system dynamics become significantly more complex. In elasto-viscous systems, the flow and solid deformation are fully coupled with the flow field, inducing fibre deformation which in turn modifies the domain for the flow. An experimental and theoretical study illustrating this coupling considered Taylor-Couette flow above a plate covered in deformable fibres (figure 3.1.c) [6]. The deformation, assumed identical for all fibres, was modelled using a nonlinear beam equation with a point force at the beam tip used to reflect the fluid stress. The system showed a shear stress reducing nonlinearity, where the effects of increasing the plate speed are outweighed by the increased effective channel width resulting from fibre bending induced by an increased fluid shear stress, ultimately reducing the shear stress on the upper plate [6].

When the assumption of uniform solid deformation across the material does not hold, continuum models that treat the material as a composite may be used [40]. The equations of poroelasticity describe the dynamics of a porous, elastic solid filled with fluid and consist of: constitutive equations relating solid deformation to solid stress and pore pressure; transport and continuity equations for the fluid and a momentum conservation equation for the total stress.

Poroelastic models have been used to model fibrous bioreactor scaffolds [135, 138]. Treating the fibrous scaffold as a cylinder with a small aspect ratio, analytical solutions were found for a time-harmonic axial loading of the scaffold [135]. The elastic modulus and Poisson ratio for the poroelastic material were estimated by fitting experimental data [138]. These models can be used to estimate an averaged microscale shear stress but in order to model the variations of the shear stress on the microscale, a multiscale model is required. Often, multiscale models are obtained by an averaging process. We will review different averaging processes in the next section.

3.1.3 Averaged models of fluid-fibre interaction

Averaging methods have been applied in developing models for wet-spinning, an industrial process used to manufacture polymer fibres such as viscose. Polymer solution is extruded through a metal plate into a bath where the fibres coagulate to form a bundle of fibres. The bundle is drawn over a series of rollers through a stationary bath before heating and spreading the bundle. To derive a model for the flow through the fibre bundle and the deformation it induces, the analytical result for drag on fibres in a periodic array was substituted as a body force in the the inviscid Navier-Stokes equations [90]. This generates an average flow equation which was coupled to fibre motion *via* a force balance of the averaged pressure drop across the fibre bundle with the fibre elasticity [90]. The result is an averaged model for a deforming porous media with model parameters given by analytical results for the flow around an periodic array of cylinders. A reduced version of this model was coupled to a surrounding lubricating flow in [120]. A similar averaged poroelastic model to describe the wet-spinning process was derived by Szaniawski [119].

A more formal volume averaging approach was taken by Stein and Shelley to derive an effective model for an ensemble of flexible fibre ensembles immersed in slow, viscous flow [117]. In general, volume averaging proceeds by defining a 'representative volume element' which characterises the microstructure of the material (figure 3.1.d). Equations are posed over this representative volume which are then averaged to obtain an effective model that describes the bulk material [130]. To treat the fluid-fibre system, fibres were treated as Euler-Bernoulli elastica coupled with the background flow field induced by other fibres *via* local slender body theory. After averaging over the representative volume element including many aligned fibres, the Brinkman equations, with a body force from the fibres, were coupled with an equation governing fibre deformation [117]. In the averaging process, the assumption of low fibre density resulted in incompressibility holding in the averaged equations. When the fibre density is high, an alternative approach is to begin with continuum equations for both the solid and fluid phase.

Motivated by the need to develop effective equations for general systems in-

volving 'bristles, carpets and brushes' interacting with slow, viscous flow, Gopinath and Mahadevhan considered continuum equations for linearly elastic material saturated with fluid [52]. Averaged equations were obtained by constructing an effective stress tensor from the linear superposition of fluid and elastic stresses, treating the 'bristles, carpets and brushes' as a continuum. The effective equations took the form of a modified Darcy's law coupled to solid deformation. By considering different constitutive equations for the constituents, the model was applied to polymer networks and ordered carpets [52].

In the effective models derived by Gopinath and Mahadevhan, it is necessary to specify the form of the model parameters using constitutive laws. In the derivation of averaged models using homogenisation *via* multiscale asymptotics (for details see section 2.1), the parameters in the effective model are obtained as part of the model derivation. Applying homogenisation *via* multiscale asymptotics to a continuum, linearly elastic material interspersed with fluid results in the equations of poroelasticity [21, 83]. The microscale problems that arise during the homogenisation process can be solved to give the elasticity tensor and the permeability.

For fluid-fibre composites, it may be more intuitive to begin with a discrete description of each string rather than treating the solid phase as a continuum. A homogenised model was derived from discrete solid elements in [9], treating sprung rods surrounded by a viscous, incompressible, Newtonian fluid. The line of rods surrounded by flow, assumed to be uniform along the axis of the rod, was extended to a two-dimensional array in [10]. A full presentation of the multiple scales derivation was not given and so it is difficult to establish how the integral constraint appearing in the force balance on the rod was transformed into multiple scales form.

In this chapter, we build on [10] to develop a homogenised model of fluid-string interaction. The force balance, which couples the string displacement to the fluid motion, gives an integral condition on a slowly varying domain. Hence, we must use the methods developed in chapter 2 to systematically derive the homogenised model.

3.2 Model setup

As outlined in chapter 1, the bioreactor scaffold consists of many aligned fibres attached to each end of the chamber. The chamber is filled with cell culture media during operation, and enclosed by a flexible membrane which allows for a large class of deformations that mimic physiological motion. As a starting point, we make a number of assumptions that simplify the analysis, enabling us to derive an effective model for the fibre-fluid composite. Throughout this chapter, we neglect the volume occupied by cells, using the fluid shear stress on the surface of the fibres as a proxy for the shear stress experienced by cells. As such, the modelling that ensues will be applicable during the early stages of bioreactor operation (for details see appendix A.1.1). We return to this assumption in the discussion, where we outline how to account for the effects of finite cell volume.

We model the cell culture media as a viscous, incompressible, Newtonian fluid with dynamic viscosity μ. The scaffold fibres are modelled as N aligned strings separated by a distance l at equilibrium, each with circular cross-section of radius b. The superscript i indexes the string under consideration: $i = 1, 2, \cdots, N$. We use Cartesian coordinates with associated coordinate directions $\hat{\boldsymbol{e}}_x$, $\hat{\boldsymbol{e}}_y$, $\hat{\boldsymbol{e}}_z$, taking the origin to be at the centre of the base of the scaffold, with the z-axis aligned with the strings' equilibrium configuration, as shown in figure 3.2.a. The equilibrium position of the centre-line of the ith string is given by $\boldsymbol{x}_0^i = \boldsymbol{x}_*^i + z\hat{\boldsymbol{e}}_z$, where $\boldsymbol{x}_*^i = (x_*^i, y_*^i, 0)$ is assumed to lie on a square periodic lattice, which covers the whole domain, as illustrated in figure 3.2.b. The curved exterior boundary of the fluid domain is $\partial\Omega_e$ and the flat boundary is denoted $\Omega_\perp$. The domain has characteristic dimension L, with a fluid region Ω_f. The region occupied by a string in a $z =$ constant plane is D_s^i and its associated boundary is ∂D_s^i. Fluid flow can be driven by imposing string motion or by prescribing a fluid velocity at one end of the domain. We envisage string-driven flow will reflect the mechanical stimulation of the chamber by the robot, while flux-driven flow can be used to model perfusion as outlined in section 1.2.1.

We model the scaffold fibres as uniform, elastic strings under tension which execute small, transverse displacements. Considering motion confined to the trans-

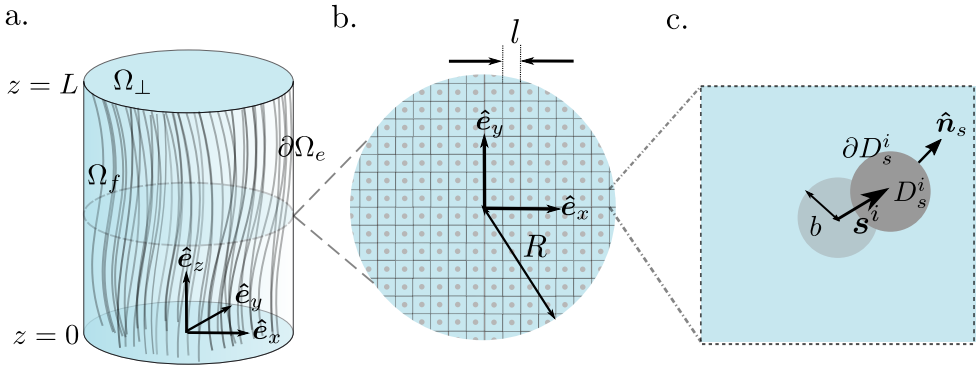

Figure 3.2: *Schematic of the model setup. a. Viscous, incompressible, Newtonian fluid in the region Ω_f surrounds strings aligned under tension in an examplar cylindrical domain with radius R and length L. Fluid is represented in blue and strings are drawn in grey. b. The approximate representation of the domain cross-section used in the homogenisation procedure. c. 'Zooming' into the macroscale domain, indicated by the dot-dashed lines, shows the unit cell which forms the domain for the microscale problem. Dashed lines show the boundaries where periodicity is imposed.*

verse plane simplifies the analysis, though we will relax this assumption in section 3.6.1. Assuming that the string cross-section does not deform, we can describe the displacement of the ith string from its equilibrium configuration *via* the displacement of its centre-line $\boldsymbol{s}^i(z,t) = (s_1^i, s_2^i)$. Thus, the region D_s^i is given by $|\boldsymbol{x}_{\perp *}^i - \boldsymbol{s}^i|^2 \leq b^2$, where $\boldsymbol{x}_{\perp *} = (x_*^i, y_*^i)$.

The surrounding media is modelled as a slow, viscous, incompressible, Newtonian fluid governed by

$$-\mu\nabla^2\boldsymbol{u} + \nabla p = \boldsymbol{0} \quad \text{in} \quad \Omega_f, \tag{3.2}$$

$$\nabla\cdot\boldsymbol{u} = 0 \quad \text{in} \quad \Omega_f. \tag{3.3}$$

where $\boldsymbol{u} = u\hat{\boldsymbol{e}}_x + v\hat{\boldsymbol{e}}_y + w\hat{\boldsymbol{e}}_z$ is the fluid velocity and p is the fluid pressure. For convenience, we decompose the velocity into its transverse and axial components, introducing $\boldsymbol{v} = (u, v)$.

No-slip conditions are imposed at the boundary of each string so that

$$\boldsymbol{v} = \frac{\partial \boldsymbol{s}^i}{\partial t} \quad \text{on} \quad \partial D_s^i, \tag{3.4}$$

$$w = 0 \quad \text{on} \quad \partial D_s^i, \tag{3.5}$$

where t denotes time, for each $0 \leq z \leq L$. We also require boundary conditions for the fluid flow on the outer edges of the domain. The exact form that these boundary conditions take will be given in section 3.4.5 after derivation of the homogenised model. Homogenisation reduces the order of the fluid problem and thus reduces the number of boundary conditions required.

We balance the fluid force exerted on the string boundary with elastic forces due to the string tension. The nondimensional number describing the relative strength of the string inertia to the string tension is $\rho T b^2/\mu^2 L^2$ for a string with mass volume density ρ and tension T. We consider strings with an aspect ratio b/L which is sufficiently small such that $\rho T b^2/\mu^2 L^2 \ll 1$. Neglecting the inertial terms, the transverse force balance on the ith string is given by

$$\int_{\partial D_s^i} \boldsymbol{\sigma}_\perp \cdot \hat{\boldsymbol{n}}_s dl + \frac{\partial}{\partial z}\left(T \frac{\partial \boldsymbol{s}^i}{\partial z}\right) = \boldsymbol{0}, \tag{3.6}$$

where $\hat{\boldsymbol{n}}_s$ is the outward pointing unit normal to ∂D_s^i, which lies on the transverse plane, and $\boldsymbol{\sigma}_\perp$ is the 2×2 fluid stress tensor for the transverse flow components. Despite neglecting inertia in both the fluid and solid momentum balances, we require an initial condition on the displacement which we set as

$$\boldsymbol{s}^i = \boldsymbol{0}. \tag{3.7}$$

The strings are fixed at their base and a displacement is imposed at the upper end,

$$\boldsymbol{s}^i = \boldsymbol{0} \quad \text{at} \quad z = 0, \tag{3.8}$$

$$\boldsymbol{s}^i = \boldsymbol{a}^i(t) \quad \text{at} \quad z = L \tag{3.9}$$

Various examples of imposed in-plane displacements, $\boldsymbol{a}^i(t)$, will be considered in section 3.5.2. We will find that homogenised model we obtain can also be driven by imposing the fluid pressure or fluid flux at the boundary. We defer specifying the form of these boundary conditions to section 3.4.5, where the form of the homogenised problem is given.

3.3 Nondimensionalisation and scaling

We assume that the characteristic lengthscale of separation between adjacent fibres l is much less than width of the domain L, introducing the small parameter $\delta = l/L \ll 1$. Motivated by the scalings used to derive Darcy's law from homogenisation of the Stokes equations in a porous material, we seek a balance between macroscopic pressure gradients and microscale viscous terms. We nondimensionalise the problem by scaling

$$\begin{aligned} (u,v,w) = U(\hat{u},\hat{v},\hat{w}), \quad (x,y,z) = L(\hat{x},\hat{y},\hat{z}), \quad t = \delta\frac{L}{U}\hat{t}, \\ \boldsymbol{s}^i = \delta L\hat{\boldsymbol{s}}^i, \quad \boldsymbol{a}^i = \delta L\hat{\boldsymbol{a}}^i, \quad p = p_a + \frac{\mu U}{\delta^2 L}\hat{p}, \quad T = \frac{\mu U L}{\delta}\mathcal{T} \end{aligned} \tag{3.10}$$

where p_a is the atmospheric pressure and hats denote nondimensional quantitities. The velocity scale U will be determined later by choosing scalings to balance terms in the string force balance. The timescale given is chosen to ensure we have a balance at leading-order in (3.4) so that string displacement drives fluid motion. This balance results in the presence of string velocity in the leading-order macroscale equations.

After nondimensionalisation and dropping hats, the Stokes equations (3.2)-(3.3) become

$$-\delta^2\nabla^2\boldsymbol{u} + \nabla p = 0 \quad \text{in} \quad \Omega_f, \tag{3.11}$$

$$\nabla\cdot\boldsymbol{u} = 0 \quad \text{in} \quad \Omega_f. \tag{3.12}$$

No-slip conditions at the string boundaries (3.4)-(3.5) give

$$\boldsymbol{v} = \frac{\partial \boldsymbol{s}^i}{\partial t} \quad \text{on} \quad \partial D_s^i, \tag{3.13}$$

$$w = 0 \quad \text{on} \quad \partial D_s^i. \tag{3.14}$$

Nondimensionalisation of the force balance (3.6) yields

$$\int_{\partial D_s^i} \boldsymbol{\sigma}_\perp\cdot\hat{\boldsymbol{n}}_s dl + \frac{\partial}{\partial z}\left(\mathcal{T}\frac{\partial \boldsymbol{s}^i}{\partial z}\right) = \boldsymbol{0}. \tag{3.15}$$

In appendix C, we show that the nondimensional tension $\mathcal{T}$ is constant at leading-order. Balancing terms in (3.15), by setting $\mathcal{T} = 1$, fixes the velocity scale of the

problem to be given by

$$U = \frac{\delta T}{\mu L}. \tag{3.16}$$

An alternative scaling would set the velocity scale by the boundary conditions imposed on the macroscale problem. The benefit of this choice would be clarity in the effects of varying string tension, although we do not consider this scaling in this chapter. At higher orders, we expect that the differences in fluid shear along the string length will induce changes in tension, though the first-order correction to the tension does not feature in our analysis. Nondimensionalising the boundary conditions on string displacement gives

$$\boldsymbol{s}^i = \boldsymbol{0} \quad \text{at} \quad z = 0, \tag{3.17}$$

$$\boldsymbol{s}^i = \boldsymbol{a}^i(t) \quad \text{at} \quad z = 1, \tag{3.18}$$

and the initial condition (3.7) becomes

$$\boldsymbol{s}^i = \boldsymbol{0} \quad \text{at} \quad t = 0. \tag{3.19}$$

3.4 Homogenisation

In this section, we use multiscale asymptotics to derive continuum equations describing the fluid and string motion on the macroscale. Instead of solving coupled equations for the string motion and flow field in a complicated domain, the aim is to obtain two simpler problems that can be solved separately: one determining microscale variations in the flow field around a single string, the second effective medium equations for the fluid-string interaction.

The slow scale $\boldsymbol{x}$ describes variation on the scale of the domain width, *i.e.* the macroscale, and we introduce a fast scale $\boldsymbol{X} = (x, y)/\delta - \lfloor (x, y)/\delta \rfloor - \boldsymbol{1}/2$, which describes variation on the scale of the string separation, *i.e.* the microscale. We assume that these two scales are independent, and that the domain cross-section can be constructed from unit cells that each contain a single fibre, as shown in figure 3.2.c. Given $\delta \ll 1$, we operate under the assumption that the number of

strings is sufficiently large that boundary effects from the breakdown of periodicity at the edge of the domain are negligible.

3.4.1 Continuum equations for string displacements

We begin by writing equations describing the string displacements in a form that can be homogenised. We assume that the displacement of neighbouring strings is sufficiently similar to allow the introduction of a continuum field for the string displacement. We introduce piece-wise constant functions for the string displacement and reference position

$$\boldsymbol{s}(\boldsymbol{x},t) = \boldsymbol{s}^i(z,t) \quad \text{in} \quad D_s^i, \tag{3.20}$$

$$\boldsymbol{x}_0(\boldsymbol{x}) = \boldsymbol{x}_0^i(z) \quad \text{in} \quad D_s^i, \tag{3.21}$$

defined over the solid region of the unit cell D_s^i. That is, the function $\boldsymbol{s}$ is defined to take the value of the displacement of the string found in the same unit cell as $\boldsymbol{x}$. Equation (3.20) cannot be transformed into multiple scales form easily and so we follow [25] in rephrasing this equation as

$$\nabla_\perp \boldsymbol{s} = 0 \quad \text{in} \quad D_s, \tag{3.22}$$

where $\nabla_\perp = (\partial_x, \partial_y)$. Within a two-dimensional unit cell, the region occupied by the string is D_s and the fluid region is D_f.

3.4.2 Multiple scales form of the governing equations

To write the differential equations in multiple scales form, we apply the chain rule to the two-dimensional gradient operator

$$\nabla_\perp = \nabla_x + \frac{1}{\delta}\nabla_X, \tag{3.23}$$

where $\nabla_x = (\partial_x, \partial_y)$ and $\nabla_X = (\partial_X, \partial_Y)$. We have introduced the fast variable only in the transverse plane, leaving the z-coordinate untouched. We seek multiple scales expansions for the fluid velocity, pressure and string displacement by

expanding as a power series in δ:

$$\boldsymbol{v} = \boldsymbol{v}_0(\boldsymbol{x}, \boldsymbol{X}, t) + \delta \boldsymbol{v}_1(\boldsymbol{x}, \boldsymbol{X}, t) + O(\delta^2), \tag{3.24}$$

$$w = w_0(\boldsymbol{x}, \boldsymbol{X}, t) + \delta w_1(\boldsymbol{x}, \boldsymbol{X}, t) + O(\delta^2), \tag{3.25}$$

$$p = p_0(\boldsymbol{x}, \boldsymbol{X}, t) + \delta p_1(\boldsymbol{x}, \boldsymbol{X}, t) + O(\delta^2), \tag{3.26}$$

$$\boldsymbol{s} = \boldsymbol{s}_0(\boldsymbol{x}, \boldsymbol{X}, t) + \delta \boldsymbol{s}_1(\boldsymbol{x}, \boldsymbol{X}, t) + O(\delta^2), \tag{3.27}$$

where the variables in all expansions are periodic in $\boldsymbol{X}$ with period $\mathbf{1}$, motivated by the microscale structure of the domain.

We substitute the expansions (3.24)-(3.27) into the Stokes equations (3.11)-(3.12) and the equation governing string displacement (3.22) written in multiple scales form. At leading-order in δ, we find

$$\nabla_X p_0 = \mathbf{0} \quad \text{in} \quad D_f, \tag{3.28}$$

$$\nabla_X \cdot \boldsymbol{v}_0 = 0 \quad \text{in} \quad D_f, \tag{3.29}$$

$$\nabla_X \boldsymbol{s}_0 = 0 \quad \text{in} \quad D_s. \tag{3.30}$$

Equation (3.28) and (3.30) imply that the leading-order pressure $p_0 = p_0(\boldsymbol{x}, t)$ and string displacement $\boldsymbol{s}_0 = \boldsymbol{s}_0(\boldsymbol{x}, t)$ are independent of the fast scale. At $O(\delta)$,

$$-\nabla_X^2 \boldsymbol{v}_0 + \nabla_x p_0 + \nabla_X p_1 = \mathbf{0} \quad \text{in} \quad D_f, \tag{3.31}$$

$$-\nabla_X^2 w_0 + \frac{\partial p_0}{\partial z} = 0 \quad \text{in} \quad D_f, \tag{3.32}$$

$$\nabla_X \cdot \boldsymbol{v}_1 + \nabla_x \cdot \boldsymbol{v}_0 + \frac{\partial w_0}{\partial z} = 0 \quad \text{in} \quad D_f, \tag{3.33}$$

$$\nabla_x \boldsymbol{s}_0 + \nabla_X \boldsymbol{s}_1 = 0 \quad \text{in} \quad D_s. \tag{3.34}$$

We can integrate (3.34) with respect to the fast variable to find

$$\boldsymbol{s}_1 = -\boldsymbol{X} \cdot \nabla_x \boldsymbol{s}_0 + \boldsymbol{d}_0, \tag{3.35}$$

where $\boldsymbol{d}_0 = \boldsymbol{d}_0(\boldsymbol{x})$ is a function from integration. Before deriving the resulting microscale and macroscale problems, we write the boundary conditions (3.13)-(3.15) in multiple scales form.

3.4.3 Transforming the boundary conditions into multiple scales form

Homogenisation *via* multiscale asymptotics in multiple spatial dimensions generally relies on the assumption of periodicity in the microscale variables in order for the microscale and macroscale equations to decouple. However, progress can also be made in scenarios where the unit cell is slowly varying as discussed in chapter 2.

At present, our microscale problem is solved over the domain shown in figure 3.2.c, which is also a function of the fast spatial scale due to higher order terms in the expansion of $\boldsymbol{s}$. Our aim is to project our equations onto the domain corresponding to the leading-order position of the string which, as established above, depends only on the slow scale, thereby facilitating multiple scales analysis. The position of the string boundary in the domain shown in 3.2.c, ∂D_s, is given by the level set $h_s = 0$ of the function

$$h_s = |\boldsymbol{X} - \boldsymbol{X}_0 - \boldsymbol{s}| - B, \tag{3.36}$$

where $B = b/\delta$ is the string radius and $\boldsymbol{X}_0 = \boldsymbol{x}_0/\delta - \lfloor \boldsymbol{x}_0/\delta \rfloor - \mathbf{1}/2$ is the equilibrium position of the string in the (x, y)-plane with respect to the microscale coordinates. Thus, the string boundary is dependent on both the fast and slow scales through the string displacement (3.27). Substituting (3.27) into (3.36), we find that the leading-order string boundary, $\partial D_{\boldsymbol{s}_0}$, is defined to be the level set $h = 0$ of the function

$$h = |\boldsymbol{X} - \boldsymbol{X}_0 - \boldsymbol{s}_0| - B. \tag{3.37}$$

As the leading-order string displacement is independent of the fast scale, the microscale domain with this boundary will be locally periodic. This results in macroscale and microscale problems that decouple. We begin by expanding the no-slip condition at the string boundary onto the leading-order domain before transforming the force balance into multiple scales form.

To be fully systematic, the expansion onto the leading-order boundary position and multiple scales expansion should be conducted in parallel. The resulting equations should then be projected onto the leading-order boundary position. However,

here we assume that the domain is that defined by (3.37). Defining the boundary to be the leading-order position of the string should result in the same homogenised problem but will significantly reduce the number of terms compared with the systematic analysis. We will return to this assumption in the chapter 5 where we discuss some implications.

3.4.3.1 No-slip conditions

We expand the no-slip condition at the string boundary (3.13) about the leading-order position $\partial D_{\boldsymbol{s}_0}$ in the fast variable. As the leading-order position depends on the slow scale, we have an $O(\delta)$ contribution to the no-slip condition from the variation in the leading-order displacement as we move around the boundary. This variation arises due to the small changes in the value of $\boldsymbol{x}$ as we move around the unit cell. In principle, this variation should be taken into account when evaluating the boundary conditions in all multiple scales problems. However, for most problems the terms obtained when accounting for this variation cancel (being slow derivatives of a lower order balance), so they are almost always ignored. In the present problem, where the string position is an unknown function of position, one of the resulting terms remains, so we need to treat the boundary conditions carefully.

We can account for the variation in $\boldsymbol{x}$ as we move around the unit cell explicitly by using a similar approach to that used in chapter 2 when considering integral constraints. The slow-fast interdependence can be dealt with by considering deviations of a macroscale point from a fixed reference point. That is, we write $\boldsymbol{x} = \hat{\boldsymbol{x}} - \delta\boldsymbol{b} + \delta\boldsymbol{X}$, where $\hat{\boldsymbol{x}}$ is an arbitrary reference point in the same unit cell as $\boldsymbol{x}$, and $\boldsymbol{b} = \hat{\boldsymbol{x}}/\delta - \lfloor \hat{\boldsymbol{x}}/\delta \rfloor$ is a constant vector joining $\hat{\boldsymbol{x}}$ to the lower left-hand corner of the unit cell. Henceforth, we take our reference point $\hat{\boldsymbol{x}}$ to be the lower left corner of the unit cell, fixing $\boldsymbol{b} = \boldsymbol{0}$. Thus if $\boldsymbol{x}$ is a point on the boundary of the string, then the velocity $\boldsymbol{u}$ is evaluated at $\boldsymbol{u}(\boldsymbol{x}, \boldsymbol{X}) = \boldsymbol{u}(\hat{\boldsymbol{x}} + \delta\boldsymbol{X}, \boldsymbol{X})$.

We expand about the leading-order position, for example

$$\boldsymbol{v}_0(\hat{\boldsymbol{x}}+\delta\boldsymbol{X},\boldsymbol{X}^b+\boldsymbol{s}_0(\hat{\boldsymbol{x}}+\delta\boldsymbol{X},t)+\delta\boldsymbol{s}_1(\hat{\boldsymbol{x}}+\delta\boldsymbol{X},\boldsymbol{X},t)+\cdots,t)= \tag{3.38}$$
$$\boldsymbol{v}_0+\delta\boldsymbol{X}\cdot\nabla_x\boldsymbol{v}_0+\delta(\boldsymbol{s}_1+\boldsymbol{X}\cdot\nabla_x\boldsymbol{s}_0)\cdot\nabla_X\boldsymbol{v}_0+O(\delta^2),$$

where $\boldsymbol{X}^b$ are points on the initial position of the string boundary and terms in the expansions are evaluated at $\boldsymbol{x}=\hat{\boldsymbol{x}}, \boldsymbol{X}=\boldsymbol{X}^b+\boldsymbol{s}_0(\hat{\boldsymbol{x}})$. Taking a similar expansion for all terms in the no-slip boundary condition, we find

$$\boldsymbol{v}_0+\delta\boldsymbol{X}\cdot\nabla_x\boldsymbol{v}_0+\delta(\boldsymbol{s}_1+\boldsymbol{X}\cdot\nabla_x\boldsymbol{s}_0)\cdot\nabla_X\boldsymbol{v}_0+\delta\boldsymbol{v}_1= \tag{3.39}$$
$$\frac{\partial\boldsymbol{s}_0}{\partial t}+\delta\boldsymbol{X}\cdot\nabla_x\left(\frac{\partial\boldsymbol{s}_0}{\partial t}\right)+\delta\frac{\partial\boldsymbol{s}_1}{\partial t}+O(\delta^2)\quad\text{on}\quad\partial D_{\boldsymbol{s}_0},$$

where terms involving the fast gradient of the leading-order string velocity vanish due to (3.30). Comparing coefficients at each order of δ, we obtain the following conditions on the leading-order fluid velocity

$$\boldsymbol{v}_0=\frac{\partial\boldsymbol{s}_0}{\partial t}\quad\text{on}\quad\partial D_{\boldsymbol{s}_0}. \tag{3.40}$$

Using (3.40), we can simplify (3.39) by cancelling the slow gradient of the leading-order velocity terms that appear on both sides of the equation at $O(\delta)$. The condition on the first-order fluid velocity becomes

$$\boldsymbol{v}_1=\frac{\partial\boldsymbol{s}_1}{\partial t}-(\boldsymbol{s}_1+\boldsymbol{X}\cdot\nabla_x\boldsymbol{s}_0)\cdot\nabla_X\boldsymbol{v}_0\quad\text{on}\quad\partial D_{\boldsymbol{s}_0}. \tag{3.41}$$

We can write (3.41) in a more convenient form using the solution to the $O(\delta)$ string problem. Substituting the expression for $\boldsymbol{s}_1$ into (3.41), we find

$$\boldsymbol{v}_1=\frac{\partial\boldsymbol{s}_1}{\partial t}-\boldsymbol{d}_0\cdot\nabla_X\boldsymbol{v}_0\quad\text{on}\quad\partial D_{\boldsymbol{s}_0}. \tag{3.42}$$

In a naive treatment of (3.4), the term involving $\boldsymbol{d}_0$ would not be present, highlighting the need for a careful treatment of the boundary condition. Repeating the analysis on (3.14), we obtain

$$w_0=w_1=0\quad\text{on}\quad\partial D_{\boldsymbol{s}_0}. \tag{3.43}$$

3.4.3.2 Force balance

To transform the force balance on the string into multiple scales form, we need to expand the integral of fluid traction on the string about the leading-order domain, account for the variation of the slow scale with the fast scale as we move around the string boundary, and expand the integrand in multiple scales form.

To project onto the leading-order domain, we use a similar expansion to that used in (3.38), writing

$$\boldsymbol{\sigma}_\perp(\hat{\boldsymbol{x}}+\delta\boldsymbol{X}, \boldsymbol{X}^b+\boldsymbol{s}_0(\hat{\boldsymbol{x}}+\delta\boldsymbol{X})+\delta\boldsymbol{s}_1(\hat{\boldsymbol{x}}+\delta\boldsymbol{X},\boldsymbol{X})+\cdots, t) = \boldsymbol{\sigma}_\perp+\delta\boldsymbol{X}\cdot\nabla_x\boldsymbol{\sigma}_\perp+\delta(\boldsymbol{s}_1+\boldsymbol{X}\cdot\nabla_x\boldsymbol{s}_0)\cdot\nabla_X\boldsymbol{\sigma}_\perp+\cdots. \tag{3.44}$$

We then write the integral in multiple scales form using the result from chapter 2, that is (2.185), which gives

$$\int_{\partial D_s}\boldsymbol{\sigma}_\perp\cdot\hat{\boldsymbol{n}}\,dl \to \delta\int_{\partial D_s}(\boldsymbol{\sigma}_\perp+\delta\mathbf{X}\cdot\nabla_{\boldsymbol{x}}\boldsymbol{\sigma}_\perp-\delta(\nabla_{\boldsymbol{X}}\cdot\boldsymbol{\sigma}_\perp)\mathbf{X}\cdot\boldsymbol{V})\cdot\hat{\boldsymbol{n}}_0\,dl_X, \tag{3.45}$$

where $\boldsymbol{V}=\nabla_{\boldsymbol{x}}\boldsymbol{s}_0$ and $dS_X = dXdY$ denotes the area element in fast scale variables. Combining (3.44) with (3.45), we find

$$\int_{\partial D_s}\boldsymbol{\sigma}_\perp\cdot\hat{\mathbf{n}}dl = \delta\int_{\partial D_{\boldsymbol{s}_0}}\boldsymbol{\sigma}_\perp\cdot\hat{\mathbf{n}}dl_X+\delta^2\int_{\partial D_{\boldsymbol{s}_0}}(\boldsymbol{s}_1+\boldsymbol{X}\cdot\nabla_x\boldsymbol{s}_0)\cdot\nabla_X\boldsymbol{\sigma}_\perp\cdot\hat{\mathbf{n}}dl_X + \delta^2\int_{\partial D_{\boldsymbol{s}_0}}\boldsymbol{X}\cdot\nabla_x\boldsymbol{\sigma}_\perp\cdot\hat{\mathbf{n}}dl_X-\delta^2\int_{\partial s_0}(\nabla_{\boldsymbol{X}}\cdot\boldsymbol{\sigma}_\perp)\mathbf{X}\cdot\boldsymbol{V}\cdot\hat{\mathbf{n}}dl_X+O(\delta^3), \tag{3.46}$$

where $dl_X = dl/\delta$ is the line element in fast coordinates and $\hat{\boldsymbol{n}}$ is the outward-facing normal to the boundary of the leading-order string position, pointing from the solid to the fluid domain. The multiple scales expansion for the fluid stress is,

$$\boldsymbol{\sigma}_\perp = -\delta^{-2}p_0I_2+\delta^{-1}[-p_1I_2+\nabla_X\boldsymbol{v}_0+(\nabla_X\boldsymbol{v}_0)^T]+O(1), \tag{3.47}$$

where $I_2=\mathrm{diag}(1,1)$. Substituting (3.47) into (3.46) gives

$$\int_{\partial D_s}\boldsymbol{\sigma}_\perp\cdot\hat{\mathbf{n}}dl = \int_{\partial D_{\boldsymbol{s}_0}}[-p_1I_2+\nabla_X\boldsymbol{v}_0+(\nabla_X\boldsymbol{v}_0)^T]\cdot\hat{\mathbf{n}}dl_X-\int_{\partial D_{\boldsymbol{s}_0}}\boldsymbol{X}\cdot\nabla_xp_0\cdot\hat{\mathbf{n}}dl_X+O(\delta), \tag{3.48}$$

where we have used (3.28). Applying the divergence theorem to each term on the right-hand side of (3.48) together with the periodicity condition, we find

$$\int_{\partial D_s} \boldsymbol{\sigma}_\perp \cdot \hat{\boldsymbol{n}} dl = -\int_{D_f} \nabla_X \cdot [-p_1 I_2 + \nabla_X \boldsymbol{v}_0 + (\nabla_X \boldsymbol{v}_0)^T] dS_X - \int_{D_{\boldsymbol{s}_0}} \nabla_x p_0 dS_X + O(\delta). \tag{3.49}$$

Since p_0 is independent of the fast scale (see (3.28)), it is straightforward to integrate $\nabla_x p_0$ over the string domain $D_{\boldsymbol{s}_0}$. Using (3.29) and (3.31), we can evaluate the right-hand side of (3.49) which gives

$$\int_{\partial D_s} \boldsymbol{\sigma}_\perp \cdot \hat{\boldsymbol{n}} dl = -\nabla_x p_0 + O(\delta). \tag{3.50}$$

Had we not accounted for the variation in the slow scale across the unit cell, the right-hand side of (3.50) would have been $-\phi_f \nabla_x p_0$, so that the forcing from the fluid shear would have been underestimated by a factor of $\phi_s \nabla_x p_0$. Here $\phi_s = \pi B^2$ denotes the solid volume fraction and $\phi_f = 1 - \phi_s$ denotes the fluid volume fraction. We deduce from (3.15) and (3.50) that the leading-order force balance at the string boundary takes the form

$$-\nabla_x p_0 + \frac{\partial^2 \boldsymbol{s}_0}{\partial z^2} = \boldsymbol{0}. \tag{3.51}$$

The homogenised force balance (3.51) forms part of the macroscale problem. This will be coupled to equations describing the macroscale variation of the fluid. We now return to the homogenisation of the fluid problem, beginning with the derivation of the cell problems.

3.4.4 Cell problems

The cell problems govern the microscale behaviour of the fluid dependent variables. We obtain the cell problems from equations (3.29), (3.31) and (3.32) which we restate here for convenience:

$$\nabla_X \cdot \boldsymbol{v}_0 = 0 \quad \text{in} \quad D_f, \tag{3.52}$$

$$-\nabla_X^2 \boldsymbol{v}_0 + \nabla_x p_0 + \nabla_X p_1 = \boldsymbol{0} \quad \text{in} \quad D_f, \tag{3.53}$$

$$-\nabla_X^2 w_0 + \frac{\partial p_0}{\partial z} = 0 \quad \text{in} \quad D_f, \tag{3.54}$$

with no-slip on the string boundary

$$\boldsymbol{v}_0 = \frac{\partial \boldsymbol{s}_0}{\partial t} \quad \text{on} \quad \partial D_{\boldsymbol{s}_0}, \tag{3.55}$$

$$w_0 = 0 \quad \text{on} \quad \partial D_{\boldsymbol{s}_0}, \tag{3.56}$$

and periodicity of $\boldsymbol{v}_0, w_0, p_0$ and p_1 in $\boldsymbol{X}$ with period $\mathbf{1}$. Exploiting the slow scale independence of the leading-order pressure and string velocity, we decompose our solution for fluid velocity and pressure as follows

$$\boldsymbol{v}_0 = \Psi_\perp \cdot \nabla_x p_0 + \Pi \cdot \frac{\partial \boldsymbol{s}_0}{\partial t}, \tag{3.57}$$

$$w_0 = \Psi_{33} \frac{\partial p_0}{\partial z}, \tag{3.58}$$

$$p_1 = \boldsymbol{\Phi} \cdot \nabla_x p_0 + \boldsymbol{\xi} \cdot \frac{\partial \boldsymbol{s}_0}{\partial t} + \overline{p}_1, \tag{3.59}$$

where $\Psi_\perp$, Π, Ψ_{33}, $\boldsymbol{\Phi}$ and $\boldsymbol{\xi}$ are defined below, while $\overline{p}_1 = \overline{p}_1(\boldsymbol{x}, t)$ is a function independent of the fast scale determined by the solvability condition for the microscale problem at $O(\delta^2)$.

The cell functions $(\Psi_\perp, \boldsymbol{\Phi})$ (a 2×2 tensor and vector respectively) satisfy the inhomogeneous problem derived from (3.53) and (3.52) with homogeneous boundary conditions, given by

$$-\nabla_X^2 \Psi_\perp + \nabla_X \boldsymbol{\Phi} + I = 0 \quad \text{in} \quad D_f, \tag{3.60}$$

$$\nabla_X \cdot \Psi_\perp = 0 \quad \text{in} \quad D_f, \tag{3.61}$$

$$\Psi_\perp \text{ and } \Phi \text{ periodic and } \Psi_\perp = 0 \quad \text{on} \quad \partial D_{\boldsymbol{s}_0}. \tag{3.62}$$

The cell functions $(\Pi, \boldsymbol{\xi})$ satisfy the homogeneous problem with inhomogeneous boundary conditions *i.e.*

$$-\nabla_X^2 \Pi + \nabla_X \boldsymbol{\xi} = 0 \quad \text{in} \quad D_f, \tag{3.63}$$

$$\nabla_X \cdot \Pi = 0 \quad \text{in} \quad D_f, \tag{3.64}$$

$$\Pi \text{ and } \xi \text{ periodic and } \Pi = I \quad \text{on} \quad \partial D_{\boldsymbol{s}_0}. \tag{3.65}$$

The microscale variation of the axial flow determined by (3.54), (3.56) and (3.58), is given by

$$\nabla_X^2 \Psi_{33} = 1 \quad \text{in} \quad D_f, \tag{3.66}$$

$$\Psi_{33} = 0 \quad \text{on} \quad \partial D_{\boldsymbol{s}_0}, \tag{3.67}$$

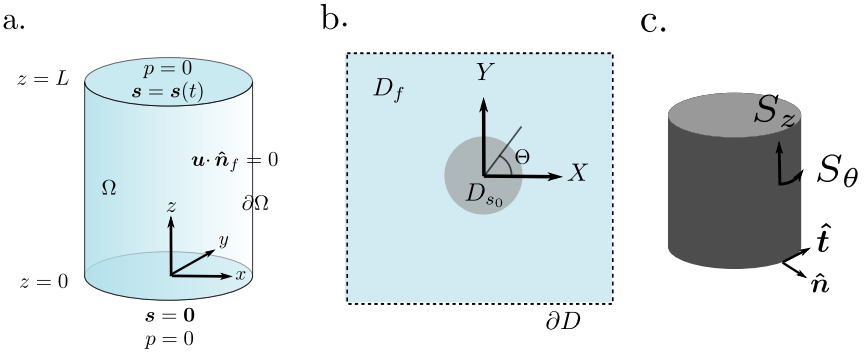

Figure 3.3: *After homogenisation the problem is reduced to two simpler problems. a. The domain of the macroscale problem where the fluid and strings are treated as a continuum. b. Domain of the microscale problem, whose averaged solutions give permeability coefficient in the macroscale equations. c. Directions of fluid-induced shear stress at the string surface.*

with Ψ_{33} is periodic in $\boldsymbol{X}$ with period $\boldsymbol{1}$.

The microscale problems are defined over the domain of the unit cell, as illustrated in figure 3.3.b. The unit cell domain defined by (3.37) will contain a single string located at a position set by the macroscale coordinate of the unit cell - its displacement from the exactly periodic equilibrium configuration is given by $\boldsymbol{s}_0 = \boldsymbol{s}_0(\boldsymbol{x}, t)$. Using the periodicity of boundary conditions, we can equivalently solve over the domain $D = D_f \cup D_{\boldsymbol{s}_0}$ shown in figure 3.3.b, where the string is placed at the origin of microscale coordinates.

The problem driven by inhomogeneous boundary conditions has an analytical solution,

$$\Pi = I \quad \text{and} \quad \boldsymbol{\xi} = \boldsymbol{0}. \tag{3.68}$$

We will present numerical solutions to the cell problems (3.60)-(3.62) and (3.66)-(3.67) in section 3.5.1. As the fast scale $\boldsymbol{X}$ has been introduced in the transverse plane, the problems are solved over a 2-dimensional domain. This will give rise to an anisotropic permeability as we have different problems determining the axial and transverse components of the permeability tensor. The effects of solid fraction on anisotropy will be explored in section 3.5.1.

3.4.5 Homogenised problem

The averaged solutions to the microscale problems (3.60)-(3.62), (3.63)-(3.65) and (3.66)-(3.67) provide the coefficients in the homogenised problem which describes variations in fluid flow and string deformation across the domain. To derive the macroscale equations, we integrate the incompressibility condition at first-order (3.33) across the fluid domain of the unit cell D_f, obtaining

$$\int_{D_f} \nabla_X \cdot \boldsymbol{v}_1 dS_X + \int_{D_f} \nabla_x \cdot \boldsymbol{v}_0 dS_X + \int_{D_f} \frac{\partial w_0}{\partial z} dS_X = 0. \tag{3.69}$$

We apply the divergence theorem to the first integral and Reynolds' transport theorem to the final two terms, which gives

$$\begin{aligned} -\int_{\partial D_{\boldsymbol{s}_0}} \boldsymbol{v}_1 \cdot \hat{\boldsymbol{n}} dl_X + \nabla_x \cdot \int_{D_f} \boldsymbol{v}_0 dS_X + \int_{\partial D_{\boldsymbol{s}_0}} \boldsymbol{v}_0 \cdot \nabla_x \boldsymbol{s}_0 \cdot \hat{\boldsymbol{n}} dl_X \\ + \frac{\partial}{\partial z} \int_{D_f} w_0 dS_X + \int_{\partial D_{\boldsymbol{s}_0}} w_0 \frac{\partial \boldsymbol{s}_0}{\partial z} \cdot \hat{\boldsymbol{n}} dl_X = 0, \end{aligned} \tag{3.70}$$

where the periodicity of $\boldsymbol{v}_1$ means that its integral over the outer boundary of the unit cell, ∂D, vanishes. The boundary terms from applying the Reynolds transport theorem to the axial velocity gradients evaluate to zero using (3.43). The integrand involving the transverse velocity is independent of the fast scale; (3.40) implies that $\boldsymbol{v}_0$ is independent of the fast scale on the boundary, meaning that the second boundary integral evaluates to zero. Applying the no-slip boundary condition (3.42) to the first term of (3.70), we find

$$-\int_{\partial D_{\boldsymbol{s}_0}} \left(\frac{\partial \boldsymbol{s}_1}{\partial t} - \boldsymbol{d}_0 \cdot \nabla_X \boldsymbol{v}_0 \right) \cdot \hat{\boldsymbol{n}} dl_X + \nabla_x \cdot \int_{D_f} \boldsymbol{v}_0 dS_X + \frac{\partial}{\partial z} \int_{D_f} w_0 dS_X = 0. \tag{3.71}$$

We use the divergence theorem to take the first term into the solid domain and use the trace of (3.34), which gives

$$\begin{aligned} -\int_{\partial D_{\boldsymbol{s}_0}} \frac{\partial \boldsymbol{s}_1}{\partial t} \cdot \hat{\boldsymbol{n}} dl_X &= -\int_{D_{\boldsymbol{s}_0}} \nabla_X \cdot \left(\frac{\partial \boldsymbol{s}_1}{\partial t} \right) dS_X \\ &= \int_{D_{\boldsymbol{s}_0}} \nabla_x \cdot \left(\frac{\partial \boldsymbol{s}_0}{\partial t} \right) dS_X \\ &= \phi_s \nabla_x \cdot \left(\frac{\partial \boldsymbol{s}_0}{\partial t} \right), \end{aligned} \tag{3.72}$$

where we have used the fast scale independence of the leading-order string velocity in evaluating the final integral of (3.72). We apply the divergence theorem to the second term of (3.71), taking the integral into the fluid region to give

$$\int_{\partial D_{\boldsymbol{s}_0}} d_{0i}\frac{\partial v_{0j}}{\partial X_i}\hat{n}_{0j}dl_X = \int_{D_f} d_{0i}\frac{\partial^2 v_{0j}}{\partial X_j \partial X_i}dS_X = 0, \tag{3.73}$$

where we have used the fast scale independence of $\boldsymbol{d}_0$, periodicity of $\boldsymbol{u}_0$ and (3.29).

Thus, (3.71) reduces to

$$\nabla_x\cdot\langle \boldsymbol{v}_0\rangle + \frac{\partial\langle w_0\rangle}{\partial z} = -\frac{\phi_s}{\phi_f}\nabla_x\cdot\left(\frac{\partial \boldsymbol{s}_0}{\partial t}\right), \tag{3.74}$$

where angled brackets denote the spatial average over the fluid domain in the unit cell, defined as

$$\langle g\rangle = \frac{1}{\phi_f}\int_{D_f} g dS_X. \tag{3.75}$$

Writing $\boldsymbol{u} = \langle \boldsymbol{u}_0\rangle$, $\nabla = (\partial_x, \partial_y, \partial_z)$, and dropping subscripts on leading-order quantities henceforth, (3.74) becomes

$$\nabla\cdot\boldsymbol{u} = -\frac{\phi_s}{\phi_f}\nabla_\perp\cdot\left(\frac{\partial \boldsymbol{s}}{\partial t}\right), \tag{3.76}$$

where $\nabla_\perp = (\partial_x, \partial_y)$. Averaging (3.57)-(3.58), we have

$$\boldsymbol{v} = -\mathcal{K}_\perp\nabla_\perp p + \frac{\partial \boldsymbol{s}}{\partial t}, \tag{3.77}$$

$$w = -\kappa_3\frac{\partial p}{\partial z}, \tag{3.78}$$

where

$$\mathcal{K}_\perp = -\langle\Psi_\perp\rangle \quad \text{and} \quad \kappa_3 = -\langle\Psi_{33}\rangle \tag{3.79}$$

are given by the averaged solutions to the cell problems (3.60)-(3.62) and (3.66)-(3.67). In evaluating $\langle\Pi\rangle = 1$, we have used (3.68).

The coefficients $\mathcal{K}_\perp$ and κ_3 give the contribution to fluid flow from transverse and axial macroscopic pressure gradients respectively. Combined with the force balance (3.51),

$$-\nabla_\perp p + \frac{\partial^2 \boldsymbol{s}}{\partial z^2} = \boldsymbol{0}, \tag{3.80}$$

we have a system of equations (3.76)-(3.78) and (3.80) describing the coupling between string displacement and fluid motion. We find the relative fluid velocity satisfies Darcy's law (3.77)-(3.78) with the condition for mass conservation (3.76) including a source term due to the presence of strings. Here, (3.76) reflects the influx of fluid into regions of the domain where strings move apart and vice versa. We can eliminate the fluid velocity from the homogenised equations, substituting (3.77)-(3.78) into (3.76) to obtain

$$\nabla\cdot\left(\mathcal{K}\nabla p\right) = \frac{1}{\phi_f}\nabla_\perp\cdot\left(\frac{\partial \boldsymbol{s}}{\partial t}\right), \tag{3.81}$$

which is coupled to (3.80). We have introduced the permeability tensor which has entries

$$\mathcal{K} = -\begin{pmatrix} \langle\Psi_{\perp_{11}}\rangle & \langle\Psi_{\perp_{12}}\rangle & 0 \\ \langle\Psi_{\perp_{21}}\rangle & \langle\Psi_{\perp_{22}}\rangle & 0 \\ 0 & 0 & \langle\Psi_{33}\rangle \end{pmatrix}, \tag{3.82}$$

combining the solutions to the cell problems for transverse and axial flow. Here, the mass conservation condition (3.81) is the same as that derived for linearly elastic media saturated by viscous fluid in [16, 52]. The momentum equation (3.80) agrees with the model consisting of continuum constituents developed in [52], where the stress of the composite is constructed from a linear superposition of macroscale pressure gradients and elastic stress.

The accompanying boundary conditions are those of flux or pressure for the fluid and string displacement at each end. We see that the homogenisation process has resulted in a lower order model for fluid flow; we are no longer able to impose no-slip conditions at the outer edge of the fluid domain. We also specify the initial string displacement or velocity.

In the next section, we consider solutions to the homogenised model in a cylindrical geometry. We impose no flux of fluid through the outer boundary

$$\boldsymbol{u}\cdot\hat{\boldsymbol{n}} = 0 \quad \text{on} \quad \partial\Omega_e, \tag{3.83}$$

and atmospheric pressure at the top of the domain. We impose either the fluid flux or pressure at the base of the domain. The string motion is fixed by imposing the displacement of each end and an initial condition. We give various examples in the next section.

3.5 Solution

In this section, we solve the homogenised model as follows. We begin in section 3.5.1 by solving the microscale problems to determine the form of the coefficients in the macroscale problem. Following this, in section 3.5.2 we solve the macroscale problem in a simple geometry, aiming to characterise the microscale shear stress dependence on model parameters.

3.5.1 Cell problem solution

We solve the microscale problems (3.60)-(3.62) and (3.66)-(3.67) using the finite element method in FEniCS [103]. As described in section 3.4.4, we can choose to solve the microscale problem on the domain where a string with circular cross-section is centred at the origin of the fast-scale coordinates as shown in figure 3.3. Details of the direct numerical solutions are given in appendix B.1.1-B.1.2. These solutions give the local variation in fluid velocity, which is used in calculating the microscale shear stress and, when averaged, the permeability coefficient in the macroscale problem.

Before discussing the solutions, we consider the symmetry of (3.60)-(3.62), which enables us to determine the form of the permeability tensor. First, we consider the transformation $X \to -X$. Writing $\overline{\Psi} = \Psi(-X, Y)$ and $\overline{\boldsymbol{\Phi}} = \boldsymbol{\Phi}(-X, Y)$, the transformed cell problem takes the form

$$-\nabla_{\boldsymbol{X}}^2 \begin{pmatrix} \overline{\Psi}_{11} & \overline{\Psi}_{12} \\ \overline{\Psi}_{21} & \overline{\Psi}_{22} \end{pmatrix} + \begin{pmatrix} -\partial_X \overline{\Phi}_1 & \partial_Y \overline{\Phi}_1 \\ -\partial_X \overline{\Phi}_2 & \partial_Y \overline{\Phi}_2 \end{pmatrix} + \begin{pmatrix} 1 & 0 \\ 0 & 1 \end{pmatrix} = 0 \quad \text{in} \quad D_f, \tag{3.84}$$

$$\begin{pmatrix} \partial_Y \overline{\Psi}_{11} - \partial_X \overline{\Psi}_{21} \\ \partial_Y \overline{\Psi}_{12} - \partial_X \overline{\Psi}_{22} \end{pmatrix} = 0 \quad \text{in} \quad D_f, \tag{3.85}$$

$$\overline{\Psi} = 0 \quad \text{on} \quad \partial D_{\boldsymbol{s}_0}, \tag{3.86}$$

with $\overline{\Psi}_\perp$ and $\overline{\boldsymbol{\Phi}}$ periodic in $\boldsymbol{X}$ with period $\mathbf{1}$. For strings with a circular cross-section, the domain, forcing and boundary condition (3.62) are unchanged under the transformation $X \to -X$. Thus, we expect that the solution to (3.60)-(3.62)

will be invariant under this transformation, which holds providing

$$\overline{\Psi}_{12} = -\Psi_{12} \quad \text{and} \quad \overline{\Psi}_{21} = -\Psi_{21}, \tag{3.87}$$

that is the off-diagonal components of $\boldsymbol{\Psi}$ are antisymmetric in X. Repeating the argument for the transformation $Y \to -Y$, we find that the off-diagonal components must also be antisymmetric in Y. Using the definition of the average (3.79), the off-diagonal components of Ψ will integrate to zero, resulting in a diagonal permeability tensor. Equations (3.60)-(3.62) have further symmetry under the transformation $X \to Y$ and $Y \to X$. We write $\widehat{\Psi}(X,Y) = \Psi_\perp(Y,X)$ and $\widehat{\boldsymbol{\Phi}}(X,Y) = \boldsymbol{\Phi}_\perp(Y,X)$, performing this transformation on (3.60)-(3.62), which gives

$$-\nabla_{\boldsymbol{X}}^2 \begin{pmatrix} \widehat{\Psi}_{11} & \widehat{\Psi}_{12} \\ \widehat{\Psi}_{21} & \widehat{\Psi}_{22} \end{pmatrix} + \begin{pmatrix} \partial_Y \widehat{\Phi}_1 & \partial_Y \widehat{\Phi}_1 \\ \partial_X \widehat{\Phi}_2 & \partial_Y \widehat{\Phi}_2 \end{pmatrix} + \begin{pmatrix} 1 & 0 \\ 0 & 1 \end{pmatrix} = 0 \quad \text{in} \quad D_f, \tag{3.88}$$

$$\begin{pmatrix} \partial_Y \widehat{\Psi}_{11} + \partial_X \widehat{\Psi}_{21} \\ \partial_Y \widehat{\Psi}_{12} + \partial_X \widehat{\Psi}_{22} \end{pmatrix} = 0 \quad \text{in} \quad D_f, \tag{3.89}$$

$$\widehat{\Psi} = 0 \quad \text{on} \quad \partial D_{\boldsymbol{s}_0}, \tag{3.90}$$

with $\widehat{\Psi}_\perp$ and $\widehat{\boldsymbol{\Phi}}$ periodic in $\boldsymbol{X}$ with period $\mathbf{1}$. Given the domain, forcing and boundary condition are unchanged under this transformation, we expect that $(\widehat{\Psi}, \widehat{\boldsymbol{\Phi}})$ should satisfy (3.60)-(3.62). For this to hold, we require $\partial_Y \widehat{\Phi}_1 = \partial_X \widehat{\Phi}_1$ and $\partial_X \widehat{\Phi}_2 = \partial_Y \widehat{\Phi}_2$, *i.e.* that $\widehat{\boldsymbol{\Phi}} = \boldsymbol{\Phi}$. From this, we conclude $\widehat{\Psi}_{12} = \widehat{\Psi}_{21}$ which, using (3.89), leads to the conclusion that $\widehat{\Psi}_{11} = \widehat{\Psi}_{22}$. We conclude that the permeability tensor must have the form $\mathcal{K} = \mathrm{diag}(\kappa_1, \kappa_1, \kappa_3)$. Here, κ_1 characterises the fluid flow relative to the moving strings for a unit pressure drop imposed in the transverse direction and κ_3 the flow response to an axial pressure drop.

The permeability coefficients for different solid fractions are plotted in figure 3.4.a. As expected, the permeability decreases as the solid fraction increases. With the permeability of an array of cylinders being inversely proportional to the fluid drag on a given cylinder [23], we have a lower drag from strings aligned with the flow direction and thus have $\kappa_3 > \kappa_1$. At low solid volume fractions, the axial permeability is twice that of the transverse permeability. Estimates for the permeability of arrays of rigid cylinders have been calculated using various methods, see for example [43, 57, 115]. Analytical methods approximating the low

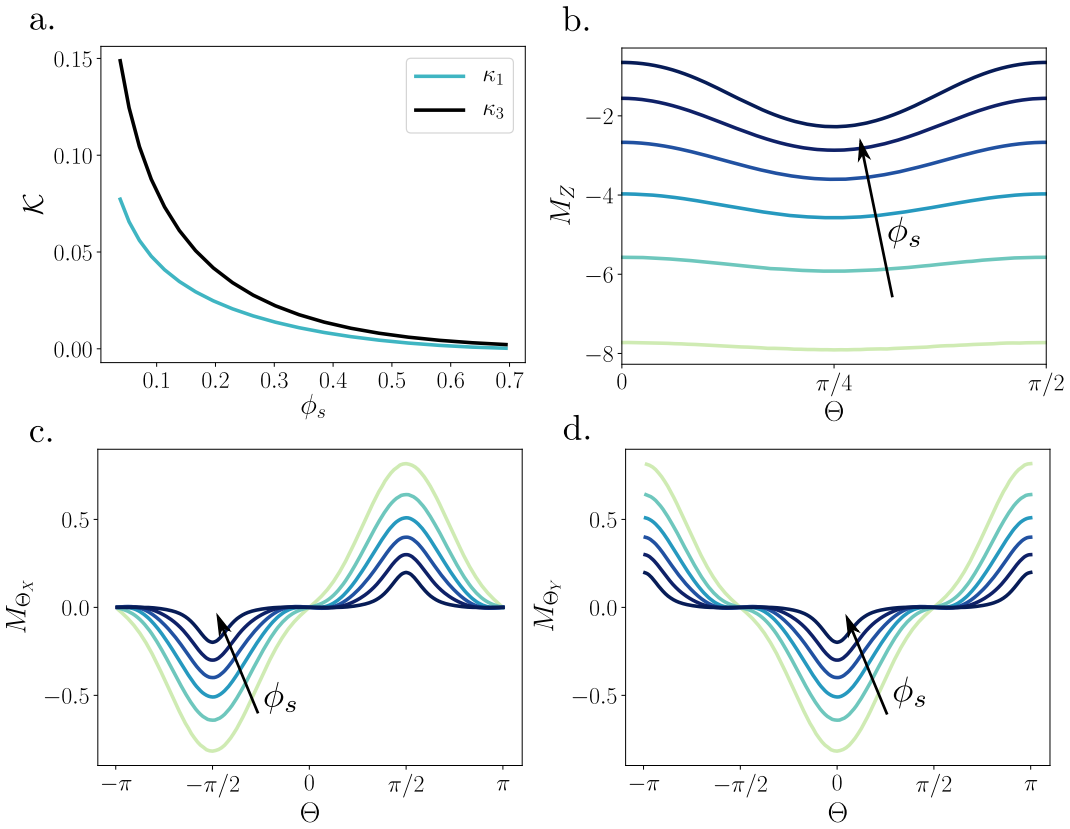

Figure 3.4: *a. Averaged solutions to the microscale problem give the coefficients which appear in the macroscale problem. We solve the microscale problem for strings with circular cross-section on the domain given in figure 3.3. b. Microscale variations in axial shear stress. Symmetry implies the variation shown repeats in all four quadrants. c.-d. Microscale variations in the transverse components of shear stress. Arrows point in the direction of increasing solid fraction. Plots are shown for* $\phi_s = 0.13, 0.2, 0.28, 0.38, 0.5, 0.64$.

density limit with flow around a single cylinder recover the ratio of 2 between the axial and transverse permeability that we obtain from numerical solutions [43].

In addition to providing coefficients in the averaged equations, solutions to the cell problems give the microscale variation in shear stress. The fluid-induced traction exerted on the string surface is given by $\boldsymbol{\sigma} \cdot \hat{\boldsymbol{n}}$, where $\boldsymbol{\sigma}$ is the multiscale

form of the stress tensor. We focus our discussion on the magnitude of microscale shear stress at the string surface, which we take to be a proxy for the microscale shear stress experienced by cells at the early stages of bioreactor operation. There are two components of shear stress in this problem illustrated in figure 3.3.c: the axial microscale shear stress S_Z, given by $\hat{\boldsymbol{e}}_z \cdot \boldsymbol{\sigma} \cdot \hat{\boldsymbol{n}}$, and the transverse microscale shear stress S_Θ, given by $\hat{\boldsymbol{t}} \cdot \boldsymbol{\sigma} \cdot \hat{\boldsymbol{n}}$, where $\hat{\boldsymbol{t}}$ is tangent to the string surface.

Using the multiple scales form given in (3.47), we find that the leading-order axial and transverse shear stress are given by

$$S_Z = \frac{1}{\delta} \hat{\boldsymbol{n}} \cdot \nabla_X w \quad \text{and} \quad S_\Theta = \frac{1}{\delta} \left[\sin(2\Theta)(v_Y - u_X) + \cos(2\Theta)(u_Y + v_X) \right] \tag{3.91}$$

respectively, where Θ is the angle measured from the X-axis in microscale coordinates (see figure 3.3.b). We calculate the gradient of the velocity with respect to the microscale variables, using the expression for velocity given in the derivation of the cell problems (3.57) and (3.58). As the microscale problem for Π has a constant solution, there is no contribution to microscale shear stress from string motion. Instead, the strings contribute to the microscale variations *via* their impact on the domain geometry, while the magnitude of the shear stress is modulated by macroscale pressure gradients. We introduce the functions M_Z and $\boldsymbol{M}_\Theta$ which capture the microscale variation in shear stress

$$M_Z = \frac{1}{\delta} \hat{\boldsymbol{n}} \cdot \nabla_X \Psi_{33}, \tag{3.92}$$

$$M_{\Theta_k} = \frac{1}{\delta} \hat{t}_i \left(\partial_{X_i} \Psi_{\perp_{jk}} + \partial_{X_j} \Psi_{\perp_{ik}} \right) \hat{n}_j, \quad k = 1, 2. \tag{3.93}$$

where $\hat{\boldsymbol{t}}$ is the unit tangent to the string boundary in the transverse plane. Variations in M_Z and $\boldsymbol{M}_\Theta$ at different points on the string boundary are plotted in figure 3.4. The components of M_Z and $\boldsymbol{M}_\Theta$ increase in magnitude with decreasing solid volume fraction, reflecting the higher velocity gradients established when imposing a fixed pressure drop across a larger fluid cross-sectional area. To simplify calculations when considering the distributions of shear stress across the macroscale domain, we introduce the averaged coefficients

$$m_Z = \frac{1}{2\pi} \int_0^{2\pi} M_Z d\Theta \quad \text{and} \quad \boldsymbol{m}_\Theta = \frac{1}{2\pi} \int_0^{2\pi} (|M_{\Theta_x}| \hat{\boldsymbol{e}}_x + |M_{\Theta_y}| \hat{\boldsymbol{e}}_y) d\Theta. \tag{3.94}$$

Characteristic values of the axial and transverse shear stress are then given by

$$S_Z = m_Z p_z \quad \text{and} \quad S_\Theta = \boldsymbol{m}_\Theta \cdot \nabla_\perp p \tag{3.95}$$

respectively. We will consider distributions of the microscale shear stress in section 3.5.2 where we solve the macroscale problem to obtain the macroscale pressure gradients.

3.5.2 Macroscale problem solution

To characterise the fluid flow and string deformation across the whole domain, we solve the macroscale equations (3.80)-(3.81) with parameters given by the averaged solution to the microscale problems as described in section 3.5.1. In section 3.5.2.1, we show that the problem can be simplified by defining a potential related to the fluid pressure. We consider flow driven by string motion in sections 3.5.2.2 and 3.5.2.3, and flow driven by an imposed pressure drop or flux in sections 3.5.2.4 and 3.5.2.5.

We are interested in gaining an understanding of how different boundary conditions and parameters influence the shear stress distribution. To this end, we consider a simple geometry, modelling the bioreactor chamber as a right-circular cylinder with length 1 and radius 1/2.

3.5.2.1 Potential formulation

To facilitate analysis, we introduce a fluid potential φ such that $p = \varphi_{zz}$. This allows us to reduce (3.80)-(3.81) to a single, scalar partial differential equation that can be solved analytically in simple geometries. The corresponding displacement is obtained by integrating the homogenised force balance (3.80) twice with respect to z,

$$\boldsymbol{s} = \nabla_\perp \varphi + \boldsymbol{a}_1 z + \boldsymbol{a}_2, \tag{3.96}$$

where $\boldsymbol{a}_1 = \boldsymbol{a}_1(x, y, t)$ and $\boldsymbol{a}_2 = \boldsymbol{a}_2(x, y, t)$ are functions of integration. We can decompose $\boldsymbol{a}_1$ and $\boldsymbol{a}_2$ as

$$\boldsymbol{a}_1 = \begin{pmatrix} \partial_x \eta_1 \\ \partial_y \eta_1 \end{pmatrix} + \begin{pmatrix} -\partial_y \psi_1 \\ \partial_x \psi_1 \end{pmatrix}, \tag{3.97}$$

$$\boldsymbol{a}_2 = \begin{pmatrix} \partial_x \eta_2 \\ \partial_y \eta_2 \end{pmatrix} + \begin{pmatrix} -\partial_y \psi_2 \\ \partial_x \psi_2 \end{pmatrix}, \tag{3.98}$$

that is into two parts, one with zero curl and the second with zero divergence. We absorb η_1 and η_2 into the definition of φ, writing

$$\boldsymbol{s} = \nabla_\perp \varphi + \begin{pmatrix} \partial_y \psi_1 \\ -\partial_x \psi_1 \end{pmatrix} z + \begin{pmatrix} \partial_y \psi_2 \\ -\partial_x \psi_2 \end{pmatrix}. \tag{3.99}$$

As the pressure depends on the second axial derivative of φ, this redefinition does not alter the expression for pressure. Returning to the homogenised model, we can rewrite (3.81) in terms of the potential as

$$\nabla \cdot (\mathcal{K} \nabla \varphi_{zz}) = \frac{1}{\phi_f} \nabla_\perp^2 \varphi_t. \tag{3.100}$$

Imposing string displacement at the top and base of the domain leads to a problem for $\psi_i = \psi_i(x, y)$, $i = 1, 2$. We can eliminate φ by cross-differentiating the boundary condition at the base, which results in a problem for ψ_1. Repeating the process at $z = 1$ gives a problem for ψ_2. After solving, we are left with a single partial differential equation for φ. We will see examples of this process in sections 3.5.2.2-3.5.2.4.

The remaining boundary conditions on the fluid potential φ correspond to zero imposed pressure

$$\varphi_{zz} = 0, \tag{3.101}$$

or no fluid flux

$$(-\mathcal{K} \nabla \varphi_{zz} + \nabla_{\perp_3} \varphi_t + \nabla \times (\psi_{1t} \hat{\boldsymbol{e}}_z) z + \nabla \times (\psi_{2t} \hat{\boldsymbol{e}}_z)) \cdot \hat{\boldsymbol{n}} = 0, \tag{3.102}$$

the latter obtained by substituting the potentials into the expression for fluid velocity (3.77)-(3.78) in the flux condition $\boldsymbol{u} \cdot \hat{\boldsymbol{n}} = 0$. We use $\nabla_{\perp_3} = (\partial_x, \partial_y, 0)$ to denote the in-plane gradient. The fluid potential φ is defined up to a linear

function of z with constant coefficients, and the displacement potentials ψ_i are defined up to an arbitrary constant. As physical quantities are related only to the derivatives of ψ_1 and ψ_2, we are free to choose a Dirichlet boundary condition on $\partial\Omega_e$, after which they are determined uniquely. We choose $\psi_1 = \psi_2 = 0$ on $\partial\Omega_e$. We must also impose an initial condition on the potential which can be obtained from the initial displacement field (3.7). In the following sections, we solve the problem for different boundary conditions.

3.5.2.2 Rigid body motion of an upper plate

Here, we consider the dynamics of the fluid-string system driven by string motion only, in the cylindrical domain illustrated in figure 3.3. The cylinder has nondimensional radius 1/2 and length 1 and we assume that the fluid-string composite fills its entire volume. We take the origin of the macroscale coordinates to be at the centre of the base, with the z-axis aligned with the cylinder's axis. We use both Cartesian and cylindrical polar coordinates (r, θ, z) to describe the problem, denoting the polar unit vectors by $\hat{\boldsymbol{e}}_r, \hat{\boldsymbol{e}}_\theta$ and $\hat{\boldsymbol{e}}_z$. Supposing strings are fixed to a rigid, porous plate at the top and bottom of the domain, we consider the effects of imposing an in-plane rigid body motion on the top plate. We assume there is no vertical pressure drop across the domain and that no fluid flows through the curved outer boundary of the cylinder.

We consider an imposed time-harmonic motion of the upper string end, decomposed into a translation and rotation, as follows

$$\boldsymbol{s} = \begin{pmatrix} A_1 \\ A_2 \end{pmatrix} \cos(\omega t) + A_3 \begin{pmatrix} y \\ -x \end{pmatrix} \cos(\omega t) \quad \text{at} \quad z = 1, \tag{3.103}$$

where A_i are constants describing the imposed motion and ω is the frequency of oscillation, nondimensionalised on the timescale given in (3.10). The position of the strings at the base of the domain is fixed (figure 3.3.a), so that

$$\boldsymbol{s} = \boldsymbol{0} \quad \text{at} \quad z = 0. \tag{3.104}$$

The condition of no pressure drop across the domain gives

$$\varphi_{zz} = 0 \quad \text{on} \quad z = 0, 1, \tag{3.105}$$

and no flux of fluid through the outer wall of the domain $\partial\Omega_e$ gives

$$(-\mathcal{K}\nabla\varphi_{zz} + \nabla_{\perp_3}\varphi_t + \nabla\times(\psi_{1t}\hat{\boldsymbol{e}}_z)z + \nabla\times(\psi_{2t}\hat{\boldsymbol{e}}_z))\cdot\hat{\boldsymbol{n}} = 0 \quad \text{on} \quad \partial\Omega_e. \quad (3.106)$$

We solve (3.100) subject to (3.103)-(3.106) by seeking time-harmonic solutions

$$\varphi = \Re[G(x,y,z)e^{i\omega t}], \quad \psi_1 = \Re[H_1(x,y,z)e^{i\omega t}], \quad \psi_2 = \Re[H_2(x,y,z)e^{i\omega t}], \quad (3.107)$$

which reduces (3.100) to

$$\nabla\cdot(\mathcal{K}\nabla G_{zz}) = \frac{i\omega}{\phi_f}\nabla^2_\perp G. \quad (3.108)$$

We now look to convert the boundary conditions (3.103)-(3.106) into conditions that determine H_1 and H_2. Following this, we can identify boundary conditions for G to close (3.108).

We begin by considering the boundary condition on string displacements (3.103)-(3.104), from which we can establish a problem for H_1 and H_2 *via* (3.99). Written in terms of potentials, the boundary condition (3.104) on displacement at $z = 0$ becomes

$$\partial_x G + \partial_y H_2 = 0, \quad (3.109)$$

$$\partial_y G - \partial_x H_2 = 0. \quad (3.110)$$

We cross-differentiate and subtract (3.109) from (3.110) to find

$$\nabla^2_\perp H_2 = 0 \quad \text{in} \quad \Omega_{z0}, \quad (3.111)$$

where Ω_{z0} is the transverse cross-section of Ω at $z = 0$. Since we chose to impose

$$H_2 = 0 \quad \text{on} \quad \partial\Omega_{z0}, \quad (3.112)$$

we find $H_2 = 0$. Undertaking a similar process with (3.103), we obtain a problem for H_1,

$$\nabla_\perp H_1 = 2A_3, \quad \text{in} \quad \Omega_{z1}, \quad (3.113)$$

$$H_1 = 0 \quad \partial\Omega_{z1}, \quad (3.114)$$

where Ω_{z1} is the transverse cross-section of Ω at $z = 1$. Solving (3.113)-(3.114), we find

$$H_1 = \frac{A_3}{2}\left(r^2 - \frac{1}{4}\right). \tag{3.115}$$

Having determined H_i, and hence ψ_i, we are able to establish the boundary conditions on the fluid potential G. At the base of the channel, (3.109) and (3.110) give $\nabla_\perp G = \mathbf{0}$ at $z = 0$ so that G is a constant, which we set to be zero without loss of generality. Integrating the following boundary conditions on string displacement at $z = 1$,

$$\partial_x G + \partial_y H_1 = A_1 + A_3 y, \tag{3.116}$$

$$\partial_y G - \partial_x H_1 = A_2 - A_3 x, \tag{3.117}$$

we find

$$G = r\left(A_1 \cos\theta + A_2 \sin\theta\right) \quad \text{at} \quad z = 1, \tag{3.118}$$

where without loss of generality, we have chosen zero constant of integration, fixing the final degree of freedom in G.

The boundary condition on the curved surface (3.102) corresponding to no fluid flux through the outer wall becomes

$$-\kappa_1 G_{rzz} + i\omega G_r = 0 \quad \text{on} \quad r = 1/2 \quad \text{for} \quad 0 < z < 1. \tag{3.119}$$

The final boundary conditions come from imposing zero fluid pressure at each end of the domain (3.105), giving

$$G_{zz} = 0 \quad \text{at} \quad z = 0, \tag{3.120}$$

$$G_{zz} = 0 \quad \text{at} \quad z = 1. \tag{3.121}$$

To summarise, it remains to solve the partial differential equation

$$\nabla\cdot\left(\mathcal{K}\nabla G_{zz}\right) = \frac{i\omega}{\phi_f}\nabla_\perp^2 G, \tag{3.122}$$

subject to

$$G = 0 \quad \text{and} \quad G_{zz} = 0 \quad \text{on} \quad z = 0, \tag{3.123}$$

$$G = r(A_1 \cos\theta + A_2 \sin\theta) \quad \text{and} \quad G_{zz} = 0 \quad \text{at} \quad z = 1, \tag{3.124}$$

$$-\kappa_1 G_{rzz} + i\omega G_r = 0 \quad \text{on} \quad r = 1/2 \quad \text{for} \quad 0 < z < 1. \tag{3.125}$$

Seeking a separable solution, we find that the boundary condition (3.125) reduces to

$$G_r = 0 \quad \text{on} \quad r = 1/2 \quad \text{for} \quad 0 < z < 1, \tag{3.126}$$

since the alternative $-\kappa_1 G_{zz} + i\omega G = 0$ cannot be satisfied by (3.122) for real forcing frequencies. Imposing (3.123), (3.124) and (3.126), we find the solution in cylindrical polar coordinates to be given by

$$G = \sum_{l=1}^{\infty} J_1(\beta_l r)\left(b_l \cos\theta + c_l \sin\theta\right) f_l(z), \tag{3.127}$$

with coefficients

$$b_l = \frac{2A_1\beta_l J_2(\beta_l)}{J_1^2(\beta_l)(\beta_l^2 - 1)}, \quad c_l = \frac{2A_2\beta_l J_2(\beta_l)}{J_1^2(\beta_l)(\beta_l^2 - 1)}, \tag{3.128}$$

where J_n is the nth Bessel function of the first kind and f_l is the solution to the following ordinary differential equation with constant coefficients

$$\frac{d^4 f_l}{dz^4} - \frac{\kappa_1\beta_l^2}{\kappa_3}\frac{d^2 f_l}{dz^2} + \frac{i\beta_l^2\omega}{\kappa_3\phi_f} f_l = 0, \tag{3.129}$$

subject to the boundary conditions $f_l(0) = 0,\ f_l(1) = 1,\ f_l''(0) = f_l''(1) = 0$. We find that

$$f_l(z) = -\frac{\alpha_-^2}{\alpha_+^2 - \alpha_-^2}\frac{\sinh(\alpha_+ z)}{\sinh(\alpha_+)} + \frac{\alpha_+^2}{\alpha_+^2 - \alpha_-^2}\frac{\sinh(\alpha_- z)}{\sinh(\alpha_-)}, \tag{3.130}$$

where

$$\alpha_-^2 = \frac{\beta_l^2\kappa_1}{2\kappa_3}\left(1 - \sqrt{1 - \frac{4i\omega\kappa_3}{\phi_f\beta_l^2\kappa_1^2}}\right), \tag{3.131}$$

$$\alpha_+^2 = \frac{\beta_l^2\kappa_1}{2\kappa_3}\left(1 + \sqrt{1 - \frac{4i\omega\kappa_3}{\phi_f\beta_l^2\kappa_1^2}}\right). \tag{3.132}$$

Here κ_1 and κ_3 are the components of the permeability tensor $\mathcal{K} = \mathrm{diag}(\kappa_1, \kappa_1, \kappa_3)$ and β_l are the ordered eigenvalues set by imposing the boundary condition at $r = 1/2$ given by the zeros of $J_1'(\beta_l/2) = 0$. The oscillation frequency and the permeabilities appear only in the function f_l - these parameters have a role in shaping the axial dependence of the solution, whereas the radial and azimuthal dependence is fixed by the spatial dependence of the boundary conditions imposed at the top and base of the domain.

The corresponding displacement in a polar basis can be calculated from (3.99) as

$$\boldsymbol{s} = \Re\left[\sum_l \begin{pmatrix} \beta_l J_1'(\beta_l r)(b_l\cos\theta + c_l\sin\theta) \\ \frac{1}{r}J_1(\beta_l r)(c_l\cos\theta - b_l\sin\theta) \end{pmatrix} f_l(z)e^{i\omega t}\right] - A_3 r\cos(\omega t)z\hat{\boldsymbol{e}}_\theta. \quad (3.133)$$

and fluid pressure is given by

$$p = \Re\left[\sum_l J_1(\beta_l r)\left(b_l\cos\theta + c_l\sin\theta\right) f_l''(z)e^{i\omega t}\right]. \quad (3.134)$$

We now consider solutions corresponding to various choices of A_1, A_2 and A_3.

Plate twist

Imposing a twist on the upper plate by setting

$$A_1 = 0, \quad A_2 = 0 \quad \text{and} \quad A_3 \neq 0, \quad (3.135)$$

we obtain the trivial solution for the fluid pressure corresponding to $p = 0$, and straight string profiles

$$\boldsymbol{s} = -A_3 rz\cos(\omega t)\hat{\boldsymbol{e}}_\theta, \quad (3.136)$$

as shown in figure 3.5. The absence of macroscale pressure gradients means there is no fluid-induced shear stress exerted at the string boundary - the fluid velocity equals the string velocity.

The assumption of local periodicity at the microscale means that we can no longer satisfy a no-slip condition on the outer wall. This breakdown of periodicity at the outer wall creates a region of $O(\delta)$ where the homogenised model interfaces with flow governed by the Stokes equations. This forms a boundary layer where we would expect pressure gradients to exist, generating a microscale shear stress varying between adjacent strings. Thus, while the microscale shear stress calculated from the homogenised model is zero, we would expect a boundary layer with non-zero shear to be present in the physical problem.

Plate translation

Pressure gradients on the macroscale are established when the upper end of the strings is translated relative to the base, corresponding to

$$A_1 \neq 0, \quad A_2 = 0 \quad \text{and} \quad A_3 = 0. \quad (3.137)$$

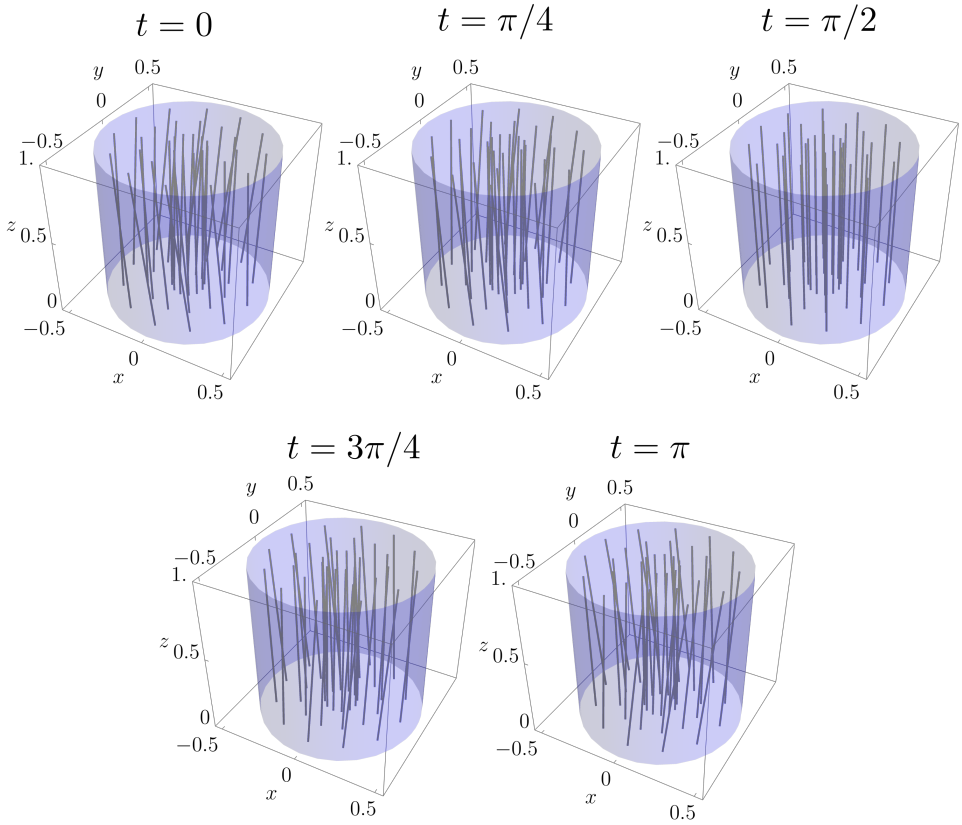

Figure 3.5: *String displacement induced by twisting the upper plate given by* $\omega = 1$, $A_1 = 0$, $A_2 = 0$ *and* $A_3 = 1$ *and* $\delta = 0.3$. *The string profiles for an imposed twist are independent of the solid volume fraction.*

These pressure gradients drive fluid flow, which modifies the string profiles from the straight lines that would be observed in the absence of fluid (figure 3.6).

The macroscale pressure gradients modulate the magnitude of the microscale shear stress. At the upper edge of the domain, we have a discontinuity in the radial derivatives of the fluid potential, resulting from the scraping flow as the upper plate is translated relative to the outer domain wall, from boundary conditions (3.124) and (3.126). We can rescale to establish the form of the singularity generated by this discontinuity, introducing local coordinates $(\tilde{r}, \tilde{\theta}, \tilde{z})$ which are defined by

$$\tilde{r} = \frac{(1/2 - r)}{\epsilon\sqrt{\kappa_1}}, \quad \tilde{\theta} = \theta, \quad \text{and} \quad \tilde{z} = \frac{(1 - z)}{\epsilon\sqrt{\kappa_3}}. \tag{3.138}$$

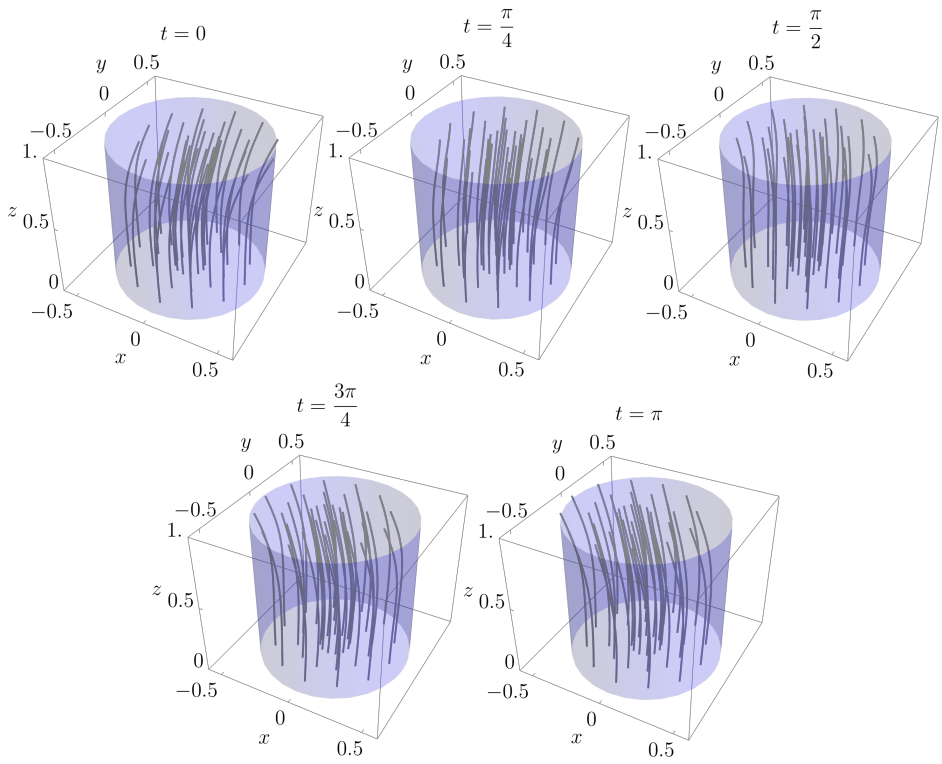

Figure 3.6: *String displacement induced by translating the upper plate given by* $\omega = 1$, $A_1 = 1$, $A_2 = 0$, $A_3 = 0$ *and* $\delta = 0.1$ *and* $\phi_s = 0.2$, *corresponding to* $\kappa_1 = 2.48 \times 10^{-2}$ *and* $\kappa_3 = 4.18 \times 10^{-2}$.

By considering the form of the problem (3.122) and (3.124)-(3.125) for $(\tilde{r}, \tilde{\theta}, \tilde{z}) = O(1)$ as $\epsilon \to 0$, we can identify the behaviour of the singularity at the upper edge of the domain. We transform (3.108) and boundary conditions (3.124)-(3.125) into local coordinates and pose the expansion $G \sim G_0 + \epsilon G_1 + \cdots$. Comparing coefficients at each order of epsilon, we find at $O(1)$

$$\frac{\partial^4 G_0}{\partial \tilde{r}^2 \partial \tilde{z}^2} + \frac{\partial^4 G_0}{\partial \tilde{z}^4} = 0, \tag{3.139}$$

with

$$G_0 = \frac{A_1}{2} \cos\tilde{\theta} \quad \text{and} \quad \frac{\partial^2 G_0}{\partial \tilde{z}^2} = 0 \quad \text{on} \quad \tilde{z} = 0, \tag{3.140}$$

$$\frac{\partial G_0}{\partial \tilde{r}} = 0 \quad \text{on} \quad \tilde{r} = 0. \tag{3.141}$$

We can integrate (3.139) twice with respect to $\tilde{z}$ which gives

$$\frac{\partial^2 G_0}{\partial \tilde{r}^2} + \frac{\partial^2 G_0}{\partial \tilde{z}^2} = a_0 \tilde{z} + a_1, \tag{3.142}$$

where $a_0 = a_0(\tilde{r})$ and $a_1 = a_1(\tilde{r})$ are functions of integration. The solution to the local problem (3.139) should match the expansion of the solution to the full problem (3.127) expanded in local coordinates. As such, the leading-order contribution to G_0 must be constant. Given the inhomogeneous forcing in (3.142) due to a_0 and a_1 respectively give rise to terms that are cubic and quadratic in the distance from the edge, we conclude that $a_0 = a_1 = 0$. Imposing the boundary condition (3.140), we must have $G_0 = (A_1/2)\cos\tilde{\theta}$ at leading-order.

Comparing coefficients at the next order of ϵ, we obtain

$$\frac{\partial^4 G_1}{\partial \tilde{r}^2 \partial \tilde{z}^2} + \frac{\partial^4 G_1}{\partial \tilde{z}^4} = 0, \tag{3.143}$$

with

$$G_1 = -A_1\sqrt{\kappa_1}\tilde{r}\cos\tilde{\theta} \quad \text{and} \quad \frac{\partial^2 G_1}{\partial \tilde{z}^2} = 0 \quad \text{on} \quad \tilde{z} = 0, \tag{3.144}$$

$$\frac{\partial G_1}{\partial \tilde{r}} = 0 \quad \text{on} \quad \tilde{r} = 0. \tag{3.145}$$

Integrating (3.143) twice with respect to $\tilde{z}$, we find

$$\frac{\partial^2 G_1}{\partial \tilde{r}^2} + \frac{\partial^2 G_1}{\partial \tilde{z}^2} = b_0 \tilde{z} + b_1, \tag{3.146}$$

where $b_0 = b_0(\tilde{r}), b_1 = b_1(\tilde{r})$ are functions of integration. Here, G_1 can grow at most linearly with $\sqrt{\tilde{z}^2 + \tilde{r}^2}$ to enable matching with the local expansion of the full solution. Hence, we conclude that $b_0 = b_1 = 0$.

As the only $\tilde{\theta}$ dependence in (3.143)-(3.145) is in the boundary condition, we can write

$$G_1 = g\cos\tilde{\theta}, \tag{3.147}$$

where g satisfies the homogeneous version of (3.146) with inhomogeneous boundary conditions. That is,

$$\frac{\partial^2 g}{\partial \tilde{r}^2} + \frac{\partial^2 g}{\partial \tilde{z}^2} = 0, \tag{3.148}$$

with

$$g = -A_1\sqrt{\kappa_1}\tilde{r} \quad \text{on} \quad \tilde{z} = 0, \tag{3.149}$$

$$\frac{\partial g}{\partial \tilde{r}} = 0 \quad \text{on} \quad \tilde{r} = 0. \tag{3.150}$$

We can solve (3.148)-(3.150) for g by introducing the complex variable $\zeta = \tilde{z} + i\tilde{r}$. As g satisfies Laplace's equation, we can write it as the imaginary part of a holomorphic function. Considering the boundary conditions (3.149)-(3.150), we identify a suitable function for the radial derivative of g to be

$$\frac{\partial g}{\partial \tilde{r}} = \Im\left[-\frac{2A_1\sqrt{\kappa_1}}{\pi}\log(\zeta)\right]. \tag{3.151}$$

Equivalently,

$$\frac{\partial g}{\partial \tilde{r}} = -\frac{2A_1\sqrt{\kappa_1}}{\pi}\arctan\left(\frac{\tilde{r}}{\tilde{z}}\right) \tag{3.152}$$

Integrating (3.152) we obtain

$$g = -\frac{2A_1\sqrt{\kappa_1}}{\pi}\left\{\tilde{r}\arctan\left(\frac{\tilde{r}}{\tilde{z}}\right) - \frac{1}{2}\tilde{z}\log(\tilde{r}^2 + \tilde{z}^2)\right\}, \tag{3.153}$$

where we have used (3.149) to establish the constant of integration. Substituting the form of g into (3.147), we find that the part of this solution that becomes singular as we approach the upper edge, G_s is given by

$$G_s = \frac{A_1\sqrt{\kappa_1}\tilde{z}}{\pi}\log\left(\tilde{r}^2 + \tilde{z}^2\right)\cos\tilde{\theta}. \tag{3.154}$$

Inverting (3.138) to write the singular part in our original coordinates, we obtain

$$G_s \propto (1-z)\ln\left(\frac{1}{\kappa_1}(\frac{1}{2} - r)^2 + \frac{1}{\kappa_3}(1-z)^2\right)\cos\theta. \tag{3.155}$$

The translating plate we consider in this example bears similarity to the Taylor scraper problem where the normal and tangential shear stress to the plate diverges with the inverse distance to the corner [47]. Calculating the tangential τ_t and normal shear stress τ_n, we find

$$\tau_{\mathrm{t}} = O\left(\left(\frac{\tilde{r}^2}{\kappa_1} + \frac{\tilde{z}^2}{\kappa_3}\right)^{-3/2}\right) \quad \text{and} \quad \tau_{\mathrm{n}} = O\left(\left(\frac{\tilde{r}^2}{\kappa_1} + \frac{\tilde{z}^2}{\kappa_3}\right)^{-3/2}\right). \tag{3.156}$$

Thus, we find that the normal and tangent shear stresses diverge much more strongly than for the scraper problem with viscous fluid alone. The reason for the strength of this singularity is due to the form of the boundary condition on the outer edge (3.126). For separable solutions, we are forced to impose $G_r = 0$ on the outer boundary, which enforces no flux of fluid but also prevents motion of the string through the outer boundary.

In principle, we could use the known local form of the singularity to increase the rate of convergence of the eigenfunction expansion by subtracting the singular part of the solution (3.154) from G and expanding the remainder. Since G_s does not satisfy the boundary conditions at $z = 0$, it would be necessary to also subtract an additional function G_1 to ensure boundary conditions on the remainder are homogeneous. We could take G_1 to be of the form

$$G_1 = -(1-z)^3 G_s(r,0) - \frac{z^2(1-z)^3}{2}\left(\frac{\partial^2 G_s}{\partial z^2}(r,0) - 6(1-z)G_s(r,0)\right) \quad (3.157)$$

for example. Writing $G = G_1 + G_s + G_r$, the remainder G_r now satisfies homogeneous boundary conditions, but an inhomogeneous equation, since $G_s + G_1$ does not satisfy equation (3.122). Crucially the remainder is less singular than G, so the eigenfunction expansion will converge more quickly. We do not pursue such an analysis further.

This behaviour near the edge of the domain means that the shear stress calculations from the homogenised model break down. While we cannot calculate the shear stress over the whole cross-section without including the effects from the boundary, we do gain insight into the axial variations through this example. The axial variation is set by the nondimensional frequency, which describes the relative magnitude of the fluid stress and tension. In the next section, we quantify this effect by considering an example with regularised boundary conditions, chosen so that there is no discontinuity in the potential derivatives at the upper corner.

3.5.2.3 Radial string motion

We now suppose that the motion of the upper end of each string is no longer constrained to rigid-body motion, considering instead imposed displacements of

the form

$$\boldsymbol{s} = \left(r - \frac{1}{2}\right)\cos(\omega t)\hat{\boldsymbol{e}}_r \quad \text{at} \quad z = 1, \tag{3.158}$$

so that the strings do not pass through the boundary $r = 1/2$. The strings are fixed at the base,

$$\boldsymbol{s} = \boldsymbol{0} \quad \text{at} \quad z = 0. \tag{3.159}$$

As in section 3.5.2.2, there is no vertical pressure drop across the domain

$$\varphi_{zz} = 0 \quad \text{at} \quad z = 0, 1, \tag{3.160}$$

and no fluid flows through the outer wall

$$\boldsymbol{u}\cdot\hat{\boldsymbol{n}} = 0 \quad \text{at} \quad r = 1/2 \quad \text{for} \quad 0 < z < 1. \tag{3.161}$$

Following a similar process to section 3.5.2.2, we seek time-harmonic solutions of the form (3.107). After imposing the boundary conditions on string displacement (3.158)-(3.159), we find

$$\psi_1 = 0 \quad \text{and} \quad \psi_2 = 0, \tag{3.162}$$

so that the problem for the fluid potential (3.108) has boundary conditions

$$G = 0, \quad G_{zz} = 0 \quad \text{at} \quad z = 0, \tag{3.163}$$

$$G = \frac{r(r-1)}{2}, \quad G_{zz} = 0 \quad \text{at} \quad z = 1, \tag{3.164}$$

$$G_r = 0 \quad \text{on} \quad r = 1/2 \quad \text{for} \quad 0 < z < 1. \tag{3.165}$$

Using separation of variables, we find that the solution is given by

$$G = d_0 + \sum_{l=1}^{\infty} d_l J_0(\beta_l r) f_l(z), \tag{3.166}$$

where β_l satisfy $J_0'(\beta_l/2) = 0$, ordered so that $\beta_1 < \beta_2 < \cdots$, and f_l is given by (3.130). The expansion coefficients are

$$d_0 = -\frac{1}{48} \quad \text{and} \quad d_l = -\frac{\int_0^{1/2} r^2(1-r)J_0(\beta_l r)dr}{2\int_0^{1/2} rJ_0(\beta_l r)dr}. \tag{3.167}$$

The form of the fluid pressure and string displacement, calculated from (3.166) using (3.99) and $p = \varphi_{zz}$, are

$$p = \Re\left[\sum_{l=1}^{\infty} d_l J_0(\beta_l r) f_l''(z) e^{i\omega t}\right] \quad \text{and} \quad \boldsymbol{s} = \Re\left[\sum_{l=1}^{\infty} d_l J_0'(\beta_l r) f_l(z) e^{i\omega t}\right] \tag{3.168}$$

respectively. Combining the macroscale pressure gradients with the microscale solution calculated in section 3.5.1, we can calculate the variation in microscale shear stress (3.91) across the domain.

For a given imposed displacement, the magnitude of the shear stress, averaged over an oscillation cycle and spatially, first around a given string then over the domain, is dependent on the dimensionless frequency ω. We define the spatio-temporal average as

$$\overline{g} = \frac{1}{|\Omega|}\frac{1}{\tau}\int_{\Omega}\int_{0}^{\tau}\int_{\partial D_{\boldsymbol{s}_0}} g(x,y,z,t)dtdv, \tag{3.169}$$

where $\tau = 2\pi/\omega$ is the period of oscillation and dv denotes the volume element in slow coordinates. We can characterise the behaviour of this average in the limits of low and high frequency by expanding (3.130).

We begin by characterising the frequency dependence of the spatio-temporal average of the magnitude of the transverse shear stress. Given there is no frequency dependence in the radial part of the separable solution, we need only identify the frequency-dependence of the axial dependence $f_l(z)$ (defined in (3.130)-(3.132)), which we restate here for convenience,

$$f_l(z) = -\frac{\alpha_-^2}{\alpha_+^2-\alpha_-^2}\frac{\sinh(\alpha_+ z)}{\sinh(\alpha_+)} + \frac{\alpha_+^2}{\alpha_+^2-\alpha_-^2}\frac{\sinh(\alpha_- z)}{\sinh(\alpha_-)}, \tag{3.170}$$

where

$$\alpha_-^2 = \frac{\beta_l^2\kappa_1}{2\kappa_3}\left(1-\sqrt{1-\frac{4i\omega\kappa_3}{\phi_f\beta_l^2\kappa_1^2}}\right), \tag{3.171}$$

$$\alpha_+^2 = \frac{\beta_l^2\kappa_1}{2\kappa_3}\left(1+\sqrt{1-\frac{4i\omega\kappa_3}{\phi_f\beta_l^2\kappa_1^2}}\right). \tag{3.172}$$

The transverse shear stress (3.91) depends on the radial pressure gradients which determine the transverse velocities, and thus each term in the expansion will be the product of a frequency-independent function with the second derivative of (3.170). Calculating the second axial derivative of (3.130), we have

$$f_l''(z) = \frac{\alpha_+^2\alpha_-^2}{\alpha_+^2-\alpha_-^2}\left(\frac{\sinh(\alpha_- z)}{\sinh(\alpha_-)} - \frac{\sinh(\alpha_+ z)}{\sinh(\alpha_+)}\right). \tag{3.173}$$

High Frequency limit

We first consider the high frequency limit, that is $\omega \gg \phi_f \beta_l^2 \kappa_1^2 / 4\kappa_3$. Expanding (3.171)-(3.172) for high frequency, we find

$$\alpha_- = \lambda(a + ib) + O(\lambda^{-1/4}) \quad \text{and} \quad \alpha_+ = \lambda(a - ib) + O(\lambda^{-1/4}), \tag{3.174}$$

where $a = \cos(\pi/8)$, $b = \sin(\pi/8)$ and $\lambda = (\omega\beta_l^2/\kappa_3\phi_f)^{1/4}$. Expanding (3.173) using (3.174), we find

$$\begin{aligned} f_l'' \sim \frac{\lambda^2}{2}\left(\frac{i}{\sqrt{2}} - 1\right) \big[& e^{\lambda b(z-1)} \left\{\cos(a\lambda(z-1)) + i\sin(a\lambda(z-1))\right\} \\ & - e^{\lambda a(z-1)} \left\{\cos(b\lambda(z-1)) - i\sin(b\lambda(z-1))\right\}\big] + \cdots \quad \text{as} \quad \omega \to \infty. \end{aligned} \tag{3.175}$$

Taking the spatio-temporal average of the magnitude of the transverse shear stress

$$\overline{|S_\Theta|} = \frac{1}{\tau}\int_0^\tau dt \frac{1}{1/2}\int_0^{r_0} dr \int_0^1 dz |S_\Theta| \tag{3.176}$$

does not change the frequency dependence of the integrand when integrating with respect to time nor transverse coordinates; the frequency dependence of the transverse shear is set by the frequency dependence of f_l''. In (3.175), we see that λ^{-1} acts a characteristic length scale for decay in the magnitude of the shear stress as we move away from the top of the chamber. From (3.175), we know that the integrand in (3.176) is $O(\lambda^2)$ but the exponential decay in the axial direction means that the dominant contribution to the microscale shear stress is concentrated in a region of size $O(1/\lambda)$. Hence, the averaged magnitude of the shear stress will scale as $O(\lambda)$. Given $\lambda \sim \omega^{1/4}$, we find the averaged magnitude and maximum value of the transverse shear stress in the high frequency limit scales as

$$\overline{|S_\Theta|} = O(\omega^{1/4}) \quad \text{and} \quad \max(|S_\Theta|) = O(\omega^{1/2}) \quad \text{as} \quad \omega \to \infty. \tag{3.177}$$

We repeat this process for the axial shear stress which has a frequency dependence dictated by the third axial derivative of f_l. Using (3.174), we find

$$\begin{aligned} f_l''' \sim \frac{\lambda^3}{2}\left(\frac{i}{\sqrt{2}} - 1\right) \big[& (b + ia) e^{\lambda b(z-1)} \left\{\cos(a\lambda(z-1)) + i\sin(a\lambda(z-1))\right\} \\ & - (a - ib) e^{\lambda a(z-1)} \left\{\cos(b\lambda(z-1)) - i\sin(b\lambda(z-1))\right\}\big] + \cdots \quad \text{as} \quad \omega \to \infty. \end{aligned} \tag{3.178}$$

Thus, we find that the magnitude of the axial shear will be $O(\lambda^3)$. We again have a boundary layer at the top of the domain of size $O(\lambda^{-1})$ and so the average magnitude and maximum values of the axial shear stress scales as

$$|\overline{S_z}| = O(\omega^{1/2}) \quad \text{and} \quad \max(|S_z|) = O(\omega^{3/4}) \quad \text{as} \quad \omega \to \infty. \tag{3.179}$$

We validate these scalings by plotting the average magnitude and maximum shear stress calculated from (3.168) in figure 3.7. We see that the averaged magnitude of the shear stress scales less strongly than the maximum shear stress with the frequency of the imposed displacement at high frequencies. At high frequencies, there are large gradients in pressure in a boundary layer of width $\lambda \sim \omega^{1/4}$ near the upper edge. Hence, the average does not scale as strongly, as the large contributions to the shear stress are distributed over a region decreasing in size as the frequency increases.

Low frequency limit

For low forcing frequencies $\omega \ll \phi_f \beta_l^2 \kappa_1^2 / 4\kappa_3$, the coefficients (3.131)-(3.131) become

$$\alpha_- = (1+i)\sqrt{\frac{\omega}{2\phi_f \kappa_1}} + O(\omega^{3/2}) \quad \text{and} \quad \alpha_+ = \beta_l \sqrt{\frac{\kappa_1}{\kappa_3}} - \frac{i}{2\phi_f \beta_k}\sqrt{\frac{\kappa_3}{\kappa_1^3}}\omega + O(\omega^2). \tag{3.180}$$

Substituting (3.180) into (3.173), we obtain the leading-order behaviour

$$f_l''(z) = \frac{i\omega}{\kappa_1 \phi_f}\left(z - \frac{\sinh\left(\sqrt{\frac{\kappa_1\beta_l^2}{\kappa_3}}z\right)}{\sinh\left(\sqrt{\frac{\kappa_1\beta_l^2}{\kappa_3}}\right)}\right) + O(\omega^2) \quad \text{as} \quad \omega \to 0. \tag{3.181}$$

Thus, the spatio-temporal average of the magnitude of the averaged transverse shear stress depends linearly on the frequency of the imposed oscillation. Taking the derivative of (3.181) with respect to z, we identify that the magnitude of the average axial shear stress also scales linearly with the frequency of the imposed oscillation for low frequencies. As there is no boundary layer for low forcing frequencies, we anticipate that the average and maximum will scale with frequency in the same way, namely

$$|\overline{S_z}| = O(\omega) \quad \text{and} \quad \max(|S_z|) = O(\omega) \quad \text{as} \quad \omega \to 0, \tag{3.182}$$

$$|\overline{S_\Theta}| = O(\omega) \quad \text{and} \quad \max(|S_\Theta|) = O(\omega) \quad \text{as} \quad \omega \to 0. \tag{3.183}$$

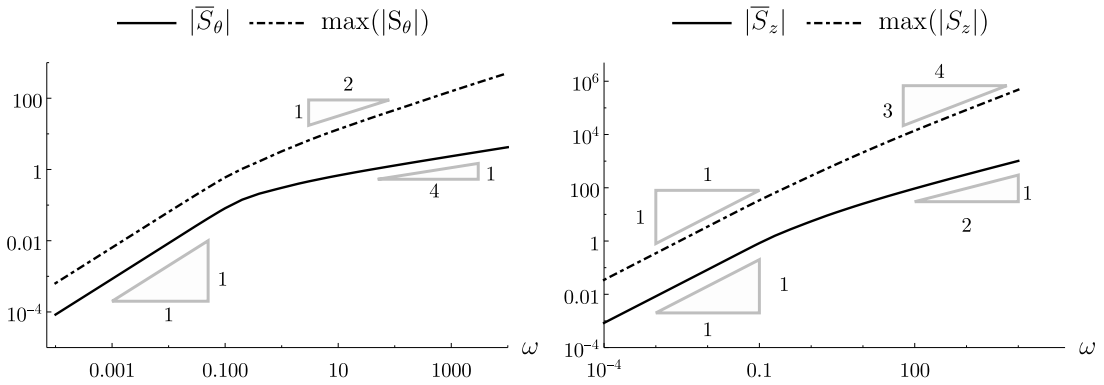

Figure 3.7: *Frequency dependence of shear stress as given by (3.168). Magnitudes of both the axial and transverse shear stress are evaluated at different points in space and time, then the average is calculated using (3.169) and the maximum value is identified. Solutions are plotted for solid fraction* $\phi_s = 0.2$. *Scaling laws are shown by triangles to identify the graph slope at low and high frequency.*

These scalings are validated by the average magnitude and maximum shear stress calculated from (3.168) as shown in figure 3.7.

In this section, we have presented solutions to the homogenised model for flow driven by string oscillation. The model can also be driven by imposing a fluid flux or pressure drop; we will consider these boundary conditions in the next sections.

3.5.2.4 Pressure driven flow

In sections 3.5.2.2-3.5.2.3, we considered the solutions to the macroscale problem when the system is driven by an imposed oscillation of the string ends. We can also drive the system by imposing a pressure or flux at the boundary. We consider solutions to (3.100) in the cylindrical domain shown in figure 3.3 driven by imposing a pressure drop in the axial direction, that is

$$p = 0 \quad \text{at} \quad z = 0, \tag{3.184}$$

$$p = p_{in} \quad \text{at} \quad z = 1. \tag{3.185}$$

We impose no flux on the sides of the chamber

$$\boldsymbol{u}\cdot\hat{\boldsymbol{n}} = 0 \quad \text{at} \quad r = 1/2, \quad 0 < z < 1, \tag{3.186}$$

and no displacement at the string ends

$$\boldsymbol{s} = \boldsymbol{0} \quad \text{at} \quad z = 0, 1. \tag{3.187}$$

Solving (3.100) subject to (3.184)-(3.187), we find that $\psi_1 = \psi_2 = 0$ and

$$\varphi = \frac{p_{in}(1-z)^3}{6}. \tag{3.188}$$

Thus, we have no string displacement $\boldsymbol{s} = \boldsymbol{0}$ and a linear pressure gradient that is uniform in the transverse direction,

$$p = p_{in}(1-z). \tag{3.189}$$

This results in a uniform axial shear stress $S_z = -m_Z p_{in}$ and zero transverse shear stress.

3.5.2.5 Flux driven flow

Next, we consider the flow in the scaffold, which results from imposing a radially varying flux at the base. For this problem, the boundary conditions for the partial differential equation (3.100) are no flux through the outer walls

$$\boldsymbol{u}\cdot\hat{\boldsymbol{n}} = 0 \quad \text{on} \quad \partial\Omega_e, \tag{3.190}$$

and fixed string ends

$$\boldsymbol{s} = \boldsymbol{0} \quad \text{at} \quad z = 0, 1. \tag{3.191}$$

The outlet is at atmospheric pressure

$$p = 0 \quad \text{at} \quad z = 1, \tag{3.192}$$

and the flow is driven by a radially varying inlet flux at the base

$$q_i = 10\left(\frac{1}{4} - r^2\right) \quad \text{at} \quad z = 0. \tag{3.193}$$

Following a similar methodology to that outlined in section 3.5.2.2, we can solve this problem for the fluid potential by separation of variables to obtain

$$\varphi = \frac{5(z^3 - 3z^2 + 2z)}{24\kappa_3} + \sum_{l=1}^{\infty} \hat{d}_l J_0(\beta_l r)\hat{f}_l(z) \tag{3.194}$$

where

$$\hat{f}_l = \frac{1}{\beta_l^3}\left(\frac{\kappa_3}{\kappa_1}\right)^{3/2} \frac{\sinh(\beta_l\sqrt{\kappa_1/\kappa_3}(z-1)) - (z-1)\sinh(\beta_l\sqrt{\kappa_1/\kappa_3})}{\cosh(\beta_l\sqrt{\kappa_1/\kappa_3})} \tag{3.195}$$

and

$$\hat{d}_l = \frac{10\left[\beta_l J_3(\beta_l/2) - 4J_2(\beta_l/2)\right]}{\kappa_3\beta_l^2\left[J_0(\beta_l/2)^2 + J_1(\beta_l/2)^2\right]}, \tag{3.196}$$

with β_l the ordered solutions to $J_0'(\beta_l/2) = 0$. Thus, for a radially varying inlet flux, the axial variation of the solution captured by $\hat{f}_l$ depends on the ratio of the transverse to axial permeability, κ_1/κ_3. The microscale shear stress for a given flux is set by the solid fraction *via* its influence on permeability. The steady string profiles that result from (3.194) are plotted in figure 3.8.a, and the variation in shear stress along the red line in figure 3.8.a for $\phi_s = 0.08$ is shown in figure 3.8.b. The effects of varying solid fraction are shown in figures 3.8c.-d., where we see that the microscale shear stress increases with increasing solid fraction.

To this point, we have considered steady and time-harmonic boundary conditions imposed on the macroscale equations. In the next section, we consider an example which explores the time dependence in (3.100) through the decay to a steady state.

3.5.2.6 Decay from an initial state

We consider a sudden change in the string displacement and characterise the time taken to relax to the steady state. For time $t > 0$, we have no imposed string displacement

$$\boldsymbol{s} = 0 \quad \text{at} \quad z = 0, 1, \tag{3.197}$$

no pressure drop across the chamber

$$p = 0 \quad \text{at} \quad z = 0, 1, \tag{3.198}$$

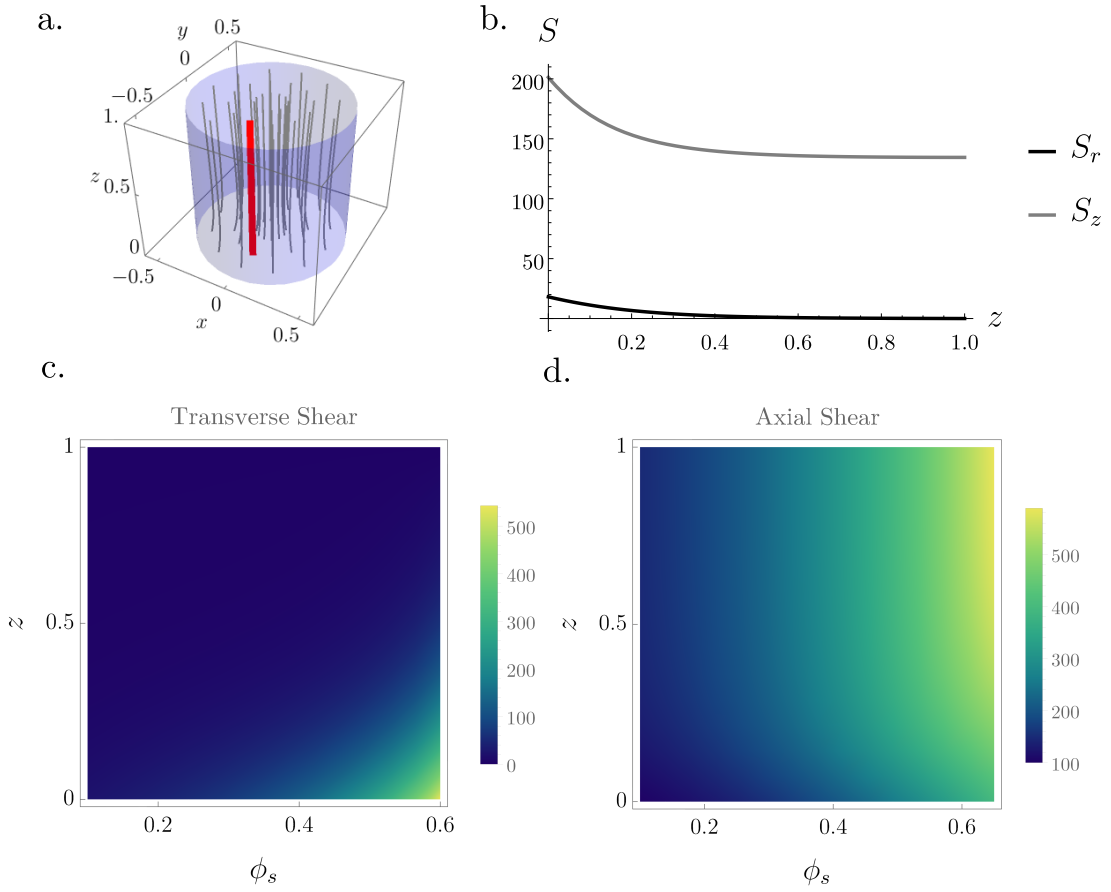

Figure 3.8: *Flux-driven flow. a. The string profiles calculated from* (3.194). *b. Shear stress along the red line in a., for* $\phi_s = 0.08$, *the solid fraction within the bioreactor scaffold. c-d. Transverse and axial shear stress along the red line in figure a. for varying solid fraction.*

and no flux through the outer wall of the chamber

$$\boldsymbol{u}\cdot\hat{\boldsymbol{n}} = 0 \quad \text{at} \quad r = 1/2, \quad \text{for} \quad 0 \leq z \leq 1. \tag{3.199}$$

The initial displacement field of the strings is prescribed

$$\boldsymbol{s} = \boldsymbol{a}(r, z) \quad \text{at} \quad t = 0. \tag{3.200}$$

Seeking a separable solution to (3.100), we obtain

$$\varphi = \sum_{l,n} A_{ln} J_0(\beta_l r) \sin(n\pi z) e^{-\gamma_{ln} t}, \tag{3.201}$$

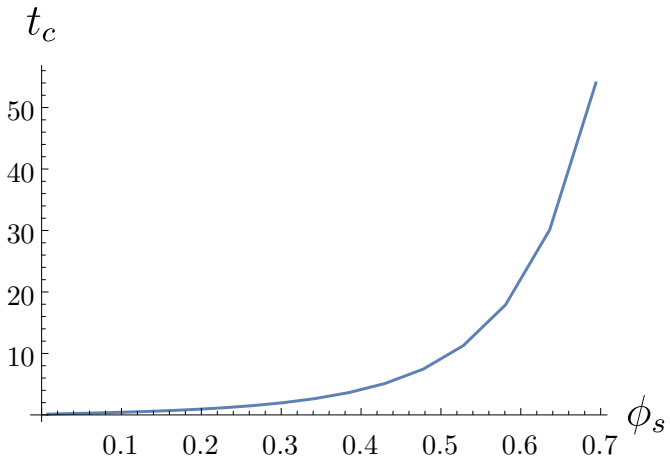

Figure 3.9: *The timescale characterising decay to steady state increases with solid fraction.*

where $n \in \mathbb{Z}$, β_l are the ordered zeros of $J_0'(\beta_l/2)$ and

$$\gamma_{ln} = n^2\pi^2\phi_f\kappa_1(1 + \frac{n^2\pi^2\kappa_3}{\beta_l^2\kappa_1}). \tag{3.202}$$

The coefficients A_{lmn} are fixed by imposing the initial condition on string displacement

$$\boldsymbol{s} = \nabla_\perp\varphi = \boldsymbol{a} \quad \text{at} \quad t = 0, \tag{3.203}$$

where $\psi_1 = \psi_2 = 0$ follows from imposing the homogeneous boundary conditions on string displacement at the top and bottom of the chamber. We do not consider a specific initial condition here, that is we do not specify the form of $\boldsymbol{a}$ in (3.200), as we are interested in the rate of decay which is independent of the initial state. The relaxation to steady state is characterised by the timescale corresponding to the smallest γ_{1n}, *i.e.*

$$t_c = \frac{1}{\kappa_1\pi^2\phi_f\left(1 + \frac{\kappa_3\pi^2}{\kappa_1\beta_1}\right)}. \tag{3.204}$$

The characteristic decay time increases with the solid fraction as shown in figure 3.9. We conjecture that the reason for this behaviour is that it is harder for fluid to pass between strings when the solid fraction is higher, increasing the time it takes for the system to relax to a steady state.

In this section, we have illustrated how the homogenised problem can be solved in a simple geometry when driven by string motion, an imposed flux or imposed pressure drop. Thanks to the linearity of the governing equations, we can combine the pressure or flux-driven flow with our string-driven solution by superposition, allowing the combined influence on flow and hence on shear stress to be explored.

3.6 Model extensions

3.6.1 Axial extension

During mechanical stimulation of the bioreactor construct, we anticipate that in addition to transverse motions of the scaffold fibres, there may be deformation along the string axis, and in some cases this mode of deformation may be dominant. In this section, we extend the model developed in sections 3.2-3.4 to include an $O(1)$ axial deformation of the strings in addition to small transverse displacements. We consider the effects of varying tension and fluid flow on string deformation.

3.6.1.1 Model setup

We consider the same geometry as that presented in section 3.2, namely N strings with a reference configuration aligned with the z-axis surrounded by slow, viscous, Newtonian flow. The strings have reference configurations $\boldsymbol{x}_0^i = \boldsymbol{x}_*^i + \tilde{z}\hat{\boldsymbol{e}}_z$ for $i = 1, ..., N$, where $\boldsymbol{x}_*^i$ lies on a square periodic lattice. The strings have undeformed length L, which is described by Lagrangian coordinates $(\tilde{x}, \tilde{y}, \tilde{z})$ with the origin at the centre of the base of the cylinder, as shown in figure 3.2. Imposing a force at the string ends parallel to the $z-$axis causes the string to deform to a length l. Positions on the string in the current configuration are described with Eulerian coordinates (x, y, z) which are defined as in section 3.2.

We are now in a position to write a kinematic description of the string deformation. We consider deformation of the string centreline comprising an axial

stretch together with displacements $\boldsymbol{s}^i = (s_1^i, s_2^i, s_3^i)$, *i.e.*

$$\boldsymbol{r}^i = \boldsymbol{x}_*^i + z(\tilde{z})\hat{\boldsymbol{e}}_z + \boldsymbol{s}^i. \tag{3.205}$$

We neglect twist of the string about its own axis throughout this section.

Next, we turn to describing the mechanics of the string motion. We begin by deriving the equation governing string deformation, following a similar argument to Antman [8]. We consider the balance of forces on a segment $\Delta\tilde{z}$ of the equilibrium configuration of the string. As for the solely transverse displacements considered in section 3.2, we consider the mechanics of the string centreline, assuming rigid body deformation so that the string has a circular cross-section in each $z =$ constant plane. Neglecting string inertia, the force balance is

$$\boldsymbol{N}^i(\tilde{z} + \Delta\tilde{z}) - \boldsymbol{N}^i(\tilde{z}) + \tilde{\boldsymbol{f}}^i(\tilde{z})\Delta\tilde{z} = \boldsymbol{0}, \tag{3.206}$$

where $\tilde{\boldsymbol{f}}^i$ is the body force per unit reference length of the ith string and $\boldsymbol{N}^i$ is the contact force. As in section 3.2, we will consider a body force due to the fluid stress, although it is convenient to work with a general body force until we have transformed the momentum balance into the Eulerian coordinates. Taylor expanding about $\tilde{z}$ for small $\Delta\tilde{z}$, we obtain

$$\frac{\partial \boldsymbol{N}^i}{\partial \tilde{z}} + \tilde{\boldsymbol{f}}^i = \boldsymbol{0}. \tag{3.207}$$

In (3.207), we have a description of the string mechanics; in order to relate this to the string deformation, we require a constitutive law. We choose to relate contact force $\boldsymbol{N}^i$ and the extension as follows:

$$\boldsymbol{N}^i = EA\frac{\partial \boldsymbol{r}^i}{\partial \tilde{z}} = T\frac{\partial \boldsymbol{r}^i}{\partial \tilde{z}}, \tag{3.208}$$

where E is the elastic modulus of a string and A is its cross-sectional area. By specifying (3.208), we ensure that the contact force is tangential to the string centreline, consistent with the inability of strings to support any shear forces. Substituting (3.208) into (3.207), we obtain

$$\frac{\partial}{\partial \tilde{z}}\left(T\frac{\partial \boldsymbol{r}^i}{\partial \tilde{z}}\right) + \tilde{\boldsymbol{f}}^i = \boldsymbol{0}. \tag{3.209}$$

The fluid problem satisfies the Stokes equations (3.2)-(3.3) with no-slip at the boundary between the string and fluid (3.4)-(3.5).

3.6.1.2 Nondimensionalisation

We nondimensionalise the problem using the following scales,

$$\begin{aligned}(u,v,w) = U(\hat{u},\hat{v},\hat{w}), \quad (x,y,z) = L(\hat{x},\hat{y},\hat{z}), \quad t = \delta\frac{L}{U}\hat{t},\\ \boldsymbol{s}^i = \delta L\hat{\boldsymbol{s}}^i, \quad \tilde{\boldsymbol{f}}^i = \delta\mu U L\hat{\tilde{\boldsymbol{f}}}^i, \quad p = p_a + \frac{\mu U}{\delta^2 L}\hat{p}, \quad U = \frac{\delta T}{\mu L},\end{aligned} \tag{3.210}$$

where the velocity scale is set by balancing the restoring force from transverse string displacements with hydrodynamic stresses and $T = EA$. We drop hats in the analysis that follows with all subsequent equations being dimensionless. Nondimensionalising the string displacement (3.205), we find

$$\boldsymbol{r}^i = z(\tilde{z})\hat{\boldsymbol{e}}_z + \delta\boldsymbol{s}^i. \tag{3.211}$$

Equation (3.209) becomes

$$\frac{\partial^2\boldsymbol{r}^i}{\partial\tilde{z}^2} + \delta\tilde{\boldsymbol{f}} = \boldsymbol{0}. \tag{3.212}$$

3.6.1.3 Model reduction

We substitute (3.211) into (3.212) and equate coefficients at each order of δ. At $O(1)$, we find

$$\frac{\partial^2 z}{\partial\tilde{z}^2} = 0. \tag{3.213}$$

The body force does not enter at leading-order, as in (3.210) we have assumed that the fluid stress is an order smaller than the imposed force that sets the axial length of the system. The accompanying boundary conditions for this problem are specification of the string ends

$$z(0) = 0 \quad \text{and} \quad z(L) = l. \tag{3.214}$$

Integrating (3.213) and imposing (3.214), we find

$$z = \nu\tilde{z}, \tag{3.215}$$

where $\nu = l/L$ is the string stretch. At next order, we find

$$\frac{\partial^2\boldsymbol{s}^i}{\partial\tilde{z}^2} + \tilde{\boldsymbol{f}} = \boldsymbol{0}. \tag{3.216}$$

Given our ultimate aim is to couple the string motion with fluid flow, we rewrite (3.216) in Eulerian coordinates so the same system is used for both the fluid and solid problem. Using (3.215), we can transform (3.216) into the Eulerian configuration,

$$\nu \frac{\partial^2 \boldsymbol{s}^i}{\partial z^2} + \boldsymbol{f} = \boldsymbol{0}, \tag{3.217}$$

where $\boldsymbol{f}$ is the body force per unit length in the Eulerian frame, related to the force per reference length *via* $\tilde{\boldsymbol{f}} = \nu \boldsymbol{f}$. We have obtained (3.217) from reducing a nonlinear force balance on the string centreline. The equivalent calculation for displacements which are assumed to be small and purely transverse (as in section 3.2) is presented in appendix C.

3.6.1.4 Body force

Neglecting gravity, the dominant body force acting on the string is the fluid stress, given by

$$\boldsymbol{f} = \int_{\partial D_s^i} \sigma \cdot \hat{\boldsymbol{n}} dl, \tag{3.218}$$

where ∂D_s is the curve around the string boundary in a $z =$ constant plane. Given the rigid-body assumption $\boldsymbol{s}^i = \boldsymbol{s}^i(\tilde{z})$, the boundary ∂D_s must be a circle.

The level set $h_1 = 0$ defines the boundary of the string, where

$$h_1(z) = |\boldsymbol{x}_\perp - \boldsymbol{x}_*^i - \delta \boldsymbol{s}_\perp^i(z - \delta s_3^i(z))| - b, \tag{3.219}$$

and $\boldsymbol{s}_\perp = I_2 \boldsymbol{s}$, $\boldsymbol{x}_\perp = I_2 \boldsymbol{x}$ for $I_2 = \mathrm{diag}(1, 1, 0)$. We Taylor expand (3.219) about z, which gives

$$h_1(z) = |\boldsymbol{x}_\perp - \boldsymbol{x}_*^i - \delta \boldsymbol{s}_\perp^i(z) + \delta^2 s_3^i \frac{\partial \boldsymbol{s}_\perp^i}{\partial z} + \cdots| - b. \tag{3.220}$$

The outward-facing normal $\hat{\boldsymbol{n}}$ to this boundary is given by

$$\hat{\boldsymbol{n}} = \frac{\nabla h_1}{|\nabla h_1|}. \tag{3.221}$$

Calculating ∇h_1, we find

$$\begin{aligned}\nabla h_1 &= \boldsymbol{x}_\perp - \boldsymbol{x}^i_{0_\perp} - \delta \boldsymbol{s}^i_\perp - \frac{\delta}{2}\left(\nabla \boldsymbol{s}^i_\perp \cdot (\boldsymbol{x}_\perp - \boldsymbol{x}^i_{0_\perp}) + (\boldsymbol{x}_\perp - \boldsymbol{x}^i_{0_\perp}) \cdot \nabla \boldsymbol{s}^i_\perp\right) + O(\delta^2) \\ &= \boldsymbol{x}_\perp - \boldsymbol{x}^i_{0_\perp} - \delta \boldsymbol{s}^i_\perp - \frac{\delta}{2}\nabla \boldsymbol{s}^i_\perp \cdot (\boldsymbol{x}_\perp - \boldsymbol{x}^i_{0_\perp}) + O(\delta^2),\end{aligned} \tag{3.222}$$

where we have used the rigid body assumption which means that the $(\boldsymbol{x}_\perp - \boldsymbol{x}^i_{0\perp}) \cdot \nabla \boldsymbol{s}^i$ term vanishes. Introducing

$$\hat{\boldsymbol{n}}_0 = \frac{\boldsymbol{x} - \boldsymbol{x}^i_0}{|\boldsymbol{x} - \boldsymbol{x}^i_0|}, \tag{3.223}$$

we find

$$\hat{\boldsymbol{n}} = \hat{\boldsymbol{n}}_0 - \delta\left(\frac{1}{2}\nabla \boldsymbol{s}^i_\perp \cdot \hat{\boldsymbol{n}}_0 + \frac{\boldsymbol{s}^i_\perp}{|\boldsymbol{x} - \boldsymbol{x}^i_0|}\right) + \delta \hat{\boldsymbol{n}}_0 \cdot \left(\frac{\boldsymbol{s}^i_\perp}{|\boldsymbol{x} - \boldsymbol{x}^i_0|} + \frac{1}{2}\nabla \boldsymbol{s}^i_\perp \cdot \hat{\boldsymbol{n}}_0\right)\hat{\boldsymbol{n}}_0 + O(\delta^2), \tag{3.224}$$

where the leading-order normal lies entirely in the transverse plane. We can simplify (3.224) to give

$$\begin{aligned}\hat{\boldsymbol{n}} &= \hat{\boldsymbol{n}}_0 - \delta \frac{\hat{\boldsymbol{t}}_0 \cdot \nabla \boldsymbol{s}^i_\perp \cdot \hat{\boldsymbol{n}}_0}{2}\hat{\boldsymbol{t}}_0 + O(\delta^2), \\ &= \hat{\boldsymbol{n}}_0 - \frac{\delta}{2}\frac{\partial \boldsymbol{s}^i_\perp}{\partial z} \cdot \hat{\boldsymbol{n}}_0 \hat{\boldsymbol{e}}_z + O(\delta^2), \\ &= \hat{\boldsymbol{n}}_0 + \delta \hat{\boldsymbol{n}}_1 + O(\delta^2)\end{aligned} \tag{3.225}$$

where we have used the fact that the leading-order tangent to the string is aligned with the z-axis. The expansion of the normal in (3.225) purely accounts for the geometrical deformation of a single string; if we were to consider the multiple scales form of the normal as required to impose Neumann conditions on a slowly varying domain, we would also need to include these terms in the expansion.

Thus, the force balance on the string (3.217) takes the form

$$\nu \frac{\partial^2 \boldsymbol{s}^i}{\partial z^2} + \int_{\partial D^i_s} \sigma \cdot \hat{\boldsymbol{n}}_0 dl + \delta \int_{\partial D^i_s} \sigma \cdot \hat{\boldsymbol{n}}_1 dl + \cdots = \boldsymbol{0}, \tag{3.226}$$

where ∂D^i_s is the projection of the string cross-section of the string onto a $z =$ constant plane.

3.6.1.5 Homogenisation

In this section we set out to write (3.226) in multiple scales form. As for the case considered above, where the string displacement was purely transverse, we begin by introducing continuum functions for the string displacement.

We define continuum functions for string displacement and undeformed position as in section 3.4.1, restated here for convenience, which gives,

$$\boldsymbol{s}(\boldsymbol{x},t) = \boldsymbol{s}^i(z,t) \quad \text{in} \quad D_s^i, \tag{3.227}$$

$$\boldsymbol{x}_0(\boldsymbol{x}) = \boldsymbol{x}_0^i(z) \quad \text{in} \quad D_s^i \tag{3.228}$$

Similarly, we introduce a continuum function for the string stretch, which we assume slowly varies with position,

$$\nu(\boldsymbol{x},t) = \nu(\boldsymbol{x}_0) \quad \text{in} \quad D_s^i, \tag{3.229}$$

for $\boldsymbol{x}_0$ defined in (3.228). Written as a continuum equation, (3.226) then becomes

$$\nu\frac{\partial^2 \boldsymbol{s}}{\partial z^2} + \int_{\partial D_s} \sigma\cdot\hat{\boldsymbol{n}}_0 dl + \delta\int_{\partial D_s} \sigma\cdot\hat{\boldsymbol{n}}_1 dl + \cdots = \boldsymbol{0}. \tag{3.230}$$

We seek multiple scales expansions for the fluid velocity, pressure and string displacement by expanding as a power series in δ using (3.24)-(3.27). In multiple scales form, the first contribution to fluid stress becomes

$$\begin{aligned}\int_{\partial D_s} \sigma\cdot\hat{\boldsymbol{n}}_0 dl = \delta\int_{\partial D_{\boldsymbol{s}_0}} \sigma\cdot\hat{\boldsymbol{n}}_0 dl_X + \delta^2\int_{\partial D_{\boldsymbol{s}_0}} (\boldsymbol{s}_1 + \boldsymbol{X}\cdot\nabla_x\boldsymbol{s}_0)\cdot\nabla_X\sigma\cdot\hat{\boldsymbol{n}}_0 dl_X \\ + \delta^2\int_{\partial D_{\boldsymbol{s}_0}} \boldsymbol{X}\cdot\nabla_x\sigma\cdot\hat{\boldsymbol{n}}_0 dl_X + \delta^2\int_{\partial D_{\boldsymbol{s}_0}} (\nabla_{\boldsymbol{X}}\cdot\sigma)\mathbf{X}\cdot\boldsymbol{V}\cdot\hat{\boldsymbol{n}}_0 dl_X + O(\delta^3),\end{aligned} \tag{3.231}$$

where dl_X is the line element in fast coordinates and for this section $\nabla_{\boldsymbol{X}} = (\partial_X, \partial_Y, 0)$ and $\nabla_{\boldsymbol{x}} = (\partial_x, \partial_y, \partial_z)$. Substituting the multiple scales expansion of the stress tensor, we find

$$\int_{\partial D_s} \sigma\cdot\hat{\boldsymbol{n}}_0 dl = \int_{\partial D_{\boldsymbol{s}_0}} (-p_1 I + \nabla_{\boldsymbol{X}}\boldsymbol{u}_0 + (\nabla_{\boldsymbol{X}}\boldsymbol{u}_0)^T)\cdot\hat{\boldsymbol{n}}_0 dl_X - \int_{\partial D_{\boldsymbol{s}_0}} \boldsymbol{X}\cdot\nabla_x p_0\hat{\boldsymbol{n}}_0 dl_X. \tag{3.232}$$

We apply the divergence theorem to each term and evaluate the resulting integrals which gives

$$\begin{aligned}\int_{\partial D_s} \sigma\cdot\hat{\boldsymbol{n}}_0 dl &= -\phi_f \nabla_{\boldsymbol{x}} p_0 - \phi_s \nabla_{\boldsymbol{x}_\perp} p_0 \\ &= -\nabla_{\boldsymbol{x}_\perp} p_0 - \phi_f \frac{\partial p_0}{\partial z}\hat{\boldsymbol{e}}_z,\end{aligned} \tag{3.233}$$

where $\nabla_{\boldsymbol{x}_\perp} = (\partial_x, \partial_y, 0)$. The second contribution to fluid stress when written in multiple scales form becomes,

$$\begin{aligned}\delta\int_{\partial D_s} \sigma\cdot\hat{\boldsymbol{n}}_1 dl &= \delta^2 \int_{\partial D_{\boldsymbol{s}_0}} \sigma\cdot\hat{\boldsymbol{n}}_1 dl_X, \\ &= \int_{\partial D_{\boldsymbol{s}_0}} p_0 \left(\frac{1}{2}\frac{\partial \boldsymbol{s}_0}{\partial z}\cdot\hat{\boldsymbol{n}}_0 \boldsymbol{e}_z\right) dl_X, \\ &= 0,\end{aligned} \tag{3.234}$$

as the fluid pressure and displacement are independent of the slow scale at leading-order.

Combining (3.233) and (3.234), the homogenised force balance then takes the form

$$-\nabla p_0 + \phi_s \frac{\partial p_0}{\partial z}\boldsymbol{e}_z + \nu\frac{\partial^2 \boldsymbol{s}_0}{\partial z^2} = 0. \tag{3.235}$$

Combining (3.235) with the leading-order equation $z = \nu\tilde{z}$, the extended form of the model enables us to consider a broader range of imposed motion. We can consider a time-dependent extension of the bioreactor chamber to set ν, combined with an additional flow problem governed by (3.235). We will outline how this result can be incorporated into a model which accounts for chamber deformation in the discussion of future work.

3.7 Discussion

In this chapter, we have developed a model for fluid-fibre interaction in the bioreactor using homogenisation *via* multiscale asymptotics. The scaffold fibres were modelled as elastic strings undergoing small, transverse oscillations and the cell

media was modelled as a slow, viscous, Newtonian fluid. The results from chapter 2 were used in deriving the multiple scales form for the integral condition that coupled string deformation to the viscous flow, balancing the elastic restoring force with hydrodynamics stresses.

We obtain two cell problems which give the role of the pressure gradients in inducing fluid flow. The microscale problem for the transverse flow is the standard problem for Stokes flow past a periodic array of cylinders [78]. Due to the string motion, we also attain an additional microscale problem with an analytical solution. From the microscale problems, we are able to obtain the microscale shear stress and an anisotropic permeability tensor which provides the one-way coupling between microscale and macroscale problems. The macroscale problem took the form of Darcy's law relative to a moving material. The mass conservation equation was modified from the case of a rigid, porous material - the effective material is not compressible but flow of the fluid into a given region drives string motion to reduce their local density. The homogenised force balance ensures the momentum of the composite is conserved and provides an additional form of coupling between the strings and fluid. We can drive the macroscale model by imposing fluid flux, pressure or string motion at the domain boundary.

We considered solutions to the macroscale model in a simple, cylindrical geometry where the problem is analytically tractable. Driving fluid motion by imposing a time-harmonic string displacement, we find that, at low forcing frequencies, both the axial and transverse average shear stresses scale linearly with the forcing frequency. At higher frequencies, the averaged shear stress and maximum scale with fractional powers of the imposed oscillation frequency. The transverse shear stress scales less strongly than axial shear stress, and for each component the average scales less strongly than the maximum. We rationalised these scalings by identifying the presence of a boundary layer at the upper edge of the domain with a thickness that scales inversely with the quartic root of the frequency. These effects are identified in the dimensionless problem, where the characteristic frequency scale is given by $\omega_c = \mu L^2 \omega / T$, suggesting that in the physical system the effects of high frequency can also be achieved by reducing the string tension. In reducing the string tension, we anticipate that the length over which the imposed displace-

ment has influence also reduces, as there is a reduced elastic energy associated with deforming the string. When fluid flow is driven by a radially-varying flux at the base of the cylinder, the distribution of the shear stress depends on the solid fraction. While the macroscale problems considered in this chapter miss many physical interactions that occur within the bioreactor system, we have identified the key parameters and explored their role in modulating the microscale shear stress distribution. We will outline in chapter 5 how the model including axial extension may be coupled to an external fluid flow and a deformable membrane to better reflect the humanoid bioreactor chamber.

In this chapter, the homogenised model includes a modified Darcy's law. This analysis is applicable where the strings occupy an appreciable fraction of the chamber volume. For a stationary array of cylinders with a separation δ and radius b nondimensionalised on the same length-scale, Darcy's law arises from the multiple scales analysis of the Stokes equations in the regime when $\delta^2 \log(\delta/b) \ll 1$ [78]. For a different dominant balance, where $\delta^2 \log(\delta/b) = O(1)$, the relevant flow model is the Brinkman equations [78]. For $\delta^2 \log(\delta/b) \gg 1$, the fraction of solid is so small as to have little effect on the flow and Stokes equations are applicable [78]. Previously, the analysis was undertaken for a rigid porous media in two and three dimensions [78]. Given the presence of strings does not influence the relative size of terms in the Stokes equation, we anticipate a similar analysis will be applicable to the problem we present here, providing a link between the coarse-grained models for fluid-structure interaction valid in the limit of low and high solid fraction [52, 117]. An understanding of this transition in flow behaviour would be beneficial in systems which begin with a sparse scaffold but which evolve into the dense regime following cell proliferation.

As the cells in the bioreactor chamber proliferate, the volume they occupy will no longer be negligible in comparison with the size of the strings. We anticipate that at the later stages of operation, cell proliferation will invalidate the assumption made throughout this chapter that the microscale shear stress experienced by cells is well captured by the fluid shear stress exerted at the string boundary. It is possible to include the effects of cell growth within the homogenisation process. Perhaps the simplest way to include growth is using a surface accretion model [91].

The growth of cells on the scaffold can be modelled as a phase change from fluid to solid at a rate dependent on the local concentration of nutrient [91]. For slow growth, the microscale geometry is unchanged at leading-order and the growth appears as a source term in the macroscale equations [91]. When growth is not slow, the evolution of the microstructure becomes significant, which results in a time-varying domain for the cell problem [35]. In this situation there is two-way coupling between the microscale and macroscale problems; the macroscale problem must be solved to obtain the local concentration field which then determines the evolution of the microstructure. Volumetric growth can be modelled by introducing a mapping between a grown state and a periodic reference configuration where homogenisation may be applied [30]. Both surface and volumetric growth could be incorporated into the fluid-string model by following the analysis in [30, 35, 91].

More broadly, the analysis presented in this chapter provides a method to develop models of fluid-structure interaction that may be applied to other physical systems. For example, the strings may be replaced by a linear beams by modifying the form of the force balance (3.6). Minor adaptations to the multiple scales presented here would produce an effective model for the small deformations of fibre beds. Large deformations of the solid phase could also be incorporated providing that they are sufficiently uniform so as to allow the microscale and macroscale to decouple. To incorporate large deformations, a mapping similar to that presented in [30, 100] would be required between the Eulerian current configuration and a periodic reference configuration. A similar approach could be used to incorporate different string densities across the domain, resulting in a spatially dependent permeability. This would be of interest mathematically as the mapping would be coupled to the macroscale variables in a similar manner to [97], rather than taking a form posed *a priori* as in [100]. Thus, the theory could be modified to develop an alternative approach to model fluid-structure interaction at low Reynolds number with applications such as cilia beds [42].

Chapter 4

Nutrient Transport

In this chapter, we use homogenisation *via* multiscale asymptotics to derive effective models for solute transport in fibrous media. We build upon the model of fluid-string interaction developed in chapter 3, where the displacement of strings is coupled to the macroscale pressure gradients. The variation in string displacement across the domain gives rise to a slowly varying microstructure and so we must account for the correct expansion of the normal when writing Robin boundary conditions in multiple-scales form [20]. There are five timescales that characterise the advection, diffusion and uptake of nutrient within the fluid-string composite: timescales of microscale advection; microscale diffusion; macroscale advection; macroscale diffusion and absorption. The relative magnitude of these timescales is set by the Péclet number and the Damköhler number. We consider four distinguished limits that give rise to different macroscale behaviour. For the case where macroscale advection balances macroscale diffusion, we see that microscale advection induced by string motion occurs much more quickly than macroscale transport, thus we introduce multiple timescales to resolve this behaviour.

The presentation of this work is as follows. An introduction to the significance of nutrient transport in tendon tissue engineering and modelling approaches is given in section 4.1. We outline the model setup in section 4.2 before nondimensionalising in section 4.3. The equations are homogenised in section 4.4 for different relative strengths of advection, diffusion and reaction. Simple solutions

to the homogenised problems are presented for each regime. Application to the bioreactor scaffold is discussed in section 4.5 and conclusions are drawn in section 4.6.

4.1 Introduction

Solute transport in porous media has been studied in the context of numerous applications including filtration, the flow of contaminants in hydrology, and nutrient transport in biological systems. We first introduce the significance of nutrient transport in the field of tendon tissue engineering in section 4.1.1. Following this, we summarise previous approaches to modelling nutrient transport in tissue engineering applications in section 4.1.2. In section 4.1.3, we review the application of homogenisation *via* multiscale asymptotics to modelling solute transport.

4.1.1 Nutrient transport in tendon tissue engineering

To grow healthy tendon tissue *in vitro*, cells require an adequate supply of nutrients in addition to a suitable mechanical environment [15]. Engineering 3D tissue constructs on a scale with clinical relevance is difficult as a suitable level of nutrient delivery throughout the whole scaffold must be achieved. For thin structures, for example skin grafts, diffusive transport may be sufficient. However, given the slow rate of diffusive transport, it may become insufficient when the constructs reach a clinically relevant size. The lack of adequate nutrient delivery can lead to tissue defects or necrotic cores which results in tissue of inferior mechanical properties that would not be suitable for tissue engineering applications [15, 70]. The limitations of diffusive transport have driven the development of bioreactors that generate advective transport by mixing or perfusion, such as the humanoid robotic bioreactor described in the chapter 1.

In tissue engineering applications, it is common to monitor the concentrations of glucose, oxygen and lactate as each of these molecules plays a key part in the health of the growing tissue. We now outline the role of each of these metabolites in

tendon tissue engineering. Throughout this chapter we use the terms nutrient and metabolite interchangeably. Glucose is the main energy source of mammalian cells which is used to fuel cellular processes. Glucose is metabolised to form pyruvate in the cytoplasm *via* anaerobic or aerobic glycolysis [125]. In aerobic glycolysis, glucose is converted into 2 molecules of pyruvate while in anaerobic conditions, pyruvate is transformed into lactate [125]. The overall reactions are

$$\begin{aligned}\text{Glucose} + 2\text{NAD}^+ + 2\text{ADP} + 2\text{P}_\text{i} \rightarrow \\ 2\text{NADH} + 2\ \text{Pyruvate} + 2\text{ATP} + 2\text{H}_2\text{O} + 4\text{H}^+, \qquad (4.1)\end{aligned}$$

$$\text{Glucose} + 2\text{ADP} + 2\text{P}_\text{i} \rightarrow 2\ \text{Lactate} + 2\text{ATP} + 2\text{H}_2\text{O} + 2\text{H}^+, \qquad (4.2)$$

for aerobic and anaerobic glycolysis respectively. Energy is stored in ATP by adding an inorganic phosphate group P_i to ADP. In the aerobic pathway, further ATP is generated in the citric acid cycle by breaking down pyruvate [125]. Depriving cells of glucose can disrupt cellular metabolism and ultimately results in cell death. At the opposite extreme, hyperglycemia (atypically high glucose levels) can cause oxidative stress, resulting in inflammation and degeneration in tendons [123]. Changes in glucose metabolism occur when tendon derived stem cells differentiate into tenocytes or chondrocytes [66]. Elevated levels of glucose and its metabolites are observed in healing tendons [66]. Oxidative stress refers to compromised cell viability caused by the alteration of the cell's redox state which can be induced by an increase in production of reactive oxygen species [59]. Reactive oxygen species are normally produced during metabolism and play various roles including acting as cell signalling molecules and regulation of gene expression [75]. However, at high concentrations, reactive oxygen species can cause cell apoptosis and necrosis *via* the damage of DNA, disruption of lipid assembly *via* peroxidation and protein modification [59].

Oxygen plays an essential part in tissue homeostasis and regeneration *via* its role in regulating processes such as metabolism, proliferation, and differentiation [29]. Typical physiological partial oxygen pressures are between $2-9$kPa, although due to the low levels of vascularisation, normoxic partial oxygen pressures in tendon tissue are thought to be at the lower end of this range [29]. To calculate the percentage oxygen in a given tissue, the ratio of the partial oxygen pressure to atmospheric pressure is expressed as a percentage. The cellular response to oxygen is mediated by hypoxia-inducible transcription factors (HIFs). Transcription fac-

tors are proteins which can recruit or block RNA polymerase, the complex which transcribes RNA to DNA. HIFs increase in stability in hypoxic conditions due to inhibition of one of their oxygen-dependent degradation pathways. In tendon cultures, experimental work has shown that proliferation of porcine primary tenocytes was enhanced and production of matrix metalloproteinase-1 decreased when cultured at 2% oxygen compared with atmospheric oxygen levels (20%) [140]. Decreased matrix-metalloproteinase-1 production increases collagen deposition which can aid tendon maturation [29, 140]. Human tendon stem cells are also oxygen sensitive, showing a greater self-renewal capacity in normoxic conditions, whereas atmospheric oxygen levels causing a decrease in stemness [137].

Lactate is a product of anaerobic glycolysis. The cellular metabolism of tendon cells has been observed to shift from aerobic to anaerobic glycolysis in response to hypoxic stress or injury [139]. Thus, in addition to ensuring the tissue is healthy, monitoring glucose, oxygen and lactate concentrations can provide insight into the cellular stress.

4.1.2 Modelling nutrient transport in tissue engineering

Nutrients of interest in tissue engineering are typically found in concentrations on the order of one millimolar and so concentrations are modelled with continuum equations [92]. Transport may occur *via* diffusion through the media, advection as the nutrient is carried by fluid flow, or a combination of the two. The relative strength of advective and diffusive processes is given by the Péclet number $Pe = UL/D$, for a fluid velocity scale U, lengthscale L and diffusion coefficient D. It is also of interest to model uptake of nutrient or production of metabolites by cells which is characterised by the Damköhler number $Da = \overline{A}/U$, the ratio of uptake velocity $\overline{A}$ to advection. Production of metabolite can be modelled by allowing $\overline{A} < 0$.

The mathematical form of the reaction term varies depending upon the bulk concentration of nutrients and metabolites. One possibility is Michaelis-Menten kinetics, which originates in describing enzymatic reactions and has a nonlinear functional form that can be derived from the law of mass action [5, 86]. For a

metabolite with concentration c_y being absorbed by cells at a rate $\mathcal{A}$, the Michaelis-Menten term is given by,

$$\mathcal{A} = -\frac{V_{\max} c_y}{K_m + c_y}, \tag{4.3}$$

where V_{max} is the maximum absorption rate and K_m is the Michaelis constant, that is the metabolite concentration for which the absorption rate is half maximal. Metabolite production can be modelled by changing the sign in (4.3). The assumption of a constant rate of uptake is suitable when the concentration in solution is much greater than the Michaelis constant *i.e.* $c_y \gg K_m$. When the nutrient concentration is low ($c_y \ll K_m$), an uptake rate proportional to the concentration is suitable, reflecting the rate limiting effect of finite concentration. These reaction terms can appear either in the boundary conditions or in the bulk according to the modelling choice for the cells in the bioreactor: if cells are predominantly found attached to the bioreactor scaffold, nutrient uptake may be modelled by reaction terms in the boundary conditions but for cells in suspension, the use of source terms in the nutrient conservation equation is appropriate.

Depending upon their density, cells may be modelled using discrete or continuum approaches. Discrete models describe each cell using a state vector which evolves based upon prescribed rules often related to the state of its neighbours, and can be combined with models of nutrient concentration, see for example [4, 132]. The focus here will be continuum approaches, where cells are described by partial differential equations governing their concentration. We now outline some continuum approaches to modelling nutrient transport in tissue engineering.

The simplest modelling assumption is that cells occupy negligible volume so that cell growth decouples from fluid flow. This approach was taken in modelling nutrient transport in a hollow fibre membrane bioreactor in [113]. Hollow fibre membrane bioreactors consist of a porous fibre with hollow centre, surrounded by an extracellular space (ECS) (see figure 4.1.a). Cells can be seeded either in the fibre wall or throughout the ECS. A flow is imposed in the lumen and the ECS outlet ports may be closed or opened to enhance nutrient perfusion through the fibre wall. Due to the stress-shielding effects of the fibre wall, higher flow rates can be used within the fibre lumen, offering the potential to increase advective nutrient transfer. In [113], analytical modelling is used to identify geometrical and oper-

ating parameters which result in suitable concentrations of nutrient throughout the bioreactor, using lubrication theory to describe flow in the lumen and Darcy's law to model flow in both the fibre wall and the extracellular space [113]. Similar continuum models were used to model a bone-cartilage bioreactor where hollow fibres running through the porous scaffold enhanced nutrient perfusion [131]. Cell proliferation was also included in [131] by assuming a doubling of the cell population in a characteristic proliferation time. The rate of uptake in the scaffold bulk was modelled as being proportional to the number of cells, appearing as a reaction term in the nutrient conservation equation [131]. While this approach incorporates the effect of increasing cell number on nutrient consumption, it does not account for the increasing volume that the cells occupy as they proliferate. In some applications, volume occlusion effects can become significant, modifying the fluid flow and in turn the transport process, see for example [31, 91, 96].

To include the influence of proliferation on fluid flow and transport, a model which accounts for the volume occupied by the cells is required. Perhaps the simplest way to include this effect is to prescribe the dependence of scaffold porosity on the cell number [111]. An alternative approach is to account for the cell volume explicitly using a multiphase approach [92]. Conservation equations for each phase, for example cells and interstitial fluid, are written which hold over the whole domain, coupled by constitutive equations for interphase forces [94]. Multiphase models can be derived by averaging the microscale equations for each phase over a representative volume element [130]. An alternative approach to deriving averaged models is homogenisation *via* multiscale asymptotics. We will review the application of this method to transport processes in the next section.

4.1.3 Multiscale modelling of transport processes

Multiscale models of transport processes in porous media have been developed to model biofilm formation, filtration processes and tissue growth [35, 91, 106]. Homogenisation *via* multiscale asymptotics elucidates the influence of the pore structure on macroscale transport processes, as well as providing a method to determine an effective properties of materials with a varying microstructure which

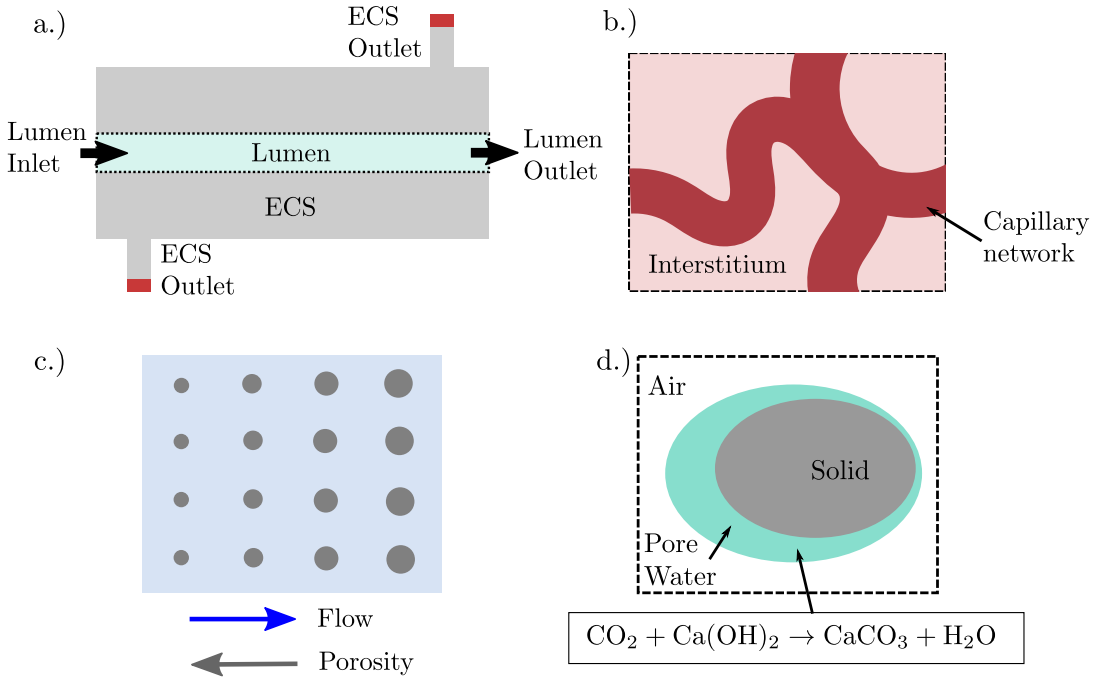

Figure 4.1: *Modelling transport processes. a.) Schematic of a hollow fibre membrane bioreactor [113]. b.) Unit cell used in modelling drug transport within a vascular tumour. The Navier-Stokes equations describes flow within the capillary network and the interstitium which consists of cells and extracellular matrix is modelled as a porous material [112]. c.) The configuration resulting in most efficient filter blocking [36]. d.) Unit cell used in modelling concrete carbonation. Carbon dioxide from the air dissolves in pore water where it reacts with aqueous calcium hydroxide dissolved from the concrete [97].*

may be difficult to simulate directly. The homogenisation technique relies upon the separation of lengthscales characterising the whole material L and the pore size δL, making the assumption that $\delta \ll 1$. As highlighted by Auriault and Adler [12], the relative size of the Péclet number to the dimensionless pore size δ determines the character of the macroscale transport model. In a study of rigid, nonreactive, porous media, it was found that for $Pe = O(\delta)$, diffusive processes dominate at both the microscale and macroscale. For $Pe = O(1)$, diffusive processes dominate at the microscale but at the macroscale, an advection-diffusion equation is obtained. With $Pe = O(\delta^{-1})$, the microscale problem is a diffusion-advection problem, with nutrient being carried along fluid streamlines on the macroscale, *i.e.* the system is advection-dominated on the macroscale. Introducing a slow timescale characterising macroscale diffusion, it was shown that dispersion is an $O(\delta)$ effect in this regime [12]. In the case of very strong advection where $Pe = O(\delta^{-2})$, a homogenised model cannot be obtained as the microscale problem is advective and so directly depends on the macroscale boundary conditions.

To model biological applications where the metabolic processes of cells influence the nutrient concentration, we must also consider reaction terms which may appear in the boundary conditions or as a source term in the transport equation. Motivated by modelling drug delivery in vascular tumours, Shipley and Chapman derive the macroscale problems that result from the different magnitudes of Damköhler number [112]. Drug uptake occurs in porous media periodically interspersed with capillaries where the Navier Stokes equations hold (see figure 4.1.b). Five distinguished limits were identified where reaction terms enter the macroscale model resulting from different combinations of Damköhler number and boundary conditions describing exchange between the porous medium and capillary [112].

The macroscale models reviewed above were obtained for porous media with an exactly periodic microstructure. When the assumption of exact periodicity at the microscale is not satisfied, standard homogenisation techniques can be extended to derive effective models for transport in materials with a slowly varying or time-dependent microstructure [34]. Diffusion in media with a spatially varying porosity in the absence of flow gives rise to an advection term in the macroscale equation which biases transport towards regions of low porosity [20]. Homogenisa-

tion of diffusion in spatially varying porous media was coupled to Robin boundary conditions on the pore walls in a study motivated by filtration applications [36]. For flow antiparallel to the porosity gradient, contaminant removal was more uniform across the filter than when no porosity gradient is present (see figure 4.1.c.) [36]. Filter blockage was considered in [35], where the removal of contaminant from solution induced evolution of the microstructure.

Where the microstructure has a fixed unit cell size, for example spheres of varying radius on a square periodic lattice, a level set function can be used to describe the boundary [20, 13]. The level set approach has been applied in developing homogenised models of tissue growth *via* surface and volume accretion [31, 61, 60]. An alternative, simpler approach is taken in [91] who model surface growth in a similar way to phase change, specifying a rate of growth that depended on the concentration rather than tracking the location of the free interface between tissue and fluid.

In systems with a more complex geometry, a mapping between the current configuration and an exactly periodic reference configuration can be used to obtain a homogenised model [100]. Generally, this mapping depends only on the slow scale so that the fast scale and slow scale decouple, allowing homogenisation to be carried out in the periodic reference configuration [30, 97, 100]. The parameters in the homogenised model depend on the mapping *via* the deformation gradient and its determinant [97, 100]. A mapping to a periodic reference configuration for transport processes was applied to study the chemical degradation of concrete, where atmospheric carbon dioxide dissolved in pore water within the concrete reacts with calcium hydroxide (a component of concrete), thereby lowering the pH of the pore water which has the potential to corrode steel supports within the concrete (see figure 4.1.d) [97]. This reaction alters the microstructure as carbon dioxide from the air is dissolved in water to participate in the reaction, resulting in a reduction in the air fraction as the products occupy a greater volume than the reactants. To treat this mathematically, Peter and Böhm [97] mapped the reaction-diffusion equations to a periodic reference configuration where the equations could be homogenised. Here, the mapping was time-dependent with an evolution governed by an equation motivated by mass conservation. Mappings have

also been applied to a deformable solid domain in modelling tissue growth, where the growth of a hyperelastic porous medium was governed by a constitutive growth law depending on the local concentration [30]. The equations governing fluid flow, solid deformation and nutrient transport were homogenised in a periodic reference configuration before applying a map to the current configuration, which consists of the composition of a growth tensor describing geometrical deformations and a deformation gradient describing the effects of elastic stresses. Elastic deformation is assumed to occur on a faster timescale than growth, the result being that only time derivatives of the growth tensor enter the macroscale model [30].

In some applications, processes of interest may be characterised by different timescales, motivating the introduction of separate scales in time as well as space. One example is found in modelling reactive decontamination of chemical agents in porous media [77]. A cleanser is typically applied at the surface of the porous material and reacts upon contact with the chemical agent. Neglecting flow, both the cleanser and agent were modelled as immiscible fluids within a porous medium, with reaction at their interface causing conversion from agent to cleanser. When the agent fully saturates the pores in a region of the material, the evolution of the macroscale front between agent and cleanser evolves more slowly than the timescale of microscale evolution due to the chemical reaction, instead being characterised by the timescale of macroscale diffusion. To resolve this, Luckins *et al.* introduced multiple timescales in an inner problem describing the evolution of the agent-cleanser interface which was then matched to an outer problem for the regions saturated with one fluid [77]. Multiple timescales were also considered in modelling thermal dissipation in a composite consisting of a linearly elastic, isotropic material with thermosensitive, viscoelastic inclusions [19]. An oscillatory mechanical load causes dissipation in the viscoelastic phase, generating a temperature rise which in turn causes a decrease in the elastic modulus. The behaviour for different ratios of timescales characterising mechanical oscillation and thermal diffusion were considered, and a macroscale model was derived for the case when mechanical oscillations occurred on a fast timescale compared with thermal diffusion [19]. Multiple timescales are also necessary to resolve secular terms which arise in the homogenisation of the wave equation in heterogeneous media when the microstructural variation is of the same size as the wavelength, thereby giving

rise to significant dispersion effects [27]. Problems with multiple spatio-temporal scales progress by introducing multiple temporal scales in a similar manner to standard spatial multiple scales problems [19]. Periodicity in the fast timescale is assumed in the coefficients of the multiple scales expansion, for example motivated by time-harmonic boundary conditions, which closes the problem. An average is taken over the period of fast oscillation with the resulting macroscale problem describing evolution on the slow spatial and temporal scales.

As we are considering advection, diffusion and absorption processes in a porous media, there are several timescales in our problem, denoted t_A, t_D, t_d, t_a and t_u, summarised in table 4.1. The timescales give the characteristic time to travel an order one distance on either the macroscale or microscale by the transport process listed, for example t_d, the timescale of macroscale diffusion is the time taken to diffuse an order 1 distance on the macroscale. As we tune the magnitude of the Péclet number in the subsequent sections, we alter the physical processes which are in balance. In section 4.4.2, we consider $Pe = O(\delta)$ which corresponds to a diffusive processes dominating on both the microscale and macroscale as $t_a/t_d = O(1/\delta)$ and $t_A/t_D = O(1/\delta^2)$. Following this in section 4.4.3, we keep $Pe = (\delta)$ but consider strong uptake with $Da = O(1/\delta)$ which we find dominates the macroscale behaviour. In section 4.4.4, when $Pe = O(1)$, we have the dominant balance where both advection and diffusion appear in the macroscale problem although the microscale evolution occurs on a faster timescale as $t_A/t_a = \delta$. By performing analysis on multiple timescales we can resolve the evolution of the metabolite concentration on both the microscale and macroscale. In section 4.4.5, where $Pe = O(1/\delta)$, we have a balance of advection and diffusion in the microscale but advection is the dominant transport process on the macroscale.

4.2 Model setup

We consider nutrient transport within a fibrous scaffold which consists of fluid regions Ω_f surrounding N strings occupying regions Ω_s^i for $i = 1, ..., N$, as shown in figure 3.2. We denote the curved, outer boundary of the domain as $\partial\Omega_e$. The strings have a radius b and their reference configuration is aligned with the $z-$axis,

Physical Process	Timescale
String motion & Microscale advection	$t_A = \frac{\delta L}{U}$
Microscale Diffusion	$t_D = \frac{\delta^2 L^2}{D}$
Macroscale Diffusion	$t_d = \frac{L^2}{D}$
Macroscale Advection	$t_a = \frac{L}{U}$
Uptake	$t_u = \frac{\delta L}{\overline{A}}$

Table 4.1: *Problem timescales. U is the fluid velocity scale, L the characteristic macroscale lengthscale, $\overline{A}$ is the uptake velocity and δ the ratio between microscale and macroscale lengthscales.*

with their endpoints $\boldsymbol{x}_0^i$ laying on a square periodic lattice. We consider cell media as a viscous, incompressible, Newtonian fluid with velocity $\boldsymbol{u}$, pressure p and viscosity μ. In the subsequent multiple scales analysis, the coefficients in the expansion of the fluid velocity will satisfy the equations presented in chapter 3 in the development of the fluid-string model.

We assume that the scaffold is uniformly coated by a layer of cells so that there is no uptake in the fluid bulk. Thus, we use a continuum model for the cells and further make the simplifying assumption that their volume is negligible (for details see Appendix A.1.1). We model the nutrient concentration c in the fluid region with the advection-diffusion equation,

$$\frac{\partial c}{\partial t} + \boldsymbol{u} \cdot \nabla c = D\nabla^2 c \quad \text{in} \quad \Omega_f, \tag{4.4}$$

where D is the diffusion coefficient of the nutrient in media. We assume that there is no flow of nutrient through the outer wall,

$$\hat{\boldsymbol{n}} \cdot (\boldsymbol{u}c - D\nabla c) = 0 \quad \text{on} \quad \partial\Omega_e, \tag{4.5}$$

where $\hat{\boldsymbol{n}}$ is the outward-facing normal to the outward surface of the domain. As

there is no flux through the outer wall, equation (4.5) reduces to

$$\hat{\boldsymbol{n}} \cdot \nabla c = 0 \quad \text{on} \quad \partial\Omega_e. \tag{4.6}$$

We assume that cells fixed on the string boundaries uptake nutrient at a velocity $\overline{A}$,

$$\hat{\boldsymbol{n}}_s \cdot \left((\boldsymbol{u} - \frac{\partial \boldsymbol{s}}{\partial t})c - D\nabla c \right) = -\overline{A}c \quad \text{on} \quad \partial\Omega_s^i, \tag{4.7}$$

where $\hat{\boldsymbol{n}}_s$ is the outward-facing normal to the string surface, taking care to use fluid velocity relative to the boundary in the specification of the nutrient flux at the string boundary. Details of the estimation of the uptake velocity are given in the appendix A.2.1. Using no-slip conditions (3.4)-(3.5), (4.7) reduces to

$$\hat{\boldsymbol{n}}_s \cdot (D\nabla c) = \overline{A}c \quad \text{on} \quad \partial\Omega_s^i. \tag{4.8}$$

A known concentration of the nutrient enters the chamber at the inlet

$$c = c_{in} \quad \text{at} \quad z = 0, \tag{4.9}$$

where $c_{in} = c_{in}(x, y)$ is given. We make the assumption of zero diffusive flux at the outflow

$$\frac{\partial c}{\partial z} = 0 \quad \text{at} \quad z = L. \tag{4.10}$$

We also prescribe the initial nutrient concentration, imposing

$$c = 0 \quad \text{at} \quad t = 0. \tag{4.11}$$

Imposing (4.11) would reflect a system where there is no nutrient initially within the bioreactor chamber. When media of known saturation is present in the chamber initially, (4.11) can be adapted to equate the initial concentration with the concentration of the nutrient in the cell media.

4.3 Nondimensionalisation and scaling

We nondimensionalise (4.4)-(4.11) as follows:

$$c = c_{in}\hat{c}, \quad (x, y, z) = L(\hat{x}, \hat{y}, \hat{z}), \quad (u, v, w) = U(\hat{u}, \hat{v}, \hat{w}), \quad t = \frac{\delta L}{U}\hat{t}, \tag{4.12}$$

where hats denote nondimensional quantities and we scale the nutrient concentration with the inlet concentration. As in chapter 3, the length-scale L is the characteristic length of the chamber, the velocity scale is given by $U = \delta T/\mu L$ and $\delta = l/L \ll 1$ is the ratio of string separation to the domain width. We have chosen to nondimensionalise on the same timescale as the fluid-string problem, namely the timescale for microscale advection.

After dropping hats, the nondimensionalised advection-diffusion equation (4.4) becomes

$$\frac{\partial c}{\partial t} + \delta \boldsymbol{u} \cdot \nabla c = \frac{\delta}{Pe} \nabla^2 c \quad \text{in} \quad \Omega_f, \tag{4.13}$$

where $Pe = UL/D$ is the Péclet number which characterises the relative strength of advection to diffusion. In sections 4.4.2 - 4.4.5, we consider the different macroscale models that arise for Péclet numbers of different magnitudes. The no-flux condition (4.6) in dimensionless form is

$$\hat{\boldsymbol{n}} \cdot \nabla c = 0 \quad \text{on} \quad \partial\Omega_e, \tag{4.14}$$

and the uptake condition becomes

$$\frac{1}{Pe} \hat{\boldsymbol{n}}_s \cdot \nabla c = Da\, c \quad \text{on} \quad \partial\Omega_s^i, \tag{4.15}$$

where $Da = \overline{A}/U$ is the Damköhler number, which gives the relative strength of uptake to advection. The condition on concentration at the inflow (4.9) becomes

$$c = 1 \quad \text{at} \quad z = 0, \tag{4.16}$$

and the outflow condition (4.10) becomes

$$\frac{\partial c}{\partial z} = 0 \quad \text{at} \quad z = 1. \tag{4.17}$$

Finally, we have the initial condition

$$c = 0 \quad \text{at} \quad t = 0. \tag{4.18}$$

4.4 Effective model derivation

To obtain effective equations for nutrient transport in the scaffold, we adopt a similar approach to chapter 3, and homogenise equations (4.13)-(4.18) under the

assumption that the separation between adjacent strings is much less than the width of the scaffold, $\delta = l/L \ll 1$. The fast scale $\boldsymbol{X} = (x, y)/\delta - \lfloor (x, y)/\delta \rfloor - \mathbf{1}/2$ characterises variation between strings and the slow scale $\boldsymbol{x} = (x, y, z)$ captures variation across the whole scaffold. Within a two-dimensional unit cell (figure 3.3.b), we denote the fluid region D_f, the region occupied by the leading-order string position $D_{\boldsymbol{s}_0}$ and outer boundary of the unit cell ∂D. The in-plane gradient operator $\nabla_\perp = (\partial_x, \partial_y)$ transforms into multiple-scales form as follows

$$\nabla_\perp = \frac{1}{\delta}\nabla_{\boldsymbol{X}} + \nabla_{\boldsymbol{x}}. \tag{4.19}$$

We only require the slow z-coordinate, assuming that the variations in axial displacement occur on a larger scale than the separation between adjacent strings. We introduce multiple-scales expansions for the concentration, string displacement and fluid velocity as follows

$$c \sim c_0(\boldsymbol{x}, \boldsymbol{X}, t) + \delta c_1(\boldsymbol{x}, \boldsymbol{X}, t) + \cdots, \tag{4.20}$$

$$\boldsymbol{s} \sim \boldsymbol{s}_0(\boldsymbol{x}, t) + \delta \boldsymbol{s}_1(\boldsymbol{x}, \boldsymbol{X}, t) + \cdots, \tag{4.21}$$

$$\boldsymbol{v} \sim \boldsymbol{v}_0(\boldsymbol{x}, \boldsymbol{X}, t) + \delta \boldsymbol{v}_1(\boldsymbol{x}, \boldsymbol{X}, t) + \cdots, \tag{4.22}$$

$$w \sim w_0(\boldsymbol{x}, \boldsymbol{X}, t) + \delta w_1(\boldsymbol{x}, \boldsymbol{X}, t) + \cdots, \tag{4.23}$$

where all coefficients are periodic in $\boldsymbol{X}$ with period $\mathbf{1}$. We have used the same expansion for fluid velocity $\boldsymbol{u} = \boldsymbol{v} + w\hat{\boldsymbol{e}}_z$ as used in the previous chapter (see equations (3.24)-(3.25)).

4.4.1 Writing the uptake condition in multiple-scales form

To write the uptake condition in multiple-scales form, we must expand the slow variation in the microscale normal as outlined in [20]. To be fully consistent, we should expand the boundary position given by the level set $h_s = 0$ defined by (3.36), that is

$$h_s = |\boldsymbol{X} - \boldsymbol{X}_0 - \boldsymbol{s}| - B, \tag{4.24}$$

in parallel with the multiple scales expansion. We would then need to expand onto the leading-order position of the boundary so that the microscale and macroscale problems decouple. If instead, we use the boundary defined by the leading-order

string displacements $\partial D_{\boldsymbol{s}_0}$, the analysis simplifies considerably. Hence, in a similar manner to chapter 3, we define the string boundary as the level set $h = 0$ for

$$h = |\boldsymbol{X} - \boldsymbol{X}_0 - \boldsymbol{s}_0| - B. \tag{4.25}$$

In using (4.25), we incur errors of $O(\delta)$ in the cross-sectional area of the string, though we should recover the same homogenised problem as obtained when using (4.24). We return to this point in chapter 5 where we discuss this assumption in further detail.

The outward, unit normal to the leading-order boundary position is given by the gradient of the level set function defining the boundary, namely

$$\hat{\boldsymbol{n}} = \frac{\nabla_{\boldsymbol{X}} h + \delta \nabla_{\boldsymbol{x}} h}{|\nabla_{\boldsymbol{X}} h + \delta \nabla_{\boldsymbol{x}} h|} = \hat{\boldsymbol{n}}_0 + \delta \hat{\boldsymbol{n}}_1 + O(\delta^2). \tag{4.26}$$

We can use (4.21) and (4.25) to calculate the expansion coefficients explicitly, which gives

$$\hat{\boldsymbol{n}}_0 = \frac{\boldsymbol{X} - \boldsymbol{X}_0 - \boldsymbol{s}_0}{|\boldsymbol{X} - \boldsymbol{X}_0 - \boldsymbol{s}_0|} \tag{4.27}$$

and

$$\hat{\boldsymbol{n}}_1 = -\frac{1}{2}(\hat{\boldsymbol{n}}_0 \cdot \nabla_{\boldsymbol{x}} \boldsymbol{s}_0 + \nabla_{\boldsymbol{x}} \boldsymbol{s}_0 \cdot \hat{\boldsymbol{n}}_0) = -\frac{1}{2}((\nabla_{\boldsymbol{x}} \boldsymbol{s}_0)^T + \nabla_{\boldsymbol{x}} \boldsymbol{s}_0) \cdot \hat{\boldsymbol{n}}_0. \tag{4.28}$$

Having established the first two terms in the expansion of the normal to the leading-order boundary, we write (4.15) in multiple-scales form by expanding the concentration gradient about this position and transforming the gradient operators into multiple-scales form. As in section 3.4.3.1, we expand in both the slow and fast variables about a fixed slow position on the leading-order position of the string boundary $(\hat{\boldsymbol{x}}, \boldsymbol{X}^b + \boldsymbol{s}_0)$, for example,

$$\begin{aligned} \nabla_{\boldsymbol{X}} c_0(\hat{\boldsymbol{x}} + \delta \boldsymbol{X}, \boldsymbol{X}^b + \boldsymbol{s}_0(\hat{\boldsymbol{x}} + \delta \boldsymbol{X}) + \delta \boldsymbol{s}_1(\hat{\boldsymbol{x}} + \delta \boldsymbol{X}, \boldsymbol{X}) + ...) = \\ \nabla_{\boldsymbol{X}} c_0 + \delta \boldsymbol{X} \cdot \nabla_{\boldsymbol{x}} \nabla_{\boldsymbol{X}} c_0 + \delta(\boldsymbol{s}_1 + \boldsymbol{X} \cdot \nabla_{\boldsymbol{x}} \boldsymbol{s}_0) \cdot \nabla_{\boldsymbol{X}} \nabla_{\boldsymbol{X}} c_0 + O(\delta^2). \end{aligned} \tag{4.29}$$

The normal expansion (4.26) can then be combined with (4.28) to write (4.15) in multiple-scales form. The full expansion of (4.15) is given in appendix D. We will see that the functional dependence of the concentration on fast and slow scales simplifies the expansion considerably.

In sections 4.4.2 - 4.4.5, we homogenise (4.13)-(4.18) to obtain the macroscale equations when $Pe = O(\delta)$ with $Da = O(1)$; $Pe = O(\delta)$ with $Da = O(1/\delta)$; $Pe = O(1)$ with $Da = O(\delta)$ and $Pe = O(1/\delta)$ with $Da = O(1)$. We refer to these regimes as *macroscale diffusion-reaction*, *macroscale uptake*, *macroscale advection-diffusion-reaction* and *macroscale advection-reaction* respectively.

4.4.2 Macroscale diffusion-reaction

4.4.2.1 Homogenisation

We consider the limit of strong diffusion, introducing the reduced Péclet number $\overline{Pe} = Pe/\delta$, which we assume is order 1 in this section. Substituting (4.20)-(4.23) into (4.13)-(4.18) written in multiple-scales form, we obtain the following equations at leading-order

$$\nabla^2_{\boldsymbol{X}} c_0 = 0 \quad \text{in} \quad D_f, \tag{4.30}$$

$$\hat{\boldsymbol{n}}_0 \cdot \nabla_{\boldsymbol{X}} c_0 = 0 \quad \text{on} \quad \partial D_{\boldsymbol{s}_0}, \tag{4.31}$$

with c_0 $\mathbf{1}$-periodic in $\boldsymbol{X}$. Thus, we have a leading-order concentration which is independent of the fast scale. At $O(\delta)$, we have

$$\nabla^2_{\boldsymbol{X}} c_1 = 0 \quad \text{in} \quad D_f, \tag{4.32}$$

$$\hat{\boldsymbol{n}}_0 \cdot \nabla_{\boldsymbol{X}} c_1 = -\hat{\boldsymbol{n}}_0 \cdot \nabla_{\boldsymbol{x}} c_0 \quad \text{on} \quad \partial D_{\boldsymbol{s}_0}, \tag{4.33}$$

with c_1 periodic in $\boldsymbol{X}$, where we have used the fast scale independence of the leading-order concentration to cancel terms. Further using the fast scale independence of c_0, we decompose the fast scale dependence of c_1 by writing

$$c_1 = -\boldsymbol{\Lambda} \cdot \nabla_{\boldsymbol{x}} c_0 + \overline{\lambda}, \tag{4.34}$$

where $\overline{\lambda} = \overline{\lambda}(\boldsymbol{x}, t)$ is a function of time and the slow scale determined by the solution to a higher order problem. The cell function $\boldsymbol{\Lambda} = (\Lambda_1, \Lambda_2)$ satisfies the following cell problem:

$$\nabla^2_{\boldsymbol{X}} \boldsymbol{\Lambda} = \mathbf{0} \quad \text{in} \quad D_f, \tag{4.35}$$

$$\hat{\boldsymbol{n}}_0 \cdot \nabla_{\boldsymbol{X}} \boldsymbol{\Lambda} = \hat{\boldsymbol{n}}_0 \quad \text{on} \quad \partial D_{\boldsymbol{s}_0}, \tag{4.36}$$

with $\mathbf{\Lambda}$ periodic in $\boldsymbol{X}$. We also impose

$$\int_{D_f} \mathbf{\Lambda} dS_X = \mathbf{0}, \tag{4.37}$$

which fixes the arbitrary constant in the solution of (4.35)-(4.36). For this Péclet number, the timescale of microscale diffusion is much faster than advection, resulting in a steady diffusion problem for microscale variations in nutrient concentration.

At $O(\delta^2)$, we have

$$\overline{Pe}\,\frac{\partial c_0}{\partial t} = \nabla_{\boldsymbol{X}} \cdot (\nabla_{\boldsymbol{X}} c_2 + \nabla_{\boldsymbol{x}} c_1) + \nabla_{\boldsymbol{x}} \cdot (\nabla_{\boldsymbol{X}} c_1 + \nabla_{\boldsymbol{x}} c_0) + \frac{\partial^2 c_0}{\partial z^2} \quad \text{in} \quad D_f, \tag{4.38}$$

with

$$\begin{aligned} \hat{\boldsymbol{n}}_0 \cdot (\nabla_{\boldsymbol{X}} c_2 + \nabla_{\boldsymbol{x}} c_1) + \hat{\boldsymbol{n}}_1 \cdot (\nabla_{\boldsymbol{X}} c_1 + \nabla_{\boldsymbol{x}} c_0) + \hat{\boldsymbol{n}}_0 \cdot (\boldsymbol{X} \cdot \nabla_{\boldsymbol{x}} (\nabla_{\boldsymbol{X}} c_1 + \nabla_{\boldsymbol{x}} c_0)) \\ + \hat{\boldsymbol{n}}_0 \cdot (\boldsymbol{d}_0 \cdot \nabla_{\boldsymbol{X}} (\nabla_{\boldsymbol{X}} c_1 + \nabla_{\boldsymbol{x}} c_0)) = Da\,\overline{Pe}\, c_0 \quad \text{on} \quad \partial D_{\boldsymbol{s}_0}, \end{aligned} \tag{4.39}$$

and c_2 periodic in $\boldsymbol{X}$. Here we have substituted (3.35) in (4.39), that is the solution $\boldsymbol{s}_1 = -\boldsymbol{X} \cdot \nabla_{\boldsymbol{x}} \boldsymbol{s}_0 + \boldsymbol{d}_0$ to eliminate some fast scale dependence in the expansion of the uptake boundary condition. To obtain the macroscale problem, we average (4.38) over the fluid region of the unit cell

$$\begin{aligned} \overline{Pe}\,\phi_f \frac{\partial c_0}{\partial t} = &\int_{D_f} \nabla_{\boldsymbol{X}} \cdot (\nabla_{\boldsymbol{X}} c_2 + \nabla_{\boldsymbol{x}} c_1) dS_X \\ &+ \int_{D_f} \nabla_{\boldsymbol{x}} \cdot (\nabla_{\boldsymbol{X}} c_1 + \nabla_{\boldsymbol{x}} c_0) dS_X + \phi_f \frac{\partial^2 c_0}{\partial z^2}, \end{aligned} \tag{4.40}$$

where we have used the fast scale independence of c_0. The fluid volume fraction ϕ_f is equivalent to the area of D_f. Applying the divergence theorem to the first integral gives,

$$\begin{aligned} \overline{Pe}\,\phi_f \frac{\partial c_0}{\partial t} = &- \int_{\partial D_{\boldsymbol{s}_0}} (\nabla_{\boldsymbol{X}} c_2 + \nabla_{\boldsymbol{x}} c_1) \cdot \hat{\boldsymbol{n}}_0 dl_X \\ &+ \int_{D_f} \nabla_{\boldsymbol{x}} \cdot (\nabla_{\boldsymbol{X}} c_1 + \nabla_{\boldsymbol{x}} c_0) dS_X + \phi_f \frac{\partial^2 c_0}{\partial z^2}, \end{aligned} \tag{4.41}$$

where periodicity of the expansion coefficients means that the integral over the exterior boundary of the unit cell vanishes. Applying (4.39), we have

$$\begin{aligned}\overline{Pe}\phi_f\frac{\partial c_0}{\partial t} = &-\int_{\partial D_{\boldsymbol{s}_0}}(\nabla_{\boldsymbol{X}}c_1+\nabla_{\boldsymbol{x}}c_0)\cdot\hat{\boldsymbol{n}}_1 dl_X - \overline{Pe}\int_{\partial D_{\boldsymbol{s}_0}} Da\, c_0\, dl_X\\ &+\int_{\partial D_{\boldsymbol{s}_0}}(\boldsymbol{X}\cdot\nabla_{\boldsymbol{x}}(\nabla_{\boldsymbol{X}}c_1+\nabla_{\boldsymbol{x}}c_0))\cdot\hat{\boldsymbol{n}}_0 dl_X\\ &+\int_{\partial D_{\boldsymbol{s}_0}}(\boldsymbol{d}_0\cdot\nabla_{\boldsymbol{X}}(\nabla_{\boldsymbol{X}}c_1+\nabla_{\boldsymbol{x}}c_0))\cdot\hat{\boldsymbol{n}}_0 dl_X\\ &+\int_{D_f}\nabla_{\boldsymbol{x}}\cdot(\nabla_{\boldsymbol{X}}c_1+\nabla_{\boldsymbol{x}}c_0)dS_X+\phi_f\frac{\partial^2 c_0}{\partial z^2},\end{aligned} \tag{4.42}$$

where we have used the fast scale independence of c_0 in evaluating the average of the time derivative. First, we show that the third and fourth integrals do not contribute to the macroscale equations. Writing the third integral in (4.42) in index notation, we have

$$\int_{\partial D_{\boldsymbol{s}_0}}(\boldsymbol{X}\cdot\nabla_{\boldsymbol{x}}(\nabla_{\boldsymbol{X}}c_1+\nabla_{\boldsymbol{x}}c_0))\cdot\hat{\boldsymbol{n}}_0 dl_X = \int_{\partial D_{\boldsymbol{s}_0}} X_i\partial_{x_i}(\partial_{X_j}c_1+\partial_{x_j}c_0)\hat{n}_{0j}dl_X. \tag{4.43}$$

We substitute (4.34) for c_1 which gives

$$\begin{aligned}\int_{\partial D_{\boldsymbol{s}_0}}(\boldsymbol{X}\cdot\nabla_{\boldsymbol{x}}(\nabla_{\boldsymbol{X}}c_1+\nabla_{\boldsymbol{x}}c_0))\cdot\hat{\boldsymbol{n}}_0 dl_X &= \int_{\partial D_{\boldsymbol{s}_0}} X_i\partial_{x_i}\left((\delta_{jk}-\partial_{X_j}\Lambda_k)\partial_{x_k}c_0\right)n_{0j}dl_X\\ &= \partial_{x_i}\partial_{x_k}c_0\int_{\partial D_{\boldsymbol{s}_0}} X_i(\delta_{jk}-\partial_{X_j}\Lambda_k)n_{0j}dl_X\\ &= \partial_{x_i}\partial_{x_k}c_0\int_{\partial D_{\boldsymbol{s}_0}} X_i(n_{0k}-n_{0k})dl_X\\ &= 0,\end{aligned} \tag{4.44}$$

where we have used the slow scale independence of the cell problem and (4.36) in the second line to eliminate $\boldsymbol{\Lambda}$.

We now consider the fourth integral in equation (4.42), writing it in index notation,

$$\int_{\partial D_{\boldsymbol{s}_0}}(\boldsymbol{d}_0\cdot\nabla_{\boldsymbol{X}}(\nabla_{\boldsymbol{X}}c_1+\nabla_{\boldsymbol{x}}c_0))\cdot\hat{\boldsymbol{n}}_0 dl_X = \int_{\partial D_{\boldsymbol{s}_0}}\left(d_{0i}\partial_{X_i}(\partial_{X_j}c_1+\partial_{x_j}c_0)\right)n_{0j}dl_X. \tag{4.45}$$

Applying the divergence theorem and using the fast scale independence of $\boldsymbol{d}_0$, we find

$$\begin{aligned}\int_{\partial D_{\boldsymbol{s}_0}} (\boldsymbol{d}_0 \cdot \nabla_{\boldsymbol{X}}(\nabla_{\boldsymbol{X}} c_1 + \nabla_{\boldsymbol{x}} c_0)) \cdot \hat{\boldsymbol{n}}_0 dl_X &= -d_{0i} \int_{D_f} \partial_{X_j} \left(\partial_{X_i}(\partial_{X_j} c_1 + \partial_{x_j} c_0)\right) dS_X \\ &= -d_{0i} \int_{D_f} \partial_{X_i} \partial_{Xj} (\partial_{X_j} c_1 + \partial_{x_j} c_0) dS_X \\ &= 0,\end{aligned} \tag{4.46}$$

where the sign appears as $\hat{\boldsymbol{n}}_0$ points from the string into the fluid domain. We have also used (4.32), (4.34) and the fast scale independence of c_0.

Returning to (4.42), we apply Reynolds transport theorem to the final integral to obtain

$$\begin{aligned}\overline{Pe}\phi_f \frac{\partial c_0}{\partial t} = \int_{\partial D_{\boldsymbol{s}_0}} (\nabla_{\boldsymbol{X}} c_1 + \nabla_{\boldsymbol{x}} c_0) \cdot ((\nabla_{\boldsymbol{x}} \boldsymbol{s}_0) \cdot \hat{\boldsymbol{n}}_0 + \hat{\boldsymbol{n}}_1) dl_X - \overline{Pe} \int_{\partial D_{\boldsymbol{s}_0}} Da\, c_0\, dl_X \\ + \phi_f \frac{\partial^2 c_0}{\partial z^2} + \nabla_{\boldsymbol{x}} \cdot \int_{D_f} (\nabla_{\boldsymbol{X}} c_1 + \nabla_{\boldsymbol{x}} c_0) dS_X,\end{aligned} \tag{4.47}$$

where the 'velocity' of the boundary is given by $\nabla_{\boldsymbol{x}} \boldsymbol{s}_0$, as positions on the leading-order string boundary in microscale coordinates are given by $\boldsymbol{X}_0 + \boldsymbol{s}_0 + B\hat{\boldsymbol{E}}_R$, where $\hat{\boldsymbol{E}}_R$ is the radial unit vector in microscale coordinates. We now illustrate that the remaining boundary integral

$$\int_{\partial D_{\boldsymbol{s}_0}} (\nabla_{\boldsymbol{X}} c_1 + \nabla_{\boldsymbol{x}} c_0) \cdot ((\nabla_{\boldsymbol{x}} \boldsymbol{s}_0) \cdot \hat{\boldsymbol{n}}_0 + \hat{\boldsymbol{n}}_1) dl_X \tag{4.48}$$

is identically zero, having no influence on the macroscale behaviour. Substituting (4.28) for $\hat{\boldsymbol{n}}_1$, we have

$$\frac{1}{2} \int_{\partial D_{\boldsymbol{s}_0}} (\nabla_{\boldsymbol{X}} c_1 + \nabla_{\boldsymbol{x}} c_0) \cdot (\nabla_{\boldsymbol{x}} \boldsymbol{s}_0 - (\nabla_{\boldsymbol{x}} \boldsymbol{s}_0)^T) \cdot \hat{\boldsymbol{n}}_0 dl_X. \tag{4.49}$$

Quantities that depend only on the slow scale will vanish upon integration round

a closed loop, leaving

$$\begin{aligned}\frac{1}{2}\int_{\partial D}\nabla_{\boldsymbol{X}}c_1\cdot(\nabla_{\boldsymbol{x}}\boldsymbol{s}_0-(\nabla_{\boldsymbol{x}}\boldsymbol{s}_0)^T)\cdot\hat{\boldsymbol{n}}_0 dl_X &= (\partial_{xj}s_{0i}-\partial_{xi}s_{0j})\int_{\partial D_{\boldsymbol{s}_0}}\partial_{Xi}c_1\hat{n}_j dl_X,\\ &= (\partial_{xj}s_{0i}-\partial_{xi}s_{0j})\int_{D_f}\partial_{Xi}\partial_{Xj}c_1 dS_X,\\ &= (\partial_{xj}s_{0i}-\partial_{xj}s_{0i})\int_{D_f}\partial_{Xi}\partial_{Xj}c_1 dS_X,\\ &= 0,\end{aligned} \tag{4.50}$$

where we have applied the divergence theorem to the first line and relabelled dummy indices in the second. Substituting (4.34) into the remaining terms of (4.47), we find

$$\overline{Pe}\,\phi_f\frac{\partial c_0}{\partial t} = -2\pi B\,\overline{Pe}\,Da\,c_0+\nabla_{\boldsymbol{x}}\cdot\int_{D_f}(I_2-\nabla_{\boldsymbol{X}}\boldsymbol{\Lambda})\cdot\nabla_{\boldsymbol{x}}c_0 dS_X+\phi_f\frac{\partial^2 c_0}{\partial z^2}, \tag{4.51}$$

where we have used the fast scale independence of c_0 to evaluate the integral around the string boundary. We introduce the effective diffusion tensor

$$\mathcal{D}_{\text{eff}} = \overline{Pe}^{-1}\begin{pmatrix}\langle I_2-\nabla_{\boldsymbol{X}}\boldsymbol{\Lambda}\rangle_{11} & \langle I_2-\nabla_{\boldsymbol{X}}\boldsymbol{\Lambda}\rangle_{12} & 0\\ \langle I_2-\nabla_{\boldsymbol{X}}\boldsymbol{\Lambda}\rangle_{21} & \langle I_2-\nabla_{\boldsymbol{X}}\boldsymbol{\Lambda}\rangle_{22} & 0\\ 0 & 0 & 1\end{pmatrix}, \tag{4.52}$$

where $I_2=\text{diag}(1,1)$. We have used the average defined in (3.75), which we restate here for convenience

$$\langle g\rangle = \frac{1}{\phi_f}\int_{D_f} g dS_X. \tag{4.53}$$

Hence, we obtain the following homogenised problem:

$$\frac{\partial c_0}{\partial t} = \nabla\cdot(\mathcal{D}_{\text{eff}}\nabla c_0)-\alpha_{\text{eff}}c_0, \tag{4.54}$$

where the effective uptake coefficient is given by

$$\alpha_{\text{eff}} = \frac{2\pi BDa}{\phi_f}, \tag{4.55}$$

and we have written $\nabla=(\partial_x,\partial_y,\partial_z)$. Thus, for $Pe=O(\delta)$, we obtain a reaction diffusion equation on the macroscale. The arrangement of the strings results in an anisotropic effective diffusion tensor (4.52). We will characterise this anisotropy in the next section by considering solutions to the cell problem.

4.4.2.2 Cell problem solution

In this section we look to solve (4.35)-(4.37) which, when averaged, gives the effective diffusion tensor in the macroscale problem. As in section 3.4.4, we can consider the string to be centred at the origin of fast scale coordinates without loss of generality, as shown in figure 3.3. We can exploit symmetries in this equation to simplify the form of the effective diffusion tensor.

Averaging the solutions to (4.35)-(4.37) over the unit cell provides the entries of (4.52). By considering the symmetries of the cell problem, we can deduce the form of the effective diffusion tensor as follows. We consider (4.35)-(4.37) under the transformation $X \to -X$ and $Y \to Y$ to deduce that $\overline{\mathbf{\Lambda}} = \mathbf{\Lambda}(-X, Y)$ must satisfy

$$\nabla^2_{\boldsymbol{X}} \overline{\mathbf{\Lambda}} = \mathbf{0} \quad \text{in} \quad D_f, \tag{4.56}$$

$$n_X \frac{\partial \overline{\Lambda}_1}{\partial X} + n_Y \frac{\partial \overline{\Lambda}_1}{\partial Y} = -n_X \quad \text{on} \quad \partial D_{\boldsymbol{s}_0}, \tag{4.57}$$

$$n_X \frac{\partial \overline{\Lambda}_2}{\partial X} + n_Y \frac{\partial \overline{\Lambda}_2}{\partial Y} = n_Y \quad \text{on} \quad \partial D_{\boldsymbol{s}_0}, \tag{4.58}$$

$$\int_{D_f} \overline{\mathbf{\Lambda}} dS_X = \mathbf{0}, \tag{4.59}$$

with $\mathbf{\Lambda}$ periodic in $\boldsymbol{X}$ and where $\hat{\boldsymbol{n}}_0 = (n_X, n_Y)$ is the leading-order normal to the domain in the original problem for $\mathbf{\Lambda}$. Thus, given that the domain and governing equation are unchanged under this transformation, and we expect $\overline{\mathbf{\Lambda}}$ to satisfy (4.35)-(4.37), we have Λ_1 antisymmetric in X. Performing similar analysis for the transformation $Y \to -Y$, we find that Λ_2 is antisymmetric in Y. In (4.52), we take the gradient of $\mathbf{\Lambda}$ giving diagonal components that are symmetric in (X, Y) and off-diagonal components that are antisymmetric. The average of the antisymmetric components will then be zero due to the symmetry of the domain, leaving a diagonal effective diffusion tensor. By considering the transformation $X \to Y$, we can deduce that the two in-plane components must be equal. Specifically, we introduce $\tilde{\mathbf{\Lambda}} = \tilde{\mathbf{\Lambda}}(X, Y) = \mathbf{\Lambda}(Y, X)$. Then, we have

$$\partial_X \tilde{\mathbf{\Lambda}} = \partial_Y \mathbf{\Lambda} \quad \text{and} \quad \partial_Y \tilde{\mathbf{\Lambda}} = \partial_X \mathbf{\Lambda}. \tag{4.60}$$

We write the normal in the transformed coordinates as $\tilde{\boldsymbol{n}} = (\tilde{n}_X, \tilde{n}_Y) = (n_Y, n_X)$.

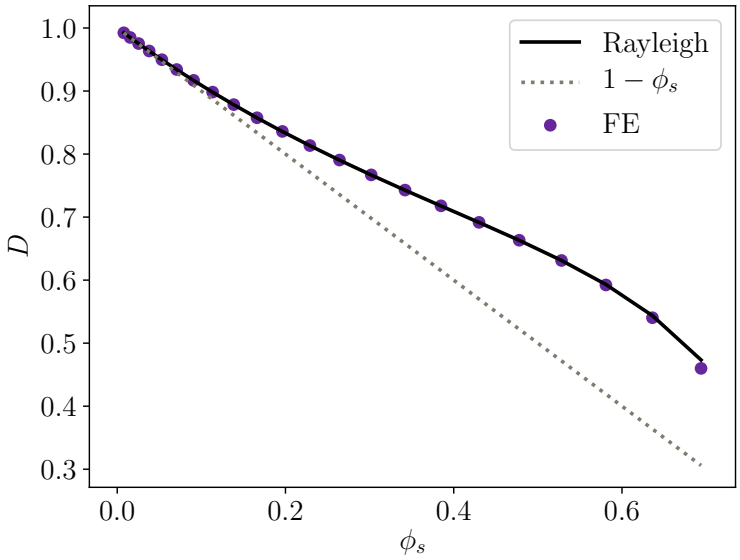

Figure 4.2: *The effective diffusion coefficient decreases with increasing solid fraction. Finite element solutions calculated from the averaged gradient of the solution to* (4.35)-(4.37) *are shown as purple dots and agree with Rayleigh's analytical result [76]. The leading-order asymptotic behaviour in the limit of small solid volume fraction* ϕ_s *is also shown.*

Using (4.35)-(4.37), we deduce

$$\nabla_X^2 \tilde{\mathbf{\Lambda}} = 0 \quad \text{in} \quad D_f, \tag{4.61}$$

$$\tilde{n}_X \frac{\partial \tilde{\Lambda}_1}{\partial X} + \tilde{n}_Y \frac{\partial \tilde{\Lambda}_1}{\partial Y} = \tilde{n}_Y \quad \text{on} \quad D_{\boldsymbol{s}_0}, \tag{4.62}$$

$$\tilde{n}_X \frac{\partial \tilde{\Lambda}_2}{\partial X} + \tilde{n}_Y \frac{\partial \tilde{\Lambda}_2}{\partial Y} = \tilde{n}_X \quad \text{on} \quad D_{\boldsymbol{s}_0}, \tag{4.63}$$

$$\int_{D_f} \tilde{\mathbf{\Lambda}} dS_X = 0. \tag{4.64}$$

Thus, $\tilde{\mathbf{\Lambda}}$ must satisfy

$$\tilde{\Lambda}_2 = \Lambda_1 \quad \text{and} \quad \tilde{\Lambda}_1 = \Lambda_2. \tag{4.65}$$

Combining (4.60) and (4.65), we must have $\partial_X \Lambda_1 = \partial_Y \Lambda_2$, and so the effective diffusion tensor must be of the form $\mathcal{D}_{\text{eff}} = Pe^{-1}\text{diag}(D, D, 1)$.

We determine D by solving (4.35)-(4.37) using the finite element method as described in the appendix B.2.1. The values of D calculated by averaging the finite element solution are shown in figure 4.2. An analytical approximation for the effective diffusion coefficient in a regular array of cylinders with circular cross-section can be calculated using Rayleigh's multipole method [20, 67, 76]. By placing image sources in the cylindrical inclusions to ensure the relevant boundary conditions on the Laplace equation are satisfied, Rayleigh calculated the conductivity by truncating the series solution for the electrical potential [76]. Using this multipole approach to calculate the effective diffusion tensor, [67] obtained the following analytical expression for the effective diffusion coefficient,

$$D = \frac{1}{1-\phi_s}\left(1 - \frac{2\phi_s}{1+\phi_s-0.3058\phi_s^4}\right). \tag{4.66}$$

The finite element solutions agree with (4.66) as shown in figure 4.2. The divergence between the two results at higher solid volume fractions may be due to slow convergence of the series solution as the solid fraction becomes large. We see that the components of the diffusion tensors characterising transport in the transverse plane are less than those for the axial direction; we have faster diffusive transport in the direction parallel to the string as expected given the anisotropy of the fluid-string composite. In the next section, we explore the effects of varying the effective diffusion coefficient on macroscale nutrient transport.

4.4.2.3 Macroscale diffusion-reaction solution

In this section, we solve (4.54), which we restate here for convenience,

$$\frac{\partial c}{\partial t} = \frac{D}{Pe}\nabla_\perp^2 c + \frac{1}{Pe}\frac{\partial^2 c}{\partial z^2} - \alpha_{\text{eff}} c, \tag{4.67}$$

where we have dropped the subscript zeros denoting leading-order quantities. To gain insight into the features of the macroscale model, we consider a simple cylindrical geometry with radius 1/2 and length 1 as illustrated in figure 3.3.a, where the problem admits analytical solutions. We rescale time as $t' = t/Pe$,

$$\frac{\partial c}{\partial t'} = D\nabla_\perp^2 c + \frac{\partial^2 c}{\partial z^2} - Da_2\, c, \tag{4.68}$$

as the problem then reduces to a single parameter problem for the boundary conditions we consider below. We have introduced the modified Damköhler number

$$Da_2 = Pe\,\alpha_{\text{eff}} = \frac{2\pi B\overline{A}L}{\delta\phi_f D}, \tag{4.69}$$

which characterises the relative strength of uptake to diffusive transport combined with the effects of solid fraction. This parameter is a modified form of the second Damköhler number which is the ratio of the reaction rate to the rate of diffusive mass transfer.

Motivated by the bioreactor setup where nutrient media is pumped through the bioreactor chamber, we consider a simplified problem where the nutrient is assumed to enter the base of a cylindrical chamber at a constant concentration

$$c = 1 \quad \text{at} \quad z = 0, \quad 0 \leq r \leq 1/2. \tag{4.70}$$

We assume that there is no nutrient is present initially, corresponding to

$$c = 0 \quad \text{at} \quad t = 0. \tag{4.71}$$

We assume that there is no diffusive flux at the outflow,

$$\frac{\partial c}{\partial z} = 0 \quad \text{at} \quad z = 1, \quad 0 \leq r \leq 1/2 \tag{4.72}$$

and that there is no fluid flux through the curved wall of the cylinder,

$$\frac{\partial c}{\partial r} = 0 \quad \text{on} \quad r = 1/2 \quad \text{for} \quad 0 < z < 1. \tag{4.73}$$

To close the problem, we must have c bounded on the z-axis, that is

$$c = O(1) \quad \text{at} \quad r = 0^+ \quad \text{for} \quad 0 < z < 1. \tag{4.74}$$

As there is symmetry under azimuthal rotation and nothing to force radial variation, we seek a solution to (4.67) that depends only on time and the axial coordinate $c = Z(z)T(t')$. After imposing (4.70)-(4.74), we find

$$c = c_s - \sum_{n=0}^{\infty} b_n \exp\left(-(Da_2 + (n+1/2)^2\pi^2)t'\right) \sin((n+1/2)\pi z), \tag{4.75}$$

where the expansion coefficients are given by

$$b_n = \frac{(2n+1)\pi}{Da_2 + \pi^2(n+1/2)^2} \tag{4.76}$$

At long times, the solution will reach the steady-state

$$c_s = \frac{\cosh(\sqrt{Da_2}(1-z))}{\cosh(\sqrt{Da_2})}. \tag{4.77}$$

Thus, we find the flow velocity scale does not influence the macroscale dynamics, as expected for the regime when advection is subdominant. The dependence of the steady-state (4.77) on Da_2 is illustrated in figure 4.3, where it is apparent that decreasing Da_2 reduces the drop in nutrient concentration as we move away from the inlet.

The time evolution of (4.75) is shown in figure 4.4. The nutrient concentration at all points away from the inlet increases with time until the steady-state is reached. The rate at which the steady-state is approached is governed by α_{eff}, with faster uptake rates reaching steady-state more quickly.

4.4.3 Macroscale uptake

In this section, we consider the regime where $Pe = O(\delta)$ and $Da = O(1/\delta)$, defining $\overline{Pe} = Pe/\delta = O(1)$ and $\widehat{Da} = \delta Da = O(1)$. In this limit, the timescale characterising uptake, t_u is much faster than the timescale characterising microscale advection t_A as $t_u = t_A/Da$. Thus, we introduce a fast timescale $\tau' = t/\delta$ which characterises the system dynamics (the timescale of uptake), as we expect the system will have reached a steady-state on the timescale of microscale advection used to nondimensionalise the problem in previous sections. The rescaled equations we seek to homogenise are

$$\frac{1}{\delta}\frac{\partial c}{\partial \tau'} + \delta \boldsymbol{u}\cdot\nabla c = \frac{1}{\overline{Pe}}\nabla^2 c \tag{4.78}$$

$$\frac{1}{\overline{Pe}}\hat{\boldsymbol{n}}\cdot\nabla c = \widehat{Da}c. \tag{4.79}$$

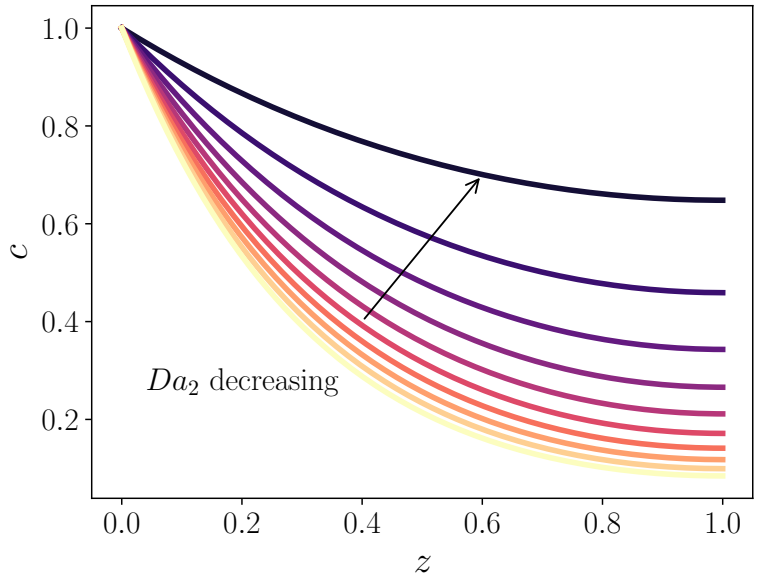

Figure 4.3: *The steady-state nutrient profile in the diffusion-reaction problem given by* (4.67)-(4.74) *is set by a single parameter* Da_2. *Analytical solutions (4.75) are shown for* $Da_2 = 1, 2, 3, 4, 5, 6, 7, 8, 9, 10$.

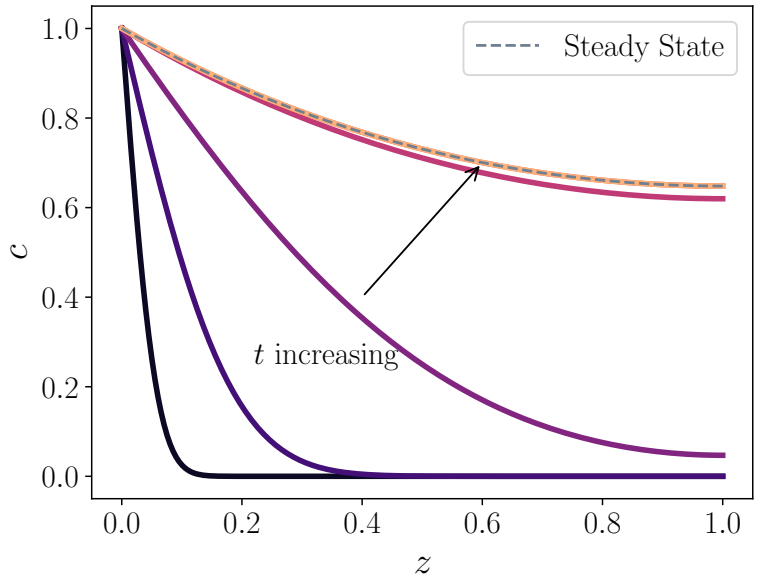

Figure 4.4: *Time evolution of solutions to the diffusion-reaction equations. Solid lines show* (4.75) *evaluated at* $t = 0.01, 0.1, 1, 10, 100$ *with* $Da_2 = 1$ *as the solution evolves to (4.77).*

4.4.3.1 Homogenisation

We write (4.78)-(4.79) in multiple scales form and pose the following multiple scales expansions for the concentration and fluid velocity

$$c \sim c_0(\boldsymbol{x}, \boldsymbol{X}, \tau') + \delta c_1(\boldsymbol{x}, \boldsymbol{X}, \tau') + \cdots, \tag{4.80}$$

$$\boldsymbol{s} \sim \boldsymbol{s}_0(\boldsymbol{x}, \tau') + \delta \boldsymbol{s}_1(\boldsymbol{x}, \boldsymbol{X}, \tau') + \cdots, \tag{4.81}$$

$$\boldsymbol{v} \sim \boldsymbol{v}_0(\boldsymbol{x}, \boldsymbol{X}, \tau') + \delta \boldsymbol{v}_1(\boldsymbol{x}, \boldsymbol{X}, \tau') + \cdots, \tag{4.82}$$

$$w \sim w_0(\boldsymbol{x}, \boldsymbol{X}, \tau') + \delta w_1(\boldsymbol{x}, \boldsymbol{X}, \tau') + \cdots. \tag{4.83}$$

Comparing coefficients of δ, we find at leading-order

$$\nabla^2_{\boldsymbol{X}} c_0 = 0 \quad \text{in} \quad D_f, \tag{4.84}$$

$$\hat{\boldsymbol{n}}_0 \cdot \nabla_{\boldsymbol{X}} c_0 = 0 \quad \text{on} \quad \partial D_{\boldsymbol{s}_0}. \tag{4.85}$$

Thus, at leading-order we have c_0 independent of the fast scale. At $O(\delta)$,

$$\frac{\partial c_0}{\partial \tau'} = \nabla^2_{\boldsymbol{X}} c_1 \quad \text{in} \quad D_f, \tag{4.86}$$

$$\hat{\boldsymbol{n}}_0 \cdot (\nabla_{\boldsymbol{X}} c_1 + \nabla_{\boldsymbol{x}} c_0) = \widehat{Da}\, c_0 \quad \text{on} \quad \partial D_{\boldsymbol{s}_0}. \tag{4.87}$$

We integrate (4.86) over the unit cell, applying the divergence theorem to the left hand side which gives,

$$\int_{D_f} \frac{\partial c_0}{\partial \tau'} dS_X = -\int_{\partial D_{\boldsymbol{s}_0}} \hat{\boldsymbol{n}}_0 \cdot \nabla_{\boldsymbol{X}} c_1 dl_X. \tag{4.88}$$

Substituting (4.87) to eliminate c_1, we find

$$\phi_f \frac{\partial c_0}{\partial \tau'} = \int_{\partial D_{\boldsymbol{s}_0}} \hat{\boldsymbol{n}}_0 \cdot \nabla_{\boldsymbol{x}} c_0 dl_X - \int_{\partial D_{\boldsymbol{s}_0}} \widehat{Da} c_0 dl_X. \tag{4.89}$$

As c_0 is independent of the fast scale, we can evaluate the integrals to obtain the macroscale problem

$$\frac{\partial c_0}{\partial \tau'} = -\frac{2\pi B \widehat{Da}}{\phi_f}\, c_0. \tag{4.90}$$

Thus, for large uptake and small Péclet number, we have concentration which decays exponentially in time. The nutrient is taken up by the cells before it can diffuse or advect on the macroscale.

4.4.4 Macroscale advection-diffusion-reaction

In this section, we consider $Pe = O(1)$ which corresponds to the limit where the macroscale diffusion and advection are in balance. Again, we consider a simplified model of the chamber, treating as a cylinder as shown in figure 3.3. We consider metabolite transport in the fluid-structure problem presented in section 3.5.2.2, where the flow is driven by a time harmonic motion of the string ends

$$\boldsymbol{s} = \boldsymbol{a}(x, y)\sin(\omega t) \quad \text{at} \quad z = 1, \tag{4.91}$$

$$\boldsymbol{s} = \boldsymbol{0} \qquad\quad \text{at} \quad z = 0. \tag{4.92}$$

There is no pressure drop across the chamber and no flux through the sides. We use time-harmonic solutions to the fluid problem found in section 3.5.2.2 and so we do not require an initial condition on the displacement.

4.4.4.1 Multiple timescales

In section 4.3, we nondimensionalised on the timescale of microscale advection $t_A = \delta L/U$. We are interested in capturing the effects of the macroscale diffusion and advection. As we assume $Pe = O(1)$ in this section, macroscale advection and diffusion occur on a comparable timescale which we write as $\tau = \delta t$, *i.e.* a slow timescale. Henceforth, we assume these two timescales are independent, transforming time derivatives into multiple-scales form as follows

$$\frac{\partial}{\partial t} \to \frac{\partial}{\partial t} + \delta\frac{\partial}{\partial \tau}, \tag{4.93}$$

introducing multiple-scales expansions in both space and time

$$c \sim c_0(\boldsymbol{x}, \boldsymbol{X}, t, \tau) + \delta c_1(\boldsymbol{x}, \boldsymbol{X}, t, \tau) + \cdots, \tag{4.94}$$

$$\boldsymbol{s} \sim \boldsymbol{s}_0(\boldsymbol{x}, t, \tau) + \delta \boldsymbol{s}_1(\boldsymbol{x}, \boldsymbol{X}, t, \tau) + \cdots, \tag{4.95}$$

$$\boldsymbol{v} \sim \boldsymbol{v}_0(\boldsymbol{x}, \boldsymbol{X}, t, \tau) + \delta \boldsymbol{v}_1(\boldsymbol{x}, \boldsymbol{X}, t, \tau) + \cdots, \tag{4.96}$$

$$w \sim w_0(\boldsymbol{x}, \boldsymbol{X}, t, \tau) + \delta w_1(\boldsymbol{x}, \boldsymbol{X}, t, \tau) + \cdots. \tag{4.97}$$

As in previous sections, we assume all expansion coefficients are periodic in the fast spatial scale with period $\mathbf{1}$. Motivated by the time-harmonic imposed dis-

placements (4.91), we also assume that the coefficients are periodic in the fast timescale with period $P = 2\pi/\omega$.

4.4.4.2 No-slip for multiple spatio-temporal scales

Before deriving the homogenised problem, we consider the form of the no-slip condition (3.13)-(3.14) on the string boundary when there are multiple-scales in both space and time. Combining the expansion of spatial multiple-scales in (3.39) with multiple time scales given by (4.93), we find

$$\begin{aligned}\boldsymbol{v}_0 + \delta \boldsymbol{X}\cdot\nabla_{\boldsymbol{x}}\boldsymbol{v}_0 + \delta(\boldsymbol{s}_1 + \boldsymbol{X}\cdot\nabla_{\boldsymbol{x}}\boldsymbol{s}_0)\cdot\nabla_{\boldsymbol{X}}\boldsymbol{v}_0 + \delta\boldsymbol{v}_1 = \\ \frac{\partial \boldsymbol{s}_0}{\partial t} + \delta\frac{\partial \boldsymbol{s}_0}{\partial \tau} + \delta\boldsymbol{X}\cdot\nabla_{\boldsymbol{x}}\left(\frac{\partial \boldsymbol{s}_0}{\partial t}\right) + \delta\frac{\partial \boldsymbol{s}_1}{\partial t} + O(\delta^2) \quad \text{on} \quad \partial D_{\boldsymbol{s}_0}.\end{aligned}$$

Thus, at leading-order we have

$$\boldsymbol{v}_0 = \frac{\partial \boldsymbol{s}_0}{\partial t} \quad \text{on} \quad \partial D_{\boldsymbol{s}_0}. \tag{4.98}$$

At next order, we find

$$\boldsymbol{v}_1 = \frac{\partial \boldsymbol{s}_0}{\partial \tau} + \frac{\partial \boldsymbol{s}_1}{\partial t} - \boldsymbol{d}_0\cdot\nabla_{\boldsymbol{X}}\boldsymbol{v}_0 \quad \text{on} \quad \partial D_{\boldsymbol{s}_0}, \tag{4.99}$$

where we have used (3.35). Repeating the process for the axial velocity, we obtain

$$w_0 = w_1 = 0 \quad \text{on} \quad \partial D_{\boldsymbol{s}_0}. \tag{4.100}$$

4.4.4.3 Homogenisation

For this section, we rescale the Damköhler number to $\overline{Da} = Da/\delta$, which we assume is $O(1)$ to ensure that the reaction term features in the leading-order macroscale model. If the Damköhler number is not rescaled, uptake terms would appear at $O(\delta)$ in the microscale problem. Writing the equation governing nutrient concentration (4.13) in multiple-scales form, we find

$$\begin{aligned}\delta\left(\frac{\partial}{\partial t} + \delta\frac{\partial}{\partial \tau}\right)c + \delta\boldsymbol{v}\cdot(\nabla_{\boldsymbol{X}} + \delta\nabla_{\boldsymbol{x}})c + \delta^2 w\frac{\partial c}{\partial z} = \\ \frac{1}{Pe}(\nabla^2_{\boldsymbol{X}} + 2\delta\nabla_{\boldsymbol{x}}\cdot\nabla_{\boldsymbol{X}} + \delta^2\nabla^2_{\boldsymbol{x}})c.\end{aligned} \tag{4.101}$$

We substitute (4.94)-(4.97) into (4.101) and the uptake boundary condition (4.15) before comparing coefficients at each order of δ. At leading-order, we find

$$\nabla^2_{\boldsymbol{X}} c_0 = 0 \quad \text{in} \quad D_f, \tag{4.102}$$

$$\hat{\boldsymbol{n}}_0 \cdot \nabla_{\boldsymbol{X}} c_0 = 0 \quad \text{on} \quad \partial D_{\boldsymbol{s}_0}, \tag{4.103}$$

with c_0 $\mathbf{1}$-periodic in $\boldsymbol{X}$. Hence, we have $c_0 = c_0(\boldsymbol{x}, t, \tau)$. At next order, we have

$$\frac{\partial c_0}{\partial t} - \frac{1}{Pe} \nabla^2_{\boldsymbol{X}} c_1 = 0 \quad \text{in} \quad D_f, \tag{4.104}$$

$$\hat{\boldsymbol{n}}_0 \cdot (\nabla_{\boldsymbol{X}} c_1 + \nabla_{\boldsymbol{x}} c_0) = 0 \quad \text{on} \quad \partial D_{\boldsymbol{s}_0}, \tag{4.105}$$

with c_1 periodic in $\boldsymbol{X}$. Given the spatial fast scale independence of c_0, we can view (4.104)-(4.105) as Poisson's equation with Neumann boundary conditions. The solvability condition is imposed by integrating (4.104) over the domain, which gives

$$\frac{\partial c_0}{\partial t} - \frac{1}{Pe\, \phi_f} \int_{D_f} \nabla^2_{\boldsymbol{X}} c_1 dS_X = 0. \tag{4.106}$$

Applying the divergence theorem to (4.106) and imposing (4.105), we find

$$\frac{\partial c_0}{\partial t} - \frac{1}{Pe\, \phi_f} \int_{\partial D_{\boldsymbol{s}_0}} \nabla_{\boldsymbol{x}} c_0 \cdot \hat{\boldsymbol{n}}_0 dl_X = 0. \tag{4.107}$$

Applying the divergence theorem again, we find the integral evaluates to zero and hence we find the leading-order concentration is independent of the fast timescale *i.e.* $c_0 = c_0(\boldsymbol{x}, \tau)$. In this limit, the microscale nutrient transport is dominated by diffusive processes characterised by the timescale $t = \delta^2 L^2 / D$. As we nondimensionalised on the timescale of microscale advection (see table 4.1), for $Pe = O(1)$, we have the timescale for microscale diffusion being relatively quick as $t_D / t_A = O(\delta)$. Thus, the concentration equilibrates on this faster timescale, leaving a steady microscale problem. We write

$$c_1 = -\boldsymbol{\Lambda} \cdot \nabla_{\boldsymbol{x}} c_0 + \overline{\lambda}, \tag{4.108}$$

where $\overline{\lambda} = \overline{\lambda}(\boldsymbol{x}, t, \tau)$ is a function of the slow scale and time, determined by the solution to a higher order problem. Substituting (4.108) into (4.104)-(4.105), where $\boldsymbol{\Lambda} = \boldsymbol{\Lambda}(\boldsymbol{X})$, we obtain the same cell problem as for the diffusion dominated limit, namely (4.35)-(4.36).

At next order in the multiple-scales analysis, we find

$$\frac{\partial c_1}{\partial t} + \frac{\partial c_0}{\partial \tau} + \boldsymbol{v}_0 \cdot (\nabla_{\boldsymbol{X}} c_1 + \nabla_{\boldsymbol{x}} c_0) + w_0 \frac{\partial c_0}{\partial z} - \frac{1}{Pe} \nabla_{\boldsymbol{X}} \cdot (\nabla_{\boldsymbol{X}} c_2 + \nabla_{\boldsymbol{x}} c_1) - \frac{1}{Pe} \nabla_{\boldsymbol{x}} \cdot (\nabla_{\boldsymbol{X}} c_1 + \nabla_{\boldsymbol{x}} c_0) - \frac{1}{Pe} \frac{\partial^2 c_0}{\partial z^2} = 0 \quad \text{in} \quad D_f, \tag{4.109}$$

subject to the boundary conditions

$$\hat{\boldsymbol{n}}_0 \cdot (\nabla_{\boldsymbol{X}} c_2 + \nabla_{\boldsymbol{x}} c_1) + \hat{\boldsymbol{n}}_1 \cdot (\nabla_{\boldsymbol{X}} c_1 + \nabla_{\boldsymbol{x}} c_0) + \hat{\boldsymbol{n}}_0 \cdot (\boldsymbol{X} \cdot \nabla_{\boldsymbol{x}} (\nabla_{\boldsymbol{X}} c_1 + \nabla_{\boldsymbol{x}} c_0)) + \hat{\boldsymbol{n}}_0 \cdot (\boldsymbol{d}_0 \cdot \nabla_{\boldsymbol{X}} (\nabla_{\boldsymbol{X}} c_1 + \nabla_{\boldsymbol{x}} c_0)) = \overline{Da}\, Pe\, c_0 \quad \text{on} \quad \partial D_{\boldsymbol{s}_0}, \tag{4.110}$$

and c_2 periodic in $\boldsymbol{X}$. We can appeal to the multiple-scales expansion of fluid incompressibility to simplify the analysis, using (3.29) and (3.33), to write

$$\boldsymbol{v}_0 \cdot \nabla_{\boldsymbol{X}} c_1 = \nabla_{\boldsymbol{X}} \cdot (\boldsymbol{v}_0 c_1), \tag{4.111}$$

$$\begin{aligned} \boldsymbol{v}_0 \cdot \nabla_{\boldsymbol{x}} c_0 + w_0 \frac{\partial c_0}{\partial z} &= \nabla_{\boldsymbol{x}} \cdot (c_0 \boldsymbol{v}_0) - c_0 \nabla_{\boldsymbol{x}} \cdot \boldsymbol{v}_0 + \frac{\partial}{\partial z}(c_0 w_0) - c_0 \frac{\partial w_0}{\partial z} \\ &= \nabla_{\boldsymbol{x}} \cdot (c_0 \boldsymbol{v}_0) + \frac{\partial}{\partial z}(c_0 w_0) + \nabla_{\boldsymbol{X}} \cdot (c_0 \boldsymbol{v}_1). \end{aligned} \tag{4.112}$$

To group terms involving the fast and slow divergence, we substitute (4.111)-(4.112) into (4.109) which gives

$$\begin{aligned} &\frac{\partial c_1}{\partial t} + \frac{\partial c_0}{\partial \tau} + \frac{\partial}{\partial z}(c_0 w_0) + \nabla_{\boldsymbol{x}} \cdot \left(\boldsymbol{v}_0 c_0 - \frac{1}{Pe} (\nabla_{\boldsymbol{X}} c_1 + \nabla_{\boldsymbol{x}} c_0) \right) \\ &+ \nabla_{\boldsymbol{X}} \cdot \left(\boldsymbol{v}_0 c_1 + \boldsymbol{v}_1 c_0 - \frac{1}{Pe} (\nabla_{\boldsymbol{X}} c_2 + \nabla_{\boldsymbol{x}} c_1) \right) - \frac{1}{Pe} \frac{\partial^2 c_0}{\partial z^2} = 0. \end{aligned} \tag{4.113}$$

The effective model is derived by integrating (4.113) over the unit cell and applying Reynolds transport theorem to the first two terms, which gives

$$\begin{aligned} &\frac{\partial \langle c_1 \rangle}{\partial t} + \frac{1}{\phi_f} \int_{\partial D_{\boldsymbol{s}_0}} c_1 \frac{\partial \boldsymbol{s}_0}{\partial t} \cdot \hat{\boldsymbol{n}} \, dl_X + \frac{\partial c_0}{\partial \tau} + \frac{1}{\phi_f} \int_{D_f} \frac{\partial}{\partial z}(c_0 w_0) \, dS_X \\ &\quad + \frac{1}{\phi_f} \int_{D_f} \nabla_{\boldsymbol{X}} \cdot \left(\boldsymbol{v}_0 c_1 + \boldsymbol{v}_1 c_0 - \frac{1}{Pe} (\nabla_{\boldsymbol{X}} c_2 + \nabla_{\boldsymbol{x}} c_1) \right) dS_X \\ &\quad + \frac{1}{\phi_f} \int_{D_f} \nabla_{\boldsymbol{x}} \cdot \left(\boldsymbol{v}_0 c_0 - \frac{1}{Pe} (\nabla_{\boldsymbol{X}} c_1 + \nabla_{\boldsymbol{x}} c_0) \right) dS_X - \frac{1}{Pe} \frac{\partial^2 c_0}{\partial z^2} = 0, \end{aligned} \tag{4.114}$$

where we have used the $\boldsymbol{X}$ independence of c_0 and $\boldsymbol{s}_0$ in evaluating the boundary terms involving derivatives with respect to the slow timescale. We apply the

divergence theorem, and substitute (4.110) into the fifth term to eliminate c_2, to find

$$\begin{aligned}\frac{\partial\langle c_1\rangle}{\partial t}+\frac{1}{\phi_f}\int_{\partial D_{\boldsymbol{s}_0}} c_1\frac{\partial \boldsymbol{s}_0}{\partial t}\cdot\hat{\boldsymbol{n}}_0 dl_X+\frac{\partial c_0}{\partial\tau}+\frac{1}{\phi_f}\int_{D_f}\frac{\partial}{\partial z}(c_0w_0)dS_X\\ -\frac{1}{\phi_f}\int_{\partial D_{\boldsymbol{s}_0}}(\boldsymbol{v}_0c_1+\boldsymbol{v}_1c_0)\cdot\hat{\boldsymbol{n}}_0dl_X-\frac{1}{Pe\,\phi_f}\int_{\partial D_{\boldsymbol{s}_0}}(\nabla_{\boldsymbol{X}}c_1+\nabla_{\boldsymbol{x}}c_0)\cdot\hat{\boldsymbol{n}}_1dl_X\\ +\frac{1}{\phi_f}\int_{\partial D_{\boldsymbol{s}_0}}\overline{Da}\,c_0dl_X+\frac{1}{\phi_f}\int_{D_f}\nabla_{\boldsymbol{x}}\cdot\left(\boldsymbol{v}_0c_0-\frac{1}{Pe}(\nabla_{\boldsymbol{X}}c_1+\nabla_{\boldsymbol{x}}c_0)\right)dS_X\\ -\frac{1}{Pe}\frac{\partial^2c_0}{\partial z^2}=0,\end{aligned} \tag{4.115}$$

where we have used (4.44) and (4.46) to evaluate the terms involving $\boldsymbol{d}_0$ and $\boldsymbol{X}$ which result from application of the boundary condition. Using (4.98), we see that the boundary terms involving the leading-order string velocity cancel. We consider

$$\begin{aligned}\int_{\partial D_{\boldsymbol{s}_0}}c_0\boldsymbol{v}_1\cdot\hat{\boldsymbol{n}}_0dl_X&=c_0\int_{\partial D_{\boldsymbol{s}_0}}\left(\frac{\partial\boldsymbol{s}_0}{\partial\tau}+\frac{\partial\boldsymbol{s}_1}{\partial t}-\boldsymbol{d}_0\cdot\nabla_{\boldsymbol{X}}\boldsymbol{v}_0\right)\cdot\hat{\boldsymbol{n}}_0dl_X\\ &=c_0\int_{\partial D_{\boldsymbol{s}_0}}\frac{\partial\boldsymbol{s}_1}{\partial t}\cdot\hat{\boldsymbol{n}}_0dl_X\\ &=-c_0\int_{D_{\boldsymbol{s}_0}}\nabla_{\boldsymbol{x}}\cdot\left(\frac{\partial\boldsymbol{s}_0}{\partial t}\right)dS_X,\end{aligned} \tag{4.116}$$

where we have used the fast scale independence of $\boldsymbol{s}_0$ and (4.99) in the first line, (3.73) in the second line and combined the divergence theorem with the trace of (3.34) in the final line. Both (3.73) and (3.34) hold in the multi-temporal scales analysis as the fluid incompressibility condition and the rigid body condition are unchanged with the introduction of two timescales. Returning to (4.115), we use (4.116) to eliminate $\boldsymbol{v}_1$ and (4.98) to eliminate $\boldsymbol{v}_0$, which gives

$$\begin{aligned}\frac{\partial\langle c_1\rangle}{\partial t}+\frac{\partial c_0}{\partial\tau}+\frac{1}{\phi_f}\int_{D_f}\frac{\partial}{\partial z}(c_0w_0)dS_X+\frac{1}{\phi_f}c_0\int_{D_{\boldsymbol{s}_0}}\nabla_{\boldsymbol{x}}\cdot\left(\frac{\partial\boldsymbol{s}_0}{\partial t}\right)dS_X\\ -\frac{1}{Pe\,\phi_f}\int_{\partial D_{\boldsymbol{s}_0}}(\nabla_{\boldsymbol{X}}c_1+\nabla_{\boldsymbol{x}}c_0)\cdot\hat{\boldsymbol{n}}_1dl_X+\frac{1}{\phi_f}\int_{\partial D_{\boldsymbol{s}_0}}\overline{Da}\,c_0dl_X\\ +\frac{1}{\phi_f}\int_{D_f}\nabla_{\boldsymbol{x}}\cdot\left(\boldsymbol{v}_0c_0-\frac{1}{Pe}(\nabla_{\boldsymbol{X}}c_1+\nabla_{\boldsymbol{x}}c_0)\right)dS_X-\frac{1}{Pe}\frac{\partial^2c_0}{\partial z^2}=0.\end{aligned} \tag{4.117}$$

Applying the Reynolds transport theorem to remove the axial derivatives from inside the integral, we have

$$\begin{aligned}\frac{\partial\langle c_1\rangle}{\partial t}+\frac{\partial c_0}{\partial\tau}+\frac{1}{\phi_f}\frac{\partial}{\partial z}\int_{D_f}c_0w_0dS_X+\frac{1}{\phi_f}c_0\int_{D_{\boldsymbol{s}_0}}\nabla_{\boldsymbol{x}}\cdot\left(\frac{\partial\boldsymbol{s}_0}{\partial t}\right)dS_X\\-\frac{1}{Pe\,\phi_f}\int_{\partial D_{\boldsymbol{s}_0}}(\nabla_{\boldsymbol{X}}c_1+\nabla_{\boldsymbol{x}}c_0)\cdot\hat{\boldsymbol{n}}_1dl_X+\frac{1}{\phi_f}\int_{\partial D_{\boldsymbol{s}_0}}\overline{Da}\,c_0dl_X\\+\frac{1}{\phi_f}\int_{D_f}\nabla_{\boldsymbol{x}}\cdot\left(\boldsymbol{v}_0c_0-\frac{1}{Pe}(\nabla_{\boldsymbol{X}}c_1+\nabla_{\boldsymbol{x}}c_0)\right)dS_X-\frac{1}{Pe}\frac{\partial^2c_0}{\partial z^2}=0,\end{aligned}\tag{4.118}$$

where we have used (4.100). We again use the Reynolds transport theorem to remove the slow transverse derivatives from the integral

$$\begin{aligned}\frac{\partial\langle c_1\rangle}{\partial t}+\frac{\partial c_0}{\partial\tau}+\frac{1}{\phi_f}\frac{\partial}{\partial z}\int_{D_f}c_0w_0dS_X+\frac{1}{\phi_f}c_0\int_{D_{\boldsymbol{s}_0}}\nabla_{\boldsymbol{x}}\cdot\left(\frac{\partial\boldsymbol{s}_0}{\partial t}\right)dS_X\\-\frac{1}{Pe\,\phi_f}\int_{\partial D_{\boldsymbol{s}_0}}(\nabla_{\boldsymbol{X}}c_1+\nabla_{\boldsymbol{x}}c_0)\cdot\hat{\boldsymbol{n}}_1dl_X+\frac{1}{\phi_f}\int_{\partial D_{\boldsymbol{s}_0}}\overline{Da}\,c_0dl_X\\+\frac{1}{\phi_f}\nabla_{\boldsymbol{x}}\cdot\int_{D_f}\left(\boldsymbol{v}_0c_0-\frac{1}{Pe}(\nabla_{\boldsymbol{X}}c_1+\nabla_{\boldsymbol{x}}c_0)\right)dS_X-\frac{1}{Pe}\frac{\partial^2c_0}{\partial z^2}\\+\frac{1}{\phi_f}\int_{\partial D_{\boldsymbol{s}_0}}\left(c_0\frac{\partial\boldsymbol{s}_0}{\partial t}-\frac{1}{Pe}(\nabla_{\boldsymbol{X}}c_1+\nabla_{\boldsymbol{x}}c_0)\right)\cdot(\nabla_{\boldsymbol{x}}\boldsymbol{s}_0)\cdot\hat{\boldsymbol{n}}_0dl_X=0,\end{aligned}\tag{4.119}$$

where we have used (4.98) to eliminate $\boldsymbol{v}_0$ on the boundary. The product of the leading-order string velocity and concentration integrates to zero around the string boundary as these variables depend only on the slow scale. As in section 4.4.2, boundary terms from applying Reynolds transport theorem cancel with those from the normal correction using (4.48)-(4.50) which leaves

$$\begin{aligned}\frac{\partial\langle c_1\rangle}{\partial t}+\frac{\partial c_0}{\partial\tau}+\frac{1}{\phi_f}\nabla\cdot\int_{D_f}c_0\boldsymbol{u}_0dS_X+\frac{c_0}{\phi_f}\int_{D_{\boldsymbol{s}_0}}\nabla_{\boldsymbol{x}}\cdot\left(\frac{\partial\boldsymbol{s}_0}{\partial t}\right)dS_X\\+\frac{1}{\phi_f}\int_{\partial D_{\boldsymbol{s}_0}}\overline{Da}\,c_0dl_X-\frac{1}{Pe\,\phi_f}\nabla_{\boldsymbol{x}}\cdot\int_{D_f}(\nabla_{\boldsymbol{X}}c_1+\nabla_{\boldsymbol{x}}c_0)dS_X-\frac{1}{Pe}\frac{\partial^2c_0}{\partial z^2}=0,\end{aligned}\tag{4.120}$$

where we have grouped the velocity components, using $\nabla=(\partial_x,\partial_y,\partial_z)$. We

substitute for c_1 in the volume integral, using (4.108), to obtain

$$\frac{\partial\langle c_1\rangle}{\partial t}+\frac{\partial c_0}{\partial\tau}+\frac{1}{\phi_f}\nabla\cdot\int_{D_f}c_0\boldsymbol{u}_0 dS_X+\frac{c_0}{\phi_f}\int_{D_{\boldsymbol{s}_0}}\nabla_{\boldsymbol{x}}\cdot\left(\frac{\partial\boldsymbol{s}_0}{\partial t}\right)dS_X$$
$$+\frac{1}{\phi_f}\int_{\partial D_{\boldsymbol{s}_0}}\overline{Da}\,c_0\,dl_X-\frac{1}{Pe\,\phi_f}\nabla_{\boldsymbol{x}}\cdot\int_{D_f}(I-\nabla_{\boldsymbol{X}}\boldsymbol{\Lambda})\cdot\nabla_{\boldsymbol{x}}c_0\,dS_X-\frac{1}{Pe}\frac{\partial^2 c_0}{\partial z^2}=0, \tag{4.121}$$

We can now evaluate the integrals over the string interior and string boundary which are independent of the fast scale

$$\frac{\partial\langle c_1\rangle}{\partial t}+\frac{\partial c_0}{\partial\tau}+\nabla\cdot(c_0\langle\boldsymbol{u}_0\rangle)+\frac{\phi_s}{\phi_f}\nabla_{\boldsymbol{x}}\cdot\left(\frac{\partial\boldsymbol{s}_0}{\partial t}\right)+\alpha_{\text{eff}}c_0-\nabla\cdot(\mathcal{D}_{\text{eff}}\nabla c_0)=0, \tag{4.122}$$

where we have introduced the effective uptake

$$\alpha_{\text{eff}}=\frac{2\pi B\overline{Da}}{\phi_f}, \tag{4.123}$$

and the effective diffusion coefficient $\mathcal{D}_{\text{eff}}$ which is given by (4.52).

In (4.122) we have obtained an equation that depends on both the fast and slow timescale. Our aim is to derive an averaged equation which describes the diffusion and advection of the leading-order concentration over the whole scaffold. To achieve this, we must average over the period of fast oscillation as is typical in multiple scales problems. We define the average over the fast timescale as

$$\overline{g}=\frac{1}{P}\int_0^P g\,dt, \tag{4.124}$$

where $P=2\pi/\omega$ is the period characterising the fast oscillation. Averaging (4.122) over the fast timescale, we obtain the homogenised problem

$$\frac{\partial c_0}{\partial\tau}+\nabla\cdot(c_0\langle\overline{\boldsymbol{u}_0}\rangle)-\nabla\cdot(\mathcal{D}_{\text{eff}}\nabla c_0)+\alpha_{\text{eff}}c_0=0, \tag{4.125}$$

where we have used periodicity of the coefficients on the fast timescale. We have also used the time average (4.124) of (3.76) which gives $\nabla\cdot\langle\boldsymbol{u}_0\rangle=0$. Thus, on the macroscale, we find the nutrient concentration is governed by an advection-diffusion-reaction equation. The nutrient is advected with velocity $\langle\overline{\boldsymbol{u}}_0\rangle$ meaning that the time harmonic string motions considered in section 3.5.2.2 do not cause advection of the nutrient across the whole domain, only local transport within a given unit cell.

4.4.4.4 Macroscale advection-diffusion-reaction solution

We seek solutions to (4.125) in the cylindrical geometry shown in figure 3.3.a with radius 1/2 and length 1.

Uniform Pressure Drop

We consider the flow field $\langle\overline{\boldsymbol{u}_0}\rangle = (0, 0, \kappa_3 p_{in})$ obtained in section 3.5.2.4 that results from imposing a pressure drop across the cylinder. Substituting this velocity into (4.125), we find

$$\frac{\partial c}{\partial \tau} = -\alpha_{\text{eff}} c + \nabla \cdot (\mathcal{D}_{\text{eff}} \nabla c) - \kappa_3 p_{in} \frac{\partial c}{\partial z}, \tag{4.126}$$

where we have dropped zeros denoting leading-order quantities. We solve (4.126) with the following boundary and initial conditions corresponding to an inlet flux of nutrient at the base

$$c = 1 \quad \text{at} \quad z = 0, \quad 0 \leq r \leq 1/2, \tag{4.127}$$

and no nutrient present initially

$$c = 0 \quad \text{at} \quad t = 0. \tag{4.128}$$

We assume that there is no diffusive flux at the outflow,

$$\frac{\partial c}{\partial z} = 0 \quad \text{at} \quad z = 1, \quad 0 \leq r \leq 1/2, \tag{4.129}$$

no flux through the curved wall of the cylinder,

$$\frac{\partial c}{\partial r} = 0 \quad \text{on} \quad r = 1/2 \quad \text{for} \quad 0 < z < 1. \tag{4.130}$$

with c bounded on the z-axis,

$$c = O(1) \quad \text{at} \quad r = 0^+ \quad \text{for} \quad 0 < z < 1. \tag{4.131}$$

As in section 4.4.2.3, rescaling time enables us to reduce the number of parameters in the problem. We introduce $\tau = \tau' Pe$ to rescale time in (4.126) which gives

$$\frac{\partial c}{\partial \tau'} = -Da_2\, c + D\nabla_\perp^2 c + \frac{\partial^2 c}{\partial z^2} - \nu \frac{\partial c}{\partial z}, \tag{4.132}$$

where $\nu = Pe\,\kappa_3\,p_{in}$ and Da_2 is given by (4.69).

Thanks to the linearity of (4.132), we can use the following decomposition

$$c = c_e + c_h, \tag{4.133}$$

where c_e satisfies the steady problem with inhomogeneous boundary conditions and c_h satisfies the initial condition and (4.132) with homogeneous boundary conditions. Using separation of variables, we obtain the following solution

$$c = c_e + \sum_{n=0}^{\infty} B_n \exp\left(\nu z/2 - A_n \tau'\right) \sin(m_2^n z), \tag{4.134}$$

where the steady solution is given by

$$c_e = \frac{\exp(\nu z/2)\cosh(m_1(z-1)-\phi_1)}{\cosh(m_1+\phi_1)}. \tag{4.135}$$

We have

$$m_2 = \frac{\sqrt{4(A-Da_2)-\nu^2}}{2}, \tag{4.136}$$

where the separation constant A is fixed by imposing the boundary condition at the top of the chamber, which requires m_2 to satisfy

$$\tan m_2 + \frac{2m_2}{\nu} = 0. \tag{4.137}$$

We denote the ordered roots of (4.137) as m_2^n and the corresponding value of the separation constant as A_n. Imposing the initial condition (4.128) fixes B_n,

$$B_n = -\frac{\int_0^1 \frac{\exp(\nu z/2)\cosh\left(m_1(z-1)-\phi_1\right)\sin(m_2^n z)}{\cosh\left(m_1+\phi_1\right)}\,dz}{\int_0^1 \sin^2(m_2^n z)\,dz}, \tag{4.138}$$

where

$$m_1 = \frac{\nu}{2}\sqrt{1+\frac{4Da_2}{\nu^2}}, \tag{4.139}$$

$$\phi_1 = \operatorname{arctanh}\left(\frac{1}{\sqrt{1+\frac{4Da_2}{\nu^2}}}\right). \tag{4.140}$$

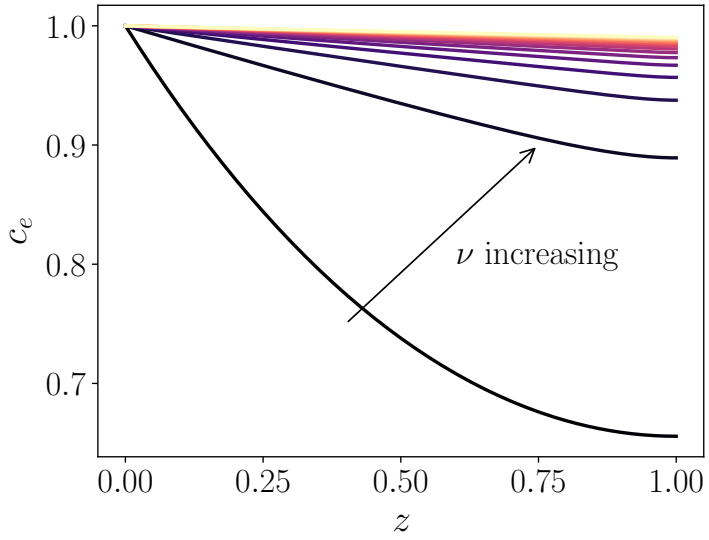

Figure 4.5: *Steady-state solutions to the advection-diffusion-reaction equation (4.135) are shown for 15 linearly spaced values of* $\nu \in [0.1, 100]$, $Da_2 = 1$

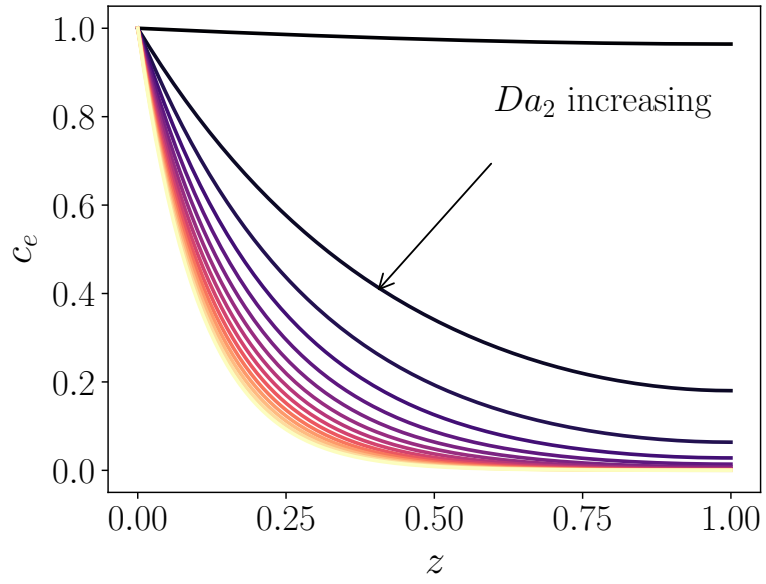

Figure 4.6: *Steady-state solutions (4.135) are shown for 50 linearly spaced values of* $Da_2 \in [0.1, 100]$, $\nu = 1$

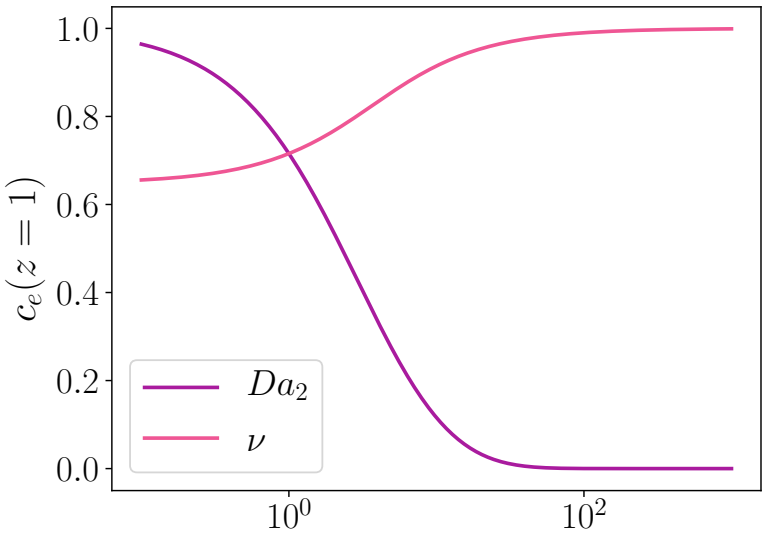

Figure 4.7: *Parameter dependence of the outlet concentration. The steady solution to the advection-diffusion-reaction equation (4.135) are plotted, varying one parameter along each curve. The parameter which is not varying along a curve is set to 1.*

The parameter dependence of the steady solution is shown in figures 4.5-4.7. We find that increasing ν increases the total nutrient in the chamber at steady-state and decreases the rate of drop off as we move away from the inlet (figure 4.5). Increasing ν can be attained by increasing the inlet pressure whilst holding the Péclet number and permeability fixed, which has the effects of increasing increasing the rate of supply of nutrient to the scaffold. Increasing Da_2 increases the relative strength of the uptake term in this example, resulting in a lower overall nutrient concentration and faster rate of decay in concentration at the inlet as shown in figure 4.6. The effect of tuning these parameters is shown in figure 4.7, where the outlet concentration is shown for varying parameter values. Increasing Da_2 decreases the outlet concentration at steady state, as can be achieved by increasing the uptake whilst keeping the Péclet number fixed. Conversely, increasing ν increases the outlet concentration in the chamber as would be expected for an increased flow rate through the chamber. The solution we obtain here is more complex than the diffusion dominated case considered in section 4.4.2.3; we learn from (4.134) that the decay rate to steady-state is determined by ν as well as Da_2.

Flux driven motion

In this section, we consider nutrient transport when fluid flow is driven by a radially varying flux imposed at the chamber base, as solved in section 3.5.2.5. The fluid velocity in this case is steady, and given by

$$\langle \overline{\boldsymbol{u}}_0 \rangle = \kappa_1 \sum_{l=1}^{\infty} d_l J_0'(\beta_l r) \hat{f}_l^{(2)} \hat{\boldsymbol{e}}_r + \kappa_3 \left[\frac{1}{8} + \sum_{l=1}^{\infty} d_l J_0(\beta_l r) \hat{f}_l^{(3)} \right] \hat{\boldsymbol{e}}_z, \tag{4.141}$$

where κ_1, κ_3 are the transverse and axial permeabilities, β_l is the lth largest positive root of $J_0'(\beta/2) = 0$, $\hat{f}_l = \hat{f}_l(z)$ is given by (3.195) and

$$d_l = -\frac{40 J_2(\beta_l/2)}{J_0(\beta_l/2)^2 + J_1(\beta_l/2)^2}. \tag{4.142}$$

We can no longer solve (4.125) with a separable solution and so we obtain solutions numerically using the finite element method. Details of the method as applied to this problem are given in appendix B.2.2. The steady-state distribution of the nutrient concentration in a radial slice of the chamber is plotted in figure 4.8 for different values of the effective absorption coefficient and Péclet number. Increasing the Péclet number for fixed absorption coefficient is tantamount to decreasing the size of the diffusion coefficient. For smaller diffusion coefficients, the nutrient distribution mirrors the fluid flow more closely, as the nutrient cannot diffuse as strongly from the streamlines. Increasing the effective absorption coefficient for fixed Péclet number causes a drop in nutrient concentration at the upper end of the chamber as shown in figure 4.8; for an increased absorption rate, the nutrient is absorbed by cells closer to the inlet.

4.4.5 Macroscale advection-reaction

In this section, we identify the form of the homogenised problem in the limit where advection is strong, assuming $\widehat{Pe} = \delta Pe = O(1)$. We also rescale the Damköhler number so that uptake terms appear at $O(\delta)$, assuming $\overline{Da} = Da/\delta = O(1)$. As in section 4.4.4, we introduce a slow scale $\tau = \delta t$ which characterises advection on the macroscale. We seek multiple-scales expansions in both space and time

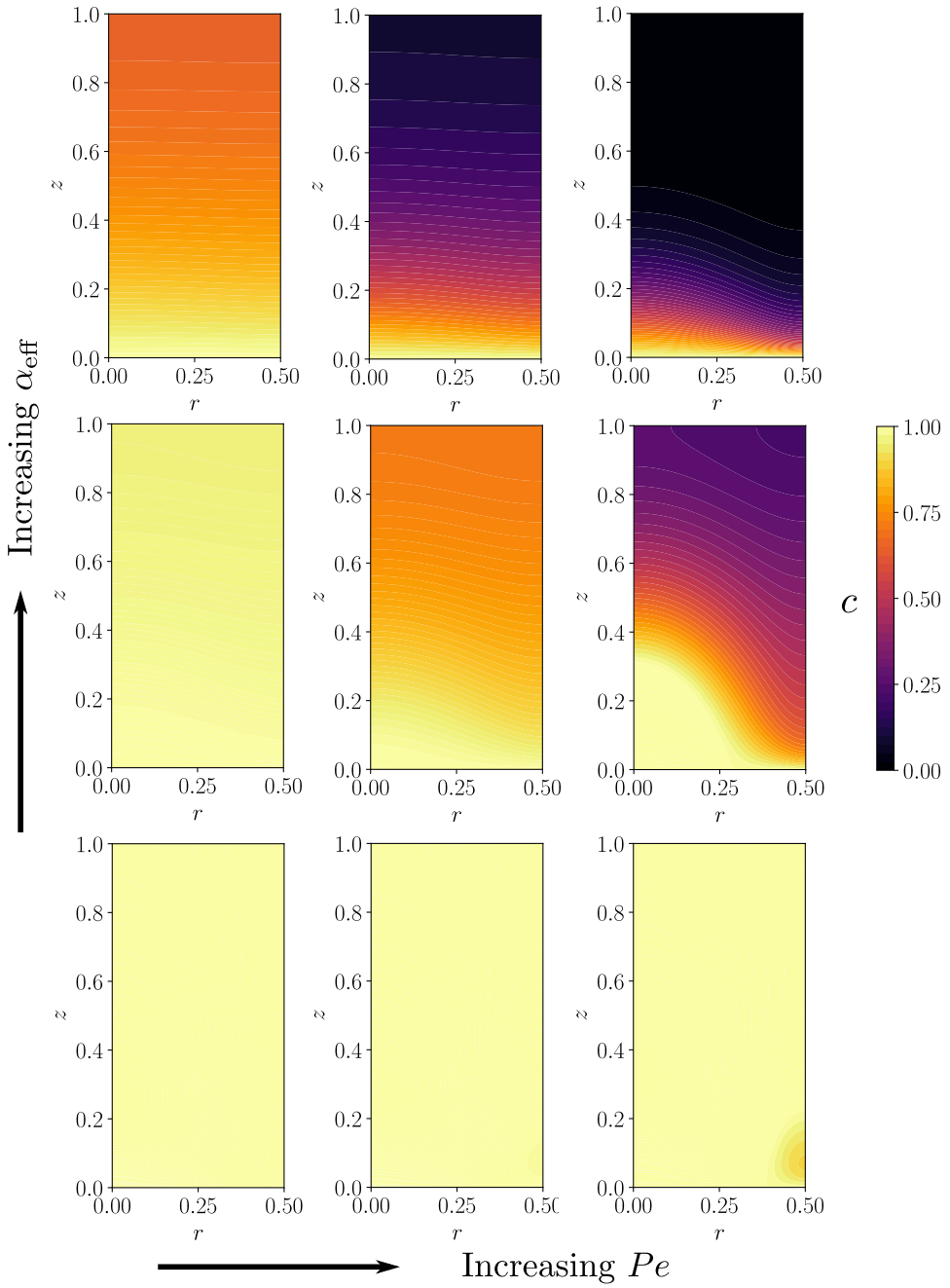

Figure 4.8: *Steady-state concentration for the flux-driven advection-diffusion-reaction macroscale problem given by the numerical solution to* (4.125) *subject to* (4.127)-(4.131) *are given for* $\phi_s = 0.2$ *and solved for* $\alpha_{\text{eff}} = 0.1, 1, 10$ *and* $Pe = 0.1, 1, 10$.

(4.94)-(4.97). Comparing coefficients at leading-order, we find

$$\frac{\partial c_0}{\partial t} + \boldsymbol{v}_0 \cdot \nabla_{\boldsymbol{X}} c_0 - \frac{1}{\widehat{Pe}} \nabla^2_{\boldsymbol{X}} c_0 = 0 \quad \text{in} \quad D_f, \tag{4.143}$$

$$\hat{\boldsymbol{n}}_0 \cdot \nabla_{\boldsymbol{X}} c_0 = 0 \quad \text{on} \quad \partial D_{\boldsymbol{s}_0}, \tag{4.144}$$

with c_0 periodic in $\boldsymbol{X}$. Thus, we conclude that c_0 is independent of the fast temporal and spatial scales as $c_0 = c_0(\boldsymbol{x}, t, \tau)$ satisfies (4.143)-(4.144). At next order, we find

$$\frac{\partial c_0}{\partial \tau} + \frac{\partial c_1}{\partial t} + \boldsymbol{v}_0 \cdot (\nabla_{\boldsymbol{X}} c_1 + \nabla_{\boldsymbol{x}} c_0) + w_0 \frac{\partial c_0}{\partial z} - \frac{1}{\widehat{Pe}} \nabla^2_{\boldsymbol{X}} c_1 = 0 \quad \text{in} \quad D_f, \tag{4.145}$$

$$\hat{\boldsymbol{n}}_0 \cdot (\nabla_{\boldsymbol{X}} c_1 + \nabla_{\boldsymbol{x}} c_0) = \widehat{\overline{Da}\,Pe} c_0 \quad \text{on} \quad \partial D_{\boldsymbol{s}_0}, \tag{4.146}$$

with c_1 periodic in $\boldsymbol{X}$. Using (4.111)-(4.112) and integrating (4.145) over the unit cell, we find

$$\begin{aligned} &\phi_f \frac{\partial c_0}{\partial \tau} + \int_{D_f} \frac{\partial c_1}{\partial t} dS_X + \int_{D_f} \nabla_{\boldsymbol{X}} \cdot (c_1 \boldsymbol{v}_0 + c_0 \boldsymbol{v}_1) dS_X \\ &\quad + \int_{D_f} \nabla_{\boldsymbol{x}} \cdot (c_0 \boldsymbol{v}_0) dS_X + \int_{D_f} \frac{\partial}{\partial z}(c_0 w_0) dS_X - \frac{1}{\widehat{Pe}} \int_{D_f} \nabla^2_{\boldsymbol{X}} c_1 dS_X = 0. \end{aligned} \tag{4.147}$$

We apply the Reynolds transport theorem to remove the fast time derivatives and apply the divergence theorem to the second integral, which gives

$$\begin{aligned} &\phi_f \frac{\partial c_0}{\partial \tau} + \frac{\partial}{\partial t} \int_{D_f} c_1 dS_X + \int_{\partial D_{\boldsymbol{s}_0}} c_1 \frac{\partial \boldsymbol{s_0}}{\partial t} \cdot \hat{\boldsymbol{n}}_0 dl_X \\ &- \int_{\partial D_{\boldsymbol{s}_0}} \left(c_1 \frac{\partial \boldsymbol{s}_0}{\partial t} + c_0 \left(\frac{\partial \boldsymbol{s}_0}{\partial \tau} + \frac{\partial \boldsymbol{s}_1}{\partial t} - \boldsymbol{d}_0 \cdot \nabla_{\boldsymbol{X}} \boldsymbol{v}_0 \right) \right) \cdot \hat{\boldsymbol{n}}_0 dl_X \\ &\quad + \int_{D_f} \nabla_{\boldsymbol{x}} \cdot (c_0 \boldsymbol{v}_0) dS_X + \int_{D_f} \frac{\partial}{\partial z}(c_0 w_0) dS_X - \frac{1}{\widehat{Pe}} \int_{D_f} \nabla^2_{\boldsymbol{X}} c_1 dS_X = 0, \end{aligned} \tag{4.148}$$

where we have used the no-slip conditions (4.98)-(4.100). The boundary terms involving the product of c_1 and the leading-order string velocity cancel. Using the fast scale independence of $\boldsymbol{s}_0$ and (4.116), the only boundary term remaining is the product of the first-order string velocity with the leading-order concentration. We use the Reynolds transport theorem to remove the slow spatial derivatives from the integrals

$$\begin{aligned} &\phi_f \frac{\partial c_0}{\partial \tau} + \frac{\partial}{\partial t} \int_{D_f} c_1 dS_X - \int_{\partial D_{\boldsymbol{s}_0}} c_0 \frac{\partial \boldsymbol{s}_1}{\partial t} \cdot \hat{\boldsymbol{n}}_0 dl_X \\ &\quad + \nabla_{\boldsymbol{x}} \cdot \int_{D_f} c_0 \boldsymbol{v}_0 dS_X + \frac{\partial}{\partial z} \int_{D_f} c_0 w_0 dS_X - \frac{1}{\widehat{Pe}} \int_{D_f} \nabla^2_{\boldsymbol{X}} c_1 dS_X = 0, \end{aligned} \tag{4.149}$$

where the contribution of the boundary terms evaluates to zero due to the fast scale independence of $\boldsymbol{s}_0$ and c_0. We apply the divergence theorem to the final integral and substitute (4.146) to eliminate c_1 in the resulting term, which gives

$$\begin{aligned}\phi_f \frac{\partial c_0}{\partial \tau} + \frac{\partial}{\partial t}\int_{D_f} c_1 dS_X - \int_{\partial D_{\boldsymbol{s}_0}} c_0 \frac{\partial \boldsymbol{s}_1}{\partial t}\cdot \hat{\boldsymbol{n}}_0 dl_X \\ + \nabla_{\boldsymbol{x}} \cdot \int_{D_f} c_0 \boldsymbol{v}_0 dS_X + \frac{\partial}{\partial z}\int_{D_f} c_0 w_0 dS_X + \int_{\partial D_{\boldsymbol{s}_0}} Da\, c_0\, dl_X = 0,\end{aligned} \tag{4.150}$$

We use the divergence theorem to take the boundary integral of the string velocity into its interior and use (3.34) to eliminate $\boldsymbol{s}_1$,

$$\begin{aligned}\phi_f \frac{\partial c_0}{\partial \tau} + \frac{\partial}{\partial t}\int_{D_f} c_1 dS_X + c_0 \int_{D_{\boldsymbol{s}_0}} \nabla_{\boldsymbol{x}} \cdot \left(\frac{\partial \boldsymbol{s}_0}{\partial t}\right)\cdot \hat{\boldsymbol{n}}_0 dl_X \\ + \nabla_{\boldsymbol{x}} \cdot \int_{D_f} c_0 \boldsymbol{v}_0 dS_X + \frac{\partial}{\partial z}\int_{D_f} c_0 w_0 dS_X + \int_{\partial D_{\boldsymbol{s}_0}} Da\, c_0\, dl_X = 0.\end{aligned} \tag{4.151}$$

We can now evaluate the remaining integrals to give

$$\frac{\partial c_0}{\partial \tau} + \frac{\partial \langle c_1\rangle}{\partial t} + c_0 \frac{\phi_s}{\phi_f}\nabla_{\boldsymbol{x}} \cdot \left(\frac{\partial \boldsymbol{s}_0}{\partial t}\right) + \nabla \cdot (c_0 \langle \boldsymbol{u}_0\rangle) + \alpha_{\text{eff}} c_0 = 0, \tag{4.152}$$

where α_{eff} is given by (4.55). Averaging over the fast timescale and using the time-periodicity of the coefficients, we obtain the following homogenised model,

$$\frac{\partial c}{\partial \tau} + \nabla \cdot (c\langle \overline{\boldsymbol{u}}\rangle) = -\alpha_{\text{eff}} c, \tag{4.153}$$

where

$$\alpha_{\text{eff}} = \frac{2\pi B \overline{Da}}{\phi_f} \tag{4.154}$$

and we have dropped zeros denoting the leading-order quantities. Thus, we see that when advection is strong, nutrient is carried along streamlines of the time-averaged flow, with the concentration decaying along streamlines according to the uptake rate. We note that this homogenised model can be obtained more directly as a sublimit of the model considered in section 4.4.4, taking $Pe \to \infty$. This limit means that the diffusive terms no longer appear in (4.125) and so we no longer need to solve the microscale problem to obtain the effective diffusion tensor.

4.4.5.1 Macroscale advection-reaction solution

We illustrate the solution method by considering the simple example of fluid flow driven by a pressure drop across a cylinder of radius 1/2 and length 1 as shown in figure 3.3.a, and discussed in section 3.5.2.4. Imposing an axial pressure drop p_{in} results in the flow field $\langle \overline{\boldsymbol{u}} \rangle = (0, 0, \kappa_3 p_{in})$. For this flow, (4.153) reduces to the following partial differential equation

$$\frac{\partial c}{\partial \tau} + \kappa_3 p_{in} \frac{\partial c}{\partial z} = -\alpha_{\text{eff}} c. \tag{4.155}$$

We suppose the concentration at the inlet is known and that there is initially no metabolite in the chamber, with

$$c = 1 \quad \text{on} \quad z = 0, \tag{4.156}$$

$$c = 0 \quad \text{at} \quad t = 0, \tag{4.157}$$

which provides the necessary initial data for the problem. We use the method of characteristics to obtain

$$c = \begin{cases} 0, & z - \kappa_3 p_{in} \tau > 0 \\ \exp\left(\frac{-\alpha_{\text{eff}} z}{\kappa_3 p_{in}}\right), & z - \kappa_3 p_{in} \tau < 0. \end{cases} \tag{4.158}$$

As for the diffusion-reaction and advection-diffusion-reaction regimes, the rate of decay of nutrient concentration as we move away from the inlet increases with increasing absorption rate. Like the diffusion-advection-reaction case, we find that increasing the pressure drop, which in turn causes higher flow rates, results in a higher concentration at the outlet as there is a higher amount of nutrient supplied to the chamber.

Having established the form of the effective equations describing nutrient transport in different parameter regimes, we turn to the bioreactor system to identify the relevant model.

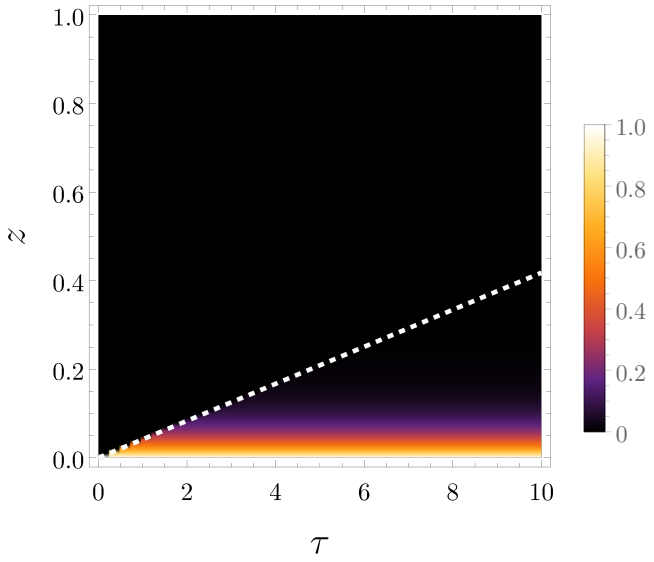

Figure 4.9: *The time evolution of concentration in the advection-reaction regime. Plot of* (4.158) *with* $p_{in} = 1$, $\alpha_{eff} = 1$, $\kappa_3 = 0.0418$, *which corresponds to* $\phi_s = 0.2$. *The dashed, white line* $z - \kappa_3 p_{in} \tau = 0$ *bounds the region of influence.*

4.5 The humanoid robotic bioreactor

In the humanoid robotic bioreactor, media is pumped through the chamber at a constant flow rate to deliver nutrient to the growing cells. The levels of glucose, lactate and oxygen are monitored in the outflow from the chamber. Glucose and oxygen are present in the nutrient media entering the chamber at known concentration. Lactate is present at trace levels in the original media but is produced at a yield of 2 from glucose by the tendon cells *via* the anaerobic glycolysis pathway (reaction 4.2).

4.5.1 Experimental parameters

We can use experimental parameters to estimate the size of the absorption coefficient and Péclet number which appear in the model nondimensionalisation in section 4.3. Typical experimental parameters are given in appendix A, which are

used to obtain the following estimates for model parameters:

$$Da_o = \frac{\overline{A}_o}{U} = 30000, \quad Da_g = \frac{\overline{A}_g}{U} = 600, \quad Da_l = 2Da_g = 1200, \tag{4.159}$$

$$Pe_o = \frac{UL}{D_o} = 150, \quad Pe_g = \frac{UL}{D_g} = 500, \quad Pe_l = \frac{UL}{D_l} = 500, \tag{4.160}$$

where Da_i and Pe_i denote the Damköhler number and Péclet number for the ith species respectively. Thus, for the $N = 200$ fibres in the bioreactor which gives $\delta = 1/\sqrt{200} = 0.07$, we have

$$Da_o = O(\delta^{-4}), \quad Da_g = O(\delta^{-2}), \quad Da_l = O(\delta^{-3}), \tag{4.161}$$

$$Pe_o = O(\delta^{-2}), \quad Pe_g = O(\delta^{-2}), \quad Pe_l = O(\delta^{-2}). \tag{4.162}$$

In the next section, we comment on the regime relevant to the bioreactor system.

4.5.2 Mathematical model

For the Péclet and Damköhler numbers listed in (4.161)-(4.162), we obtain the following equations at leading-order in the multiple-scales analysis

$$\frac{\partial c_0}{\partial t} + \boldsymbol{v}_0 \cdot \nabla_{\boldsymbol{X}} c_0 = 0, \tag{4.163}$$

$$c_0 = 0 \quad \text{at} \quad t = 0. \tag{4.164}$$

Since $\boldsymbol{v}_0$ is the transverse component of the fluid velocity, equations (4.163)-(4.164) have the solution $c_0 = 0$ meaning that we are unable to satisfy the macroscale boundary conditions at the inlet (4.16). A boundary layer where there are large gradients in nutrient concentration must then be present to satisfy the inlet boundary condition. To characterise the nutrient concentrations in this boundary layer, matched asymptotics could be explored, building on the studies of [77]. Physically, this corresponds to uptake being so strong that all the nutrient in the inlet feed of media is absorbed by cells in the boundary layer, preventing any nutrient from reaching the scaffold bulk. Clearly, this would be a sub-optimal operating regime for the bioreactor, as without sufficient nutrient supply the cells in the scaffold centre would die. The Damköhler numbers (4.159) which underpin this

prediction seem large. The calculation of these parameter values was based upon maximal nutrient consumption rates presented in [93] which may exceed typical values observed in bioreactor operation. Exploring this assumption could be a focus of future work.

It would be beneficial to operate the bioreactor in the advection regime. In this regime nutrients are supplied cell along streamlines of the flow, as uptake becomes a subdominant effect. For cases such as the pressure-driven flow considered in section 3.5.2.4, where the solution has a constant axial velocity, this would result in uniform nutrient delivery across the scaffold. Given the Péclet number increases with increasing characteristic velocity scale and the Damköhler number decreases with increasing velocity scale, attaining this regime cannot be obtained by tuning the velocity scale alone; increasing the velocity scale does not change the relative size of terms in the uptake boundary condition. As the diffusion coefficient and uptake rate of species are harder to control experimentally, the characteristic length scale becomes a significant factor in determining whether reaction terms are present in the leading-order macroscale model. Increasing the flow rate not only influences the rate of nutrient delivery but also the fluid-induced shear stress. In future work, it would be beneficial to combine the modelling of nutrient transport and fluid flow to identify regimes that provide suitable mechanical forcing as well as sufficient nutrient delivery.

4.6 Discussion

In this chapter, we have presented the homogenisation of nutrient transport equations in fluid-fibre media. We have identified four distinguished limits informed by considering the various balances between the timescales which characterise uptake, advection and diffusion on both the macroscale and microscale. A summary of the different macroscale models obtained is given in figure 4.10. If the uptake is reduced by an order of magnitude, the reaction term will not appear in the homogenised equations. Hence, the diffusion regime and advection regime in figure 4.10 can be obtained as sublimits of the analysis we presented in section 4.4.2 and 4.4.5 respectively. We have also not presented the analysis for the uptake regime

in figure 4.10 obtained when $Pe = O(1)$ and $Da = O(1)$. In this limit, a diffusion equation is obtained at leading-order. At first order, the reaction term appears in the uptake boundary condition which leads to the same macroscale model obtained in section 4.4.3. If uptake is increase by an order of magnitude, it will appear in the lower order microscale problem. It is difficult to obtain a macroscale model using homogenisation alone in the greyed region in the figure 4.10; in this regime, a diffusion-reaction or advection-diffusion-reaction is obtained as the leading-order microscale problem. This may mean that additional techniques need to be employed, for example matched asymptotics, to characterise the transport behaviour.

To obtain these macroscale equations, it was necessary to identify the correct way to write Neumann conditions on a moving boundary in multiple-scales form. To do this, we used a level set function to define the boundary and expanded about a fixed position in the slow coordinate in a similar method to dealing with integral constraints [20, 25]. Multiple timescales were required in the case where macroscale advection balances diffusion, reflecting the separation between timescales characterising the string velocity and macroscale transport. The model derivation presented here could be modified to treat transport in fibrous beds, with applications such as cilia dynamics, by changing the solid model from a string to an elastic beam.

For each macroscale model, we presented analytical solutions for simple geometries with boundary conditions mimicking perfusion of nutrient through the bioreactor chamber. When diffusive processes dominate on the macroscale, we found a single parameter - the product of the effective absorption and the Péclet number - determined the steady-state distribution of nutrient. Increasing this parameter increased the rate of spatial decay of nutrient concentration at greater distances from the inlet, and resulted in a lower concentration at the outlet. Similar behaviour was observed for macroscale advection-diffusion-reaction, although the effects of varying the Péclet number and absorption rate are not identical in this regime. When advection dominates at the macroscale, nutrient is carried along streamlines of the averaged flow field, decaying at a rate set by the effective absorption coefficient. Based upon experimental parameters, the regime most relevant to the humanoid robotic bioreactor was identified to have a solution of

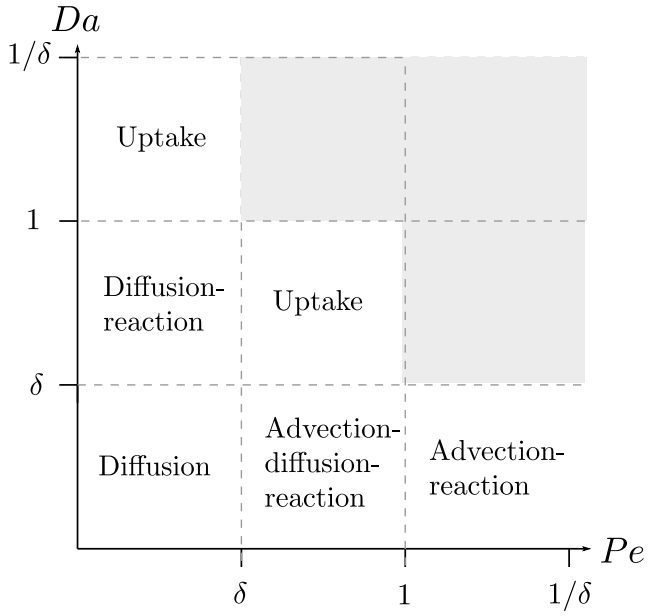

Figure 4.10: *Homogenised models in different parameter regimes.*

zero concentration within the scaffold. In future work, it would be interesting to simulate the fluid problem in scenarios which capture experimental setup more faithfully, for example including the effects of axial scaffold deformation and the non-uniformity of the inlet condition. We will expand on these points in chapter 5.

In this work, we made the simplifying assumption that the cells occupied negligible volume. The model could be extended to explore the role of cell proliferation in modifying transport processes. One way to achieve this could be to prescribe the solid volume fraction as a function of time, treating the strings and cells combined as the solid phase. As in [111], the number of cells could be described using a modified Fisher's equation. The effects of fluid shear or nutrient concentration could be included in the equation for cell number which would then be used to update the solid domain in the microscale problem. In general, this would result in a slow variation in the solid fraction across the domain and so multiple solutions to the microscale problem would be required to characterise the difference in permeability across the domain.

Chapter 5

Discussion

We conclude in this chapter with a summary of the research presented and an outline of potential avenues for future research. In section 5.1, we discuss the main results presented in each chapter. In 5.2, we highlight some areas which may provide interesting problems for future research.

5.1 Summary of results

In this thesis, we have presented the development of models for the interaction between slow-flowing fluid and an ensemble of aligned strings, motivated by modelling the scaffold of a humanoid robotic bioreactor. Throughout, the models developed were based upon the method of homogenisation *via* multiscale asymptotics.

In chapter 2, we began by developing methodology required for later chapters. The main result of this chapter is equation (2.184), which gives the multiple scales form of an integral condition on a slowly varying domain. Chapter 2 serves to justify this equation by showing that using (2.184) recovers the homogenised model obtained as the limit of a problem obtained *via* established homogenisation techniques. We outline how considering a one-dimensional problem and the flux transport theorem informed the proposed multiple scales form. We anticipate

that this result will be applicable to other homogenisation problems with integral constraints on a slowly-varying domain. Unlike the electrostatics problem we considered (that of perfectly dielectric inclusions in an insulator), for some systems the homogenised model cannot be obtained as the limit of an established multiple scales problem. Thus, this result should facilitate homogenisation of a larger class of problems, for example that of rigid inclusions in a linearly elastic material.

We applied the result from chapter 2 in chapter 3, where we obtained a homogenised model for fluid-structure interaction within a fluid-string composite. Using homogenisation *via* multiscale asymptotics, we derived an effective model for the fluid-string composite that was easier to solve than the full problem, whilst maintaining some description of the microscale features. The macroscale model was for a deforming porous medium, which we solved analytically in a simple geometry. We demonstrated how combining the solution to the microscale and macroscale problems could be used to calculate the microscale shear stress for various macroscale boundary conditions. For flow driven by time-harmonic motion of the string ends, we found that the microscale shear stress scaled with the frequency of the impose displacement. When an imposed flux drives fluid flow, the shear stress depends on the solid fraction which sets the values of the permeability.

In chapter 4, we developed a model for nutrient transport within the fluid-string composite. By varying the scaling of the Péclet number and Damköhler number, we identified four different macroscale models: diffusion-reaction, uptake, advection-diffusion-reaction and advection-reaction. In each case, we illustrated the role of the parameters in the macroscale problem by considering solutions to the governing equations in a cylindrical geometry.

Combined, the work presented in chapters 3 and 4 lays the foundation for effective models in bioreactor systems with an aligned fibrous scaffold. In the next section, we outline how this work may be extended to incorporate other features of the humanoid robotic bioreactor and identify other potential applications.

5.2 Future work

5.2.1 Humanoid robotic bioreactor

The models presented in chapters 3 and 4 were concerned with fluid flow and nutrient transport within the bioreactor scaffold, with all macroscale solutions presented for the scaffold contained within a rigid cylinder. In reality, the chamber will extend and deform as the robotic arm abducts and adducts. The first step towards incorporating axial deformation was made in section 3.6.1, where we obtained the model for the scaffold where strings undergo an imposed $O(1)$ axial deformation with $O(\delta)$ displacements set by the fluid-structure interaction. A time-varying $O(1)$ axial deformation could be imposed to mimic the scaffold extension generated by the bioreactor arm. Based on the analysis in section 3.6.1, this would result in a time-varying tension at leading-order and allow the effects of cyclic stretching to be explored in addition to the fluid shear stress.

To account for this effect, we would need to incorporate elasticity into the scaffold casing. The 'toy' problems presented throughout chapters 3 and 4 were solved in a rigid cylindrical domain. Replacing the rigid outer boundary with a membrane model could significantly complicate matters. If the membrane is sufficiently flexible, the increase in fluid pressure induced by string motion could induce membrane deformation, which in turn could alter the fluid flow. Thus, including elasticity of the outer membrane may lead to a further source of fluid-structure interaction.

In the macroscale problems we considered in chapters 3 and 4, the scaffold interfaced directly with the boundary and the strings were assumed to be uniformly spaced across the cross-section to leading-order. Experimentally, the fibres are observed to occupy the central region of the chamber and are surrounded by a fluid annulus, as seen in figure 5.1.a. Hence, a more faithful representation of the bioreactor chamber could couple the macroscale model developed in chapter 3 to an exterior fluid layer. This would also allow for more representative modelling of the media inlet condition. As shown in figure 5.1.b, the media enters outside of the scaffold fibres. The flow distribution is likely to be altered by the inclusion of

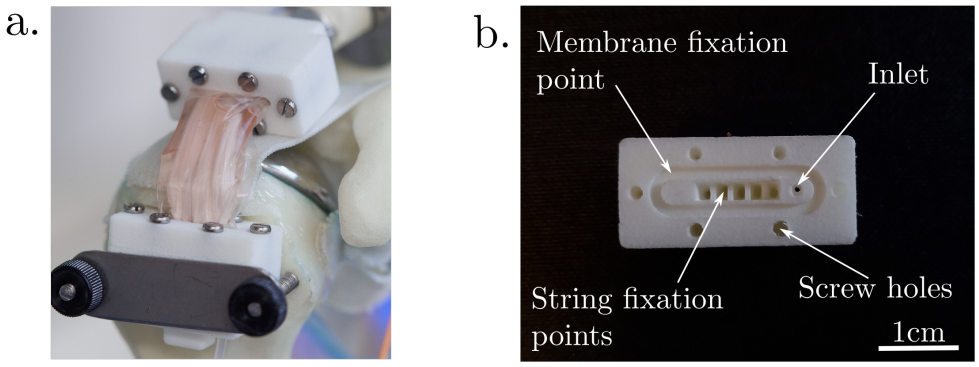

Figure 5.1: *a. Image of the bioreactor in operation showing the layer of nutrient media that surrounds the scaffold fibres. b. Cross-section of the chamber base before assembly. Photographs are with thanks to Nicole Dvorak, NDORMS*

the modified inlet condition and a fluid annulus. The exterior region will have a significantly lower flow resistance than the bioreactor scaffold and thus it would be interesting to explore how this diverts flow from the scaffold interior. Alterations in the flow field will also change the distribution of fluid-induced shear stress and nutrient transport.

Thus far, our discussions have focused on modelling the mechanics of the cell media and strings, taking the fluid-induced shear stress as a proxy for the fluid-induced shear stress experienced by the cells. While this approach is suitable for the early stages of bioreactor operation, as the cells proliferate and deposit ECM, their volume will no longer be negligible in comparison with the bioreactor scaffold. In this regime, the cell volume should be accounted for as it would influence the flow field. A first approach could prescribe the growth rate of the cells as a function of time and space. This would result in permeability coefficients that change with time as the solid fraction will increase with cell proliferation. Depending on the experimental regime, it may be the case that the rate of cell proliferation is unknown *a priori* but rather depends on the microscale shear stress and nutrient concentration. This modelling would become more complex as the microstructural evolution would be coupled with the macroscale variables. Relating the cell proliferation to nutrient concentration complicates the solution to the

macroscale nutrient transport problem when advection is present. Unlike chapter 4 where the transport problem could be solved after specifying the fluid velocity, the fluid and nutrient problems are fully coupled as the nutrient distribution alters the solid domain *via* its influence on cell growth, which in turn modifies the flow field and hence nutrient transport. Future work could build upon the studies of growing tissues presented in [31, 91] to incorporate these effects in the fluid-string composite.

One aspect of the models which we have not yet explored is the effects of varying tension across the bioreactor scaffold. The scaffold fibres are tied in bundles of forty fibres and glued to the base of the chamber at the fixation points labelled in figure 5.1.b. As such, the tension of each individual fibre is not controlled directly. The effects of tension variation across the scaffold width could be included by introducing a function of the slow scale describing the varying tension in equation (3.15), rather than setting the tension to be constant as considered in section 3.3.

Throughout, our discussion has been motivated by developing methods to model the shear stress and nutrient transport within the bioreactor scaffold. Ultimately, the aim would be to compare modelling predictions with experimental data. This comparison could provide model validation, informing model iterations which may inform experimental work. Examples of experimental studies which may provide model validation include particle image velocimetry measurements of fluid flow within the scaffold for typical perfusion velocities. A knowledge of the flow field in the absence of cells may be compared with the solution obtained as the solution to the homogenised model. Imaging flow through the scaffold would also provide some insight into scaffold motion, offering insight into whether the assumptions used in chapter 3 of the scaffold fibres deforming a small amount from an originally periodic reference configuration are suitable. Further, studies of the flow field would also help to identify the significance of the exterior fluid annulus and the effects of the inlet position relative to the bioreactor scaffold. To characterise the stress due to scaffold deformation, imaging the chamber throughout a typical loading cycle would be beneficial. These measurements would provide the boundary conditions on a model which includes general chamber deformation. After establishing a suitable model for fluid flow and scaffold deformation,

experiments that explore the response of cells to different bioreactor operating parameters would be of interest. For example, imaging the spatial distribution of cells at multiple time points would provide insight into whether the predictions of cell viability are suitable, as well as identifying their proliferation rate. These measurements will provide parameters reflecting cell growth that may be incorporated into later models which reflect scaffold evolution as the tissue develops. Spatially resolved imaging of gene expression associated with mechanical stress in tenocytes would also offer validation for model predictions of shear stress.

5.2.2 Further applications

While the work presented was principally motivated by developing models for the humanoid robotic bioreactor, the methods may be applied to other systems which involve flexible, slender filaments interacting with slow flow. In this section we outline some possible applications.

5.2.2.1 Cilia

Cilia are microscale, hair-like structures which coat the surfaces of many cells, including human epithelial cells which line the ventricles in the brain, oviducts and the respiratory tract, and the surfaces of organisms such as comb jellies, blue mussels and paramecia [18]. Cilia serve various functions including mucus clearance in the respiratory tract, bacterial locomotion and sensing of the chemical and mechanical environment [18]. While cilia can generate fluid flows [95], the flow is also thought to play a role in cilia synchronisation [81]. In addition to having some mechanical function, cilia have implications in signalling, for example cilia lining the brain ventricles have chemoreceptors for molecules which play a role in neuromodulation [50]. The density of these cilia is around $200/\text{mm}^2$ [54] and flow rates induced by cilia in the ventricles are slow [95], suggesting that a modified form of the fluid-string interaction model may be applicable. To reflect cilia motion, a beam model could be used in place of the string model within the methods presented in chapter 3. While incorporating a linear beam model would likely

only alter the model by the introduction of fourth derivatives reflecting bending in the form of the homogenised force balance, including large deformations would require more significant changes. We will outline a potential method to include large deformations in section 5.2.3.

5.2.2.2 Microvilli

Microvilli are actin-supported protrusions arranged on a hexagonal lattice on the surface of brush border cells that line the proximal tubule in the kidney and the small intestine [33, 53]. The microvilli morphology facilitates an increase in mass transport across the cell membrane as well mechanosensitivity *via* its deformation in response to flow [44]. The flow rate through the proximal tubule has been linked to changes in the reabsorption rate of various ions *via* the flow-dependent deformation of microvilli [127]. A homogenised fluid-beam interaction model as outlined above could complement approaches which capture one-way coupling between fluid and solid, by incorporating the effect of microvilli deformation on the fluid shear stress [53].

5.2.2.3 Endothelial glycocalyx

The endothelial glycocalyx is a thin (≈ 0.5 μm) gel layer lining the interior walls of blood vessels [128]. The endothelial glycocalyx fulfils a variety of functions: transducing fluid shear stress to intracellular signalling, modulating fluid transfer out of microvessels and the inflammatory response [49, 128]. The layer consists of membrane-bound proteoglycans and glycoproteins which associate with proteins and other molecules in the blood to form the extended glycocalyx layer [128]. The degree of association is dependent on the concentration of blood components, and these interactions can cause a modification in proteoglycan structure [128]. It has been suggested that fluid induced shear stress in the physiological range does not cause significant deformation to the proteoglycan brushes, but deformation does occur in response to the passage of a white blood cell or red blood cell arrest [128]. Previously, these effects have been modelled by treating the proteoglycans

as thin beams embedded in porous media with flow given by the Brinkman equations [55, 129]. The drag computed by solving the Brinkman equations was used to calculate the fluid drag exerted on beams and thus compute its deformation. Again, modifying the solid model used in chapter 3 could be used to develop a complementary approach. In particular, a homogenised model of the interaction could offer a way to incorporate the effects of proteoglycan deformation on the modulation of flow out of microvessels [37].

In addition to the three examples considered above, a number of other applications could be explored, for example transport processes in the cytoplasm driven by the cytoskeleton [117], fluid flow in muscles [80], deformable filters [7] or microfluidic pumps [52].

5.2.3 Problems of mathematical interest

In this section, we suggest some problems which could be explored in future work which build on the mathematical methods used in this thesis.

In section 4.4.1, rather than systematically expanding boundary position, we instead took only the leading-order term of the expansion of the string position, which greatly simplified analysis. This approach is commonly used implicitly when treating circular inclusions with a slowly varying radius as in chapter 2; by using the level sets $h = 0$ for $h = |\boldsymbol{x} - \boldsymbol{x}_0| - a(\boldsymbol{x})$ to define the inclusion boundaries, we are actually specifying a geometry which is elliptical on the macroscale as shown by figure 5.2.a in dashed lines. The analogous approximation we have used in chapters 3 and 4 is shown in figure 5.2b.-c., where keeping only the leading-order terms in the expansion of the string displacement gives a geometry which is exactly circular on the microscale (figure 5.2.c, grey dashed), but elliptical on the macroscale (figure 5.2.b, grey dashes). In future, it would be useful to systematically check that choosing a geometry to be periodic on the microscale or macroscale results in the same homogenised problem. This analysis could be performed using the electrostatics problem with finite permittivity considered in chapter 2. The radius could be written as a piece-wise constant function a ensuring an exactly circular geometry on the macroscale. To write this in multiple scales form, we would set

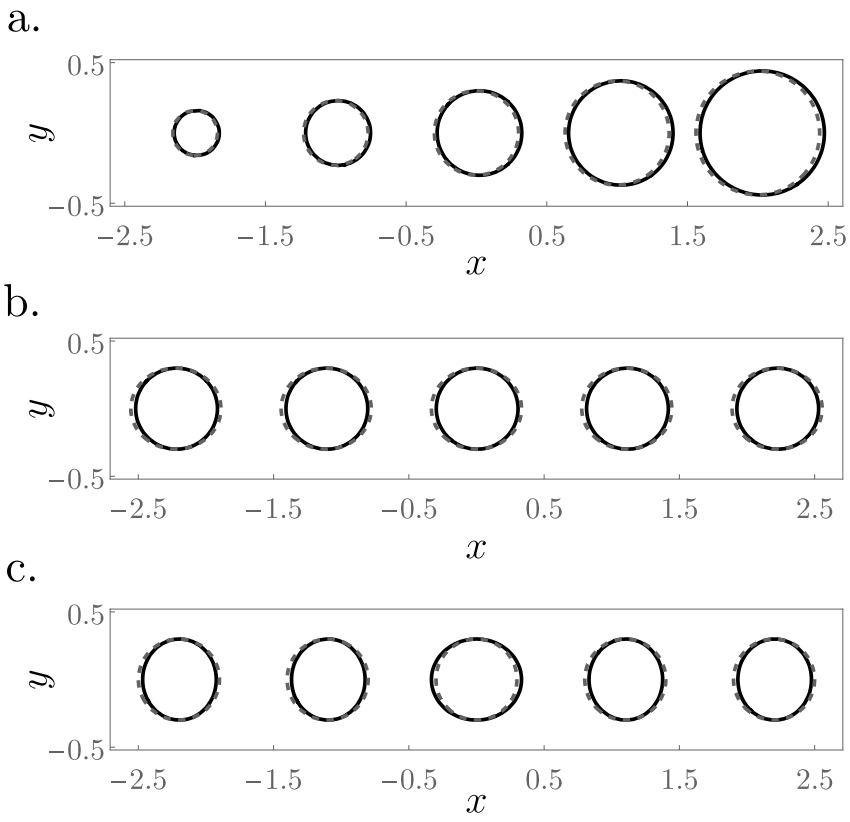

Figure 5.2: *a. Circular inclusions on a periodic lattice with a slowly varying radius such as considered in chapter 2. An inclusion which gives an exactly periodic microscale geometry (solid, black lines) will be elliptical when viewed on the macroscale (dashed, grey lines) as the radius varies with the slow coordinate. b. The macroscale geometry and c. microscale geometry of the string cross-section for an imposed displacement* $\boldsymbol{s} = x\hat{\boldsymbol{e}}_x - \delta(X\hat{\boldsymbol{e}}_x + x\hat{\boldsymbol{e}}_x) + O(\delta^2)$*. In b.-c. solid, black lines show the geometry from considering both the leading- and first-order terms in the expansion; the inclusions are then circular to* $O(\delta^2)$ *when viewed on the macroscale (b. black lines) but are elliptical in the cell problem (c. black lines). Keeping only the leading-order term in the string displacement, the inclusions are then elliptical on the macroscale (b. grey dashes) but exactly circular on the microscale (c. grey dashes).*

the gradient of this function to be zero, performing a multiple scales expansion for the radius which would give a circular microscale geometry at leading-order. All equations would be expanded onto this leading-order geometry and the problem could then be homogenised.

Throughout this thesis, we assumed that the string deformations induced by fluid flow were small, which results in linear equations that can be homogenised directly. In some applications, the deformation of the solid components may be nonlinear but still vary slowly across the material. To model large deformations, we would need to introduce Lagrangian coordinates which describe the periodic reference configuration and Eulerian coordinates to describe the current configuration of the solid. If the deformation gradient which maps from the Lagrangian to Eulerian configurations is only a function of the slow scale at leading-order, it may be possible to homogenise the problem in the periodic reference configuration before inverting the mapping to obtain the macroscale model. This approach has been applied previously in modelling a growing poroelastic medium [30] and the electric potential in a beating heart [100], the result being the coefficients in the macroscale problem which depend on the deformation gradient.

Another problem which may be explored using a coordinate mapping to a periodic reference configuration is that in which the density of strings significantly changes across the width of the domain. As it stands, changes in string density appear in chapter 3 in the scaffold mass conservation equation in the macroscale model. If the reference positions of the strings are not on an exactly periodic lattice but rather have a slowly varying spacing, the permeability coefficient may become a function of slow spatial position, resulting in a series of cell problems that must be solved.

In addition to varying the distance between strings, it may be of interest to explore the effects of varying solid fraction on the form of the macroscale model. In the discussion of chapter 3, we proposed that an analysis similar to that conducted by Lévy [78] may also be applicable to the fluid-string composite, highlighting the change in macroscale model from Stokes flow to Darcy's law *via* the Brinkman equations. It could be beneficial to perform this analysis, providing a systematic link between models of fluid-structure interaction in string assemblies at low and

high solid fraction, where distinct techniques are typically employed.

5.3 Conclusion

In this thesis, we have considered the application of homogenisation *via* multiscale asymptotics to strings interacting with Stokes flow. The multiscale method for integral constraints expands the homogenisation method to problems with integral constraints in a slowly varying domain. The development of the fluid-string model and the associated transport problem should be transferable to modelling fluid-structure interaction in other systems as outlined in 5.2.

Appendix A

Experimental parameters

A.1 Fluid-string interaction

A.1.1 Assumption of negligible cell volume

In this section, we estimate the volume of cells, fluid and scaffold in the bioreactor chamber to provide motivation for the assumption of negligible cell volume.

- Fibroblasts, the cell type used in seeding the bioreactor, are $\approx 10\mu$m in diameter. For one million seeded cells we obtain a cell volume in the chamber of $V_c = 1 \times 10^{-9} m^3$
- The fibres making up the bioreactor scaffold have dimensions $30\mu m \times 500\mu m \times 3cm$. For 200 fibres, we have a total scaffold volume $V_s = 9 \times 10^{-8} m^3$.
- The total volume of the bioreactor is approximately $3 \times 10^{-6} m^3$. Subtracting the volume occupied by the scaffold and cells, we arrive at the fluid volume in the chamber, $V_f = 3 \times 10^{-6} m^3$ to 1 significant figure.

Thus, we have $V_c \ll V_s \ll V_f$, justifying the assumption of negligible cell volume. We expect that the cell volume will be comparable to the string volume when

Flow rate	$1 \times 10^{-3} mL/s$
Number of fibres	200
Fibre cross-section	$30 \times 500 \mu m^2$
Cell density	$1.67 \times 10^5 cells/m$ per fibre
Maximum oxygen absorption rate	$3.60 \times 10^{-10} (mol) s^{-1}$ per cell [93]
Maximum glucose absorption rate	$9.79 \times 10^{-10} (mol) s^{-1}$ per cell [93]
Lactose yield from glucose	2
Inlet glucose concentration	$25mM$
Inlet oxygen concentration	$0.2mM$
Chamber length	$3cm$
Diffusion coefficient of glucose in media	$6 \times 10^{-10} m^2 s^{-1}$ [3]
Diffusion coefficient of oxygen in media	$2 \times 10^{-9} m^2/s$ [58]
Diffusion coefficient of lactate in media	$6 \times 10^{-10} m^2 s^{-1}$ [118]
Elastic modulus	$800\,Pa$

Table A.1: Experimental parameters

the number of cells in the chamber reaches 9×10^7. Thus, we expect the models developed subject to the assumption of negligible cell volume may be relevant in the first 4 hours of operation (assuming a proliferation period of 30 minutes). Beyond this period, it is expected that the cell volume will influence the string deformation and so models which account for the cell volume explicitly should be used.

A.2 Nutrient transport

A.2.1 Uptake velocity

The uptake boundary condition (4.8) is

$$\hat{\boldsymbol{n}}_s \cdot (D\nabla c) = \overline{A}c \quad \text{on} \quad \partial\Omega_s^i. \tag{A.1}$$

By dimensional analysis, we see that $\overline{A}$ must have dimensions of velocity $[\,\overline{A}\,] = L/t$. Experimental measurements can be used to obtain the maximum uptake rates of oxygen and glucose per cell (table A.1). To convert this to an uptake velocity, we multiply by the cell density per unit area of the scaffold and divide by the characteristic concentration, i.e.

$$\overline{A}_i = \frac{\text{maximum uptake rate } \times \text{ cell density per unit area}}{\text{concentration scale}}, \quad \text{for} \quad i = o, g, \tag{A.2}$$

for glucose and oxygen. To calculate the reaction velocity for lactate $\overline{A}_l$ we use

$$\overline{A}_l = -2\overline{A}_g, \tag{A.3}$$

as lactate is produced by tendon cells from glucose with yield 2 during anaerobic glycolysis. We discuss numerical values for the uptake velocity relevant to the humanoid robotic bioreactor in section A.2.2.

A.2.2 Estimating the Péclet and Damköhler numbers

In this section, we obtain estimates for the model parameters in the nutrient transport problem, namely the Damköhler and Péclet numbers, from the experimental

values listed in table A.1.

First, we obtain an estimate for the cell area density. We assume that the cells are uniformly distributed over the surface of the fibres. Using the cell number, number of fibres and dimensions in table A.1, we obtain a cell density per unit area of $1.57 \times 10^8 m^{-2}$.

Using (A.2)-(A.3), we obtain the reaction velocities

$$\overline{A}_o = 0.3ms^{-1} \quad , \overline{A}_g = 6 \times 10^{-3} ms^{-1}, \quad \overline{A}_l = -1.2 \times 10^{-2} ms^{-1}. \tag{A.4}$$

Assuming $3mL$ of fluid is in the chamber, the cross-section of the chamber is $1cm^2$, resulting in a velocity scaling of $1 \times 10^{-5} m/s$ assuming that the inlet flux is distributed evenly across the chamber cross-section. Dividing (A.4) by this fluid velocity, we obtain the Damköhler numbers

$$Da_o = 30000, \quad Da_g = 600, \quad Da_l = 1200. \tag{A.5}$$

Diffusion coefficients for glucose, oxygen and lactate D_g, D_o D_l are given in table A.1. We can then use these to calculate the Péclet number for each species:

$$Pe_o = \frac{UL}{D_o} = 150, \quad Pe_g = \frac{UL}{D_g} = 500, \quad Pe_l = \frac{UL}{D_l} = 500, \tag{A.6}$$

where we have used the length of the chamber to set the length scale.

Appendix B

Numerical methods

In this appendix, we provide details on the methods used to derive numerical solutions to partial differential equations. In section B.1, we outline the application of the finite element method to the cell problems of the fluid-string model. In section B.2, we apply the finite element method to the nutrient transport problem.

In all examples we consider, meshes were generated with the Gmsh software [51]. The variational forms of each problem were solved in FEniCS [103].

B.1 Fluid-string interaction

B.1.1 Axial Cell Problem

The cell problem for the axial flow velocity (3.66)-(3.67) takes the form

$$\nabla^2_{\boldsymbol{X}} \Psi_{33} = 1 \quad \text{in} \quad D_f, \tag{B.1}$$

$$\Psi_{33} = 0 \quad \text{on} \quad \partial D_{\boldsymbol{s}_0}, \tag{B.2}$$

with Ψ_{33} periodic in $\boldsymbol{X}$ with period $\mathbf{1}$. We solve this problem using the finite element method. We begin by writing the problem in variational form by multiplying

(B.1) by a test function v and integrating over the domain,

$$\int_{D_f} v\nabla^2_{\boldsymbol{X}}\Psi_{33}dS_X = \int_{D_f} vdS_X. \tag{B.3}$$

We use integration by parts on the left-hand side to shift the derivatives from Ψ_{33} onto the test function

$$-\int_{D_f} \nabla_{\boldsymbol{X}}\Psi_{33}\cdot\nabla_{\boldsymbol{X}}vdS_X - \int_{\partial D_{\boldsymbol{s}_0}} v\nabla_{\boldsymbol{X}}\Psi_{33}\cdot\hat{\boldsymbol{n}}dl_X = \int_{D_f} vdS_X, \tag{B.4}$$

where the integrals over the outer boundary of unit cell vanish due to periodicity and $\hat{\boldsymbol{n}}$ is the normal pointing into the fluid region.

We have a Dirichlet condition (B.2) on the string boundary and so the test function vanishes on this boundary. The boundary integral in (B.4) then vanishes and we are left with

$$\int_{D_f} \nabla_{\boldsymbol{X}}\Psi_{33}\cdot\nabla_{\boldsymbol{X}}vdS_X = -\int_{D_f} vdS_X, \tag{B.5}$$

Thus, to find solutions to the cell problem, we look for $\Psi_{33}\in V$ such that (B.5) is satisfied for all $v\in V$, where $V=\{v\in L^2(D_f) : v=0 \text{ on } \partial D_{\boldsymbol{s}_0}\}$ for the space L^2 of square-integrable functions. We make the Galerkin approximation, restricting (B.5) to a finite-dimensional space and use degree 2 Lagrange polynomials to construct this space. We check the convergence of this method by comparing the difference between the minimum value of the numerical solution to the minimum of the solution calculated on a mesh with the largest number of elements Ψ^f_{33} (figure B.1).

B.1.2 Transverse Cell Problem

Defining $\boldsymbol{\psi}=\Psi_{\perp j}$, the jth column of $\Psi_\perp$ and $\phi=-\boldsymbol{\Phi}_j$, the jth component of Φ, the cell problem for transverse flow (3.60)-(3.62) driven by pressure gradients is

$$\nabla_{\boldsymbol{X}}\cdot(\nabla_{\boldsymbol{X}}\boldsymbol{\psi}+\phi I) = \hat{\boldsymbol{e}}_j \quad j=1,2 \quad \text{in} \quad D_f, \tag{B.6}$$

$$\nabla_{\boldsymbol{X}}\cdot\boldsymbol{\psi} = 0 \quad \text{in} \quad D_f, \tag{B.7}$$

$$\boldsymbol{\psi} = \boldsymbol{0} \quad \text{on} \quad \partial D_{\boldsymbol{s}_0}, \tag{B.8}$$

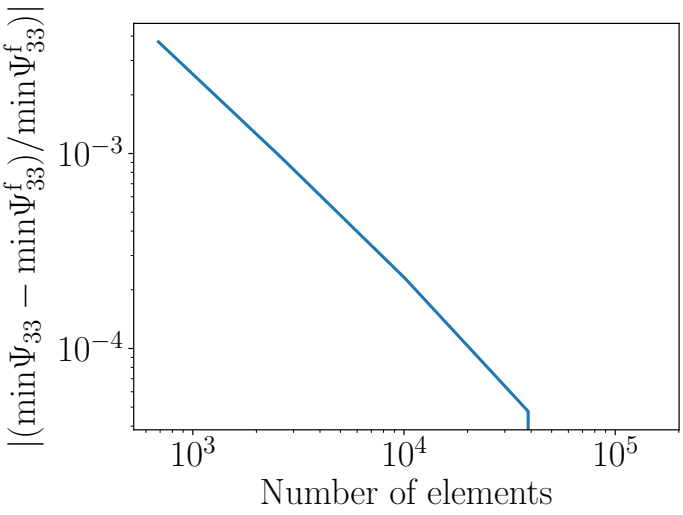

Figure B.1: Convergence check for the axial cell problem. *Solutions were solved on a mesh with* $\phi_s = 0.69$.

with $(\boldsymbol{\psi}, \phi)$ periodic in $\boldsymbol{X}$ with period $\mathbf{1}$, where $\hat{\boldsymbol{e}}_j$ is the jth column unit vector. Thus, the transverse cell problem looks like Stokes equations on a periodic domain with no-slip at the solid boundary and a constant body force.

We dot (B.6) with a vector test function $\boldsymbol{v}$, multiply the second equation (B.7) by a scalar test function q and sum the two, which gives

$$\int_{D_f} \boldsymbol{v} \cdot (\nabla_{\boldsymbol{X}} \cdot (\nabla_{\boldsymbol{X}} \boldsymbol{\psi} + \phi I))\, dS_X + \int_{D_f} q \nabla_{\boldsymbol{X}} \cdot \boldsymbol{\psi} dS_X = \int_{D_f} \boldsymbol{v} \cdot \hat{\boldsymbol{e}}_j dS_X. \tag{B.9}$$

Integrating the first term by parts, we have

$$\begin{aligned} -\int_{D_f} \nabla_{\boldsymbol{X}} \boldsymbol{v} : (\nabla_{\boldsymbol{X}} \boldsymbol{\psi} + \phi I) dS_X + \int_{D_f} \nabla_{\boldsymbol{X}} \cdot (\boldsymbol{v} \cdot (\nabla_{\boldsymbol{X}} \boldsymbol{\psi} + \phi I)) dS_X \\ + \int_{D_f} q \nabla_{\boldsymbol{X}} \cdot \boldsymbol{\psi} dS_X = \int_{D_f} \boldsymbol{v} \cdot \hat{\boldsymbol{e}}_j dS_X. \end{aligned} \tag{B.10}$$

We apply the divergence theorem to the second integral which gives

$$-\int_{D_f} \nabla_{\boldsymbol{X}} \boldsymbol{v} : (\nabla_{\boldsymbol{X}} \boldsymbol{\psi} + \phi I) dS_X + \int_{D_f} q \nabla_{\boldsymbol{X}} \cdot \boldsymbol{\psi} dS_X = \int_{D_f} \boldsymbol{v} \cdot \hat{\boldsymbol{e}}_j dS_X, \tag{B.11}$$

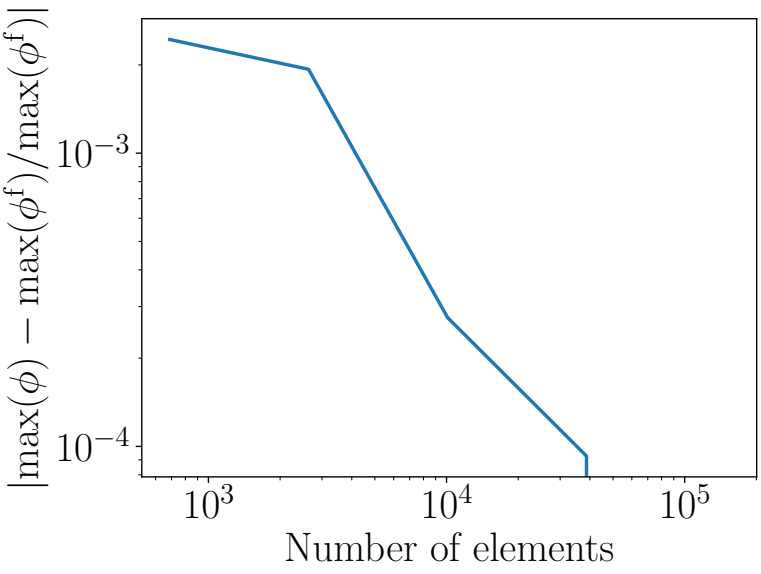

Figure B.2: Convergence check for the transverse cell problem

where the integral over the exterior boundary evaluates to zero due to periodicity and the integral over the string boundary vanishes as we impose Dirichlet conditions on $\boldsymbol{\psi}$ here. The variational problem becomes to find $(\boldsymbol{\psi}, \phi) \in V \times Q$ such that (B.11) is satisfied, where $V = \{L^2(D_f) : \boldsymbol{v} = \mathbf{0} \text{ on } \partial D_{\boldsymbol{s}_0}\}$ and $Q = \{q \in L^2(D_f) : \int_{D_f} q dS_X = 0\}$. We use Taylor-Hood elements to construct the finite dimensional approximation to (B.11). We check convergence by plotting the relative error in the maximum value of the pressure (compared with the solution from the finest mesh ϕ^f) as a function of the number of mesh elements as shown in figure B.2.

B.2 Nutrient transport

B.2.1 Cell problem

In this section, we solve (4.35)-(4.37) using the finite element method on the domain shown in figure 3.3. We first transform (4.35)-(4.37) into variational form by multiplying (4.35) by a vector test function $\boldsymbol{v}$ and integrating over the fluid region

of the unit cell

$$\int_{D_f} \boldsymbol{v} \cdot \nabla^2_{\boldsymbol{X}} \boldsymbol{\Lambda} dS_X = 0. \tag{B.12}$$

Applying the divergence theorem and using (4.36) to move the derivatives onto the test function in the usual way, we find

$$-\int_{D_f} \nabla_{\boldsymbol{X}} \boldsymbol{v} : \nabla_{\boldsymbol{X}} \boldsymbol{\Lambda} dS_X - \int_{\partial D_{s_0}} \boldsymbol{v} \cdot \hat{\boldsymbol{n}}_0 dl_X = 0. \tag{B.13}$$

We introduce a Lagrange multiplier $\boldsymbol{c}$ and associated test function $\boldsymbol{d}$ to impose the constraint (4.37). We expect $\boldsymbol{c}$ to be constant as we are imposing a global constraint. Adding this constraint to (B.13) we find the following variational form for the problem: find $(\boldsymbol{\Lambda}, \boldsymbol{c}) \in (V, \Re^2)$ such that

$$\int_{D_f} \nabla_{\boldsymbol{X}} \boldsymbol{v} : \nabla_{\boldsymbol{X}} \boldsymbol{\Lambda} dS_X + \int_{D_f} \boldsymbol{c} \cdot \boldsymbol{v} dS_X + \int_{D_f} \boldsymbol{d} \cdot \boldsymbol{\Lambda} dS_X = -\int_{\partial D_{s_0}} \boldsymbol{v} \cdot \hat{\boldsymbol{n}}_0 dl_X, \tag{B.14}$$

for all $(\boldsymbol{v}, \boldsymbol{d}) \in (V, \Re^2)$, where $V = H^2$, the Hilbert space in two-dimensions where functions have square-integrable weak derivatives. We solve (B.14) in FEniCS [103] using first order Lagrange elements for $\boldsymbol{\Lambda}$ and constant elements for $\boldsymbol{c}$.

B.2.2 Advection-diffusion-reaction

We are looking to solve the macroscale advection-diffusion-reaction equation (4.125) which we restate here, dropping zeros which denote leading order quantities:

$$\frac{\partial c}{\partial \tau} + \nabla \cdot (c\boldsymbol{u}) - \nabla \cdot (\mathcal{D}_{\text{eff}} \nabla c) + \alpha_{\text{eff}} c = 0, \tag{B.15}$$

To solve (B.15) numerically, we discretise time, solving a steady problem at each time increment $\Delta\tau$. We use a backward Euler discretisation in time, using c_n to denote the concentration at time $n\Delta\tau$. Applying this discretistion to (B.15), we have

$$\frac{c_{n+1} - c_n}{\Delta\tau} + \nabla \cdot (c_{n+1}\boldsymbol{u}_{n+1}) - \nabla \cdot (\mathcal{D}_{\text{eff}} \nabla c_{n+1}) + \alpha_{\text{eff}} c_{n+1} = 0. \tag{B.16}$$

We multiply (B.16) by a test function v, integrate over the domain and use the divergence theorem to shift derivatives from the concentration to the test function,

$$\int_\Omega \frac{(c_{n+1}-c_n)v}{\Delta\tau}ds - \int_\Omega \boldsymbol{u}_{n+1}c_{n+1}\cdot\nabla v ds + \int_{\partial\Omega} v c_{n+1}\boldsymbol{u}_{n+1}\cdot\hat{\boldsymbol{n}}dl \\ - \int_{\partial\Omega} v\mathcal{D}_{\text{eff}}\nabla c_{n+1}\cdot\hat{\boldsymbol{n}}dl + \int_\Omega \mathcal{D}_{\text{eff}}\nabla v\cdot\nabla c_{n+1}ds + \int_\Omega \alpha_{\text{eff}} v c_{n+1}ds = 0. \tag{B.17}$$

The boundary terms vanish on the sections of the boundary where Dirichlet boundary conditions are imposed as the test function vanishes on these boundaries. Contribution to boundary terms are given by inhomogeneous Neumann boundary conditions. For the flux-driven flow problem considered in section 3.5.2.5, the boundary conditions on nutrient concentration become

$$c = 0 \quad \text{at} \quad z = 0, \tag{B.18}$$

$$\frac{\partial c}{\partial z} = 0 \quad \text{at} \quad z = 1, \tag{B.19}$$

$$\frac{\partial c}{\partial r} = 0 \quad \text{at} \quad r = 0, 1/2. \tag{B.20}$$

Thus, the boundary terms in (B.17) involving the diffusion coefficient evaluate to zero. The only remaining boundary contribution is due to the fluid flux at the upper boundary which leaves,

$$\int_\Omega \frac{(c_{n+1}-c_n)v}{\Delta\tau}ds - \int_\Omega \boldsymbol{u}_{n+1}c_{n+1}\cdot\nabla v ds + \int_{\partial\Omega(z=1)} v c_{n+1}\boldsymbol{u}_{n+1}\cdot\hat{\boldsymbol{n}}dl \\ + \int_\Omega \mathcal{D}_{\text{eff}}\nabla v\cdot\nabla c_{n+1}ds + \int_\Omega \alpha_{\text{eff}} v c_{n+1}ds = 0. \tag{B.21}$$

We solved (B.21) in FEniCS using 1st order Lagrange elements with the flow field given in (4.141) [103]. To check convergence of the scheme, we solved the equations on meshes of varying refinement and compared the minimum numerical value of the solution with the minimum value as calculated on the finest mesh (figure B.3).

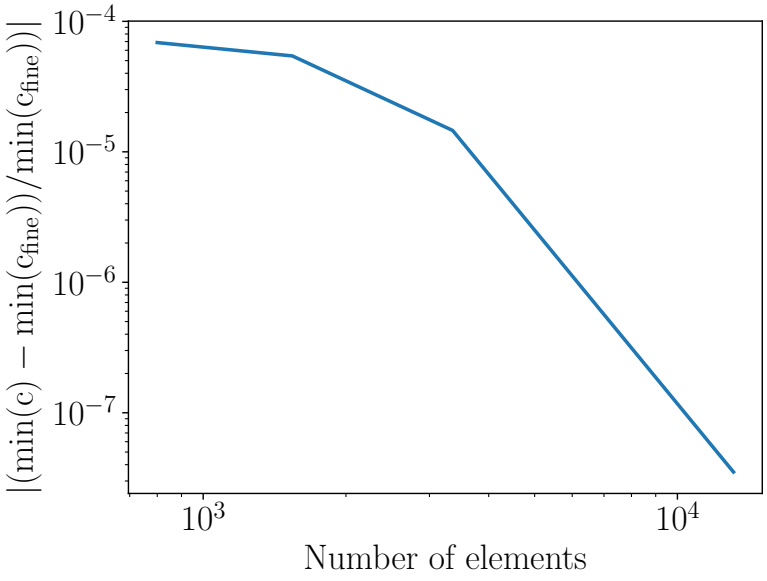

Figure B.3: Convergence of the minimum concentration

Appendix C

String force balance

In this section we provide justification for the statement in section 3.3 that the tension is constant at leading-order for strings executing a purely transverse displacement. We also reconcile the force balance written for transverse displacements of the string in (3.6) with the reduction from a nonlinear deformation presented in section 3.6.1. We show that for small, purely transverse displacements, the approach presented in section 3.6.1 results in the same equations as written in section 3.2.

We consider N strings with a reference configuration aligned with the z-axis surrounded by slow, Newtonian flow; the reference configuration of the ith string is $\boldsymbol{x}_0^i = \boldsymbol{x}_*^i + z\hat{\boldsymbol{e}}_z$, where $\boldsymbol{x}_*^i$ lies on a square periodic lattice. Points on the centreline in the current configuration of the string are given by

$$\boldsymbol{r}^i = \boldsymbol{x}_*^i + z\hat{\boldsymbol{e}}_z + \delta\boldsymbol{s}, \tag{C.1}$$

where we have nondimensionalised with respect to the scales given in (3.210). We assume that the displacement $\boldsymbol{s} = (s_x, s_y, 0)$ is purely transverse, considering displacements of a string with fixed endpoints.

We take a similar approach to Antman [8], balancing forces on a segment Δz of the equilibrium configuration of the string centreline. Neglecting string inertia,

the force balance is

$$\boldsymbol{N}^i(z+\Delta z) - \boldsymbol{N}^i(z) + \boldsymbol{f}^i(z)\Delta z = \boldsymbol{0}, \tag{C.2}$$

where $\boldsymbol{f}^i$ is the body force per unit length on the ith string. In our problem, this body force will be due to the fluid stress. Taylor expanding about z for small Δz, we obtain

$$\frac{\partial \boldsymbol{N}^i}{\partial z} + \boldsymbol{f}^i = \boldsymbol{0}. \tag{C.3}$$

After nondimensionalisation using the scales in 3.10, (C.3) becomes

$$\frac{\partial \boldsymbol{N}^i}{\partial z} + \delta \boldsymbol{f}^i = \boldsymbol{0}. \tag{C.4}$$

The contact force $\boldsymbol{N}^i$ is related to the deformation as follows

$$\boldsymbol{N}^i = T^i \frac{\partial \boldsymbol{r}^i}{\partial z} \Big/ \left| \frac{\partial \boldsymbol{r}^i}{\partial z} \right|, \tag{C.5}$$

where we have assumed that the string can support no bending moments. We require a constitutive law to relate the tension T^i to stretch $|\partial \boldsymbol{r}^i/\partial z|$. For purely transverse displacements of an elastic string, we must use the following constitutive law [69],

$$T^i = \alpha \left| \frac{\partial \boldsymbol{r}^i}{\partial z} \right|, \tag{C.6}$$

where α describes the elastic properties of the string. Assuming the string material is uniform, we take α to be constant. Substituting the known form of the deformation at leading-order (C.1), we obtain

$$T^i = \alpha \left(1 + \frac{\delta^2}{2} \left| \frac{\partial \boldsymbol{s}^i}{\partial z} \right|^2 + O(\delta^4) \right). \tag{C.7}$$

Thus, we have a tension which is constant at leading-order.

Using (C.6) in (C.4), we find

$$\frac{\partial}{\partial z} \left(\alpha \frac{\partial \boldsymbol{r}^i}{\partial z} \right) + \delta \boldsymbol{f}^i = \boldsymbol{0}. \tag{C.8}$$

We substitute the expansion of the centreline (C.1) into (C.8) and compare coefficients of δ. At leading-order, we find the equation is automatically satisfied as there is no axial displacement of the string centreline.

Comparing coefficients in (C.8) at $O(\delta)$, we find

$$\frac{\partial}{\partial z}\left(\alpha\frac{\partial \boldsymbol{s}^i}{\partial z}\right) + \boldsymbol{f}^i = \boldsymbol{0}. \tag{C.9}$$

Thus, writing $\alpha = T$ which holds with errors of $O(\delta^2)$, we recover (3.6). We note that there is an inconsistency in (C.9). The body force $\boldsymbol{f}^i$ due to the hydrodynamic stress has terms of equal magnitude in each component but we have assumed that the string displacements are entirely transverse. To reconcile this, we would require a fictitious force in (C.9) which balances the axial fluid stress to ensure that there is no axial displacement. We consider a more realistic scenario in section 3.6.1 where we allow axial displacements of the string, removing the need to introduce the fictitious force.

Appendix D

Uptake boundary condition

In this appendix we write the uptake boundary condition (4.15) in multiple scales form. We transform spatial derivatives using (4.19) and expand the normal using (4.26). We expand onto the leading order position of the string boundary $(\hat{\boldsymbol{x}}, \boldsymbol{X}^b + \boldsymbol{s}_0)$ as follows

$$\begin{aligned}
&c(\hat{\boldsymbol{x}} + \delta\boldsymbol{X}, \boldsymbol{X}^b + \boldsymbol{s}_0(\hat{\boldsymbol{x}} + \delta\boldsymbol{X}) + \delta\boldsymbol{s}_1(\hat{\boldsymbol{x}} + \delta\boldsymbol{X}, \boldsymbol{X}) + \delta^2\boldsymbol{s}_2(\hat{\boldsymbol{x}} + \delta\boldsymbol{X}, \boldsymbol{X}) + ...) \\
&\quad = c(\hat{\boldsymbol{x}} + \delta\boldsymbol{X}, \boldsymbol{X}^b + \boldsymbol{s}_0 + \delta(\boldsymbol{s}_1 + \boldsymbol{X}\cdot\nabla_{\boldsymbol{x}}\boldsymbol{s}_0) + \delta^2(\boldsymbol{s}_2 + \boldsymbol{X}\cdot\nabla_{\boldsymbol{x}}\boldsymbol{s}_1 + \boldsymbol{X}\cdot\nabla_{\boldsymbol{x}}\nabla_{\boldsymbol{x}}\boldsymbol{s}_0\cdot\boldsymbol{X})) \\
&\quad = c + \delta\left[\boldsymbol{X}\cdot\nabla_{\boldsymbol{x}}c + (\boldsymbol{s}_1 + \boldsymbol{X}\cdot\nabla_{\boldsymbol{x}}\boldsymbol{s}_0)\cdot\nabla_{\boldsymbol{X}}c\right] + \delta^2[\boldsymbol{X}\cdot\nabla_{\boldsymbol{x}}\nabla_{\boldsymbol{x}}c\cdot\boldsymbol{X} + ... \\
&\qquad + (\boldsymbol{s}_1 + \boldsymbol{X}\cdot\nabla_{\boldsymbol{x}}\boldsymbol{s}_0)\cdot\nabla_{\boldsymbol{X}}\nabla_{\boldsymbol{X}}c\cdot(\boldsymbol{s}_1 + \boldsymbol{X}\cdot\nabla_{\boldsymbol{x}}\boldsymbol{s}_0) + ... \\
&\qquad\quad + (\boldsymbol{s}_2 + \boldsymbol{X}\cdot\nabla_{\boldsymbol{x}}\boldsymbol{s}_1 + \boldsymbol{X}\cdot\nabla_{\boldsymbol{x}}\nabla_{\boldsymbol{x}}\boldsymbol{s}_0\cdot\boldsymbol{X})\cdot\nabla_{\boldsymbol{X}}c] + O(\delta^3).
\end{aligned} \tag{D.1}$$

Substituting the multiple scales expansion (4.20), and performing the expansion (D.1) for all terms, we find

$$\begin{aligned}
&\frac{1}{Pe}\hat{\boldsymbol{n}}_0\cdot\nabla_{\boldsymbol{X}}c_0+\delta\frac{1}{Pe}\hat{\boldsymbol{n}}_0\cdot[\boldsymbol{X}\cdot\nabla_{\boldsymbol{x}}\nabla_{\boldsymbol{X}}c_0+(\boldsymbol{s}_1+\boldsymbol{X}\cdot\nabla_{\boldsymbol{x}}\boldsymbol{s}_0)\cdot\nabla_{\boldsymbol{X}}\nabla_{\boldsymbol{X}}c_0+\nabla_{\boldsymbol{X}}c_1+\nabla_{\boldsymbol{x}}c_0]\\
&\quad+\delta\frac{1}{Pe}\hat{\boldsymbol{n}}_1\cdot\nabla_{\boldsymbol{X}}c_0+\delta^2\frac{1}{Pe}\hat{\boldsymbol{n}}_0\cdot[\boldsymbol{X}\cdot\nabla_{\boldsymbol{x}}\nabla_{\boldsymbol{x}}\nabla_{\boldsymbol{X}}c_0\cdot\boldsymbol{X}+...\\
&\qquad+(\boldsymbol{s}_1+\boldsymbol{X}\cdot\nabla_{\boldsymbol{x}}\boldsymbol{s}_0)\cdot\nabla_{\boldsymbol{X}}\nabla_{\boldsymbol{X}}\nabla_{\boldsymbol{X}}c_0\cdot(\boldsymbol{s}_1+\boldsymbol{X}\cdot\nabla_{\boldsymbol{x}}\boldsymbol{s}_0)+...\\
&\qquad\quad+(\boldsymbol{s}_2+\boldsymbol{X}\cdot\nabla_{\boldsymbol{x}}\boldsymbol{s}_1+\boldsymbol{X}\cdot\nabla_{\boldsymbol{x}}\nabla_{\boldsymbol{x}}\boldsymbol{s}_0\cdot\boldsymbol{X})\cdot\nabla_{\boldsymbol{X}}\nabla_{\boldsymbol{X}}c_0+\boldsymbol{X}\cdot\nabla_{\boldsymbol{x}}(\nabla_{\boldsymbol{X}}c_1+\nabla_{\boldsymbol{x}}c_0)+...\\
&\qquad\qquad+(\boldsymbol{s}_1+\boldsymbol{X}\cdot\nabla_{\boldsymbol{x}}\boldsymbol{s}_0)\cdot\nabla_{\boldsymbol{X}}(\nabla_{\boldsymbol{X}}c_1+\nabla_{\boldsymbol{x}}c_0)+\nabla_{\boldsymbol{X}}c_2+\nabla_{\boldsymbol{x}}c_1]+...\\
&\qquad\qquad\quad+\delta^2\frac{1}{Pe}\hat{\boldsymbol{n}}_1\cdot[\boldsymbol{X}\cdot\nabla_{\boldsymbol{x}}\nabla_{\boldsymbol{X}}c_0+(\boldsymbol{s}_1+\boldsymbol{X}\cdot\nabla_{\boldsymbol{x}}\boldsymbol{s}_0)\cdot\nabla_{\boldsymbol{X}}\nabla_{\boldsymbol{X}}c_0+\nabla_{\boldsymbol{X}}c_1+\nabla_{\boldsymbol{x}}c_0]+...\\
&\qquad\qquad\qquad+\delta^2\frac{1}{Pe}\hat{\boldsymbol{n}}_2\cdot\nabla_{\boldsymbol{X}}c_0=\delta Da(c_0+\delta c_1)+O(\delta^3).
\end{aligned}\tag{D.2}$$

When c_0 is independent of the fast scale, as in sections 4.4.2-4.4.5, (D.2) simplifies considerably to give,

$$\begin{aligned}
&\frac{1}{Pe}\hat{\boldsymbol{n}}_0\cdot\nabla_{\boldsymbol{X}}c_0+\delta\frac{1}{Pe}\hat{\boldsymbol{n}}_0\cdot[\nabla_{\boldsymbol{X}}c_1+\nabla_{\boldsymbol{x}}c_0]+\delta^2\frac{1}{Pe}\hat{\boldsymbol{n}}_0\cdot[\boldsymbol{X}\cdot\nabla_{\boldsymbol{x}}(\nabla_{\boldsymbol{X}}c_1+\nabla_{\boldsymbol{x}}c_0)+...\\
&\qquad+(\boldsymbol{s}_1+\boldsymbol{X}\cdot\nabla_{\boldsymbol{x}}\boldsymbol{s}_0)\cdot\nabla_{\boldsymbol{X}}\nabla_{\boldsymbol{X}}c_1+\nabla_{\boldsymbol{X}}c_2+\nabla_{\boldsymbol{x}}c_1]+...\\
&\qquad\qquad+\delta^2\frac{1}{Pe}\hat{\boldsymbol{n}}_1\cdot[\nabla_{\boldsymbol{X}}c_1+\nabla_{\boldsymbol{x}}c_0]=\delta Da(c_0+\delta c_1)+O(\delta^3).
\end{aligned}\tag{D.3}$$

Bibliography

[1] Creative commons license. `http://creativecommons.org/licenses/by/4.0/`. Accessed: 2023-03-16.

[2] R. I. Abousleiman, Y. Reyes, P. McFetridge, and V. Sikavitsas. Tendon tissue engineering using cell-seeded umbilical veins cultured in a mechanical stimulator. *Tissue engineering part A*, 15(4):787–795, 2009.

[3] A. Al-Ani, D. Toms, D. Kondro, J. Thundathil, Y. Yu, and M. Ungrin. Oxygenation in cell culture: Critical parameters for reproducibility are routinely not reported. *PLOS ONE*, 13(10):1–13, 10 2018.

[4] T. Alarcón, H. Byrne, and P. Maini. A cellular automaton model for tumour growth in inhomogeneous environment. *Journal of Theoretical Biology*, 225(2):257–274, 2003.

[5] U. Alon. *An introduction to systems biology: design principles of biological circuits*. Chapman and Hall/CRC, 2006.

[6] J. Alvarado, J. Comtet, E. Langre, and A. E. Hosoi. Nonlinear flow response of soft hair beds. *Nature Physics*, 13(10):1014–1019, 2017.

[7] T. Q. Aminu and D. F. Bahr. Flow-induced bending deformation of electrospun polymeric filtration membranes using the "leaky" bulge test. *Polymer*, 235:124274, 2021.

[8] S. S. Antman. *Nonlinear problems of elasticity*. Applied mathematical sciences (Springer-Verlag New York Inc.) ; v. 107. Springer, New York, 2nd ed. edition, 2005.

[9] G. Artini and D. Broc. A homogenisation method for a fsi problem: Application to a tube bundle row. *Pressure Vessels and Piping Conference*, 5: High-Pressure Technology; ASME Nondestructive Evaluation, Diagnosis and Prognosis Division (NDPD); SPC Track for Senate, 2017.

[10] G. Artini and D. Broc. Fluid Structure Interaction Homogenization for Tube Bundles: Significant Dissipative Effects. *Pressure Vessels and Piping Conference*, 4: Fluid-Structure Interaction, 2018.

[11] Y. Asano, K. Okada, and M. Inaba. Design principles of a human mimetic humanoid: Humanoid platform to study human intelligence and internal body system. *Science Robotics*, 2(13), 2017.

[12] J. Auriault and P. Adler. Taylor dispersion in porous media: Analysis by multiple scale expansions. *Advances in Water Resources*, 18(4):217–226, 1995.

[13] L. Auton, S. Pramanik, M. Dalwadi, C. MacMinn, and I. Griffiths. A homogenised model for flow, transport and sorption in a heterogeneous porous medium. *Journal of Fluid Mechanics*, 932:A34, 2022.

[14] A. J. Banes, K. Donlon, G. W. Link, Y. Gillespie, A. G. Bevin, H. D. Peterson, D. Bynum, S. Watts, and L. Dahners. Cell populations of tendon: a simplified method for isolation of synovial cells and internal fibroblasts: confirmation of origin and biologic properties. *Journal of Orthopaedic Research*, 6(1):83–94, 1988.

[15] J. J. Bara and F. Guilak. Chapter 10 - engineering functional tissues: in vitro culture parameters. In R. Lanza, R. Langer, J. P. Vacanti, and A. Atala, editors, *Principles of Tissue Engineering (Fifth Edition)*, pages 157–177. Academic Press, fifth edition edition, 2020.

[16] S. I. Barry and M. Holmes. Asymptotic behaviour of thin poroelastic layers . *IMA Journal of Applied Mathematics*, 66(2):175–194, 04 2001.

[17] T. P. Bennett, G. D'Alessandro, and K. R. Daly. Multiscale models of metallic particles in nematic liquid crystals. *SIAM Journal on Applied Mathematics*, 78(2):1228–1255, 2018.

[18] R. A. Bloodgood. Sensory reception is an attribute of both primary cilia and motile cilia. *Journal of cell science*, 123(4):505–509, 2010.

[19] C. Boutin and H. Wong. Study of thermosensitive heterogeneous media via space-time homogenization. *European Journal of Mechanics - A/Solids*, 17(6):939–968, 1998.

[20] M. Bruna and S. J. Chapman. Diffusion in spatially varying porous media. *SIAM Journal on Applied Mathematics*, 75(4):1648–1664, 2015.

[21] R. Burridge and J. B. Keller. Poroelasticity equations derived from microstructure. *The Journal of the Acoustical Society of America*, 70(4):1140–1146, 1981.

[22] A. Carr, C. Cooper, M. K. Campbell, J. Rees, J. Moser, D. J. Beard, R. Fitzpatrick, A. Gray, J. Dawson, J. Murphy, H. Bruhn, D. Cooper, and C. Ramsay. Effectiveness of open and arthroscopic rotator cuff repair (UKUFF). *The Bone & Joint Journal*, 99-B(1):107–115, 2017.

[23] K. Chamsri and L. S. Bennethum. Permeability of fluid flow through a periodic array of cylinders. *Applied Mathematical Modelling*, 39(1):244–254, 2015.

[24] S. J. Chapman and S. E. McBurnie. A unified multiple-scales approach to one-dimensional composite materials and multiphase flow. *SIAM Journal on Applied Mathematics*, 71(1):200–217, 2011.

[25] S. J. Chapman and S. E. McBurnie. Integral constraints in multiple-scales problems. *European Journal of Applied Mathematics*, 26(5):595–614, 2015.

[26] H.-C. Chen and Y.-C. Hu. Bioreactors for tissue engineering. *Biotechnology letters*, 28(18):1415–1423, 2006.

[27] W. Chen and J. Fish. A Dispersive Model for Wave Propagation in Periodic Heterogeneous Media Based on Homogenization With Multiple Spatial and Temporal Scales . *Journal of Applied Mechanics*, 68(2):153–161, 08 2000.

[28] S. Chung and M. W. King. Design concepts and strategies for tissue engineering scaffolds. *Biotechnology and applied biochemistry*, 58(6):423–438, 2011.

[29] M. R. Citeroni, M. C. Ciardulli, V. Russo, G. Della Porta, A. Mauro, M. El Khatib, M. Di Mattia, D. Galesso, C. Barbera, N. R. Forsyth, N. Maffulli, and B. Barboni. In vitro innovation of tendon tissue engineering strategies. *International Journal of Molecular Sciences*, 21(18):6726, Sep 2020.

[30] J. Collis, D. L. Brown, M. E. Hubbard, and R. D. O'Dea. Effective equations governing an active poroelastic medium. *Proceedings of the Royal Society A: Mathematical, Physical and Engineering Sciences*, 473(2198):20160755, 2017.

[31] J. Collis, M. E. Hubbard, and R. D. O'Dea. A multi-scale analysis of drug transport and response for a multi-phase tumour model. *European Journal of Applied Mathematics*, 28(3):499–534, 2017.

[32] J. L. Cook, E. Rio, C. R. Purdam, and S. I. Docking. Revisiting the continuum model of tendon pathology: what is its merit in clinical practice and research? *British Journal of Sports Medicine*, 50(19):1187–1191, 2016.

[33] S. W. Crawley, M. S. Mooseker, and M. J. Tyska. Shaping the intestinal brush border. *Journal of Cell Biology*, 207(4):441–451, 2014.

[34] M. P. Dalwadi. Asymptotic homogenization with a macroscale variation in the microscale. In A. Gerisch, R. Penta, and J. Lang, editors, *Multiscale Models in Mechano and Tumor Biology*, pages 27–43, Cham, 2017. Springer International Publishing.

[35] M. P. Dalwadi, M. Bruna, and I. M. Griffiths. A multiscale method to calculate filter blockage. *Journal of Fluid Mechanics*, 809:264–289, 2016.

[36] M. P. Dalwadi, I. M. Griffiths, and M. Bruna. Understanding how porosity gradients can make a better filter using homogenization theory. *Proceedings of the Royal Society A: Mathematical, Physical and Engineering Sciences*, 471(2182), 2015.

[37] M. P. Dalwadi, J. R. King, R. J. Dyson, and K. P. Arkill. Mathematical model to determine the effect of a sub-glycocalyx space. *Physical Review Fluids*, 5(4):043103, 2020.

[38] K. Daly and T. Roose. Determination of macro-scale soil properties from pore-scale structures: model derivation. *Proceedings of the Royal Society A: Mathematical, Physical and Engineering Sciences*, 474(2209):20170141, 2018.

[39] H. F. Davis, A. D. Snider, and C. T. Davis. *Introduction to vector analysis*. Allyn and Bacon London, 1979.

[40] E. Detournay and A. H.-D. Cheng. *Comprehensive Rock Engineering: Principles, Practice and Projects. Chapter 5: Fundamentals of Poroelasticity*, volume II. Oxford ; New York : Pergamon Press, 1993.

[41] A. C. Devkota and P. S. Weinhold. A tissue explant system for assessing tendon overuse injury. *Medical engineering & physics*, 27(9):803–808, 2005.

[42] Y. Ding, J. C. Nawroth, M. J. McFall-Ngai, and E. Kanso. Mixing and transport by ciliary carpets: a numerical study. *Journal of Fluid Mechanics*, 743:124–140, 2014.

[43] J. Drummond and M. Tahir. Laminar viscous flow through regular arrays of parallel solid cylinders. *International Journal of Multiphase Flow*, 10(5):515–540, 1984.

[44] Z. Du, Y. Duan, Q. Yan, A. M. Weinstein, S. Weinbaum, and T. Wang. Mechanosensory function of microvilli of the kidney proximal tubule. *Proceedings of the National Academy of Sciences*, 101(35):13068–13073, 2004.

[45] O. du Roure, A. Lindner, E. N. Nazockdast, and M. J. Shelley. Dynamics of Flexible Fibers in Viscous Flows and Fluids. *Annual Review of Fluid Mechanics*, 51(1):539–572, Jan 2019.

[46] N. A. Dyment, J. G. Barrett, H. A. Awad, C. A. Bautista, A. J. Banes, and D. L. Butler. A brief history of tendon and ligament bioreactors: Impact and future prospects. *Journal of Orthopaedic Research*, 38(11):2318–2330, 2020.

[47] J. Eggers and M. A. Fontelos. *Local singular expansions*, page 89–114. Cambridge Texts in Applied Mathematics. Cambridge University Press, 2015.

[48] T. Fatima, N. Arab, E. P. Zemskov, and A. Muntean. Homogenization of a reaction–diffusion system modeling sulfate corrosion of concrete in locally periodic perforated domains. *Journal of Engineering Mathematics*, 69(2):261–276, 2011.

[49] J. A. Florian, J. R. Kosky, K. Ainslie, Z. Pang, R. O. Dull, and J. M. Tarbell. Heparan sulfate proteoglycan is a mechanosensor on endothelial cells. *Circulation research*, 93(10):e136–e142, 2003.

[50] J. L. Fuchs and H. D. Schwark. Neuronal primary cilia: a review. *Cell biology international*, 28(2):111–118, 2004.

[51] C. Geuzaine and J.-F. Remacle. Gmsh: A 3-d finite element mesh generator with built-in pre-and post-processing facilities. *International journal for numerical methods in engineering*, 79(11):1309–1331, 2009.

[52] A. Gopinath and L. Mahadevan. Elastohydrodynamics of wet bristles, carpets and brushes. *Proceedings of the Royal Society A: Mathematical, Physical and Engineering Sciences*, 467(2130):1665–1685, 2011.

[53] P. Guo, A. Weinstein, and S. Weinbaum. A hydrodynamic mechanosensory hypothesis for brush border microvilli. *American Journal of Physiology-Renal Physiology*, 279(4):F698–F712, 2000.

[54] C. A. d. S. Haemmerle, M. I. Nogueira, and I.-s. Watanabe. The neural elements in the lining of the ventricular-subventricular zone: making an old story new by high-resolution scanning electron microscopy. *Frontiers in Neuroanatomy*, 9:134, 2015.

[55] Y. Han, S. Weinbaum, J. A. Spaan, and H. Vink. Large-deformation analysis of the elastic recoil of fibre layers in a brinkman medium with application to the endothelial glycocalyx. *Journal of Fluid Mechanics*, 554:217–235, 2006.

[56] J. A. Hannafin, S. P. Arnoczky, A. Hoonjan, and P. A. Torzilli. Effect of stress deprivation and cyclic tensile loading on the material and morphologic

properties of canine flexor digitorum profundus tendon: an in vitro study. *Journal of Orthopaedic Research*, 13(6):907–914, 1995.

[57] J. Happel. Viscous flow relative to arrays of cylinders. *AIChE Journal*, 5(2):174–177, 1959.

[58] J. R. Hazel and B. D. Sidell. A method for the determination of diffusion coefficients for small molecules in aqueous solution. *Analytical Biochemistry*, 166(2):335–341, 1987.

[59] Y. Higuchi. Chromosomal dna fragmentation in apoptosis and necrosis induced by oxidative stress. *Biochemical pharmacology*, 66(8):1527–1535, 2003.

[60] E. C. Holden, S. J. Chapman, B. S. Brook, and R. D. O'Dea. A multiphase multiscale model for nutrient-limited tissue growth, part ii: A simplified description. *The ANZIAM Journal*, 61(4):368–381, 2019.

[61] E. C. Holden, J. Collis, B. S. Brook, and R. D. O'Dea. A multiphase multiscale model for nutrient limited tissue growth. *The ANZIAM Journal*, 59(4):499–532, 2018.

[62] M. H. Holmes. *Introduction to Perturbation Methods*, volume 20 of *Texts in Applied Mathematics*. Springer, New York, NY, 2 edition, 2013.

[63] K. Hood, M. S. S. Jammalamadaka, and A. E. Hosoi. Marine crustaceans with hairy appendages: Role of hydrodynamic boundary layers in sensing and feeding. *Physical Review Fluids*, 4:114102, 2019.

[64] U. Hornung. *Homogenization and porous media*. Interdisciplinary applied mathematics ; v. 6. Springer, New York, 1996.

[65] A. E. Hosoi. Corrsin lecture on hairy hydrodynamics. *Physical Review Fluids*, 4:110508, 2019.

[66] S. Izumi, S. Otsuru, N. Adachi, N. Akabudike, and M. Enomoto-Iwamoto. Control of glucose metabolism is important in tenogenic differentiation of progenitors derived from human injured tendons. *PLOS ONE*, 14(3):1–15, 03 2019.

[67] H. Jóhannesson and B. Halle. Solvent diffusion in ordered macrofluids: A stochastic simulation study of the obstruction effect. *The Journal of Chemical Physics*, 104(17):6807–6817, 1996.

[68] J. B. Keller. Darcy's law for flow in porous media and the two-space method. In *Nonlinear partial differential equations in engineering and applied science*, pages 429–443. Routledge, 1980.

[69] J. B. Keller. Large amplitude motion of a string. *American Journal of Physics*, 27(8):584–586, 1959.

[70] K. Kellner, G. Liebsch, I. Klimant, O. S. Wolfbeis, T. Blunk, M. B. Schulz, and A. Göpferich. Determination of oxygen gradients in engineered tissue using a fluorescent sensor. *Biotechnology and Bioengineering*, 80(1):73–83, 2002.

[71] K. B. Kiradjiev, C. J. Breward, I. Griffiths, and D. W. Schwendeman. A homogenized model for a reactive filter. *SIAM Journal on Applied Mathematics*, 81(2):591–619, 2021.

[72] M. Lavagnino, M. E. Wall, D. Little, A. J. Banes, F. Guilak, and S. P. Arnoczky. Tendon mechanobiology: Current knowledge and future research opportunities. *Journal of Orthopaedic Research*, 33(6):813–822, 2015.

[73] A. Lindner and M. Shelley. Elastic fibers in flows. *Fluid-structure interactions in low-Reynolds-number flows*, 168, 2015.

[74] A. Lomas, C. Ryan, A. Sorushanova, N. Shologu, A. Sideri, V. Tsioli, G. Fthenakis, A. Tzora, I. Skoufos, L. Quinlan, G. O'Laighin, A. Mullen, J. Kelly, S. Kearns, M. Biggs, A. Pandit, and D. Zeugolis. The past, present and future in scaffold-based tendon treatments. *Advanced Drug Delivery Reviews*, 84:257 – 277, 2015. Scaffolds, cells, biologics: At the crossroads of musculoskeletal repair.

[75] U. G. Longo, F. Olivia, V. Denaro, and N. Maffulli. Oxygen species and overuse tendinopathy in athletes. *Disability and rehabilitation*, 30(20-22):1563–1571, 2008.

[76] . Lord Rayleigh Sec. R.S. On the influence of obstacles arranged in rectangular order upon the properties of a medium. *The London, Edinburgh, and Dublin Philosophical Magazine and Journal of Science*, 34(211):481–502, 1892.

[77] E. Luckins, C. J. W. Breward, I. M. Griffiths, and Z. Wilmott. Homogenisation problems in reactive decontamination. *European Journal of Applied Mathematics*, 31(5):782–805, 2020.

[78] T. Lévy. Fluid flow through an array of fixed particles. *International Journal of Engineering Science*, 21(1):11–23, 1983.

[79] R. Ma, R. Chow, L. Choi, and D. Diduch. Arthroscopic rotator cuff repair: Suture anchor properties, modes of failure and technical considerations. *Expert Review of Medical Devices*, 8(3):377–387, 2011.

[80] S. A. Malingen, K. Hood, E. Lauga, A. Hosoi, and T. L. Daniel. Fluid flow in the sarcomere. *Archives of Biochemistry and Biophysics*, 706:108923, 2021.

[81] Y. Man and E. Kanso. Multisynchrony in active microfilaments. *Physical Review Letters*, 125(14):148101, 2020.

[82] I. Martin, D. Wendt, and M. Heberer. The role of bioreactors in tissue engineering. *TRENDS in Biotechnology*, 22(2):80–86, 2004.

[83] C. C. Mei and B. Vernescu. *Homogenization methods for multiscale mechanics*. World scientific, 2010.

[84] P. A. Mouthuy, N. Zargar, O. Hakimi, E. Lostis, and A. J. Carr. Fabrication of continuous electrospun filaments with potential for use as medical fibres. *Biofabrication*, 2015.

[85] P.-A. Mouthuy, S. Snelling, R. Hostettler, A. Kharchenko, S. Salmon, A. Wainman, J. Mimpen, C. Paul, and A. Carr. Humanoid robots to mechanically stress human cells grown in soft bioreactors. *Communications Engineering*, 1(1):1–11, 2022.

[86] J. D. Murray. *Mathematical biology. I, An introduction [electronic resource].* Interdisciplinary applied mathematics ; 17. Springer, New York ; London, 3rd ed. edition, 2002.

[87] A. Nasto, P.-T. Brun, and A. E. Hosoi. Viscous entrainment on hairy surfaces. *Physical Review Fluids*, 3:024002, 2018.

[88] A. Nasto, M. Regli, P.-T. Brun, J. Alvarado, C. Clanet, and A. E. Hosoi. Air entrainment in hairy surfaces. *Physical Review Fluids*, 1:033905, Jul 2016.

[89] E. Nazockdast, A. Rahimian, D. Needleman, and M. Shelley. Cytoplasmic flows as signatures for the mechanics of mitotic positioning. *Molecular Biology of the Cell*, 28(23):3261–3270, 2017.

[90] H. Ockendon and E. L. Terrill. A mathematical model for the wet-spinning process. *European Journal of Applied Mathematics*, 4(4):341–360, 1993.

[91] R. D. O'Dea, M. R. Nelson, A. J. El Haj, S. L. Waters, and H. M. Byrne. A multiscale analysis of nutrient transport and biological tissue growth in vitro. *Mathematical Medicine and Biology: A Journal of the IMA*, 32(3):345–366, 10 2014.

[92] R. O'Dea, H. Byrne, and S. Waters. *Continuum Modelling of In Vitro Tissue Engineering: A Review*, pages 229–266. Springer Berlin Heidelberg, Berlin, Heidelberg, 2013.

[93] M. J. Osiecki, S. D. McElwain, and W. B. Lott. Modelling mesenchymal stromal cell growth in a packed bed bioreactor with a gas permeable wall. *PloS one*, 13(8):e0202079, 2018.

[94] N. C. Pearson, R. J. Shipley, S. L. Waters, and J. M. Oliver. Multiphase modelling of the influence of fluid flow and chemical concentration on tissue growth in a hollow fibre membrane bioreactor. *Mathematical Medicine and Biology: A Journal of the IMA*, 31(4):393–430, 09 2013.

[95] N. Pellicciotta, D. Das, J. Kotar, M. Faucourt, N. Spassky, E. Lauga, and P. Cicuta. Cilia density and flow velocity affect alignment of motile cilia from brain cells. *Journal of Experimental Biology*, 223(24):jeb229310, 2020.

[96] R. Penta, D. Ambrosi, and R. J. Shipley. Effective governing equations for poroelastic growing media. *Quarterly Journal of Mechanics and Applied Mathematics*, 67(1):69–91, 2014.

[97] M. A. Peter and M. Böhm. Multiscale modelling of chemical degradation mechanisms in porous media with evolving microstructure. *Multiscale Modeling & Simulation*, 7(4):1643–1668, 2009.

[98] G. Printsypar, M. Bruna, and I. M. Griffiths. The influence of porous-medium microstructure on filtration. *Journal of Fluid Mechanics*, 861:484–516, 2019.

[99] N. Ray, T. van Noorden, F. Frank, and P. Knabner. Multiscale modeling of colloid and fluid dynamics in porous media including an evolving microstructure. *Transport in Porous Media*, pages 669–696, 2012.

[100] G. Richardson and S. J. Chapman. Derivation of the bidomain equations for a beating heart with a general microstructure. *SIAM Journal on Applied Mathematics*, 71(3):657–675, 2011.

[101] C. M. Rooney, C. P. Please, and S. D. Howison. Homogenisation applied to thermal radiation in porous media. *European Journal of Applied Mathematics*, 32(5):784–805, 2021.

[102] L. A. Rossi, S. A. Rodeo, J. Chahla, and M. Ranalletta. Current Concepts in Rotator Cuff Repair Techniques: Biomechanical, Functional, and Structural Outcomes. *Orthopaedic Journal of Sports Medicine*, 7(9):1–8, 2019.

[103] A. M. S., J. Blechta, J. Hake, A. Johansson, K. B., A. Logg, R. C., J. Ring, M. E. Rognes, and G. N. Wells. The fenics project version 1.5. *Archive of Numerical Software*, 3(100), 2015.

[104] H. Sano, I. Wakabayashi, and E. Itoi. Stress distribution in the supraspinatus tendon with partial-thickness tears: an analysis using two-dimensional finite element model. *Journal of shoulder and elbow surgery*, 15(1):100–105, 2006.

[105] A. D. Schoenenberger, J. Foolen, P. Moor, U. Silvan, and J. G. Snedeker. Substrate fiber alignment mediates tendon cell response to inflammatory signaling. *Acta biomaterialia*, 71:306–317, 2018.

[106] R. Schulz and P. Knabner. An effective model for biofilm growth made by chemotactical bacteria in evolving porous media. *SIAM Journal on Applied Mathematics*, 77(5):1653–1677, 2017.

[107] R. Schulz, N. Ray, F. Frank, H. S. Mahato, and P. Knabner. Strong solvability up to clogging of an effective diffusion–precipitation model in an evolving porous medium. *European Journal of Applied Mathematics*, 28(2):179–207, 2017.

[108] A. Scott, K. Khan, J. Heer, J. Cook, O. Lian, and V. Duronio. High strain mechanical loading rapidly induces tendon apoptosis: an ex vivo rat tibialis anterior model. *British Journal of Sports Medicine*, 39(5):e25–e25, 2005.

[109] H. R. Screen, J. C. Shelton, D. L. Bader, and D. A. Lee. Cyclic tensile strain upregulates collagen synthesis in isolated tendon fascicles. *Biochemical and biophysical research communications*, 336(2):424–429, 2005.

[110] A. Shafiee and A. Atala. Tissue engineering: Toward a new era of medicine. *Annual Review of Medicine*, 68(1):29–40, 2017.

[111] M. Shakeel, P. C. Matthews, R. S. Graham, and S. L. Waters. A continuum model of cell proliferation and nutrient transport in a perfusion bioreactor. *Mathematical Medicine and Biology: A Journal of the IMA*, 30(1):21–44, 10 2011.

[112] R. J. Shipley and S. J. Chapman. Multiscale modelling of fluid and drug transport in vascular tumours. *Bulletin of Mathematical Biology*, 72(6):1464–1491, August 2010.

[113] R. J. Shipley and S. L. Waters. Fluid and mass transport modelling to drive the design of cell-packed hollow fibre bioreactors for tissue engineering applications. *Mathematical Medicine and Biology: A Journal of the IMA*, 29(4):329–359, 11 2011.

[114] J. G. Snedeker and J. Foolen. Tendon injury and repair – A perspective on the basic mechanisms of tendon disease and future clinical therapy. *Acta Biomaterialia*, 63:18–36, 2017.

[115] E. M. Sparrow and A. L. Loeffler JR. Longitudinal laminar flow between cylinders arranged in regular array. *AIChE Journal*, 5(3):325–330, 1959.

[116] E. M. Spiesz, C. T. Thorpe, S. Chaudhry, G. P. Riley, H. L. Birch, P. D. Clegg, and H. Screen. Tendon extracellular matrix damage, degradation and inflammation in response to in vitro overload exercise. *Journal of Orthopaedic Research*, 33(6):889–897, 2015.

[117] D. B. Stein and M. J. Shelley. Coarse graining the dynamics of immersed and driven fiber assemblies. *Physical Review Fluids*, 4:073302, 2019.

[118] H. Suhaimi, S. Wang, and D. B. Das. Glucose diffusivity in cell culture medium. *Chemical Engineering Journal*, 269:323–327, 2015.

[119] A. Szaniawski. Equations of steady flow through slightly curved multifilament bundles. *Archives of Mechanics*, 29:519–530, 1977.

[120] E. L. Terrill and J. G. Byatt-Smith. A mathematical model for washing a tow of fibres: Part 1. *European Journal of Applied Mathematics*, 5(4):525–535, 1994.

[121] C. T. Thorpe and H. R. C. Screen. *Metabolic Influences on Risk for Tendon Disorders*. Springer International Publishing, Cham, 2016.

[122] C. Thorpe, P. Clegg, and H. Birch. A review of tendon injury: why is the equine superficial digital flexor tendon most at risk? *Equine veterinary journal*, 42(2):174–180, 2010.

[123] Y. Ueda, A. Inui, Y. Mifune, R. Sakata, T. Muto, Y. Harada, F. Takase, T. Kataoka, T. Kokubu, and R. Kuroda. The effects of high glucose condition on rat tenocytes in vitro and rat achilles tendon in vivo. *Bone & joint research*, 7(5):362–372, June 2018.

[124] T. L. van Noorden. Crystal precipitation and dissolution in a porous medium: effective equations and numerical experiments. *Multiscale Modeling & Simulation*, 7(3):1220–1236, 2009.

[125] D. Voet and J. G. Voet. *Biochemistry*, chapter 17. Wiley, 2011.

[126] T. Wang, B. S. Gardiner, Z. Lin, J. Rubenson, T. B. Kirk, A. Wang, D. W. Xu, J.and Smith, D. G. Lloyd, and M. H. Zheng. Bioreactor design for tendon/ligament engineering. *Tissue engineering. Part B, Reviews*, 19:133–146, 2013.

[127] S. Weinbaum, Y. Duan, L. M. Satlin, T. Wang, and A. M. Weinstein. Mechanotransduction in the renal tubule. *American Journal of Physiology-Renal Physiology*, 299(6):F1220–F1236, 2010.

[128] S. Weinbaum, J. M. Tarbell, and E. R. Damiano. The structure and function of the endothelial glycocalyx layer. *Annual Review of Biomedical Engineering*, 9:121–167, 2007.

[129] S. Weinbaum, X. Zhang, Y. Han, H. Vink, and S. C. Cowin. Mechanotransduction and flow across the endothelial glycocalyx. *Proceedings of the National Academy of Sciences*, 100(13):7988–7995, 2003.

[130] S. Whitaker. The transport equations for multi-phase systems. *Chemical Engineering Science*, 28(1):139–147, 1973.

[131] R. J. Whittaker, R. Booth, R. Dyson, C. Bailey, L. Parsons Chini, S. Naire, S. Payvandi, Z. Rong, H. Woollard, L. J. Cummings, S. L. Waters, L. Mawasse, J. B. Chaudhuri, M. J. Ellis, V. Michael, N. J. Kuiper, and S. Cartmell. Mathematical modelling of fibre-enhanced perfusion inside a tissue-engineering bioreactor. *Journal of Theoretical Biology*, 256(4):533–546, 2009.

[132] S. Wolfram. Cellular automata as models of complexity. *Nature*, 311(5985):419–424, October 1984.

[133] E. Yamamoto, K. Hayashi, and N. Yamamoto. Effects of stress shielding on the transverse mechanical properties of rabbit patellar tendons. *Journal of biomechanical engineering*, 122(6):608–614, 2000.

[134] G. Yang, R. C. Crawford, and J. H. Wang. Proliferation and collagen production of human patellar tendon fibroblasts in response to cyclic uniaxial stretching in serum-free conditions. *Journal of biomechanics*, 37(10):1543–1550, 2004.

[135] R. S. Yerrabelli, S. M. Somers, W. L. Grayson, and A. A. Spector. Modeling the mechanics of fibrous-porous scaffolds for skeletal muscle regeneration. *Medical & Biological Engineering & Computing*, 59(1):131–142, 2021.

[136] D. W. Youngstrom and J. G. Barrett. Engineering tendon: scaffolds, bioreactors, and models of regeneration. *Stem Cells International*, 2016, 2016.

[137] Y. Yu, L. Lin, Y. Zhou, X. Lu, X. Shao, C. Lin, K. Yu, X. Zhang, J. Hong, and Y. Chen. Effect of hypoxia on self-renewal capacity and differentiation in human tendon-derived stem cells. *Medical science monitor : international medical journal of experimental and clinical research*, 23:1334–1339, March 2017.

[138] D. Yuan, S. M. Somers, W. L. Grayson, and A. A. Spector. A poroelastic model of a fibrous-porous tissue engineering scaffold. *Scientific reports*, 8(1):1–10, 2018.

[139] K. Zhang, M. W. Hast, S. Izumi, Y. Usami, S. Shetye, N. Akabudike, N. J. Philp, M. Iwamoto, I. Nissim, L. J. Soslowsky, and M. Enomoto-Iwamoto. Modulating glucose metabolism and lactate synthesis in injured mouse tendons: Treatment with dichloroacetate, a lactate synthesis inhibitor, improves tendon healing. *The American Journal of Sports Medicine*, 46(9):2222–2231, 2018.

[140] Y. Zhang, B. Wang, W. J. Zhang, G. Zhou, Y. Cao, and W. Liu. Enhanced proliferation capacity of porcine tenocytes in low o2 tension culture. *Biotechnology Letters*, 32(2):181–187, February 2010.